



Thèse

2024

Open Access

This version of the publication is provided by the author(s) and made available in accordance with the copyright holder(s).

---

## Exploring Ferroelectric Domain-Wall Dynamics through Power-Law Distributions via Scanning Probe Microscopy

---

Bulanadi, Ralph Adam Yap

### How to cite

BULANADI, Ralph Adam Yap. Exploring Ferroelectric Domain-Wall Dynamics through Power-Law Distributions via Scanning Probe Microscopy. Doctoral Thesis, 2024. doi: 10.13097/archive-ouverte/unige:179348

This publication URL: <https://archive-ouverte.unige.ch/unige:179348>

Publication DOI: [10.13097/archive-ouverte/unige:179348](https://doi.org/10.13097/archive-ouverte/unige:179348)

# Exploring Ferroelectric Domain-Wall Dynamics through Power-Law Distributions via Scanning Probe Microscopy

THÈSE

*présentée à la Faculté des Sciences de l'Université de Genève  
pour obtenir le grade de docteur ès Sciences, mention Physique*

par

**Ralph Bulanadi**  
de  
Auckland (Nouvelle-Zélande)

Thèse n° 5836



**UNIVERSITÉ  
DE GENÈVE**

**FACULTÉ DES SCIENCES**

DOCTORAT ÈS SCIENCES, MENTION PHYSIQUE

**Thèse de Monsieur Ralph Adam Yap BULANADI**

intitulée :

**«Exploring Ferroelectric  
Domain-Wall Dynamics through  
Power-Law Distributions via  
Scanning Probe Microscopy»**

La Faculté des sciences, sur le préavis de

Madame P. PARUCH, professeure associée et directrice de thèse  
Département de physique de la matière quantique

Monsieur T. GIAMARCHI, professeur ordinaire  
Département de physique de la matière quantique

Monsieur R. VASUDEVAN, docteur  
Center for Nanophase Materials Sciences, Oak Ridge National Laboratory, Tennessee,  
United States

Madame M. ARREDONDO, docteur  
Centre for Quantum Materials and Technologies (CQMT), School of Mathematics and  
Physics, Queen's University Belfast, Belfast, Ireland

autorise l'impression de la présente thèse, sans exprimer d'opinion sur les propositions qui y sont énoncées.

Genève, le 23 juillet 2024

**Thèse - 5836 -**

**Le Décanat**

---

## Résumé (en Français)

---

Nous utilisons ici la microscopie à sonde à balayage, sensible aux propriétés structurales et fonctionnelles des domaines ferroélectriques, afin de modifier, mesurer et caractériser la variété des transitions (et des comportements de type transition dans la dynamique hautement non linéaire qui accompagne l'inversion ou la commutation de la polarisation) observées, dans le but final de mieux comprendre ces transitions à l'échelle nanométrique, pour leur universalité à d'autres systèmes et leur applicabilité à d'éventuels dispositifs futurs.

Dans le chapitre 2, nous commençons par une brève introduction aux ferroélectriques et à la ferroélectricité, avec un accent particulier sur l'épitaxie de couches minces et les matériaux ferroélectriques que sont le titanate de plomb et la ferrite de bismuth. Nous passons ensuite à une introduction complète aux distributions de loi de puissance et à leur analyse, ainsi qu'à la manière dont elles se caractérisent et sont pertinentes pour les matériaux ferroélectriques en termes de dynamique de commutation de polarisation et, plus généralement, de déformation plastique sous contrainte.

Dans le chapitre 3, nous fournissons au lecteur le contexte expérimental de base nécessaire pour effectuer les différentes mesures réalisées au cours de cette thèse. Nous nous concentrons ici sur deux types d'expériences : la microscopie à sonde locale, que nous utilisons pour imager les échantillons et leurs configurations de domaines ferroélectriques ; et la diffraction des rayons X, que nous utilisons pour imager et confirmer la structure cristallographique de nos matériaux.

Après ces chapitres introductifs, nous passons aux résultats techniques et scientifiques de cette thèse. Dans le chapitre 4, nous détaillons la production et les capacités de *Hystorian*, un outil de traitement et un package Python développé en collaboration avec Loïc Musy pour optimiser et améliorer les vastes quantités de traitement de données au cœur de nos deux thèses. Ce travail, particulièrement axé sur l'analyse de la microscopie à sonde locale et



## 0. Résumé (en Français)

---

de la diffraction des rayons X, nous a permis à tous les deux d'améliorer la qualité et la clarté de nos résultats scientifiques.

Dans le chapitre 5, nous nous concentrons ensuite sur la dynamique des loi de puissance appliquées aux ensembles de données bidimensionnels. Nous nous demandons, à supposer que nous ayons une dynamique de loi de puissance dans un ensemble de données bidimensionnel, à quoi elle ressemblerait ? Comment savons-nous qu'elle existe ? Et comment la caractériser ? Nous nous concentrons tout d'abord sur la génération de tels ensembles de données d'images bidimensionnelles ayant un comportement suivant une loi de puissance, puis nous étudions les meilleures méthodes d'extraction des relations de puissance par le biais de trois techniques développées en interne que nous appelons la "mise en boîte rectangulaire", la "mise en boîte aléatoire" et le "suivi d'interface". Nous identifions ce dernier processus de suivi des interfaces comme la technique optimale dans la grande majorité des cas, et nous évaluons en outre sa capacité par le biais de différentes méthodologies statistiques. Nous nous concentrons également sur sa réalisation expérimentale et vérifions que cette technique est adaptée à l'étude de la dynamique en loi de puissance du mouvement de la paroi du domaine.

Dans le chapitre 6, nous nous concentrons entièrement sur le mouvement des parois de domaines ferroélectriques à  $180^\circ$  observés par microscopie à sonde locale. Sachant que les statistiques d'avalanche reposent sur le mouvement collectif dans les matériaux désordonnés, nous nous demandons si et comment la génération intentionnelle de défauts de force d'épingle et de dimensionnalité différentes peut affecter la dynamique de commutation. Nous détaillons d'abord la croissance et la caractérisation d'un ensemble de cinq films de titanate de plomb, conçus pour présenter des défauts linéaires épars avec un fort potentiel de pincement, dont quatre ont subi des niveaux variables de bombardement de  $\text{He}^{2+}$  dans le but d'introduire des concentrations variables de défauts ponctuels. Nous utilisons ensuite notre technique de suivi d'interface mise en évidence précédemment pour caractériser leur dynamique de commutation de polarisation ; nous constatons que l'échelle critique globale est universelle pour les cinq échantillons. Nous nous concentrons ensuite sur le mouvement local des parois de domaine et identifions des différences caractéristiques dans la localisation spatiale de ces événements de commutation entre les échantillons bombardés et non bombardés, car les défauts ponctuels interagissent avec les défauts linéaires et modulent le paysage potentiel auquel sont soumises les parois de domaine de  $180$  degrés.

Dans le chapitre 7, nous utilisons la microscopie à sonde locale pour étudier une transition de phase différente dans un matériau ferroélectrique - la transition structurelle de type martensitique entre la phase de type tétragonale et la phase de type rhomboédrique dans le ferrite de bismuth sous application d'une contrainte. Nous utilisons un microscope à force atomique

---

de nouvelle génération, utilisant un interféromètre différentiel à quadrature de phase, pour mesurer la déformation plastique de films à couches minces de titanate de plomb à bombardement de défauts précédemment développés, et nous montrons un comportement d'avalanche bien prédit par la théorie du champ moyen. Nous utilisons ensuite cette même méthodologie sur des ferrites de bismuth stabilisées par des défauts et présentant principalement une phase de type tétragonal, et nous mesurons et vérifions les caractéristiques d'échelle lorsque la déformation plastique s'accompagne d'une transition de type martensitique.

Enfin, dans le chapitre 8, nous discutons brièvement d'une collection de travaux inachevés et futurs, tous liés aux outils informatiques et aux expériences automatisées. Nous mettons d'abord en évidence certains résultats d'études sur le mouvement des parois de domaine dans le ferrite de bismuth, et montrons comment sa structure rhomboédrique permet une dynamique des parois de domaine plus compliquée, mais corrélée, et l'évolution des caractéristiques des parois de domaine entre 71, 109 et 180 degrés. Nous expliquons également comment l'intégration de l'analyse dans la mesure permet une acquisition de données de meilleure qualité. Enfin, nous nous attarderons sur les outils supplémentaires développés pour imager, visualiser et interpréter les structures cristallographiques à partir d'études de diffraction des rayons X.

En résumé, cette thèse vise à compiler une collection de mes travaux sur la dynamique des lois de puissance qui se produisent dans les films minces ferroélectriques. Avec la microscopie à sonde locale comme outil de choix, nous espérons que ce travail détaille les améliorations techniques clés dans la mesure et l'analyse de la dynamique des lois de puissance, et les découvertes scientifiques clés dans la description du comportement de leurs domaines ferroélectriques et structurels.

*For those who've inspired me,  
those who've sacrificed for me,  
those who've made me,  
And for those who are yet to come.*

---

## List of Publications

---

The present thesis is principally based upon the following publications, prepared by the author while at the University of Geneva.

- [1] L. Musy, R. Bulanadi, I. Gaponenko, and P. Paruch, “Hystorian: a processing tool for scanning probe microscopy and other n-dimensional datasets”, *Ultramicroscopy*, 113345 (2021).
- [2] R. Bulanadi and P. Paruch, “Identifying and analyzing power-law scaling in two-dimensional image datasets”, *Physical Review E* **109**, 064135 (2024).
- [3] R. Bulanadi, K. Cordero-Edwards, P. Tückmantel, G. Morpurgo, Q. Zhang, L. W. Martin, V. Nagarajan, and P. Paruch, “The interplay between point and extended defects and their effects on jerky domain-wall motion in ferroelectric thin films”, *Physical Review Letters* [Accepted].

Some materials, and methods of fabrication, are also based on the following publications, co-authored at the University of New South Wales prior to and during this PhD.

- [4] D. Sando, T. Young, R. Bulanadi, X. Cheng, Y. Zhou, M. Weyland, P. Munroe, and V. Nagarajan, “Designer defect stabilization of the super tetragonal phase in >70-nm-thick BiFeO<sub>3</sub> films on LaAlO<sub>3</sub> substrates”, *Japanese Journal of Applied Physics* **57**, 0902B2 (2018).
- [5] P. Sharma, D. Sando, Q. Zhang, X. Cheng, S. Prosandeev, R. Bulanadi, S. Prokhorenko, L. Bellaiche, L.-Q. Chen, V. Nagarajan, et al., “Conformational domain wall switch”, *Advanced Functional Materials* **29**, 1807523 (2019).

## LIST OF PUBLICATIONS

---

- [6] S. R. Burns, O. Paull, R. Bulanadi, C. Lau, D. Sando, J. M. Gregg, and N. Valanoor, “Empirical approach to measuring interface energies in mixed-phase bismuth ferrite”, *Physical Review Materials* **5**, 034404 (2021).

---

# Contents

---

<b>Résumé (en Français)</b>	<b>iii</b>
<b>List of Publications</b>	<b>vii</b>
<b>1 Introduction and Motivation</b>	<b>1</b>
<b>2 Avalanche Statistics in Ferroelectric Thin Films</b>	<b>5</b>
2.1 What is a Ferroelectric? . . . . .	5
2.1.1 Piezoelectricity and the Piezoelectric Effect . . . . .	9
2.2 Ferroelectric Thin Films . . . . .	9
2.2.1 Pulsed Laser Deposition . . . . .	12
2.3 Material Systems . . . . .	15
2.3.1 Lead Titanate ( $\text{PbTiO}_3$ ) and Related Ferroelectrics . . . . .	15
2.3.2 Bismuth Ferrite ( $\text{BiFeO}_3$ ) . . . . .	17
2.4 What are Power-Law Distributions? . . . . .	18
2.4.1 Why Care about Probability Distributions? . . . . .	19
2.4.2 Intuiting the Physical Implications of Power-Law Dis- tributions . . . . .	21
2.5 Mathematical Descriptions of Power-Law Distributions . . . . .	23
2.5.1 Generation of a Standard Power-Law Spectrum . . . . .	23
2.5.2 Maximum Likelihood Estimation of Power-Law Dis- tributions . . . . .	24
2.6 Analysing and Interpreting Plots of Power-Law Distributions . . . . .	25
2.6.1 Power-Law Event Spectra . . . . .	25
2.6.2 Log-Log Plots . . . . .	27
2.6.3 Maximum Likelihood Estimation Plots . . . . .	28

## CONTENTS

---

2.7	Why do Power-Law Distributions Exist in Nature? . . . . .	29
2.7.1	Scale-Free Networks, Critical Phenomena and Self-Organised Criticality . . . . .	30
2.7.2	Inversion About a Zero Value . . . . .	33
2.7.3	The Yule Model . . . . .	34
2.8	Avalanche Statistics in Ferroelectric Thin Films . . . . .	35
2.8.1	Avalanche Statistics in Domain Switching . . . . .	38
2.8.2	Avalanche Statistics in Structural Phase Transformations . . . . .	39
2.8.3	Avalanche Statistics via Compression and Nanoindentation . . . . .	39
2.8.4	Avalanche Statistics in Domain Wall Motion . . . . .	40
	References . . . . .	40
<b>3</b>	<b>Sample Characterisation</b>	<b>47</b>
3.1	Scanning Probe Microscopy and Atomic Force Microscopy . . . . .	47
3.1.1	General Description of Atomic Force Microscopy . . . . .	48
3.1.2	Position of Tip . . . . .	50
3.1.3	Methods of Cantilever Excitation . . . . .	53
3.1.4	Other Options for Atomic Force Microscopy . . . . .	65
3.1.5	Practical Piezoresponse Force Microscopy . . . . .	69
3.2	X-Ray Diffraction . . . . .	77
3.2.1	Bragg's law and Reciprocal Space Mapping . . . . .	78
3.2.2	Ewald's sphere and other practical considerations . . . . .	80
3.2.3	X-Ray Diffraction for Materials Characterisation . . . . .	81
3.2.4	Crystalline X-Ray Diffraction in Practice . . . . .	82
3.2.5	Rocking Curves ( $\omega$ Scans) . . . . .	84
3.2.6	$2\theta$ - $\omega$ Scans . . . . .	84
3.2.7	Reciprocal Space Mapping . . . . .	86
3.2.8	X-Ray Reflectivity, Fringes, and Film Thickness . . . . .	88
	References . . . . .	90
<b>4</b>	<b><i>Hystorian</i>: A Processing Tool for Scanning Probe Microscopy and Other <math>n</math>-Dimensional Datasets</b>	<b>93</b>
4.1	Introduction . . . . .	94
4.2	Working Principle . . . . .	95
4.2.1	Unification of File Structures . . . . .	96
4.2.2	File Conversion . . . . .	97
4.2.3	<code>m_apply</code> and Data Processing . . . . .	98
4.2.4	Archiving, Compression, and Regeneration . . . . .	99
4.3	Pre-Implemented Functions . . . . .	99
4.3.1	Distortion Correction . . . . .	99
4.3.2	Piezoresponse Force Microscopy Analysis . . . . .	101
4.3.3	X-Ray Diffraction Analysis (2-Axes) . . . . .	101

4.3.4	Data Visualisation . . . . .	102
4.4	Synthesising Disparate Data Sources . . . . .	102
4.4.1	Conversion of Raw Data . . . . .	103
4.4.2	Domain Wall Extraction from Piezoresponse Force Microscopy . . . . .	103
4.4.3	Domain Wall Extraction from Second Harmonic Gen- eration . . . . .	104
4.4.4	Correlating and Visualising Domain Walls . . . . .	104
4.5	Conclusions . . . . .	105
	References . . . . .	105
<b>5</b>	<b>Identifying and Analysing Power-Law Scaling in 2-Dimensional Image Datasets</b>	<b>109</b>
5.1	Introduction . . . . .	110
5.2	Sequential 2-Dimensional Datasets . . . . .	112
5.2.1	Generation of Sequential 2-Dimensional Datasets . . .	112
5.2.2	Comparison with Experimental Sequential 2-Dimensional Image Datasets . . . . .	115
5.3	Power-Law Extraction Through Different Boxing and Tracking Techniques . . . . .	117
5.3.1	Rectangular Boxing . . . . .	117
5.3.2	Random Boxing . . . . .	122
5.3.3	Interface Tracking . . . . .	124
5.4	Improving Power-Law Extraction via Multiple Consistent Estimators . . . . .	127
5.4.1	Differentiation of Power-Law Distributions from Non- Power-Law Distributions via Multiple Consistent Esti- mators . . . . .	127
5.4.2	Power-Law Analysis of 2-Dimensional Sequential Datasets via Multiple Consistent Estimators . . . . .	128
5.4.3	Effect of Number of Image Datasets on Rectangular Boxing, Random boxing, and Interface Tracking Tech- niques . . . . .	131
5.4.4	Interface Tracking and Real Datasets . . . . .	132
5.5	Conclusions . . . . .	133
	References . . . . .	133
<b>6</b>	<b>The Interplay Between Point and Extended Defects and their Effects on Jerky Domain-Wall Motion in Ferroelectric Thin Films</b>	<b>137</b>
6.1	Introduction . . . . .	138
6.2	Growth and Characterisation of Ion-Bombarded PbTiO <sub>3</sub> Thin Films . . . . .	139



**CONTENTS**

---

6.3 Power-Law Distributions and Global Switching Dynamics . . 144

6.4  $\alpha$ -Domain Contributions and Local Switching Dynamics . . . 151

6.5 Conclusions . . . . . 156

References . . . . . 156

**7 Tracking the Nanoscale Dynamics of Martensitic-like Phase Transitions via Interferometric Nanoindentation 161**

7.1 Introduction . . . . . 162

7.2 Nanoindentation and Critical Scaling from Plastic Deformation 164

7.2.1 Verification of Measured Scaling Parameters . . . . . 171

7.3 Nanoindentation and Critical Scaling of a Martensitic-like Phase Transition . . . . . 176

7.4 Martensitic-like Phase Transitions and Plastic Deformation . 180

7.5 Conclusions . . . . . 181

References . . . . . 181

**8 Current Investigations in Domain Wall Dynamics, Automated Experiments, and Visualisation Tools 185**

8.1 Domain-Wall Orientation and its Effect on Domain-Wall Dynamics, as Measured by Automated Experiments . . . . . 186

8.1.1 Growth of (110)-oriented BFO Thin Films . . . . . 187

8.1.2 Verification of Domain-Wall Orientation . . . . . 187

8.1.3 Domain-Wall Tracking and Improvements through Automated Experiments . . . . . 190

8.1.4 Preliminary Domain-Wall Dynamics Results . . . . . 191

8.2 Tools for Reciprocal Space Visualisation and Analysis . . . . 193

References . . . . . 196

**9 Conclusions and Perspectives 197**

References . . . . . 199

**A False Power-Law Distributions through Inverting Optical Beam Deflection 201**

**Abbreviations 205**

**Acknowledgements 207**

# CHAPTER 1

---

## Introduction and Motivation

---

Ferroelectrics are materials that spontaneously maintain an electric polarisation—and from such a premise has risen a volume of literature with a size orders of magnitude greater than could ever be read by even the most studious of PhD students. Those external to this precise branch of solid-state physics (and many internal to it), could justly be forgiven if they open this thesis with only one inquisitive question: Why? Why, of all things, ferroelectrics?

Moving past the multitude of rhetorical answers one could give, I do believe that at its core, this (and any) research is driven by two ends<sup>1</sup>:

First, the functional. Ferroelectrics, like all other materials, can act as building blocks for something much greater. Similar to how biological cells form tissues, tissues form organs, and organs form organisms, the crystallographic unit cells of these materials form ferroelectric domains, and devices, and from there, machines that we have used, do use, and will continue to use each and every day. Classically, ferroelectric memories have been exploited for fast, low-power, radiation-resistant information storage in everything from gaming consoles to military aircraft. Today, lead zirconate titanate is still the primary functional component behind the actuators and transducers in devices ubiquitous to modern life. In the future, hafnium oxide could lead to a resurgence in ferroelectric memories, and perhaps this, or neuromorphic computing, or multiferroic spintronics, or rewritable domain-wall electronics could drive the devices of the coming decades. Any

---

<sup>1</sup>Or, alternatively, the two ‘funs’.

## 1. Introduction and Motivation

---

understanding of the dynamics of ferroelectric polarisation switching or domain-wall motion could make key step towards those goals.

Second, more abstract and yet more concrete in this thesis in particular, is the fundamental. Ferroelectrics are a powerful model system in which we can investigate universal phenomena. The ‘Up’ and ‘Down’ polarisations we consider in our more simple ferroelectric thin films can, with a simple change in order parameter, be used to model correlated behaviour in everything from ferromagnets to wildfire growth. Phase transformations between ferroelectric and non-ferroelectric phases are accompanied by a structural change, and such ferroelectric–ferroelastic coupling can give us unparalleled control of the structure-property relationship. And looking at multiferroics, and the emergence of magnetoelectric coupling, can provide us new understanding of the interplay between these physically distinct material properties.

At the end of the day, all these things, all these dynamic *transitions*, are guided by avalanche statistics and power-law distributions. These power-law distributions, described most simply as a logarithmic increase of event size with a logarithmic decrease of probability, let us describe, characterise, and control the fascinating physics innate to ferroelectrics—and with it, the *universality* of these scaling distributions lets us extend our knowledge to future research and applications.

To measure and investigate ferroelectric domain and domain-wall dynamics, we need to utilise, create, and advance tools and techniques sensitive to these nanoscale phenomena. It is for this reason that we use scanning probe microscopy, a powerful and adaptable form of microscopy that lets us image and characterise the vast range of functional properties present in ferroelectric samples.

It is at the junction of these three topics—ferroelectric domains, power-law distributions, and scanning probe microscopy—that this thesis is situated. We here leverage scanning probe microscopy, sensitive to both structural and functional properties of ferroelectric domains, in order to change, measure, and characterise the variety of transitions (and transition-like behaviours in the highly nonlinear dynamics accompanying polarisation reversal or switching) observed, with the end goal of better understanding these nanoscale transitions, for their universality to other systems and applicability to potential future devices.

To this end, the following two chapters briefly recapitulate the fundamental and technical background through which we contextualise and understand this thesis. In Chapter 2, we start with a brief introduction to ferroelectrics and ferroelectricity, with a particular focus on thin film epitaxy, and the ferroelectric materials lead titanate and bismuth ferrite. We then divert to a comprehensive introduction to power-law distributions and their analysis, as well as how they feature in and are relevant to ferroelectric materials in terms of polarisation switching dynamics, and more broadly, plastic deformation

---

under applied stress.

In Chapter 3, we provide the reader with the core experimental background necessary to perform the different measurements carried out during this thesis. We focus here on two types of experiments: scanning probe microscopy, which we use to image the samples and their ferroelectric domain configurations; and x-ray diffraction, which we use to image and confirm the crystallographic structure of our materials.

After these introductory chapters, we then proceed to the technical and scientific outputs of this thesis. In Chapter 4 we detail the production and capabilities of *Hystorian*, a processing tool and Python package developed with Loïc Musy to optimise and improve the vast amounts of data processing central to both our theses. This work, with its particular focus on analysing scanning-probe microscopy and x-ray diffraction, has allowed the two of us to improve the quality and clarity of our scientific outputs.

In Chapter 5, we then focus on power-law scaling and 2-dimensional datasets. We ask ourselves, supposing we do have power-law dynamics in a 2-dimensional dataset, what would it look like? How do we know it is there? And how do we characterise it? We first focus on the generation of such 2-dimensional, power-law scaling image datasets, and then investigate the best methods of extracting power-law relationships via three techniques developed in-house we call ‘rectangular boxing’, ‘random boxing’ and ‘interface tracking’. We identify this last interface-tracking process as the optimal technique in a vast majority of cases, and further assess its capability through different statistical methodologies. We also spend some time focusing on its experimental realisation, and verify the suitability of this technique for investigating the power-law dynamics of domain wall motion.

In Chapter 6, we focus fully on ferroelectric 180° domain-wall motion as observed via scanning probe microscopy. Knowing that avalanche statistics rely on collective motion in disordered materials, we ask if and how the intentional generation of defects of different pinning strength and dimensionality can affect switching dynamics. We first detail the growth and characterisation of a set of five films of lead titanate, engineered to present sparse line defects with strong pinning potential, of which four undergo varying levels of  $\text{He}^{2+}$  bombardment with the goal of introducing varying point defect concentrations. We then leverage our previously highlighted interface tracking technique to characterise their polarisation switching dynamics; where we find that the global critical scaling is universal across all five of our samples. We then focus in on the local domain-wall motion, and identify characteristic differences in the spatial location of these switching events between bombarded and non-bombarded samples as the point defects interact with the line defects and modulate the potential landscape to which the 180° domain walls are subjected.

In Chapter 7, we use scanning probe microscopy to investigate a different

## 1. Introduction and Motivation

---

phase transition in a ferroelectric material—the martensitic-like structural transition between the tetragonal-like phase and rhombohedral-like phase in bismuth ferrite under applied stress. We employ the use of a quadrature-phase differential interferometer in next-generation atomic force microscopes to measure the plastic deformation of the previously grown defect-bombarded lead titanate thin films, and show avalanche behaviour well predicted by mean-field theory. We then use this same methodology on defect-stabilised, predominantly tetragonal-like phase bismuth ferrite, and measure and verify the scaling characteristics when plastic deformation is accompanied by the martensitic-like transition.

Finally, in Chapter 8, we briefly discuss a collection of unfinished and future works, all related to computational tools and automated experiments.. We first highlight some results of investigations of domain-wall motion in bismuth ferrite, and show how its rhombohedral structure allows for more complicated, but correlated, domain wall dynamics and evolution of domain wall character between  $71^\circ$ ,  $109^\circ$  and  $180^\circ$ . We also recount how the integration of analysis into the measurement allow for higher-quality data acquisition. Finally, we spend some time discussing additional tools developed to image, view, and interpret crystallographic structures from x-ray diffraction studies.

In sum, this thesis intends to compile a collection of my work in investigating the power-law dynamics that occur in ferroelectric thin films. With scanning probe microscopy as our tool of choice, we hope that this work details key technical improvements in the measurement and analysis of power-law dynamics, and key scientific discoveries in describing the behaviour of both their ferroelectric and structural domains.

---

## Avalanche Statistics in Ferroelectric Thin Films

---

### 2.1 What is a Ferroelectric?

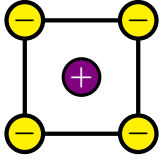
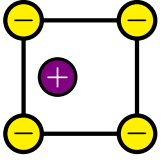
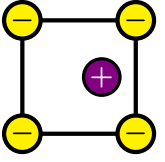
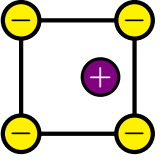
Ferroelectricity is a phenomenon in which a stable macroscopic electric dipole or polarisation state can be switched by an external field, and maintained after the removal of said field. A ferroelectric is a material that exhibits this trait. Highly comparable to a ferromagnetic material (which maintains a spontaneous magnetic dipole), a ferroelectric material undergoes a transition to a ferroelectric phase when cooled below a particular critical temperature, the Curie temperature  $T_C$ . Once below this temperature, an external applied electric field (conjugate to the polarisation order parameter) can *switch* the ferroelectric polarisation to align with the direction of the applied field. Once this field is removed, and in the absence of any other electric fields, the applied polarisation is spontaneously maintained. These characteristics are shown schematically in Table. 2.1.

The source of the ferroelectric effect is related to the crystallographic structure of the material. Many common ferroelectric materials, such as lead titanate ( $\text{PbTiO}_3$ ), have a *perovskite* crystal structure (Fig. 2.1). The perovskite structure consists of three components:

- One positive cation at the *A-site*, the vertices of the unit cell. In the case of lead titanate, these are lead cations.
- An additional cation at the *B-site*, the centre of the unit cell. For lead titanate, these are titanium cations.

## 2. Avalanche Statistics in Ferroelectric Thin Films

**Table 2.1:** *Characteristics of a ferroelectric material.* External changes in temperature and field (proceeding in columns from left to right) may cause characteristic changes in the structure and polarisation of the ferroelectric material. Adapted from Ref. [1].

Temperature	$T > T_c$	$T < T_c$	$T < T_c$	$T < T_c$
Electric Field			$\xrightarrow{E}$	
Schematic Structure				
Polarisation		$\xleftarrow{P}$	$\xrightarrow{P}$	$\xrightarrow{P}$
Description	Non-ferroelectric phase	Ferroelectric phase	Ferroelectric phase switch	Ferroelectric polarisation maintained

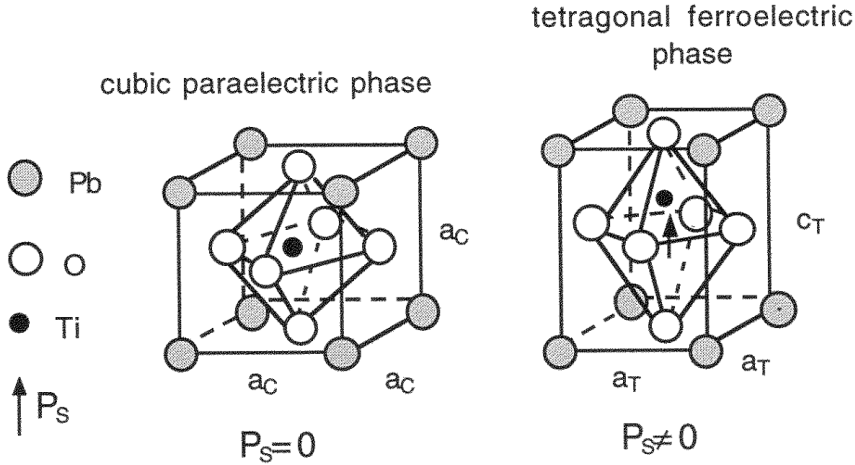


**Figure 2.1:** *The perovskite structure of lead titanate.* From Ref. [2].

- Surrounding the B-site cation is an octahedral ‘cage’ of anions. In the case of most inorganic perovskites, like lead titanate, these are oxygen anions.

Cubic perovskites are typically centrosymmetric, and thus are not ferro-

electric. However, if the perovskite undergoes a symmetry change, such as becoming tetragonal (Fig. 2.1), it can become energetically favourable for the B-site cation to shift towards a particular vertex of the oxygen octahedron, which itself can shift in the opposite direction. This slight displacement of electric charge (or more accurately the Born effective charge resulting from both the ionic shifts and the changes in electronic density as a result of the mixed ionic-covalent nature of the bonds in the unit cell [3]) creates a dipole, stabilised structurally by the increased coordination between the cations and anions—the so called ‘softening’ then ‘freezing-in’ of a soft phonon mode of lattice displacement. This phase transition, from a high-symmetry to a low-symmetry phase, creates a stable ferroelectric polarisation. This ferroelectric polarisation or dipole is a measurable *order parameter* that marks the phase transition.

These ferroelectric phases bring with it a series of boundary conditions that restrict the possibilities of polarisation configurations. A tetragonal crystal, for example, has edge of a particular length (often denoted as  $c$ ), and two edges of another length (denoted as  $a$ ). It would be *elastically* unfavourable if one unit cell were ‘rotated’ next to another, and thus for the  $c$ -axis of one unit cell to coincide with the  $a$ -axis of another. Meanwhile, the local buildup of charge between two adjacent and opposite dipoles pointing to one another would make such structures *electrostatically* unfavourable.

These elastic and electrostatic boundary conditions help drive collective and cooperative behaviour between adjacent unit cells. This leads to the creation of ferroelectric *domains*, regions much larger than individual unit cells, which all share the same ferroelectric polarisation. Between two distinct domains, we have a *domain wall*, often spanning a single-digit number of unit cells, allowing re-equilibration along electrostatic and elastic boundary conditions. The application of sufficiently large external fields tends to switch these ferroelectric domains, and thus leads to the motion of their associated domain walls.

The macroscale behaviour of ferroelectric materials under applied external fields follows a *hysteresis loop* (Fig. 2.2), showing the following regimes:

1. Initially (point  $A$ ), the net polarisation of a ferroelectric may be 0, due to a large variety of domains oriented in random directions—or, for polycrystalline samples, crystallographic grains doing the same.
2. A material’s dielectric permittivity means that when low external fields are applied (the interval  $AB$ ) a slight polarisation builds up in the material.
3. With further increasing external fields, the polarisation increases more rapidly (the interval  $BC$ ). Ferroelectric domains start to reorient, aligning with the field, a process referred to as switching.



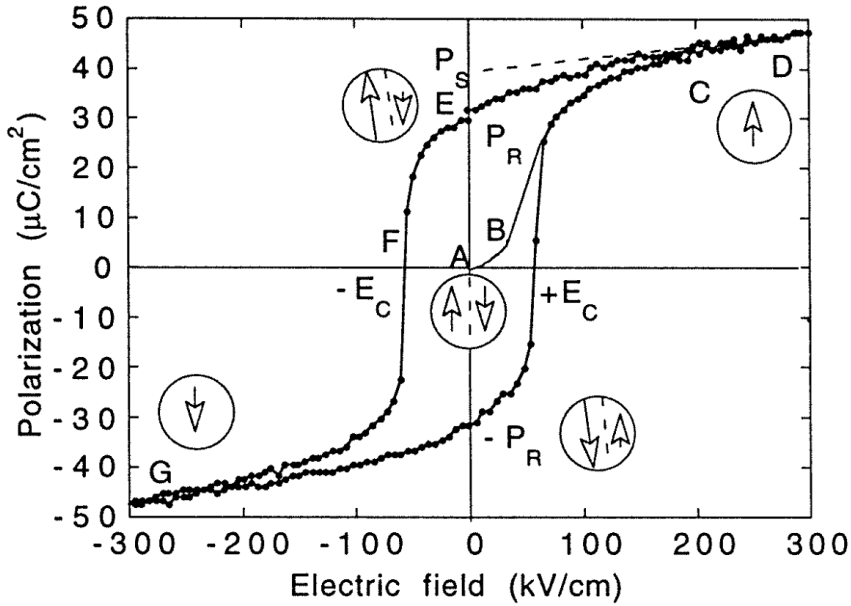


**Figure 2.2:** A sample hysteresis loop on a sample of lead zirconate titanate. From Ref. [2].

4. Eventually, all ferroelectric domains are fully switched. With even further increasing external fields (the interval  $CD$ ), a linear dielectric response is observed once more.
5. If the electric field is removed, some remanent polarisation,  $P_R$  remains (point  $E$ ). This remanent polarisation may be less than the maximum spontaneous polarisation,  $P_S$ , if elastic or electrostatic boundary conditions cause some polarisation dipoles to switch back.
6. An electric field applied in the opposite direction to the initial polarity will eventually yield a polarisation of 0 (point  $F$ ). The electric field that must be applied to arrive at this state is known as the coercive field,  $E_C$ .
7. If this opposite polarity electric field increases in magnitude even further, the polarisation will continue to switch (interval  $FG$ ). From this position, polarisation can be switched once again (interval  $GD$ ) and the process can repeat.

### 2.1.1 Piezoelectricity and the Piezoelectric Effect

While spontaneous polarisation domains and hysteresis are unique to ferroelectrics, the presence of ferroelectricity itself implies a menagerie of other properties, of interest both industrially and for further research. All ferroelectrics are *pyroelectric*, for example, which means they can generate an electric field with a change in temperature (this is observed when a ferroelectric material moves past the Curie temperature, via the temperature dependence of the polarisation).

Of particular interest to this thesis, however, is another functional property, *piezoelectricity*. The piezoelectric effect is the buildup of electric charge resulting from an applied external stress (and, inversely, a mechanical strain resulting from an applied external field) inherent in a polar material. Piezoelectricity arises in all ferroelectrics as a result of their non-centrosymmetric nature; a mechanical distortion of the unit cell will lead to a change in polarisation.

The piezoelectric effect is described mathematically by the relationship:

$$D_i = d_{ijk}X_{jk} \quad (2.1)$$

where  $D_i$  is the charge density that results from the applied stress  $X_{jk}$ . Here,  $d_{ijk}$  is a third-rank tensor containing a set of piezoelectric coefficients.

Of these coefficients, the most relevant for this thesis is the longitudinal piezoelectric coefficient,  $d_{33}$ , which describes the surface charge resulting from stress applied along the same axis. The  $d_{33}$  is typically the largest and most easily measured piezoelectric coefficient, and becomes a primary figure of merit for many applications of ferroelectrics [4].

In ferroelectrics, the existing ferroelectric polarisation means that the observed strain is hysteretic. A plot of strain as a function of electric field (Fig. 2.3) shows that an applied electric field oriented opposite the ferroelectric polarisation causes a reduction in strain, reaching a minimum at the coercive voltage. Beyond the coercive voltage, increasing the magnitude of the electric field will continue to increase the strain. A plot of strain–electric field hysteresis is thus known as a *butterfly loop*.

This section has broadly discussed the entire class of ferroelectric materials. In order to become more useful, we will now focus on the particular material format used in this thesis: thin films.

## 2.2 Ferroelectric Thin Films

Thin films are, precisely as the name suggests, materials that are particularly thin, forming a coating or film on the surface of some other material (the ‘substrate’). Conventionally, thin films range in thicknesses from a single-digit

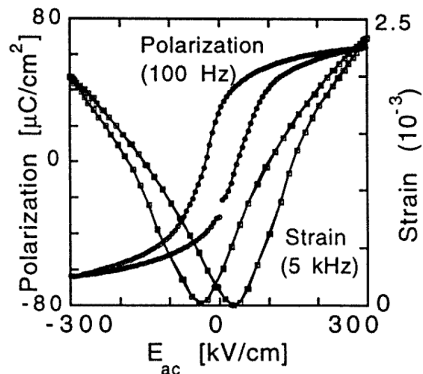


**Figure 2.3:** A strain–electric field hysteresis loop (butterfly loop) overlaid on a corresponding polarisation–electric field hysteresis loop. From Ref. [2].

number of unit cells at minimum, up to hundreds-of-nanometres-thick or a few tens of micrometres. The main characteristic difference between thin films and other material formats, however, is that their small thickness means that their surface properties dominate over their bulk properties, yielding a vast array of unique functionalities and applications.

Thin films grown under specific, optimal conditions can also be *epitaxial*, where the termination and crystallographic orientation of the substrate directly guides and constrains the subsequent growth and crystallographic orientation of the film, rendering it quasi-single-crystal-like. For ferroelectric materials, epitaxial growth also allows for the *strain engineering* of new and unique ferroelectric phases.

A schematic diagram showing strain engineering in epitaxial thin film growth is presented in Fig. 2.4. In Fig. 2.4(a), we show a diagram representing repeating unit cell of some material that would compose a thin film, and in Fig. 2.4(b) we show a (smaller) unit cell for the substrate the film is grown on. If growth is epitaxial, the in-plane lattice parameter of the film is strained to match the corresponding in-plane lattice parameter of the substrate; this is called the *misfit strain*,  $\epsilon_m$  and described by the equation:

$$\epsilon_m = 1 - \frac{a_f}{a_s} \quad (2.2)$$

where  $a_f$  and  $a_s$  are the in-plane lattice parameters of the film and substrate respectively.

These misfit strains are also associated with an effective misfit *stress* which, due to Poisson’s ratio and an attempt to conserve unit cell volume, means that an in-plane compressive (tensile) strain generally results in an out-of-plane tensile (compressive) strain [Fig. 2.4(c)].

In ferroelectric materials this misfit strain can break symmetry, and either

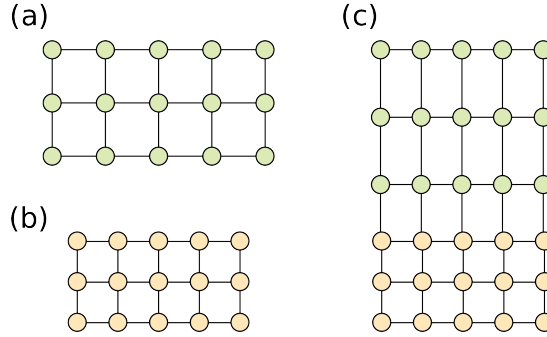


**Figure 2.4:** *Strains from thin film epitaxy.* (a) A larger unit cell, intended to represent a thin material. (b) A smaller unit cell, intended to represent the substrate. (c) When the thin film is grown epitaxially on the substrate, the thin film undergoes an in-plane compressive strain and an out-of-plane tensile strain. These crystals are intended to represent crystals which repeat infinitely laterally; in real crystals, there may be some relaxation of this strain towards the edges. Moreover, with increasing film thickness a critical point is reached at which the thin film begins to relax to its bulk unit cell dimensions, accompanied by some combination of dislocations, twinning and other crystalline defects.

stabilise a ferroelectric phase, increase the magnitude of the ferroelectric polarisation, or cause particular ferroelectric polarisations to dominate (see and Refs. [5, 6], and Section 2.3). This strain therefore provides another parameter for which to control ferroelectric or related properties; different substrates can be used to apply different misfit strains (Fig. 2.5), and in some cases thin films can accommodate strains up to 7% [7].

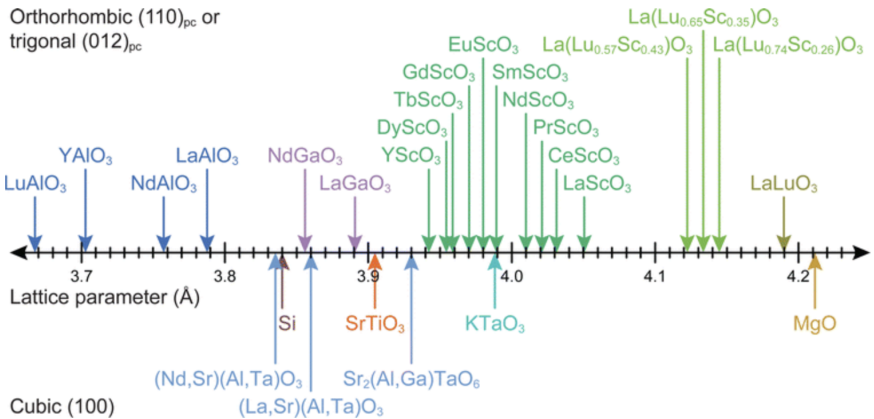


**Figure 2.5:** *Some particular substrates used for the growth of oxide thin films.* From Ref. [7].

## 2. Avalanche Statistics in Ferroelectric Thin Films

---

In this thesis, our ferroelectric thin films have been grown on strontium titanate ( $\text{SrTiO}_3$ , STO) or lanthanum aluminate ( $\text{LaAlO}_3$ , LAO) substrates, with different orientations, to allow for particular stable polarisation orientations.

### 2.2.1 Pulsed Laser Deposition

For this thesis, thin films were primarily grown by pulsed laser deposition (PLD), a type of physical vapour deposition in which a thin film is grown layer-by-layer on a crystallographic substrate. A schematic diagram of a pulsed-laser deposition is shown in Fig. 2.6.

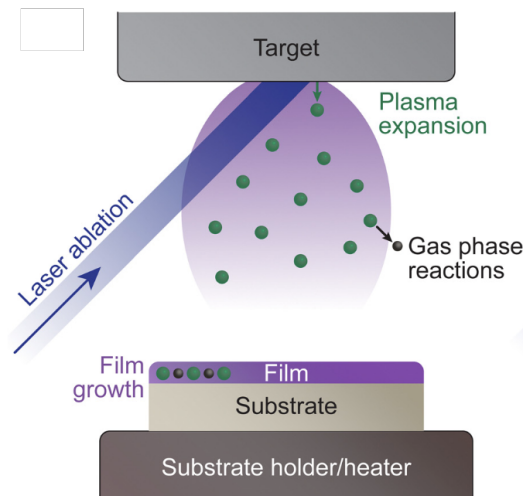


**Figure 2.6:** Schematic diagram showing the principles behind PLD. From Ref. [7].

The PLD system consists of the following major components:

- The substrate, on which the thin film is grown;
- A target material, which is ablated to form a film;
- A high-powered laser system that can ablate the target material, and;
- A vacuum chamber, heater, and associated gas lines to control the external growth conditions.

In principle, the repeated periodic laser pulses rapidly to heat and excite the target material in controlled atmospheric conditions. At each pulse, this rapid ablation process creates a plume of plasma, whose composition

depends on the composition of the target material. Parts of the plume can then slowly deposit onto the substrate material. During this entire process, the substrate can also be heated to a controlled temperature to improve the kinetics of the incident atoms or ions. This means that the ions inside the plume can deposit and nucleate onto the substrate, and then slowly grow in size upon it.

In this system, the key control parameters include:

- Substrate material and quality, which apply crystallographic constraints on the thin film.
- Target stoichiometry. The stoichiometry of the target affects the stoichiometry of the film, but these are not necessarily one-to-one. For example, in the growth of bismuth ferrite films, bismuth is substantially more volatile than iron, and thus a film of bismuth oxide would likely be iron-deficient if the bismuth ferrite oxide film is at a stoichiometric composition. Instead, to grow films of stoichiometric bismuth ferrite, the target may consist of up to 5% or even 10% excess bismuth.
- Target quality. Targets for PLD are often initially prepared by compacting a powder. Beyond stoichiometry, preparation of this target itself also has a further effect on film growth. For example, a poorly prepared or insufficiently high-density target could lead to incomplete ablation and particle formation in the film.
- Laser energy, duration, and frequency. A high-powered laser is used to ablate the target, and so, insufficient energy or pulse frequency can reduce the rate and quality of the growth. On the other hand, if the energy is too high, then large clusters of material may be ablated at once, leading to particles on the sample surface. High energy and pulse duration could also lead to thermal evaporation or significant additional scattering events between ions in the plume, which may also lead to an overall reduction in growth rate as well [7].
- Substrate temperature. Ideally, film growth is dominated by diffusion of material along the substrate surface to create a layer-by-layer growth regime. Diffusion is promoted by high substrate temperature. Such high temperature also has the side-benefit of helping remove impurities that may have previously adsorbed onto the surface. On the other hand, if the temperature is too high, thermal evaporation or undesirable phase transitions could occur in either the substrate or film.
- Pressure and atmosphere. PLD must be performed at a low pressure so that any ablated material can actually deposit onto the substrate (rather than being obstructed by gas in the chamber). The laser ablation

## 2. Avalanche Statistics in Ferroelectric Thin Films

---

process does introduce chemical species into the chamber (of which some portion ideally lands onto the substrate), however, so too low an pressure would be undesirable and impossible. To ensure that growth is consistent, we therefore perform PLD with flowing gas at a consistent, low pressure. This gas, for the growth of ferroelectric oxides, tends to be oxygen, which can help promote the ideal formation of oxide films on the substrate.

- Cooling. After growth is complete, the sample should be cooled in a controlled manner. This cooling is typically performed at a controlled rate (to prevent quenching in a high-energy phase, or cracking of the film due to thermal expansion) and in a controlled atmosphere at an intermediate pressure between growth and ambient pressures (to maintain oxygen stoichiometry in the film).

While these constraints are the main variables in PLD growth, this list is not exhaustive. Many seemingly minor parameters can affect film growth. For example, chamber geometry and substrate-to-target distance has been credited with the formation of bismuth oxide pockets in bismuth ferrite films, which stabilise particular phases [8].

Experimentally, PLD is performed with roughly the following procedure.

1. The substrate is attached onto a sample holder with some type of thermal paste. The sample on the sample holder is then placed inside the PLD chamber, possibly directly or via a series of transfer rods.
2. The PLD chamber is brought down to a low vacuum pressure, to ensure the chamber is clean and free of obvious impurities.
3. Conditions inside the PLD chamber are set to particular, generally experimentally determined target values. The substrate is heated, and flowing gas is introduced to control the chamber pressure and atmosphere.
4. Once conditions are stabilised, the target material is ablated and deposited onto the film. The target may also be pre-ablated prior to film growth, while the substrate is shielded, to bring the target and laser into a thermal steady state.
5. After growth, the sample is allowed to cool under controlled conditions, and then removed from the chamber for further experiments.

This process was used to grow ferroelectric thin films for this thesis. Other physical vapour deposition methods are also frequently used, such as radio-frequency magnetron sputtering, or molecular beam epitaxy. These methods also involve the removal of material from a target and subsequent deposition onto the substrate.

## 2.3 Material Systems

With methods of thin-film growth established, we will now proceed to discuss the details of particular material systems investigated in this thesis.

### 2.3.1 Lead Titanate ( $\text{PbTiO}_3$ ) and Related Ferroelectrics

Lead titanate ( $\text{PbTiO}_3$ , PTO) is a well-understood perovskite ferroelectric. It has a single phase transition from a cubic paraelectric phase to a tetragonal ferroelectric phase at 766 K [9], and in this ferroelectric phase, has  $a = 3.88 \text{ \AA}$ , and  $c = 4.29 \text{ \AA}$  [10]. Under external pressure/epitaxial stress, and in the presence of doping, the  $T_C$  has been observed to vary significantly [11], and the nature of the transition was reported to change from first to second order [5].

This tetragonality allows PTO thin films to be grown below  $T_C$  with various domain structures as a result of different misfit strains. At highly compressive strains, PTO forms  $c$ -domains, where the  $c$ -axis points out of the plane of the film. At highly tensile strains, PTO forms  $a_1$ - or  $a_2$  domains, where the  $c$ -axis points in the plane of the film. At intermediate strains, some mixture of all three domains can coexist simultaneously (Fig. 2.7; also see Ref. [5]). Some configurations of these domains are shown in Fig. 2.8.

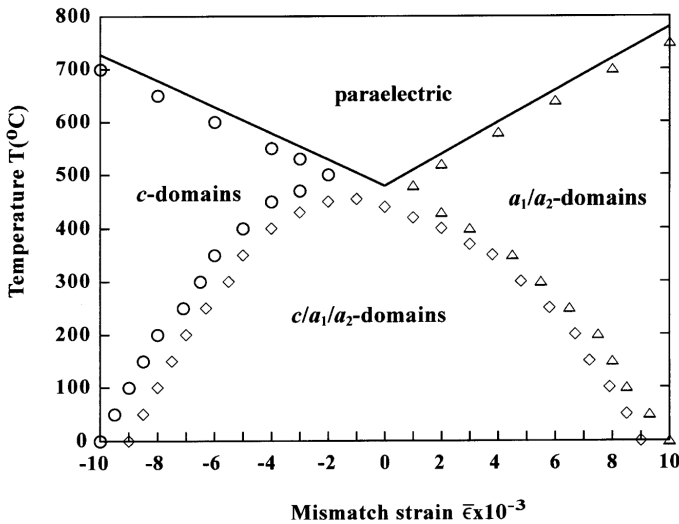
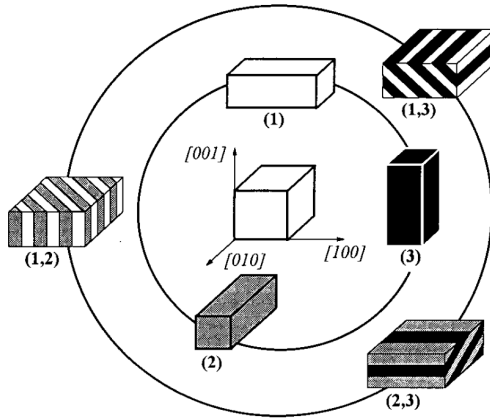


Figure 2.7: Diagram showing domains and phases of PTO thin films From Ref. [12].





**Figure 2.8:** *Diagram showing some possible domain structures in PTO thin films. From Ref. [13].*

The relatively simple domain structure and phase transition in PTO means it is a suitable ‘material of choice’ for further research into ferroelectrics as a whole. For example, PTO has been used in key research on size effects [14, 15], flexoelectricity [16], or defect engineering [17], in ferroelectric thin films, to just name a few. Meanwhile, the seminal works on topological vortex structures and ferroelectric skyrmions were all reported on PTO superlattices [18, 19].

PTO, when some titanium is substituted with zirconium, is known as lead zirconium titanate or lead zirconate titanate ( $\text{Pb}[\text{Zr}_x\text{Ti}_{1-x}]\text{O}_3$ ,  $[0 \leq x \leq 1]$ , abbreviated to PZT). PZT is the most used industrial ferroelectric today, primarily in actuator or sensor applications, due to its high piezoelectric response.

These high piezoelectric responses occur because PZT, with a zirconium substitution of about 52%, reaches what is called a morphotropic phase boundary (MPB)—a boundary between two morphotrophically distinct phases. At this MPB, we have a competition in structure between the tetragonal phase preferred by PTO, and the rhombohedral phase preferred by lead zirconate ( $\text{PbZrO}_3$ ). This allows for the formation of an intermediate monoclinic phase, whose intermediate symmetry allows for particularly higher shifts of atom positions, and thus higher strains from applied electric field [20].

Beyond these piezoelectric applications, PZT has also classically found some use in ferroelectric memory applications [21].

### 2.3.2 Bismuth Ferrite ( $\text{BiFeO}_3$ )

If it is the simplicity of PTO that drives its interest, then for bismuth ferrite ( $\text{BiFeO}_3$ —BFO) it is precisely the opposite. BFO, like PTO, is a ferroelectric perovskite. Unlike PTO, however, BFO undergoes a great variety of complex phase structures (Fig. 2.9). While BFO is rhombohedral (R-phase) in the bulk, under tensile strain it can stabilise as a monoclinic or orthorhombic phase. Meanwhile, at compressive strain, it can stabilise as a rhombohedral-like monoclinic phase (R'-phase), a tetragonal-like monoclinic phase (T'-phase) or a fully tetragonal phase (T-phase). This list is not conclusive, however; for example, coexisting T'- and R'-phases creates a highly compressed R'-phase known as the S'-phase [22], while triclinic phases of BFO have been reported on highly anisotropic substrates [23].

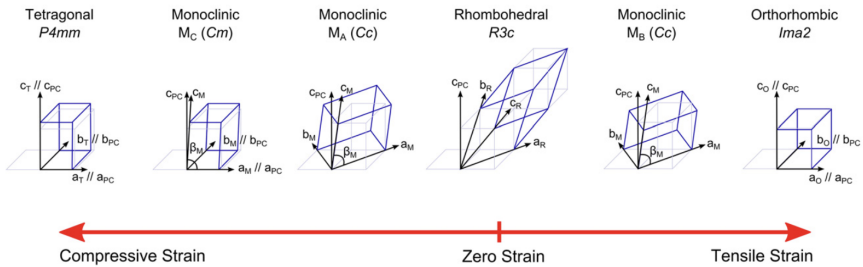


**Figure 2.9:** Diagram showing some possible phases structures in BFO thin films. From Ref. [24].

Perhaps the most recognisable property of BFO, however, is that it is a room temperature *multiferroic*, in which ferroelectricity and magnetic order exist within the same material (for more detail, see Refs. [24, 25] and references therein). In bulk BFO, the ferroelectric polarisation is oriented along the  $\langle 111 \rangle$  axes, with a remanent polarisation as high as  $100 \mu\text{C cm}^{-2}$  [25]. Viewed naively, the iron ions in BFO would typically have antiferroelectric ordering, where spins are antiparallel and would therefore lead to no net magnetisation. However, magnetoelectric coupling between these spin moments and the polarisation vector via inverse Dzyaloshinskii Moriya interaction leads to a slight angular offset or canting of the spins, leading to a net magnetisation, which slowly tilts unit-cell-by-unit-cell, leading to the formation of a *spin cycloid* along the  $[110]$  direction (Fig. 2.10). This magnetoelectric coupling suggests grand potential for *spintronics*; advanced electronic devices where, in addition to electric transport, spin transport is driven and observed, increasing the information density that would otherwise be transmitted.

Beyond this magnetoelectric coupling, BFO also has a variety of other fascinating properties which have led to extensive research. BFO has a

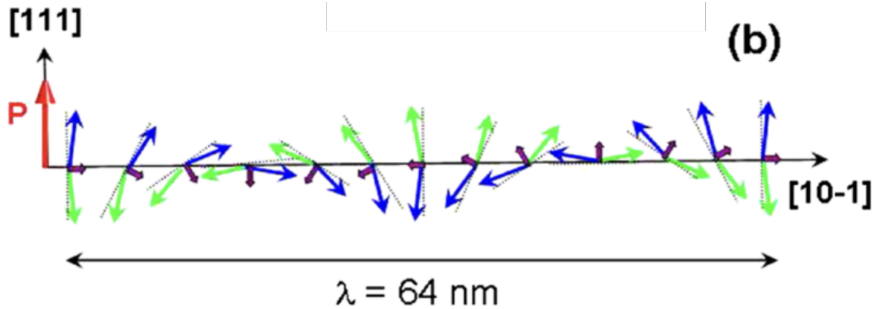


**Figure 2.10:** *The magnetic spin cycloid in BFO.* The slightly angled (canted) antiferromagnetic spins (blue and green arrows) create a net magnetic moment (purple arrows). This creates a spin cycloid with a periodicity of approximately 64 nm. From Ref. [26].

particularly low band gap of 2.6 to 3.0 eV, for example, which allows for potential photovoltaic applications [27–29]. Domain walls in BFO are also known to be conductive, and this conductivity is reported to dependant on the domain-wall orientation, allowing for potential domain-wall electronics [30–33]. Meanwhile, the relationship between the polarisation vector of BFO and its termination (so-called BFO ‘happiness’) is known to affect water affinity and could be used for water splitting and renewable energy applications [34]. These various possibilities have helped continue to drive research into BFO thin films; a trend that is continued into this thesis work.

With the establishment of ferroelectric materials in general, and the particular material systems we use in particular, we now pivot to the power-law distributions which we here use to understand our ferroelectrics and their behaviour. We shall first describe what power-law distributions are and how they exist in nature, before going into the mathematical detail that characterise their analysis, and how they relate to the ferroelectric materials we have thus far discussed.

## 2.4 What are Power-Law Distributions?

Power-law distributions are a statistical construct that is most easily described as a linearly decreasing trend of event frequency and event size on a log-log scale. Mathematically, this relationship can be described by the probability density function (PDF):

$$p_X(x) = \frac{\alpha - 1}{x_{min}} \left( \frac{x}{x_{min}} \right)^{-\alpha} \quad (2.3)$$

Year of Birth	Mean Body Height in cm ( $\sigma$ )	
	Men	Women
1919–1929	172.3 (6.7)	159.9 (6.7)
1930–1939	173.1 (6.4)	161.1 (6.0)
1940–1949	174.7 (6.4)	162.5 (6.0)
1950–1959	176.2 (6.9)	163.9 (6.4)
1960–1969	177.6 (6.9)	164.9 (6.4)
1970–1979	178.7 (7.0)	166.2 (6.5)
1980–1989	178.9 (6.9)	166.2 (6.5)
1990–1997	179.4 (7.4)	165.9 (6.3)

**Table 2.2:** Height distributions of people in Switzerland as a function of age. From Ref. [35].

where  $\alpha$  is a *scaling parameter*, and  $x_{min}$  is the minimum value of  $x$  for which the distribution is valid.

### 2.4.1 Why Care about Probability Distributions?

With such a seemingly arbitrary distribution established, I find it prudent to first motivate our research in power-law distributions, and how they become relevant to ferroelectric materials.

The first reason such distributions are studied is for their ability to *describe*, and therefore *analyse* observed physical phenomena. Say that one wanted to determine whether there has been a change in the average height of people in Switzerland, as a function of the year of birth, for example. One could simply directly report the raw data gathered from a survey, and separate the data by birth year, but this would be difficult and inconvenient to analyse and compare. Rather, the most useful way to describe such a statistical study may instead be via the mean,  $\mu$ , which describes the expected value in the dataset; and the standard deviation,  $\sigma$ , which describes a range around the mean in which most datapoints would appear in. A statistician could then simply report both the mean and standard deviation of the subsets (Table. 2.2), and a reader could tell immediately, for example, that women born in the years 1990–1997 are taller, on average, than women born in the years 1940–1949.

Many random variables in nature are well described by their mean and standard deviation, like height in this example. These variables also mark a *normal distribution*, which is described by PDF:

$$p(x) = \frac{1}{\sigma\sqrt{2\pi}} \exp\left\{-\frac{1}{2}\left(\frac{x-\mu}{\sigma}\right)^2\right\} \quad (2.4)$$

Not all natural phenomena follow a normal distribution, however, and so

## 2. Avalanche Statistics in Ferroelectric Thin Films

---

a mean and a standard deviation is not always the most suitable, or even complete, description. Consider, for example, the distribution of earthquake sizes in California, between January 1910 and May 1992 (Fig. 2.11). The vast majority of earthquakes are incredibly small, with well over 10000 earthquakes having a magnitude of 3 or lower on the Richter (logarithmic) scale. Earthquakes that are orders of magnitude larger do occur, but with orders of magnitude lesser frequency; only 10–100 earthquakes occurred with a magnitude above 6. We will need different parameters to describe—and therefore compare—distributions like this. For such phenomena, as shown in Eq. 2.3, and Section 2.5, these parameters are the scaling parameter,  $\alpha$ , and a minimum event cutoff,  $x_{min}$ .

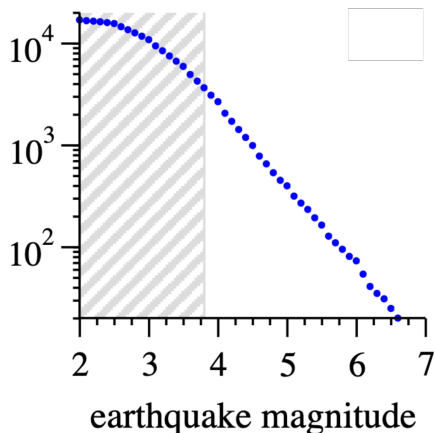


**Figure 2.11:** *Distribution of earthquake intensities in California.*  $y$ -axis measures the number of earthquakes detected, while  $x$ -axis marks their detected magnitude on the Richter scale. From Ref. [36].

The second reason to study power-law (and other) distributions is their *predictive power*; if previously gathered random variables follow some distribution, we can reasonably predict that future random variables gathered the same way would follow the same distribution. As such, given the information in Table 2.2 (or collected otherwise), a reasonable architect should not expect to build a home for 5-cm-tall newlyweds, nor a tailor to sew a suit for a 22-m-tall toddler.

Good power-law distributions provide this same predictive power. Given the power-law distribution shown in Fig. 2.11, we can expect that in the next 80-year period, we would again expect 10–100 earthquakes of magnitude greater than 6, and we can further extrapolate the data to predict the probability of a 7, 8, 9, or higher magnitude earthquake in the same period. One could use this information if they, for example, wanted to build a

structure to last 100 years. One could take into account the probability of the building being struck by an earthquake of a particular magnitude within this time interval, and weigh this probability against the cost of preparation to establish a suitable structural integrity. It would be unwise to build a structure here that were so unstable as to collapse if struck by a magnitude 5 earthquake; it would be similarly unwise to spend excess cost to protect against a hypothetical magnitude 12 earthquake, without a particularly pertinent reason.

### 2.4.2 Intuiting the Physical Implications of Power-Law Distributions

This combined descriptive and predictive power ensures that power-law distributions, like many other distributions, are worthy of study. However, power-law distributions and the parameters contained therein also provides information about some physical phenomena. As stated prior in Eq. 2.3, power-law distributions are characterised by  $\alpha$ , the scaling parameter, and  $x_{min}$ , the minimum event cutoff, and both these parameters have implications for the physics of the system.

Power-law distributions describe phenomena where event frequency decreases logarithmically with an increase in logarithmic event size, and the scaling parameter  $\alpha$  describes the degree to which the frequency reduces as a function of an event size. While this is discussed in more detail in Section 2.6, the important result is that a higher scaling parameter describes a more rapid cutoff of event size. On one extreme, at higher values (say,  $\alpha \gg 5$ ), this cutoff is so rapid that the its characterisation as a power-law distribution no longer becomes physically meaningful (if  $\alpha = 5$ , then 93.75% of events will have a size  $x_{min} < X < 2x_{min}$ ; only 0.01% of events will have a size  $X > 10x_{min}$ ). On the other extreme, at lower values (that is, as  $\alpha \rightarrow 1$ ), larger values become relatively more prominent (if  $\alpha = 1.1$ , then 10% of events will have a size  $X > 10^{10}x_{min}$ ). Intermediate values immediately provide similar information: if some power-law distribution is characterised with  $\alpha = 1.5$ , we know to expect particularly large events with any reasonably sized dataset; while if a power-law distribution is, has, say,  $\alpha = 3$ , we know that the distribution is tilted more closely to  $x_{min}$ .

We will come to see in Section 2.8 that power-law distributions describe various distinct phenomena in ferroelectric materials. In that section, we will discuss where power-law distributions occur in ferroelectric materials, and how they arise, but we will here focus on a general description of the distribution. It is sufficient to state at the moment that ferroelectric switching follows a power-law distribution, and thus, the event size here is the amount of ferroelectric that is switched. In these contexts, the scaling parameter tells us the distribution of the sizes of ferroelectric switching events, which,

## 2. Avalanche Statistics in Ferroelectric Thin Films

---

in turn, can tell us the process by which ferroelectric switching occurs. A higher scaling parameter (with a more rapid cutoff of event size) describes situations where the buildup of large events is relatively less probable, which can be characterised by lower energy barriers [37] in cases where multiple phase transitions or defects are prominent. A lower scaling parameter (with a larger distribution of event sizes), meanwhile, describes regimes where the buildup of large events is relatively more probable. This can occur when the energy barrier has the potential to be much greater, potentially through lower disorder or lower temperatures that drive the creep regime [38].

$x_{min}$ , the minimum event cutoff, also has its own physical implications. Mathematically, the  $x_{min}$  describes the lowest value at which the distribution is valid. This means that, physically, ideally,  $x_{min}$  could be the minimum unit of the system (for ferroelectric switching, perhaps a singular unit cell) or the resolution of the experimental technique. In real situations, however, a single power-law distribution is unlikely to describe the entire event space—for example, a measurement may take a physical power-law distribution coincident with some normally distributed error. As power-law distributions do allow for particularly large events to occur with a higher probability than similarly sized events in other distributions, power-law distributions tend to dominate over all other distributions at higher event sizes, however. The scaling parameter of these power-law ‘tails’ therefore provide the same descriptive and predictive powers described earlier [39], but in these real systems  $x_{min}$  is increased such that it moves above the threshold at which these other distributions become relevant. Thus, for ferroelectrics, an  $x_{min}$  closer to experimental resolution describes phenomena where the power-law distribution is more ‘complete’ in describing the system, while a greater  $x_{min}$  describes more complex phenomena that may be associated with multiple distinct distributions.

While it has no bearing on the mathematical model of power-law distributions we describe here in this thesis, physically and realistically there also exists an upper bound, or maximum event cutoff,  $x_{max}$ , at which the power-law distribution is relevant. For our systems, the absolute maximum upper bound is the size of the system that is measured. As the experiment progresses, the size of the remaining unswitched area also decreases, which can apply a decreasing ‘soft limit’ on the upper bound; the impact of this is discussed in Chapter 5. For these experiments, the size of this upper bound is also further modulated by other properties of the system; for example, the finite interaction area of a scanning probe could also affect the upper bound. An upper bound that is too low, particularly if  $\alpha$  is also low, can restrict the information and results gained from a potential power-law distribution.

With the importance of power-law distributions now described, through the following sections of this chapter, we will focus on power-law distributions and how they relate to ferroelectric materials. We will first derive Eq. 2.3

mathematically, and then explain why probability distributions like this one are interesting and useful for further research. We will then pivot to why such power-law distributions appear in nature, and then finally conclude this chapter with some particular occurrences of power-law distributions in phenomena related to ferroelectric materials.

## 2.5 Mathematical Descriptions of Power-Law Distributions

### 2.5.1 Generation of a Standard Power-Law Spectrum

We have thus far described how power-law distributions are most intuitively understood as a linearly decreasing trend on a log-log plot<sup>1</sup>. This means, precisely, that:

$$\log n = -\alpha \log x + c \quad (2.5)$$

where  $n$  describes the number of events of size  $x$ ,  $\alpha$  is the characteristic *scaling parameter*, and  $c$  is some other constant. The distribution can then be restated as the probability density function (PDF) where:

$$p_X(x)dx = \Pr(x \leq X < x + dx) = Cx^{-\alpha}dx \quad (2.6)$$

Here,  $C = e^c$  is now the normalisation constant. To evaluate  $C$ , an integral can be taken for all  $x$ ; however, in the limit of  $x \rightarrow 0$ ,  $p_X(x) \rightarrow \infty$ . There is therefore a constraint for  $x \geq x_{min}$ , where  $x_{min} > 0$  is some minimum value. This allows for the integration:

$$\int_{x_{min}}^{\infty} p_X(x)dx = 1 \quad (2.7)$$

Given  $\alpha > 1$ , the normalisation constant can then be calculated as  $C = \frac{\alpha-1}{x_{min}^{1-\alpha}}$  to produce the normalised PDF in Eq. 2.3:

This normalised PDF can then be used to generate the associated cumulative distribution function (CDF):

$$P_X(x) = 1 - \left( \frac{x}{x_{min}} \right)^{1-\alpha} \quad (2.8)$$

In general, a random variable  $X$  can be drawn by inverse sampling the associated CDF,  $P_X$ , by calculating  $X = P_X^{-1}(U)$ , where  $U$  is a random

---

<sup>1</sup>This section is an adaptation of the supplementary material of the article, *Identifying and analyzing Power-Law Scaling in 2-Dimensional Image Datasets*, published in *Physical Reviews E* (American Physical Society), by R. Bulanadi and P. Paruch [40].



variable uniformly distributed in the interval  $[0, 1)$ . Thus, a random number  $x$  within a power-law distribution with a minimum value  $x_{min}$  and a scaling parameter  $\alpha$  can be generated from:

$$x = P_X^{-1}(u) = x_{min}(1 - u)^{\frac{1}{1-\alpha}} \quad (2.9)$$

where  $0 \leq u < 1$  is randomly sampled from a uniform distribution.

### 2.5.2 Maximum Likelihood Estimation of Power-Law Distributions

Maximum likelihood estimation (MLE) is a technique to estimate model parameters, and is commonly used to analyse power-law distributions in empirical data. This method of estimating the scaling parameter is also known as *Hill estimation* and is well-outlined in Ref. [41]. In brief, MLE generally relies on estimating the value of some parameter  $\theta$  by maximising its *likelihood*, given the  $n$  observations  $x_1, x_2, \dots, x_n$ . In this case, the likelihood,  $L(\theta)$  is defined as:

$$L(\theta) = \prod_{i=1}^n f(x_i; \theta) \quad (2.10)$$

where  $f(x_i; \theta)$  is the associated PDF. Given Eq. 2.8, the likelihood of  $\alpha$  in a power-law relationship is therefore:

$$L(\alpha) = \prod_{i=1}^n \frac{\alpha - 1}{x_{min}} \left( \frac{x_i}{x_{min}} \right)^{-\alpha} \quad (2.11)$$

As the maxima of the likelihood should correspond to the maxima of the log-likelihood,  $\ell$ , this can then be simplified to:

$$\begin{aligned} \ell(\alpha) &= \log(L(\alpha)) \\ &= \log \left( \prod_{i=1}^n \frac{\alpha - 1}{x_{min}} \left( \frac{x_i}{x_{min}} \right)^{-\alpha} \right) \\ &= n \log(\alpha - 1) - n \log(x_{min}) - \alpha \sum_{i=1}^n \log \left( \frac{x_i}{x_{min}} \right) \end{aligned} \quad (2.12)$$

The position of the maxima can then be calculated by finding where  $\partial \ell / \partial \alpha = 0$ . This means that  $\alpha$  can be estimated by finding its maximum likelihood:

$$\hat{\alpha} = 1 + n \left( \sum_{i=1}^n \log \frac{x_i}{x_{min}} \right)^{-1} \quad (2.13)$$

## 2.6 Analysing and Interpreting Plots of Power-Law Distributions

The error of  $\hat{\alpha}$ ,  $\sigma$ , can be calculated as:

$$\sigma = \frac{\hat{\alpha} - 1}{\sqrt{n}} + O(1/n) \quad (2.14)$$

This suggests that as  $n \rightarrow \infty$ , then  $\sigma \rightarrow 0$ .

Also note that in Eq. 2.13,  $\hat{\alpha}$  is a function of the choice of  $x_{min}$ . As  $x_i \geq x_{min}$ , choosing a larger  $x_{min}$  reduces the amount of data used for the fit, reducing  $n$  and correspondingly increasing  $\sigma$ . On the other hand, in experimental datasets, smaller values would be disproportionately affected by random noise or other non-power-law phenomena.

There are multiple methods to identify the best value of  $x_{min}$ . Unless otherwise stated, this thesis uses the Kolmogorov-Smirnov statistic, which is the maximum difference between the data and the fitted model; that is:

$$D = \max_{x \geq x_{min}} |S(x) - P(x)| \quad (2.15)$$

Here  $S(x)$  is the CDF for the experimental dataset (for observations  $x_i \geq x_{min}$ ), and  $P(x)$  is the CDF of the power-law model given the scaling parameter  $\hat{\alpha}$ . The value for  $x_{min}$  where  $D$  is minimised,  $\hat{x}_{min}$ , can then be substituted into Eq. 2.13 and the observations selected such that  $x_i \geq \hat{x}_{min}$ .

An alternative method of calculating the optimal  $x_{min}$  is detailed in Ref. [39], where a double-bootstrap method is applied. In this technique, random samples of the dataset  $x_i \geq x_{min}$  are taken and analysed by two consistent estimators of  $\alpha$ .  $\hat{x}_{min}$  is chosen as the value of  $x_{min}$  where the differences in  $\hat{\alpha}$  are minimised between both estimators. These double-bootstrap methods are used to find the scaling parameters with different, consistent estimators.

## 2.6 Analysing and Interpreting Plots of Power-Law Distributions

In sum, we effectively have three distinct, but mathematically related, means to present and interpret power-law distributions. The first is through a power-law spectrum; effectively a list of event size and power-law distributions. The second is through the log-log plot of event size and frequency. The third, and final, is a plot of the maximum-likelihood scaling parameter as a function of minimum event size cutoff.

### 2.6.1 Power-Law Event Spectra

As discussed in Section 2.5, we can generate a power-law distribution of event sizes by Eq. 2.9. Two such power-law spectra consisting of 100 000

## 2. Avalanche Statistics in Ferroelectric Thin Films

events and  $x_{min} = 1$ , one with  $\alpha = 2$  and one with  $\alpha = 3$ , are presented in Fig. 2.12.

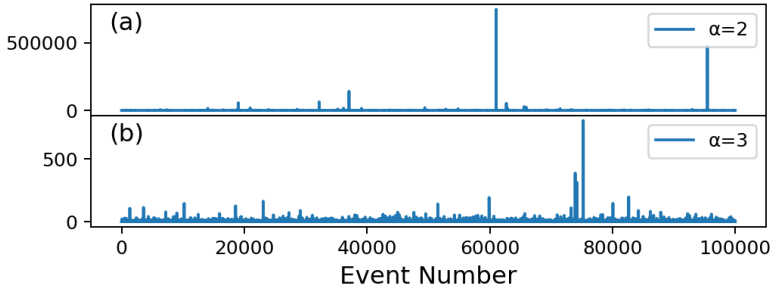


**Figure 2.12:** Simulated event spectra with  $x_{min} = 1$ , and different critical exponents. (a)  $\alpha = 2$ . (b)  $\alpha = 3$ .

Even from this ‘raw’ data, differences in key trends are visible between these two power-law distributions:

- The first is the particularly distinct differences in maximum event size. With a change in scaling parameter from 2 to 3, the maximum size of the events decreases by multiple orders of magnitude.
- The second is the visible appearance of these power-law spectra. In this case, the distribution with a lower scaling parameter has fewer prominent ‘spikes’ in the dataset (but those spikes are much, much larger in magnitude). In the same way, the smaller events in the higher scaling parameter distribution are more similar in value to the larger events, than the equivalent events are in the lower scaling parameter case.

These trends continue to some extent. As the scaling parameter  $\alpha \rightarrow 1$ , a singular spike becomes increasingly prominent with increasing values. With a scaling parameter  $\alpha \gg 5$ , we no longer observe a difference between large and small events, and discussions of power-law distributions no longer become meaningful.

Note that at this stage, a change in  $x_{min}$  only linearly affects the magnitude of the events; if we set  $x_{min} = 5$  instead of  $x_{min} = 1$ , the distribution would be similar in shape, but with all values increased by a factor of 5.

It should also be clear that if two power-law distributions were to be added or appended to each other, the distribution would be dominated by the lower-scaling parameter distribution; this lower parameter distribution would have events of much greater magnitude than the higher parameter

## 2.6 Analysing and Interpreting Plots of Power-Law Distributions

distribution. Power-law distributions (particularly those with lower scaling parameters) also tend to dominate over random noise for these same reasons.

The  $x$ -axis in Fig. 2.12 is ‘Event Number’, and here each event is entirely random. In real datasets, if this ‘Event Number’ is physically meaningful (eg. time, applied force, etc.) then larger events may cluster together. Regardless, we should still see this distribution of large and small events, and with the large events orders of magnitude greater than the small ones.

### 2.6.2 Log-Log Plots

To convert such power-law spectra into a log-log plot of event size and frequency, we first need to bin our dataset (if our maximum event size is 500000 and we have 100000 events, we will not even populate every integer, let alone the infinite values between them).

When binning a dataset, it is important to bin *logarithmically*. The distinction is shown in Fig. 2.13. Fig. 2.13(a) has logarithmic binning, and we can see a clear linear trend. In Fig. 2.13(b), the first two bins are particularly large on this logarithmic scale; and from any two points we would naturally expect to see a line (and therefore a supposed power-law distribution). This effect is particularly prominent if the maximum event size is orders of magnitude greater than the minimum event size. To establish a good power-law fit by linearity on a log-log plot, logarithmic binning is most valid.

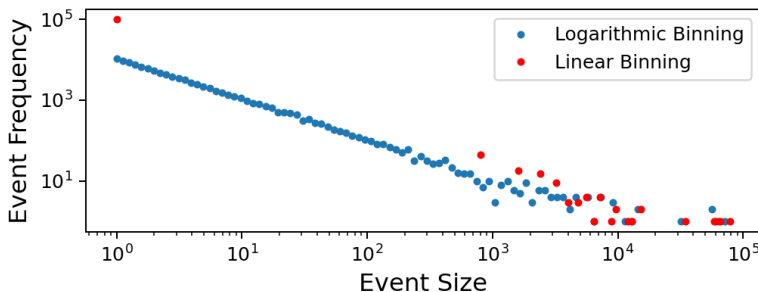


**Figure 2.13:** Log-Log plot of a power-law distribution with  $x_{min} = 1$  and  $\alpha = 2$ , and 100 bins of different size. (a) Bins are logarithmically spaced. (b) Bins are linearly spaced.

It is important to note that while we have our observed linear trend, and our scaling parameter  $\alpha$ , these two values are not precisely the same numerically. Rather, the gradient  $m$  of the linear trend is:

$$m = 1 - \alpha \quad (2.16)$$

As  $\alpha \rightarrow 1$ , this plot becomes more and more horizontal; we can associate this with the increasingly large maximum value. As  $\alpha$  increases, on the other hand, the gradient becomes steeper downwards, and large events become less likely.

I also note that the  $y$ -axis in Fig. 2.13 is of ‘Event Frequency’. We can easily shift this to ‘Event Probability’ by normalising this value against the total number of events. The gradient would also need to be adjusted accordingly in this case.

### 2.6.3 Maximum Likelihood Estimation Plots

The final type of plots we use are MLE plots, which are themselves quite different from the other plots discussed. In an MLE plot, we are plotting our best estimate of  $\alpha$  (which we have discussed at length but not been able to extract) as calculated via the MLE method, which we call  $\hat{\alpha}$ , against our estimate of  $x_{min}$ , which we call  $x_{min}^{\hat{}}$  (both of which we have thus far dismissed in this section).

Recall that physically the  $x_{min}$  describes the minimum value that we consider for our power-law set; that is, we are now ignoring every event below  $x_{min}^{\hat{}}$ , and only then calculating  $\hat{\alpha}$ . The value of the MLE plot is that if  $\hat{\alpha}$  is stable for a large range in  $x_{min}^{\hat{}}$ , then we can probably assume that  $\alpha$  is similar to this stable  $\hat{\alpha}$ .

The  $x_{min}^{\hat{}}$  plotted on the  $x$ -axis of MLE plots can share the same range as the  $x$ -axis of an associated log-log plot (and by extension, the  $y$ -axis of the event spectra), but the meaning of these values are completely distinct. Since they do describe events that occur at the same time, we can plot them with a shared  $x$ -axis, but it is important to keep the physical differences in mind.

It is important to work with the true, raw data when generating the MLE plot (as in the power-law spectra), and not the data binned to generate a power-law plot.

A sample MLE plot is shown in Fig. 2.14, along with its associated log-log plot. A ‘plateau’ in which  $\hat{\alpha}$  is stable is apparent when  $10^0 < x_{min}^{\hat{}} < 10^4$ . In this range  $\hat{\alpha} = 2$ , and thus we can assume that  $\alpha = 2$ ; this is incidentally correct for this synthetic case.

When  $x_{min}^{\hat{}} < 10^0$ , we are far away from  $\alpha$ . Comparison with the associated log-log plot explains why; we do not actually have data, and thus, do not have a meaningful power-law distribution for  $x_{min}^{\hat{}} < 10^0$ . Rather, we can conclude that since the power-law distribution starts at  $x_{min}^{\hat{}} = 10^0$ , we can indeed state that  $x_{min} = 10^0$ . This is, once again, correct for this synthetic dataset.

When  $x_{min}^{\hat{}} > 10^4$ , our value of  $\hat{\alpha}$  is no longer stable or consistent. Once more, the associated log-log plot explains why; we lose substantial amounts

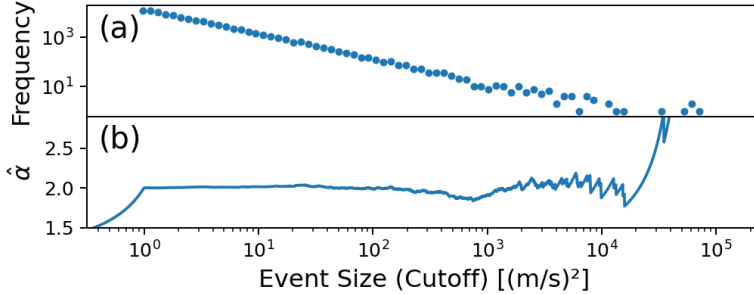


**Figure 2.14:** *Log-Log and MLE plots of a power-law distribution with  $x_{min} = 1$  and  $\alpha = 2$  (a) Log-Log plot, as with Fig. 2.13 (b) MLE plot.*

of information once we set our value of  $x_{min}$  this high, and are only working with a double- or even single-digit number of events.

When power-law distributions have a mixed character, as discussed with the raw power-law spectra, the lower-scaling parameter distribution tends to dominate. However, there are some signs of mixed-power-law distributions evident in the MLE plot; these are discussed in Ref. [42].

## 2.7 Why do Power-Law Distributions Exist in Nature?

As described earlier, the descriptive and predictive power of power-law distributions, in addition to the physical information they convey about the system, ensures that such statistic distributions are worthy of study. However, what makes power-law distributions particularly interesting is their ubiquity in nature; they exist in such diverse natural and sociological conditions that developing an understanding of the mechanics and processes of one phenomenon can be deeply useful in understanding another phenomenon that is wholly distinct. For ferroelectrics, a model system for more complex materials, this universality is particularly important.

The ubiquity of power-law distributions leads to the question: why should such varied phenomena follow such a seemingly arbitrary distribution? Various models are used to explain the origin of this observation. In this section, I will introduce three such models. The first, revolving around critical phenomena, is the main mechanism used to describe power-law dynamics in ferroelectric materials. While less common a mechanism, an division by a random variable around a zero value creates apparent power-law dynamics that will also be addressed in this thesis, and so is discussed here. Finally, the Yule process will be briefly discussed for its ubiquity in the power-law

statistics literature.

### 2.7.1 Scale-Free Networks, Critical Phenomena and Self-Organised Criticality

The most physically relevant origin of power-law distributions for this thesis occurs due to the critical phenomena of phase transitions, and the subsequent concept of self-organised criticality.

Consider a 2-dimensional array, with cells of size  $a$  and a total array area of  $X$ . Each point on this array can be of state 1 or state 0, and the probability of each point being in state 1 is  $P$ .

Let  $x$  be the area of a cluster of adjacent cells of state 1. As such, a single cell at state 1, surrounded by points of state 0 will have a cluster area of  $x = a$ . If this point of state 1 were instead bound by two points of state 1, and those two points were bounded by no additional points of state 1, then this cluster of three points of state 1 will have a size of  $x = 3a$ .

In this setup, we will show that in some particular circumstances, the probability  $p(x)$  of a particular cluster having the size  $x$ , follows a power-law distribution.

Consider a case where  $P = 1$ ; that is, all points are of state 1. In this case,  $x = X$ , and any subsequent change of the overall array would change the size of the singular cluster (and thus the average cluster size of the system).

Contrarily, consider a case where  $P \rightarrow 0$ ; that is, most points are of state 0, with very few of state 1. We would here expect the vast majority of clusters to be of size 1, or otherwise very low. This fact would not change with an increase in the array size  $X$ ; the average cluster size would still be low, and, contrary to the case of high  $P$ , at low  $P$ ,  $x$  is independent of  $X$ .

In this situation, there must be a minimum value of  $p$  in which  $x$  increases with  $X$ . This value, the *percolation threshold*, a so called *critical point*, can be determined as  $P_c = 0.5927\dots$ . Above this value, our network is fully percolating through the grid.

Let us now try and determine  $p(x)$  at percolation. The variables that change  $p(x)$  could, at maximum, be every variable we have defined here: the cluster size of interest  $x$ , the cluster expectation size  $\langle x \rangle$ , the area described by a cell on the array  $a$ , the array size  $X$ , and the probability of each point being in state 1,  $P$ .

Let us consider a very large system ( $X \rightarrow \infty$ ) at the percolation threshold ( $P = P_c$ ). As established, when  $P \geq P_c$ , percolation occurs and as such an infinite array  $X$  would have an infinite expected cluster size  $\langle x \rangle$ ; that is,  $\langle x \rangle \rightarrow \infty$  as well. The only remaining variables are  $x$  and  $a$ . As the probability  $p(x)$  is a dimensionless quantity, we can say

$$p(x) = Cf(x/a) \tag{2.17}$$

## 2.7 Why do Power-Law Distributions Exist in Nature?

---

where  $f(x/a)$  is some arbitrary function, and  $C$  is a normalisation constant.

Let us now consider an alternative array, where the area of each cell in the array is of a different size; that is,  $a = 1/b$ , where  $b$  is some arbitrary constant (we are here effectively ‘zooming in’ and ‘zooming out’). At the percolation threshold, we can calculate  $p(x)$ , like with Eq. 2.17, as:

$$p(x) = C' f(bx) \quad (2.18)$$

where  $C'$  is another normalisation constant.

Meanwhile, by direct substitution of  $x \rightarrow bx$ ,  $a \rightarrow 1$  in Eq. 2.17:

$$p(bx) = C f(bx) \quad (2.19)$$

and substitution of Eq. 2.18 to Eq. 2.19 yields:

$$\begin{aligned} p(bx) &= \frac{C}{C'} p(x) \\ &= g(b) p(x) \end{aligned} \quad (2.20)$$

Here,  $g(b)$  can be determined by substitution of  $x = 1$  into Eq. 2.20. This yields the identical result:

$$p(bx) = \frac{p(b)}{p(1)} p(x) \quad (2.21)$$

Eqs. 2.20 and 2.21 describes what is called a *scale-invariant system*, because any change in the scale (or unit of measurement)  $b$  changes only the scale of the result, and no other trends (that is to say, the relevant observables in critical phenomena and the percolation threshold are always scale invariant). In other words, the statistical physics of this system is effectively independent of its microscopic description.

As an example, let us say some variable  $x$  (earthquake intensities, city populations, cuteness of dogs...) follows a power-law distribution, and  $x = 100$  occurs at double the frequency of  $x = 1000$ . In this case, the change in scale  $b = 1000/100 = 10$ , and  $g(b) = 2$ . Therefore:

$$p(10x) = \frac{1}{2} p(x) \quad (2.22)$$

and this holds for all  $x$ ; so  $x = 200$  would be twice as likely as  $x = 2000$ ,  $x = 1000$  would be twice as likely as  $x = 10000$ , and so on.

This exponential, scale-invariant behaviour is also power-law behaviour. We can prove this following Eq. 2.21. If this equation holds for all  $b$ , we can differentiate both sides by  $b$  to yield:

$$x p'(bx) = \frac{p'(b)}{p(1)} p(x) \quad (2.23)$$



## 2. Avalanche Statistics in Ferroelectric Thin Films

---

Taking the specific case  $b = 1$  yields:

$$xp'(x) = \frac{p'(1)}{p(1)}p(x) \quad (2.24)$$

This can be solved as a linear first-order differential equation to finally yield:

$$\ln(p(x)) = \frac{p(1)}{p'(1)} \ln(x) + C \quad (2.25)$$

where  $C$  is an integration constant. This trend is linearity on a log-log plot; that is to say, a power-law distribution.

Therefore we establish that in such a completely generalised and abstract 2-state system at the percolation threshold, we get scale-invariant behaviour and therefore a power-law distribution. But why would we tend to be at the percolation threshold?

Drossel and Schwabl suggest that some phenomena may naturally oscillate around the percolation threshold, and this *self-organising criticality* is what maintains the power-law distribution [43]. As a concrete example, Drossel and Schwabl proposed their model to explain the power-law distribution of bushfire sizes thus:

1. In general, trees grow and forests will expand; so the probability  $p$  of any area being covered by a tree will naturally increase over time.
2. If  $p$  is *above* the percolation threshold, the trees will form a percolating network, and forest fires will also percolate through.  $p$  will therefore decrease below the percolation threshold as a result.
3. Once  $p$  is *below* the percolation threshold, then fires will no longer percolate. This will allow  $p$  to slowly increase until it exceeds the percolation threshold once more.

In sum,  $p$  will increase when below the percolation threshold, and  $p$  will decrease when above the percolation threshold. This will lead to oscillation around the percolation threshold, and thus, overall scale-invariant behaviour and a power-law distribution.

These ideas were later developed by Bak, Tang, and Wiesenfeld [44]. This self-ordered criticality is quite likely an origin for power-law behaviours in many ferroelectric thin film systems [45]. In the case of ferroelectric domain-wall motion, for example, defects and disorder can act as pinning sites for the domain wall position [46]. An increase in external field without domain-wall motion past the pinning site is analogous to a system rising above a local percolation threshold. Once the domain wall does move past this pinning site, the local vicinity must energetically re-equilibrate. For a particularly

strong local pinning potential to be overcome, a large domain-wall switching event would occur, and if the pinning were not so significant, the subsequent switching event would not need to be so large. This re-equilibration is analogous to a local fall below the percolation threshold, and the process can repeat continuously at subsequent pinning sites in a randomly varying potential energy landscape.

This model of critical phenomena and scale-free networks, in combination with self-organised criticality, suggests a likely origin for power-law behaviour in ferroelectric thin films.

### 2.7.2 Inversion About a Zero Value

Other origins for power-law distributions, beyond just criticality, have also been put forward. One such origin that was observed in the preparation of this thesis (Appendix. A is that of the inversion of quantities around a zero value.

Consider a random variable  $p_Y(y)$ , and a random variable of interest  $p_U(u)$  where  $u = 1/y$ . Say  $y$  follows some linear distribution that stretches from some negative value, through 0 to some positive value, such as:

$$Y \sim \text{Unif}(-a, a) \quad (2.26)$$

In this case, as  $y \rightarrow 0$ ,  $u \rightarrow \infty$  [Fig. 2.15(a)], and a plot of  $p(u)$  follows a power-law distribution. In mathematical detail, this occurs because a continuous random distribution  $p_Y(y)$  can be transformed into another  $p_U(u)$  by:

$$p_U(u) = p_Y(y) \frac{dy}{du} \quad (2.27)$$

Given that  $u = 1/y$ , then:

$$p_U(u) = -p_Y(y)u^{-2} \quad (2.28)$$

which is a power-law distribution with a scaling parameter  $\alpha = 2$  [Fig. 2.15(b)]. In cases where our  $y$  is around 0, our  $u$  is particularly large and this apparent power-law relationship dominates.

Newman *et al.* warn that this power-law relationship is not itself a stochastic power-law distribution, but rather a mathematical result; that is,  $\alpha = 2$  describes the mathematical consequence of calculating the derivative of the physical result of the reciprocal  $u = 1/y$ .  $u = 1/y$  is here being measured, without a true stochastic power-law distribution in  $p_U(u)$  itself.

To emphasise the difference, consider [Fig. 2.15(a)] once more. If our ‘raw data’ is  $y$ , we get a linear trend and no power-law distribution. It only appears from  $u$  because we calculate  $u = 1/y$ .

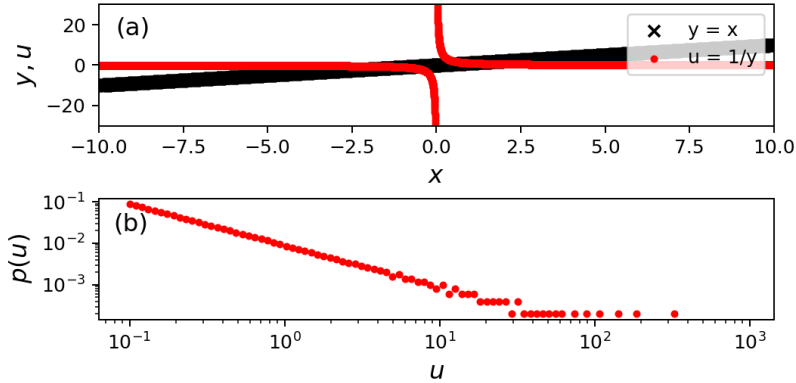


**Figure 2.15:** *How inversion about a zero value can create a false power-law distribution* (a) Two distributions; the non-power-law relationship  $y = x$  and the transformation  $u = 1/y$ . (b) The apparent power-law distribution observed in  $u$ .

To see how inversion about a zero value can create a false power-law distribution, see Appendix A.

### 2.7.3 The Yule Model

An alternative origin of power-law behaviour was proposed by Yule, suggesting that power-law trends can originate from the increasing accumulation of existing value [36]. While not directly applicable to ferroelectric thin films, its ubiquity in explaining various distinct phenomena in the literature justifies its brief inclusion here.

This model was described to explain how the number of species in each genus appears to follow a power-law distribution. This model assumes the following:

1. New species periodically form in existing genera.
2. The rate at which new species form in a genus is proportional to the existing number of species in that genus.
3. Intermittently, a new genus will form with one species in it.
4. Species are never removed from any genus.

If the premises are held true, then Yule shows that if a new genus is formed after  $m$  species are formed, then the distribution of species has a power-law tail, with a scaling parameter  $\alpha = 2 + (1/m)$ .

The Yule process is used to explain power-law distributions in various phenomena where an event begets more events, such as in city populations or human economic wealth. Beyond its use in explaining apparent power-law distributions in publication citations, however, the Yule process is not directly relevant to ferroelectrics research; any over-accumulation of charge tends to be met with strong electrostatic screening and depolarisation fields.

## 2.8 Avalanche Statistics in Ferroelectric Thin Films

When the frequency and size of a particular event can be modelled by these scale-invariant power-law distributions, we say that this event follows *avalanche statistics*<sup>2</sup>. Such avalanche statistics are particularly common in ferroelectrics.

The origin of power-law distributions in ferroelectrics is can be understood from a phenomenological description of ferroelectrics under an Ising model. The Ising model, as applied to ferromagnetic materials under an external field  $H$ , is described by the Hamiltonian [47]:

$$\mathcal{H} = -J \sum_{ij} \sigma_i \sigma_j - H \sum_i \sigma_i \quad (2.29)$$

as a cubic crystal with  $N$  sites, each with a spin  $\sigma_i = \pm 1$ , for  $i = 1, 2, \dots, N$ . This simplest form of the Ising model describes the Hamiltonian as a function of the interaction  $J > 0$  between adjacent sites. To minimise the Hamiltonian, the spins orient themselves to match the external field, but modulated by interaction between adjacent spins to some particular steady state.

Mean field theory can be used to simplify this relationship to measure the Hamiltonian as a function of the mean magnetisation,  $m$ , which can be calculated to show:

$$m \propto t^\beta \quad (2.30)$$

and equivalently the magnetic susceptibility can be found as:

$$\chi \propto t^{-\gamma} \quad (2.31)$$

where  $t = (T - T_c)/T_c$ , and in turn  $T$  is the temperature and  $T_c$  is the critical temperature. Here, the critical exponents  $\beta$  and  $\gamma$  depend on macroscopic characteristics of the system, but not the precise details; these exponents, and the exponents of analogous phenomena can likewise be determined by

---

<sup>2</sup>By this point, it should not be surprising that the size and frequency of mountain avalanches, like other phenomena, tend to follow power-law distributions and avalanche statistics [36].

## 2. Avalanche Statistics in Ferroelectric Thin Films

---

broad factors like the dimensionality of the system, or the type of interactions between adjacent sites. In our case, we use this *universality* of phenomena in the ferromagnetic Ising model to discuss ferroelectrics by considering instead changes of polarisation as a function of external electric field; similar treatments can be used to adjust the Ising model to discuss other transitions, like liquid-gas transitions, or binary alloy compositions, for example.

The introduction of disorder can introduce avalanche statistics into this universal behaviour. If the bond energy is not uniform (that is,  $J_{ij} = J + \delta J_{ij}$  for some small and random  $\delta J_{ij}$ ) then our *random-bond Ising model* can be described as:

$$\mathcal{H} = - \sum_{ij} J_{ij} \sigma_i \sigma_j - H \sum_i \sigma \quad (2.32)$$

We can also introduce some random field term  $h_i$  to create a *random-field Ising model* described as:

$$\mathcal{H} = -J \sum_{ij} \sigma_i \sigma_j - \sum_i h_i \sigma_i - H \sum_i \sigma \quad (2.33)$$

The random-exchange-interaction term  $J_{ij}$  of the random-bond Ising model, and the random-field term  $h_i$  of the random-field Ising model are both assumed to be drawn from Gaussian distributions in the broader framework of disordered elastic systems. In both cases, as with the simplified Ising model, if  $H(t)$  changes from some negative to some positive value, then some spins  $S_i = -1$  will likewise flip to  $S_i = +1$ . This changes the sign of the interaction term, which can trigger adjacent spins to also flip—creating an avalanche. While the above cases are considered at zero temperature, another kind of randomness can result from thermal fluctuations at finite temperature, which can also activate spin flipping and avalanches.

The precise behaviour is, however, conditional on the disorder term. In cases where the disorder (either in  $J_{ij}$  or in  $h_i$ ) is zero, then the system will ‘snap’ and the entire system will switch in one singular jump, to the equilibrium influenced by the universal conditions of the system. In cases where the disorder is particularly high, however, each site will change independently of one another, and no avalanches (or even no domains) are observed. It is at ‘intermediate’ values of disorder that avalanche behaviour occurs, and this avalanche character should be further affected by model, the dimensionality, and the amount of disorder in the system.

As stated, this ferromagnetic Ising model is universal, and can be made applicable to other systems directly relevant to our ferroelectric thin films. Most intuitively, ferroelectric dipole switching is directly analogous to ferromagnetic spin switching, and thus the switching events of these ferroelectric domains, under disordered conditions, is also expected to follow avalanche statistics (Section 2.8.1). Second, we can also consider structural transformations and plastic deformation under strain fields, redistributed to adjacent

sites and affected by disorder, under these Ising models to yield additional avalanche behaviour (Sections 2.8.2, 2.8.3). In these cases, at the critical threshold, we obtain our characteristic avalanche behaviour.

The different universality classes in the framework of disordered elastic systems can also be explored not only in terms of avalanche statistics, but also by the characteristic center-of-mass motion. Here, we consider the motion of the domain-wall interface between domains, as pinned by weak, collectively acting, random disorder (Fig. 2.16). Here, random-bond disorder represents short-range correlations (the local and symmetric variation of the depth of the ferroelectric double well potential, related to uncharged structural point defects), while random-field disorder represents long-range correlations (the local variation of internal field, related to charged defects, which asymmetrise the ferroelectric double well potential).

As a result of the disorder, when the interface is driven by some external force  $F$  (for ferroics, as a result of applying the conjugate field of the appropriate order parameter), it presents a complex and highly nonlinear dynamic response, with three distinct regimes determined by how  $F$  compares to some critical force  $F_C$  (Fig. 2.16) [48, 49]. At subcritical forces  $F \ll F_C$  at zero temperature there is in fact no motion. However, at finite temperature, thermal fluctuations allow activation of the interface and extremely slow (quasistatic) dynamics, either via *thermally assisted flux flow* (for a characteristic energy barrier height, giving rise to a velocity linear in the force and exponentially suppressed by the size of the typical barrier) or via *creep* (in a scale invariant random potential landscape, for which the energetic barrier encountered by an interface diverges when the applied force vanishes, giving rise to  $\ln(v) \sim F^{-\mu}$  where  $\mu$  is the creep exponent). Interface progress is thus via metastable, erratic jumps, which follow avalanche behaviour.

When  $F \sim F_C$ , the interface starts to depin, with a velocity response resembling the behaviour of a first order phase transition (hence this dynamic regime is often referred to as the depinning transition):  $v \sim (F - F_C)^\beta$ , where  $\beta$  is the depinning exponent. At finite temperature, this depinning transition shows thermal rounding. In this regime, again the velocity and the shape of the interface have a universal scaling behavior and the dynamics is characterised by large and scale-free avalanches.

Finally, as the force increases well above critical threshold,  $F \gg F_C$  then the applied force effectively overrides the pinning effects of the disorder, and a linear dynamic response  $F \sim F$  is recovered, modulated simply by the effective friction of the interface related to the disorder.

For a review of the dynamic response of ferroelectric domain walls under an external driving force, please see Refs. [46, 50, 51], and references therein.

Experimental observations of this phenomena are highlighted in Section 2.8.4.

For the remainder of this chapter, we will briefly review some of the ex-

## 2. Avalanche Statistics in Ferroelectric Thin Films

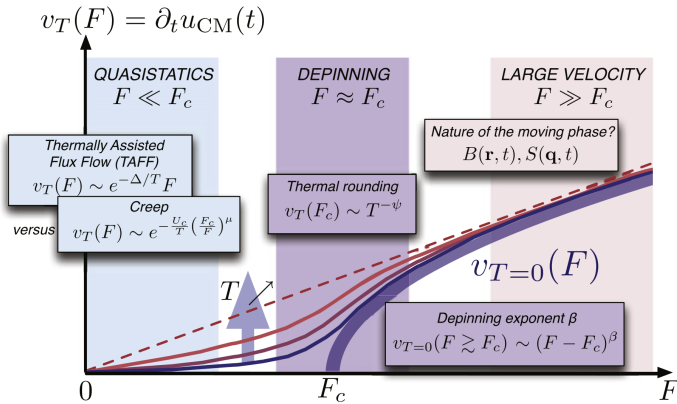


**Figure 2.16:** Velocity of a disordered elastic interface against the external force. Vertical arrow corresponds to an increase in temperature. From Ref. [48].

isting literature in which avalanche statistics are investigated in ferroelectric thin films.

### 2.8.1 Avalanche Statistics in Domain Switching

Classical experiments into avalanche statistics in ferroic materials all relate to the idea of *Barkhausen noise*. Barkhausen noise is a phenomenon in which a magnetic material that is being magnetised under a slowly increasing external magnetic field releases a distinct energy spectrum. In 1919, Heinrich Barkhausen measured this energy spectrum by winding a coil around the material as it was being magnetised, and then amplifying this current in a loudspeaker [45, 52, 53]. This created an acoustic and audible *crackling noise*. This crackling noise consisted of a series of small and large jumps, whose size follows a power-law distribution and avalanche statistics. This process helped improve our understanding of ferromagnetic switching, and showed that such switching processes are neither continuous nor linear, but rather occur through these discrete jumps.

Non-magnetic ferroics—ferroelectrics and ferroelastics—also express Barkhausen noise and avalanche statistics during their own switching events under the appropriate conjugate field [54]. In work by Tan, Flannigan, *et al.* [55, 56], ferroelectric Barkhausen noise with a critical exponent of  $1.64 \pm 0.15$  was acquired by measuring the current and polarisation response to a changing external electric field. The Omori exponent for aftershocks was also found to be  $0.95 \pm 0.03$ . As with ferromagnetic materials, this external field causes local domain switching, which results in a sudden and measurable current change—these sudden jumps follow avalanche statistics.

Similar methods can also be used to analyse ferroelectric switching in

thin films. For example, in 2020, Yazawa *et al.* [57] reported Barkhausen noise on 300 nm thick PZT thin films as measured by a  $\sim 50 \mu\text{m}^2$  Pt probe, although no direct critical exponent was reported. Individual Barkhausen pulses have also been directly imaged by transmission electron microscopy, as reported by Ignatans *et al.* [58].

### 2.8.2 Avalanche Statistics in Structural Phase Transformations

Another, and even more general phenomenon governed by avalanche statistics are structural phase transformations. These phase transformations, which often result in topographical changes in the material, can indeed be observed optically. High-speed optical images or video can therefore be used to image the such structural phase transformations in ferroelectric materials and thin films.

In 2019, Casals *et al.* showed how the different reflection and transmission characteristics of  $a$ - $c$  twins are distinct from those of  $a_1$ - $a_2$  twins in cryogenic STO, and established avalanche statistics for this phase transformation [59]. A critical energy exponent of 1.4 was reported, albeit with an MLE plateau of only approximately one order of magnitude. In 2020, a similar investigation was performed on room temperature BaTiO<sub>3</sub>; the ferroelectric and ferroelastic change in orientation was here determined by measuring the transmission of polarised light [60]. The critical energy exponent was here measured as 1.6, with a plateau of width 1–2 orders of magnitude. Casals *et al.* confirmed similar behaviour in the relaxor ferroelectric Pb(Mg<sub>1/3</sub>Nb<sub>2/3</sub>)O<sub>3</sub>-PbTiO<sub>3</sub> in 2021, in which they observe consistent energy exponents of approximately 1.3 (at the coercive field) and 1.6 (closer to the creep regime) between both BaTiO<sub>3</sub> and Pb(Mg<sub>1/3</sub>Nb<sub>2/3</sub>)O<sub>3</sub>-PbTiO<sub>3</sub> [61]. The authors suggests from this that there is some universal switching behaviour between these materials at the coercive field. This work was corroborated by Scott *et al.* in investigations on purely ferroelastic LAO [62], with energy exponents at approximately 1.3 (at lower temperatures) and 1.6 (at higher temperatures).

Structural phase transitions and related avalanche statistics will be discussed more at length in Chapter 7.

### 2.8.3 Avalanche Statistics via Compression and Nanoindentation

Most generally, porous materials as a whole express avalanche statistics during their failure under compression [63]. These measurements can be observed purely acoustically, and have been extensively performed in ferroelastic and ferroelectric ceramics like BaTiO<sub>3</sub> [63–66], where a field-integrated mean value of the energy exponent has been predicted and observed to have



a value of approximately 1.67.

These measurements typically rely on macroscale materials and measurements, and are more difficult to envisage and implement in thin films—where the impact of the substrate, and otherwise small size of the material are prohibitive. In 2023, however, Nguyen *et al.* reported the analysis of avalanche statistics in PTO films as measured by a nanoscale diamond probe through a variant of atomic force microscopy they call ‘crackling noise microscopy’ [67], in which critical exponents of 2.3 to 3.0 are reported with half-order-of-magnitude-length plateaus under MLE. The veracity and implications of this report motivated the studies performed in Chapter 7 of this thesis.

### 2.8.4 Avalanche Statistics in Domain Wall Motion

While Barkhausen noise was initially thought to mark the switching by *de novo* nucleation and growth of ferromagnetic domains (and which can still be the case), these jumps were eventually attributed primarily to the jerky motion of domain walls of existing domains; and equivalently, sudden jumps in the size of ferromagnetic domains [68]. This means that imaging and measuring the size of ferroelectric domains, and equivalently the individual motion of domain walls, could also reveal universal avalanche statistics governing their motion. Initial work towards this goal has been performed by Yang, Jo *et al.* [69] and Tückmantel *et al.* [38, 51] using piezoresponse force microscopy (PFM)—a nanoscale technique that allowed direct imaging of ferroelectric domains.

The work by Tückmantel *et al.* motivated much of the research discussed in Chapters 5 and 6, and so its detailed analysis will be discussed in that context. Further, attempts to increase compatibility between the PFM work by Tückmantel *et al.*, and the work with optical microscopy by Casals, Scott, and others motivated much of the work in Chapter 4. Most immediately, in the following Chapter 3, we will discuss in more detail the *scanning probe* techniques, like PFM, which allow imaging of ferroelectric domains.

## References

- [1] M. E. Lines and A. M. Glass, *Principles and applications of ferro-electrics and related materials* (Oxford university press, 2001).
- [2] D. Damjanovic, “Ferroelectric, dielectric and piezoelectric properties of ferroelectric thin films and ceramics”, *Reports on Progress in Physics* **61**, 1267 (1998).
- [3] P. Ghosez, J.-P. Michenaud, and X. Gonze, “Dynamical atomic charges: the case of ABO<sub>3</sub> compounds”, *Physical Review B* **58**, 6224 (1998).

- 
- [4] S. Trolier-McKinstry and P. Muralt, “Thin film piezoelectrics for MEMS”, *Journal of Electroceramics* **12**, 7–17 (2004).
  - [5] N. Pertsev, A. Zembilgotov, and A. Tagantsev, “Effect of mechanical boundary conditions on phase diagrams of epitaxial ferroelectric thin films”, *Physical Review Letters* **80**, 1988 (1998).
  - [6] D. G. Schlom, L.-Q. Chen, C. J. Fennie, V. Gopalan, D. A. Muller, X. Pan, R. Ramesh, and R. Uecker, “Elastic strain engineering of ferroic oxides”, *Mrs Bulletin* **39**, 118–130 (2014).
  - [7] N. A. Shepelin, Z. P. Tehrani, N. Ohannessian, C. W. Schneider, D. Pergolesi, and T. Lippert, “A practical guide to pulsed laser deposition”, *Chemical Society Reviews* (2023).
  - [8] D. Sando, T. Young, R. Bulanadi, X. Cheng, Y. Zhou, M. Weyland, P. Munroe, and V. Nagarajan, “Designer defect stabilization of the super tetragonal phase in >70-nm-thick BiFeO<sub>3</sub> films on LaAlO<sub>3</sub> substrates”, *Japanese Journal of Applied Physics* **57**, 0902B2 (2018).
  - [9] R. E. Cohen, “Origin of ferroelectricity in perovskite oxides”, *Nature* **358**, 136–138 (1992).
  - [10] The Materials Project, *TiPbO<sub>3</sub>*, *mp-20459*, <https://next-gen.materialsproject.org/materials/mp-20459>, Accessed: 2024-05-13.
  - [11] G. A. Rossetti Jr, L. E. Cross, and K. Kushida, “Stress induced shift of the curie point in epitaxial PbTiO<sub>3</sub> thin films”, *Applied Physics Letters* **59**, 2524–2526 (1991).
  - [12] Y. Li, S. Hu, Z. Liu, and L. Chen, “Effect of substrate constraint on the stability and evolution of ferroelectric domain structures in thin films”, *Acta materialia* **50**, 395–411 (2002).
  - [13] S. P. Alpay and A. L. Roytburd, “Thermodynamics of polydomain heterostructures. III. domain stability map”, *Journal of Applied Physics* **83**, 4714–4723 (1998).
  - [14] C. Lichtensteiger, J.-M. Triscone, J. Junquera, and P. Ghosez, “Ferroelectricity and tetragonality in ultrathin PbTiO<sub>3</sub> films”, *Physical Review Letters* **94**, 047603 (2005).
  - [15] D. D. Fong, G. B. Stephenson, S. K. Streiffer, J. A. Eastman, O. Auciello, P. H. Fuoss, and C. Thompson, “Ferroelectricity in ultrathin perovskite films”, *Science* **304**, 1650–1653 (2004).
  - [16] G. Catalan, A. Lubk, A. Vlooswijk, E. Snoeck, C. Magen, A. Janssens, G. Rispens, G. Rijnders, D. H. Blank, and B. Noheda, “Flexoelectric rotation of polarization in ferroelectric thin films”, *Nature Materials* **10**, 963–967 (2011).

## 2. Avalanche Statistics in Ferroelectric Thin Films

---

- [17] L. He and D. Vanderbilt, “First-principles study of oxygen-vacancy pinning of domain walls in  $\text{PbTiO}_3$ ”, *Physical Review B* **68**, 134103 (2003).
- [18] A. Yadav, C. Nelson, S. Hsu, Z. Hong, J. Clarkson, C. Schlepütz, A. Damodaran, P. Shafer, E. Arenholz, L. Dedon, et al., “Observation of polar vortices in oxide superlattices”, *Nature* **530**, 198–201 (2016).
- [19] S. Das, Y. Tang, Z. Hong, M. Gonçalves, M. McCarter, C. Klewe, K. Nguyen, F. Gómez-Ortiz, P. Shafer, E. Arenholz, et al., “Observation of room-temperature polar skyrmions”, *Nature* **568**, 368–372 (2019).
- [20] R. Guo, L. Cross, S. Park, B. Noheda, D. Cox, and G. Shirane, “Origin of the high piezoelectric response in  $\text{PbZr}_{1-x}\text{Ti}_x\text{O}_3$ ”, *Physical Review Letters* **84**, 5423 (2000).
- [21] J. F. Scott and C. A. Paz de Araujo, “Ferroelectric memories”, *Science* **246**, 1400–1405 (1989).
- [22] D. Sando, B. Xu, L. Bellaiche, and V. Nagarajan, “A multiferroic on the brink: uncovering the nuances of strain-induced transitions in  $\text{BiFeO}_3$ ”, *Applied Physics Reviews* **3** (2016).
- [23] O. Paull, C. Xu, X. Cheng, Y. Zhang, B. Xu, K. P. Kelley, A. de Marco, R. K. Vasudevan, L. Bellaiche, V. Nagarajan, et al., “Anisotropic epitaxial stabilization of a low-symmetry ferroelectric with enhanced electromechanical response”, *Nature Materials* **21**, 74–80 (2022).
- [24] D. Sando, A. Barthélémy, and M. Bibes, “ $\text{BiFeO}_3$  epitaxial thin films and devices: past, present and future”, *Journal of Physics: Condensed Matter* **26**, 473201 (2014).
- [25] G. Catalan and J. F. Scott, “Physics and applications of bismuth ferrite”, *Advanced Materials* **21**, 2463–2485 (2009).
- [26] D. Lebeugle, D. Colson, A. Forget, M. Viret, A. Bataille, and A. Gukasov, “Electric-field-induced spin flop in  $\text{BiFeO}_3$  single crystals at room temperature”, *Physical Review Letters* **100**, 227602 (2008).
- [27] T. Choi, S. Lee, Y. Choi, V. Kiryukhin, and S.-W. Cheong, “Switchable ferroelectric diode and photovoltaic effect in  $\text{BiFeO}_3$ ”, *Science* **324**, 63–66 (2009).
- [28] R. Moubah, G. Schmerber, O. Rousseau, D. Colson, and M. Viret, “Photoluminescence investigation of defects and optical band gap in multiferroic  $\text{BiFeO}_3$  single crystals”, *Applied Physics Express* **5**, 035802 (2012).
- [29] R. Palai, R. Katiyar, H. Schmid, P. Tissot, S. Clark, J. Robertson, S. Redfern, G. Catalan, and J. Scott, “ $\beta$  phase and  $\gamma$ - $\beta$  metal-insulator transition in multiferroic  $\text{BiFeO}_3$ ”, *Physical Review B* **77**, 014110 (2008).

- 
- [30] J. Seidel, L. W. Martin, Q. He, Q. Zhan, Y.-H. Chu, A. Rother, M. Hawkrige, P. Maksymovych, P. Yu, M. e. Gajek, et al., “Conduction at domain walls in oxide multiferroics”, *Nature Materials* **8**, 229–234 (2009).
  - [31] G. Catalan, J. Seidel, R. Ramesh, and J. F. Scott, “Domain wall nanoelectronics”, *Reviews of Modern Physics* **84**, 119 (2012).
  - [32] S. Farokhipoor, C. Magén, S. Venkatesan, J. Íñiguez, C. J. Daumont, D. Rubi, E. Snoeck, M. Mostovoy, C. De Graaf, A. Müller, et al., “Artificial chemical and magnetic structure at the domain walls of an epitaxial oxide”, *Nature* **515**, 379–383 (2014).
  - [33] H. Béa and P. Paruch, “A way forward along domain walls”, *Nature Materials* **8**, 168–169 (2009).
  - [34] I. Efe, N. A. Spaldin, and C. Gattinoni, “On the happiness of ferroelectric surfaces and its role in water dissociation: the example of bismuth ferrite”, *The Journal of Chemical Physics* **154** (2021).
  - [35] S.-M. Müller, J. Floris, S. Rohrmann, K. Staub, and K. L. Matthes, “Body height among adult male and female swiss health survey participants in 2017: trends by birth years and associations with self-reported health status and life satisfaction”, *Preventive Medicine Reports* **29**, 101980 (2022).
  - [36] M. E. Newman, “Power laws, Pareto distributions and Zipf’s law”, *Contemporary Physics* **46**, 323–351 (2005).
  - [37] M. Porta, T. Castán, A. Saxena, and A. Planes, “Influence of the number of orientational domains on avalanche criticality in ferroelastic transitions”, *Physical Review E* **100**, 062115 (2019).
  - [38] P. Tückmantel, I. Gaponenko, N. Caballero, J. C. Agar, L. W. Martin, T. Giamarchi, and P. Paruch, “Local probe comparison of ferroelectric switching event statistics in the creep and depinning regimes in  $\text{Pb}(\text{Zr}_{0.2}\text{Ti}_{0.8})\text{O}_3$  thin films”, *Physical Review Letters* **126**, 117601 (2021).
  - [39] I. Voitalov, P. van der Hoorn, R. van der Hofstad, and D. Krioukov, “Scale-free networks well done”, *Physical Review Research* **1**, 033034 (2019).
  - [40] R. Bulanadi and P. Paruch, “Identifying and analyzing power-law scaling in two-dimensional image datasets”, *Physical Review E* **109**, 064135 (2024).
  - [41] A. Clauset, C. R. Shalizi, and M. E. Newman, “Power-law distributions in empirical data”, *SIAM Review* **51**, 661–703 (2009).

- [42] E. K. Salje, A. Planes, and E. Vives, “Analysis of crackling noise using the maximum-likelihood method: power-law mixing and exponential damping”, *Physical Review E* **96**, 042122 (2017).
- [43] B. Drossel and F. Schwabl, “Self-organized critical forest-fire model”, *Physical Review Letters* **69**, 1629 (1992).
- [44] P. Bak, C. Tang, and K. Wiesenfeld, “Self-organized criticality: an explanation of the  $1/f$  noise”, *Physical Review Letters* **59**, 381 (1987).
- [45] J. P. Sethna, K. A. Dahmen, and C. R. Myers, “Crackling noise”, *Nature* **410**, 242–250 (2001).
- [46] P. Paruch and J. Guyonnet, “Nanoscale studies of ferroelectric domain walls as pinned elastic interfaces”, *Comptes Rendus Physique* **14**, 667–684 (2013).
- [47] H. Nishimori and G. Ortiz, *Elements of phase transitions and critical phenomena* (Oxford university press, 2011).
- [48] E. Agoritsas, V. Lecomte, and T. Giamarchi, “Disordered elastic systems and one-dimensional interfaces”, *Physica B: Condensed Matter* **407**, 1725–1733 (2012).
- [49] E. E. Ferrero, L. Foini, T. Giamarchi, A. B. Kolton, and A. Rosso, “Creep motion of elastic interfaces driven in a disordered landscape”, *Annual Review of Condensed Matter Physics* **12**, 111–134 (2021).
- [50] J. Guyonnet, *Ferroelectric domain walls: statics, dynamics, and functionalities revealed by atomic force microscopy* (Springer Science & Business Media, 2014).
- [51] P. Tückmantel, *Scanning probe studies of structural and functional properties of ferroelectric domains and domain walls* (Springer Nature, 2021).
- [52] H. Barkhausen, “Zwei mit hilfe der neuen verstärker entdeckte erscheinungen”, *Phys. Z* **20**, 401–403 (1919).
- [53] O. Perković, K. Dahmen, and J. P. Sethna, “Avalanches, barkhausen noise, and plain old criticality”, *Physical Review Letters* **75**, 4528 (1995).
- [54] T. Nattermann, S. Stepanow, L.-H. Tang, and H. Leschhorn, “Dynamics of interface depinning in a disordered medium”, *Journal de Physique II* **2**, 1483–1488 (1992).
- [55] C. Tan, C. Flannigan, J. Gardner, F. Morrison, E. Salje, and J. Scott, “Electrical studies of Barkhausen switching noise in ferroelectric PZT: critical exponents and temperature dependence”, *Physical Review Materials* **3**, 034402 (2019).

- [56] C. Flannigan, C. Tan, and J. Scott, “Electrical studies of Barkhausen switching noise in ferroelectric lead zirconate titanate (PZT) and BaTiO<sub>3</sub>: critical exponents and temperature-dependence”, *Journal of Physics: Condensed Matter* **32**, 055403 (2019).
- [57] K. Yazawa, B. Ducharne, H. Uchida, H. Funakubo, and J. E. Blendell, “Barkhausen noise analysis of thin film ferroelectrics”, *Applied Physics Letters* **117** (2020).
- [58] R. Ignatans, D. Damjanovic, and V. Tileli, “Individual barkhausen pulses of ferroelastic nanodomains”, *Physical Review Letters* **127**, 167601 (2021).
- [59] B. Casals, S. van Dijken, G. Herranz, and E. K. Salje, “Electric-field-induced avalanches and glassiness of mobile ferroelastic twin domains in cryogenic SrTiO<sub>3</sub>”, *Physical Review Research* **1**, 032025 (2019).
- [60] B. Casals, G. F. Nataf, D. Pesquera, and E. K. Salje, “Avalanches from charged domain wall motion in BaTiO<sub>3</sub> during ferroelectric switching”, *APL Materials* **8**, 011105 (2020).
- [61] B. Casals, G. F. Nataf, and E. K. Salje, “Avalanche criticality during ferroelectric/ferroelastic switching”, *Nature Communications* **12**, 345 (2021).
- [62] J. J. Scott, B. Casals, K.-F. Luo, A. Haq, D. Mariotti, E. K. Salje, and M. Arredondo, “Avalanche criticality in LaAlO<sub>3</sub> and the effect of aspect ratio”, *Scientific Reports* **12**, 14818 (2022).
- [63] E. K. Salje and K. A. Dahmen, “Crackling noise in disordered materials”, *Annu. Rev. Condens. Matter Phys.* **5**, 233–254 (2014).
- [64] Y. Xu, G. Shao, J. Pang, Y. Zhou, X. Ding, J. Sun, T. Lookman, E. Salje, and D. Xue, “Avalanches during ferroelectric and ferroelastic switching in barium titanate ceramics”, *Physical Review Materials* **6**, 124413 (2022).
- [65] E. Salje, D. Xue, X. Ding, K. A. Dahmen, and J. Scott, “Ferroelectric switching and scale invariant avalanches in BaTiO<sub>3</sub>”, *Physical Review Materials* **3**, 014415 (2019).
- [66] E. Salje, “On the dynamics of ferroelastic domain boundaries under thermal and elastic forcing”, *Phase Transitions* **83**, 657–669 (2010).
- [67] C.-P. T. Nguyen, P. Schoenherr, E. K. Salje, and J. Seidel, “Crackling noise microscopy”, *Nature Communications* **14**, 4963 (2023).
- [68] C. Kittel, “Physical theory of ferromagnetic domains”, *Reviews of Modern Physics* **21**, 541 (1949).

- [69] S. M. Yang, J. Y. Jo, D. J. Kim, H. Sung, T. W. Noh, H. N. Lee, J.-G. Yoon, and T. Song, “Domain wall motion in epitaxial pb (zr, ti) o<sub>3</sub> capacitors investigated by modified piezoresponse force microscopy”, *Applied Physics Letters* **92** (2008).

### 3.1 Scanning Probe Microscopy and Atomic Force Microscopy

Microscopy describes a diverse family of techniques used to investigate phenomena that would be too small to look at with the naked eye. This broad microscopy family can itself be subdivided into different groups based on the mechanism used to investigate different kinds of small-scale phenomena, such as optical microscopy (which uses optical light for magnification) or electron microscopy (which uses electrons for magnification) (Fig. 3.1). *Scanning probe microscopy* (SPM), is another group of microscopy techniques, and it is with SPM that much of the key scientific results of this thesis were acquired.

In brief, SPM images a sample by moving a probe across its surface. The response of the probe (or tip) to the sample surface, and any other stimulation applied, are then measured and analysed. From these measurements, a physical description of the sample and sample surface can be extracted.

SPM can itself be subdivided into several subgroups. The original scanning probe microscopes were scanning tunnelling microscopes [1], where electron tunnelling is used to probe some conductive material. Other variants have also been developed, like scanning near-field optical microscopy [2], which uses a probe as an optical source to bypass the standard optical resolution limit.

The variant of SPM where a mechanical probe is used, and its cantilever



### 3. Sample Characterisation

---

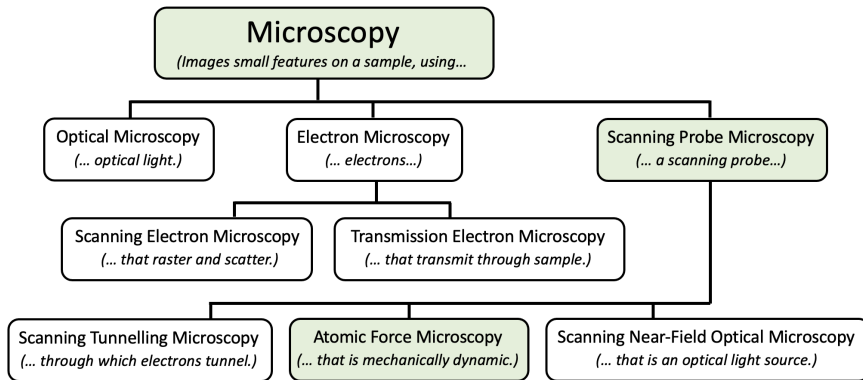


**Figure 3.1:** A ‘family tree’ of microscopy techniques. In light green is the path to atomic force microscopy, the focus of this thesis.

dynamics observed, is known as atomic force microscopy (AFM) [3], and is what we focus on here.

In this section, we will first provide a general description of how an AFM can be used, most simply, to measure a sample surface topography through direct contact. From this general description, we will then talk about how an AFM can be altered or modified to investigate the fascinating breadth of properties in ferroelectrics.

#### 3.1.1 General Description of Atomic Force Microscopy

At its core, a working AFM setup requires three components:

- A **probe**, or tip, that makes direct or indirect contact with a sample. The interactions between the tip and the sample are what provides the physics and data to be analysed. As such, the quality and mechanical or electrical properties of the tip are of paramount importance.
- A set of **piezoelectric actuators**, typically at least three. SPM is so named because the probe scans across the sample in typically a raster (zig-zag) pattern. This two dimensional motion ( $x$  and  $y$  motion) requires at least two piezoelectric actuators. Additional actuators are required to adjust the height of the tip relative to the sample ( $z$  motion). Depending on the model of the machine, the actuators may be placed either on the side of the tip or the side of the sample.
- A **mechanism to identify tip position**. The standard method involves reflecting a beam off the back plate of the tip, and tracking the deflection of this beam with a set of photodetectors.

### 3.1 Scanning Probe Microscopy and Atomic Force Microscopy

---

If all three of these components provide feedback to one another, a simple AFM setup is fully possible. Perhaps the most physically and practically simple form of SPM is known as *contact-mode* AFM, and assuming optical beam deflection is used to determine tip motion, proceeds thus:

1. The sample of interest is placed on a plate inside the scanning probe microscope. The actuators can now be used to move the sample relative to the tip, which is itself attached to a cantilever.
2. The optical beam is aligned onto the back of the cantilever, and the photodetector is zeroed such that a tilt in the cantilever as a result of a tip-sample interaction changes the response measured by the photodetector (Fig. 3.3).
3. The sample and tip are made to slowly approach one another using the  $z$  piezoelectric actuator. At different length scales, different interactions are dominant: van der Waals interactions between two otherwise neutrally charged objects, increasingly attractive at shorter and shorter separation, mean that the tip will at first slowly, then finally quickly, be ‘pulled’ onto the sample surface. Once in ‘contact’, however, highly repulsive Pauli exclusion becomes dominant (Fig. 3.2).
4. The attraction of the tip causes a deflection of the optical beam on the back of the cantilever, and a corresponding change in its position on the photodetector. This attraction means the tip can be considered to be ‘in contact’ when the deflection falls below some set threshold.
5. The  $x$  and  $y$  piezoelectric actuators are activated to move the tip and sample in a raster pattern relative to one another. The topography of the sample surface causes a corresponding change in the  $z$ -position of the tip, which mechanically tilts the cantilever and thus creates a response that can be detected by the photoelectric diode.
6. To minimise tip wear from the strong contact forces of the tip being dragged across the sample, the  $z$  piezoelectric actuator is used to raise or lower the cantilever chip to keep the deflection at some predetermined value (the *set point*).
7. The deflection and data from the  $z$  piezoelectric actuator can be reported for each point in the raster tip path. Each can be used to generate and interpret an image of the sample surface topography.

The raster path of the scanning probe ensures that each ‘point’ on the captured image can be measured twice: once on a forward motion (the ‘trace’) and once in backward motion (the ‘retrace’). The axis of trace and retrace is known as the fast-scan axis. The perpendicular direction is known

### 3. Sample Characterisation

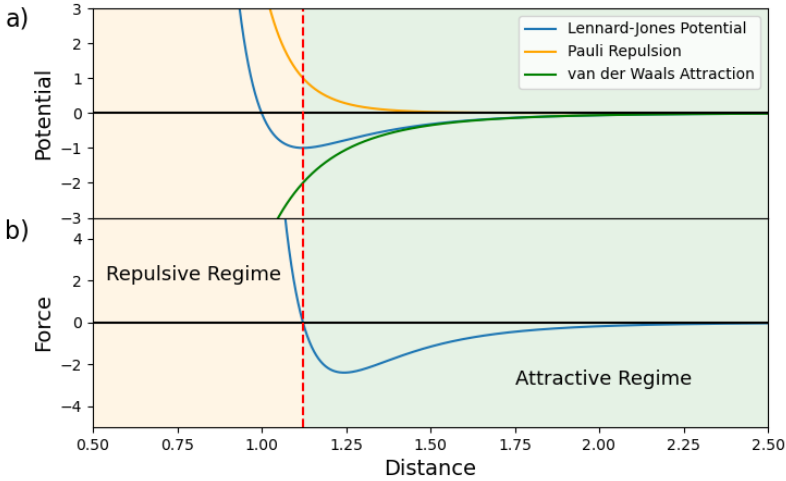


**Figure 3.2:** The Lennard-Jones potential used to model tip-sample interaction. a) shows this Lennard-Jones potential  $U(r) = 4U_0 \left[ (R_a/r)^{12} - (R_a/r)^6 \right]$ , which describes the potential between two neutral atoms as the difference between an attractive van der Waals force proportional to  $1/r^6$  (where  $r$  is the distance) and Pauli repulsion proportional to  $1/r^{12}$ . Here,  $U_0$  is the depth of the potential well, and  $R_a$  is the distance at which  $U(r)$  is 0. b) The effective force  $F = U'(r)$  resulting from this potential. The dashed line shows the border between where repulsive forces and attractive forces dominate. Figure reproduced from Ref. [4]

as the slow-scan axis. As they are directly measured in the same motion, measurements along the same line in the fast-scan axis tend to be highly accurate with respect to one another; direct comparison between points along the slow-scan axis may be less reliable.

There are, however, variations of this general process which may be considered variations or subsets of SPM. We will here describe differences in SPM, first by where above the sample the tip is, and then the type of physics the tip is used to measure. As it forms the bulk of this thesis, we will place special emphasis on piezoresponse force microscopy (PFM) and particular subvariants of this technique. We will then highlight some other general options that can be used to modify existing SPM variants.

#### 3.1.2 Position of Tip

The general process above describes a situation in which the tip rasters while in direct physical contact with the sample surface (or at least, when Pauli repulsion is greater than van der Waals attraction). This is known as a ‘contact mode’ scan and forms the baseline of a number of SPM variants.

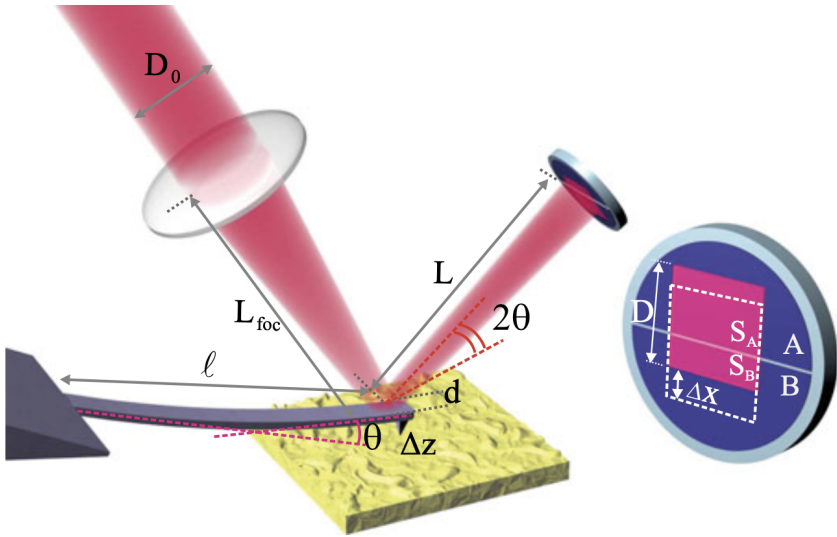


**Figure 3.3:** A schematic showing how optical beam deflection can monitor changes in tip position. A bend of the cantilever by an angle  $\theta$  causes the beam to deflect by  $2\theta$ . This causes a shift of the centre of the deflected beam on the photodetector by  $\Delta x$ , which causes a relative increase the intensity  $S_A$  collected by the split photodiode at A, compared to the intensity  $S_B$  collected by the split photodiode at B. Photodiodes can further be split in quadrature to also measure lateral deflection responses. Figure from Ref. [4]

It may however be preferable for the tip to avoid constant contact along the sample surface, and so variants of SPM where the tip is raised to be in intermittent-contact (*tapping*) or non-contact with the sample are made possible.

#### 3.1.2.1 Tapping Mode

Tapping mode, or intermittent-contact mode, or AC mode, is the standard method of imaging surface topography for materials physics. For topography acquisition in AFM, tapping mode presents a clear advantage over contact mode by reducing tip wear, and thus, is capable of overall improved image quality over contact mode imaging. This can also reduce artefacts obtained from the application of too great forces onto a sample surface.

For tapping mode measurements, a piezoelectric actuator is used to oscillate the cantilever around its resonance frequency (this is highly dependent on the material and elastic properties of the tip, but usually ranges from 10 to 1000 kHz). Before any actual imaging or experiments, this resonance frequency is found (the system is said to be *tuned* to the

### 3. Sample Characterisation

---

cantilever's resonance frequency).

From a raised position, like with contact-mode measurements, the tip and sample are made to approach one another. For tapping mode, however, the cantilever is made to oscillate during the approach. Repulsion between the tip and sample will occur whenever the tip is made to 'contact' the sample during this oscillation. These strong repulsive forces cause an approximately linear reduction in the amplitude of oscillation [5, 6]. When this oscillation amplitude reduces below some particular amplitude (again called the *set point*), the tip is considered to be fully approached, and measurement can begin.

Like with contact-mode measurements, the tip performs a raster scan. The  $z$  piezoelectric actuator is used to maintain the cantilever oscillations at a consistent amplitude, akin to the process for contact mode for a consistent deflection. The  $z$  piezoelectric actuator and deflection can again be used to determine the height of the sample surface. This can also be supplemented with two additional sources of data that result from the oscillation of the tip: the *amplitude* of the tip oscillation, and the *phase* of the tip oscillation with respect to the phase of the driving piezoelectric actuator. The amplitude and phase can be used to verify the accuracy of the measured  $z$  position and deflection, and also to suggest material properties of the surface; a higher amplitude in some region may suggest a lower elastic modulus than a lower amplitude in an adjacent region during the same measurement, for example.

#### 3.1.2.2 Non-Contact Mode

While tapping mode measurements avoid constantly having the probe drag across the sample surface, they do still rely on the repulsive forces that occur from the intermittent contact between the tip and sample. In particularly soft samples, like polymeric or other biologic samples, even this intermittent contact may cause damage to the sample.

To avoid this intermittent contact, the probe can instead be oscillated in the attractive van der Waals regime above the sample [4, 7]. These attractive forces still act on the tip and adjust both the resonant frequency and amplitude of oscillation, which can be measured and used to determine sample topography.

For our ferroelectric thin films, on single crystal substrates, the intermittent contact is not a significant problem, and so the more simply performed and analysed tapping mode is preferred to determine sample topography.

#### 3.1.2.3 Constant Distance Modes

The three discussed modes of tip position (contact, tapping mode, and non-contact mode) all assume that sample topography and height is a variable to be measured. This is not always the case, however, and many variations of

## 3.1 Scanning Probe Microscopy and Atomic Force Microscopy

---

SPM may wish to control the sample–tip distance to analyse other physics. This can be useful to observe, for example, magnetic forces (Section 3.1.3.4), which are distance-dependent but would be difficult to measure in contact.

To realise this experimentally, a dual-pass measurement is normally performed. On the initial trace of the scanning probe, the height is determined through one of the earlier discussed methods. On the subsequent retrace, the tip is raised to a known height above the sample, and the topography determined earlier is followed such that the tip is raised at a constant height. As these two passes occur immediately after one another, the impact of drift between the two passes is considered negligible, and thus the tip is considered to be at a constant height above the sample through this second pass.

### 3.1.3 Methods of Cantilever Excitation

#### 3.1.3.1 Piezoresponse Force Microscopy

Piezoresponse force microscopy (PFM) is an electroactive variant of AFM that images samples based on the local inverse piezoelectric response, and thus is immensely useful to image ferroelectric domains and domain walls [8]. PFM itself has several possible subvariants each with their own advantages and disadvantages. As with AFM before, we will first discuss one of the more simple methods (in this case, off-resonance single-frequency out-of-plane PFM) before discussing how variations of PFM affect measurements and results.

To recall briefly, the piezoelectric effect is an electrical potential buildup that emerges as a response to external mechanical strain (and inversely, a strain response to an externally generated potential difference). For a ferroelectric material, an electric field parallel to the ferroelectric dipole the material causes an expansion of the material in the polarisation axis; an electric field antiparallel to the polarisation causes a contraction of the material in the polarisation axis.<sup>1</sup>

In PFM, a conductive probe is chosen (the probe can be made of a conductor, doped, or coated with a conductive layer) and is subsequently used as a top electrode. Through sample preparation, a second (bottom) electrode is also constructed. In thin film growth, this can most simply be done by growing an electrically conductive film (eg. strontium ruthenate, lanthanum nickelate, lanthanum strontium manganate) below the (ferroelectric) film of interest. This bottom electrode is then electrically connected to the SPM (in many systems, the bottom plate on which the sample is placed is treated as

---

<sup>1</sup>It is worth remarking that that piezoelectric actuators are a core functional component of an AFM system in itself; they are distinct from the piezoelectric material, or ferroelectric material, that is being investigated, but may themselves bring additional artefacts in measurement

### 3. Sample Characterisation

---

the bottom electrode, so the experimentalist must simply short the bottom electrode to the sample plate, often with conductive paint).

Through this thesis, strontium ruthenate ( $\text{SrRuO}_3$ , SRO) is typically used as our bottom electrode.

With the sample prepared, the following process can occur:

1. As with contact-mode AFM, the sample is placed on the sample plate, and the photodetector is zeroed in preparation. The sample and probe are again brought into contact by a drop in deflection below some set point. In the case of PFM, this process also creates an electric circuit; from the top electrode (the conductive probe) through a ferroelectric thin film, through the conductive film, and finally through the external bottom electrode into the system. The AFM can then establish a potential difference between both electrodes and thus an electric field across the thickness of the film.
2. An alternating electric field is then applied across the sample. Consider how a constant electric field can cause either expansion or contraction of a ferroelectric material; an alternating field would therefore cause alternating expansion and contraction, whose phase (with respect to the electric field) depends on the polarisation orientation of the ferroelectric. Analysis is most simple if the frequency is far below the resonant frequency of the tip-sample complex (a driving voltage of  $\sim 2$  V and frequency of  $\sim 10$  kHz is typical), so that the amplitude of oscillation is largely independent of any changes in this resonant frequency; this will be discussed in more detail in Section 3.1.3.1.3.
3. The alternating expansion and contraction of the ferroelectric material causes an oscillation of the scanning probe tip, which can be detected via eg. optical beam deflection once again. A lock-in amplifier can be used to isolate the amplitude and phase of this tip oscillation with respect to the AC voltage applied to the sample.
4. Measurement can then proceed as with contact-mode AFM: the tip is rastered across the sample, with the  $z$  piezoelectric actuator used to ensure the tip-surface contact, and this  $z$  measurement and the tip deflection can be reported. However, this topography data is now supplemented with the unique PFM data: the amplitude of the oscillation and the phase offset of the oscillation (with respect to the externally applied voltage) allows mapping of the piezoelectric domains across the sample surface.

PFM is the standard method of imaging ferroelectric domains, as the *amplitude* and *phase* channels are sensitive to the magnitude and direction

### 3.1 Scanning Probe Microscopy and Atomic Force Microscopy

of ferroelectric polarisation, and this can be correlated with the topography data gathered simultaneously.

Model data of PFM on a ferroelectric PTO thin film can be seen in Fig. 3.4. The first data channel we may look at is the height channel [Fig. 3.4(a)], where we observe only very small variations in topography—on the order of a nanometre. This is an important result; it tells us that any data we get from amplitude and phase channels are more likely to be real, are not simply changes in topography that cause a false reading in the phase or amplitude channels (this phenomena, where one channel affects another, is known as ‘crosstalk’).

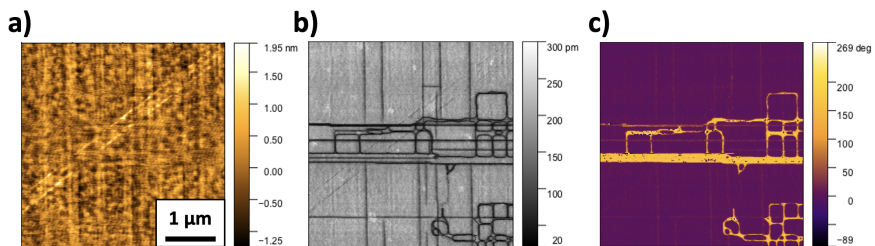


**Figure 3.4:** PFM measurement from an as-grown ferroelectric PTO thin film. a) Height channel. b) Amplitude channel. c) Phase channel.

The amplitude channel [Fig. 3.4(b)] is one channel that helps us map ferroelectric domains. It shows large regions with high-magnitude piezoelectric response, cut by lines of low-magnitude piezoelectric response. These high-amplitude regions mark a strong out-of-plane piezoresponse, which in turn suggests an out-of-plane ferroelectric polarisation in those same regions. The low-amplitude lines mark a reduced out-of-plane piezoresponse. This could potentially be non-piezoelectric (and therefore, non-ferroelectric) regions, but more likely corresponds to a regions where the ferroelectric polarisation rotates away from being fully out-of-plane. We must look to the phase channel [3.4(c)] for more clarification.

The phase channel is markedly distinct, with two distinct values of phase offset; the majority of the image has a phase offset around ‘0 degrees’ (purple), with small regions around ‘180 degrees’ (yellow)<sup>2</sup>. We know from the amplitude data that both of these domains show regions of high piezoresponse, but this  $\sim 180^\circ$  phase shift suggests these two domains have polarisation out of phase with one another. That is to say, if one region has a downwards-pointed polarisation, the other is pointed upwards, and vice versa.

This phase data helps explain some of the minima observed at the

<sup>2</sup>The choice of what this ‘phase offset’ is offset against is wholly arbitrary; here, we measure the offset against the majority (purple) domain, so its offset is 0 degrees with respect to itself.



### 3. Sample Characterisation

---

amplitude. It can be seen that the greatest minima in the amplitude channel occur at the boundaries between domains of different polarisation. These *domain walls* have a very local drop of amplitude to 0, because the domains on each side are oscillating out of phase with one another; continuity suggests that these domain walls would have no net out-of-plane polarisation.

The other minima in amplitude, which do not correspond to distinct features in the phase channel, cannot be fully clarified by this PFM measurement. While we will eventually see that these correspond to an in-plane polarisation tilt of the sample (strain-relieving *a*-domains), this cannot be elucidated from this simple vertical PFM measurement alone, and we would instead supplement this information with either a knowledge of the material properties, other results from complementary analytical techniques (like x-ray diffraction), or PFM measurements that are sensitive to in-plane polarisation.

#### 3.1.3.1.1 Out-of-Plane vs. In-Plane

In this section, we have thus far assumed that ferroelectric polarisation can only point in and out of the sample surface. This need not be the case; polarisation vectors can potentially point in any direction in 3-dimensional space, and the applied electric field can therefore cause a complex tensorial piezoelectric response. By measuring only the vertical deflection of the PFM tip, we are (or at least hope we are) mostly sensitive to the out-of-plane piezoelectric response (and thus, out-of-plane ferroelectric polarisation) of the sample.

If, instead of looking at the *vertical* deflection of the cantilever and optical beam, we look at the *lateral* deflection of the cantilever and optical beam, we can gain some insight into the in-plane polarisation of the ferroelectric polarisation. This in-plane PFM may also be referred to as lateral PFM, in contrast to out-of-plane PFM, which may be referred to as vertical PFM.

The principle of in-plane PFM is otherwise identical to that of out-of-plane PFM. In out-of-plane PFM, the potential difference between the tip and the bottom electrode leads to alternating contraction and expansion of the ferroelectric material, and thus, vertical deflection. For in-plane PFM, in the proximity of the probe, electric fields will at first radiate away (or into) the probe, before moving into the bottom electrode. If there is an in-plane piezoelectric effect in the sample (as there would be if there were an in-plane ferroelectric polarisation), this would similarly cause alternating expansion and contraction of the sample; in this case, however, this expansion and contraction would occur laterally, in the plane of the measurement. This expansion and contraction creates a corresponding twist or torsion on the scanning probe, and therefore, deflection of the optical beam laterally. This lateral deflection can be analysed in much the same way as the vertical

### 3.1 Scanning Probe Microscopy and Atomic Force Microscopy

---

deflection can be analysed.

There do remain key distinctions and implications in the physics and analysis of in-plane PFM over out-of-plane PFM measurements, however. I highlight some below:

- In-plane PFM measures cantilever torsion, and thus, is sensitive to in-plane domains perpendicular to the cantilever. Motion parallel to the cantilever direction causes the cantilever to buckle, and thus causes a vertical shift in the photodetector signal—the same shift that would be observed by out-of-plane polarisation, thus leading to unavoidable crosstalk. There is no simple way to resolve in-plane responses parallel to the cantilever; the most practical way is to physically rotate the sample with respect to the cantilever, such that torsion can be measured in two orthogonal in-plane directions.
- The sensitivity to torsion means PFM measurements are typically performed with the cantilever aligned perpendicular to the fast scan axis; this way, we are sensitive to responses along the more reliable fast-scan axis of the SPM. This does reduce the overall measurement flexibility, however, and can make measurements more difficult or of lower quality if, for example, topographical features were also aligned in this fast-scan axis.
- Crosstalk with height changes is much more significant with lateral PFM than vertical PFM. This is made particularly prominent by the nature of PFM as a contact-mode technique; the tip is forced to drag across the sample, creating a torsion and change in the lateral deflection. Any change in height naturally changes this torsion and may falsely be perceived as in-plane polarisation.
- While in vertical PFM,  $180^\circ$  shifts in phase are standard for a reversal of out-of-plane polarisation, the higher physical complexity of lateral plane means such a large phase-shift is not nearly as likely. This can make noise more present and thus increase analysis difficulty.
- The resonant frequency of cantilever torsion tends to be significantly higher than that of a vertical oscillation [9]. This can increase experimental difficulty of on-resonance in-plane PFM, and make measurements more susceptible to high-frequency noise (see Section 3.1.3.1.3).

#### 3.1.3.1.2 Switching Voltages and Maximising Signal-to-Noise

For ferroelectrics, the applied voltage is critical. The larger the voltage, the larger the observed strain response is, and therefore, the better signal-to-noise ratio. However, if the voltage is too high, ferroelectric switching is possible;

### 3. Sample Characterisation

---

this is a distinct phenomena to the piezoelectric response, and therefore, results may change significantly. The coercive voltage in a real setup depends greatly on material, film thickness, and electric contact, but for many thin films drive voltages above  $\sim 2$  V may indeed cause ferroelectric switching.

This is both advantageous and disadvantageous. On the one hand, this means that ferroelectric poling and nanolithography can be done in an SPM without any additional setup; instead of an AC voltage, a DC voltage can be applied through the conductive probe. On the other, this does create a maximum usable voltage, which may be prohibitively low for particularly thin films.

So how else can the signal-to-noise be increased, beyond the application of increased driving voltages? This has motivated the development of many ‘advanced’ PFM subvariants, and we shall here approach each in turn.

#### 3.1.3.1.3 On Resonance vs. Off Resonance

The example PFM method describes a measurement performed off-resonance PFM. In this setup, the driving frequency is chosen simply to be high enough for many, many oscillations to be observed at each point of the raster (if the probe scans at 1 line/s, with 512 points/line, then at 10 kHz,  $\sim 20$  oscillations occur at each point). We could instead oscillate the cantilever at a resonant frequency to maximise the amplitude response. As the tip is now in contact, we can no longer use the resonant frequency of the cantilever on its own (as we did for tapping and non-contact modes) but instead use the *contact-resonance* frequency of the tip-sample complex. This contact-resonance frequency is usually  $\sim 5\times$  higher than the resonant frequency of the free cantilever. At this resonant frequency, significantly higher signal-to-noise can be achieved.

The problem lies in the sample physics; the resonant frequency is highly dependent on tip-sample interaction and the sample surface. The ‘true’ resonant frequency can change significantly over the span of a measurement, and any change in the resonant frequency would bring with it significant changes in amplitude and phase of the cantilever oscillations. This therefore can end up introducing *more* noise into the measurement rather than less. While off-resonance measurements may have low oscillation amplitudes and therefore low signal-to-noise, improper on-resonance measurements can accidentally ‘measure’ changes in tip-sample contact rather than real ferroelectric polarisation changes.

For single-frequency PFM scans, to go off-resonance or on-resonance therefore becomes a critical question. Off-resonance tends to be preferred for thicker films that can withstand higher applied voltages, or samples with inconsistent topography, while on-resonance may be used if topography is known to be consistent and lower applied voltages are required.

### 3.1.3.1.4 Dual AC Resonance Tracking

We now know a key issue with on-resonance scans are changes in the contact-resonance frequency of the tip-sample complex. One could therefore ask: is there any way to track this frequency change? This is indeed possible, and this technique is known as dual AC resonance tracking (DART) or dual frequency resonance tracking (DFRT) [10].

DART relies on the following principles:

- A resonant frequency exists for every position on the raster.
- In a homogeneous sample, this resonant frequency is not expected to change significantly from moment to moment.
- The amplitude is expected to have a rapid, but not immediate, dropoff at each side of the resonant frequency

DART-PFM requires two separate lock-in amplifiers, but otherwise could be performed on any AFM system with appropriate software and real-time control. Here, rather than tune to a single frequency fully on resonance, each lock-in can drive a frequency on either side of the resonant frequency ( $\sim 5$  kHz apart), with the second lock-in providing a reference value with respect to the first (Fig. 3.5). If the amplitude at the first frequency (say, the lower frequency) increases, and the amplitude at the second frequency (say, the higher frequency) decreases, then it can be inferred that the true resonant frequency is shifting towards the first frequency (in this case, the lower one). As such, both drive frequencies can be shifted (here, to a lower value) to equalise the change in amplitude response between the two. This process can occur over the entire scan, continually adjusting the drive frequencies according to relative changes between them. In this way the resonant frequency is ‘tracked’ by the two AC voltages (at two distinct frequencies).

DART also provides additional information not available from single-frequency PFM. First, since two drive frequencies are used, two sets of data for amplitude and phase are acquired. This provides an additional sanity check; significant characteristic changes between the two amplitudes or the two phases imply errors in data acquisition. Second, the calculated (tracked) resonant frequency is data in itself, and could provide some information on the tip-sample complex or the quality of contact.

### 3.1.3.1.5 Band Excitation

We have discussed how PFM can most simply be performed at one frequency (on- or off-resonance), and how two frequencies can be used and slightly altered to determine the resonance frequency. This raises another question;

### 3. Sample Characterisation

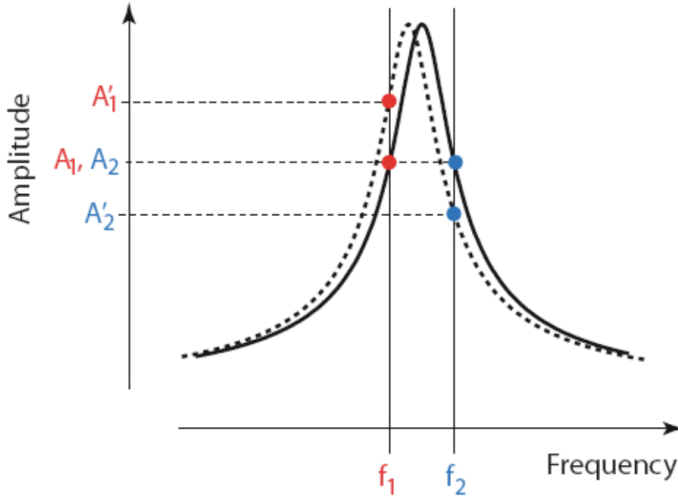


**Figure 3.5:** *The principle behind DART.* Two drive frequencies are set at  $f_1$  and  $f_2$ , such that on an initial tune (solid black line) the amplitudes  $A_1$  and  $A_2$  are identical. If the contact-resonance frequency shifts (dashed black line), the new amplitudes  $A'_1$  and  $A'_2$  change accordingly and can be used to determine the subsequent changes in drive frequencies. Figure from Ref. [10]

why not apply more frequencies? If we are already applying two frequencies, why not apply many, many more? (or, rather, much more, as we intend to approach a continuous distribution)

Here, a *band* of excitation frequencies, spaced between two values, is sent simultaneously through the tip as it scans [11]. This band of excitation frequencies causes a complex mechanical response, but via an inverse Fourier transform the amplitude corresponding to each component of the frequency band can be isolated. This allows simultaneous acquisition of the entire resonance peak (instead of one point, in single-frequency modes, or two points, in DART), and, in turn, this entire resonance peak can be fit to a model for a simple harmonic oscillator.

In this case, while the directly captured data is in itself rather simple (a highly convoluted deflection response of the cantilever), this deflection can be fit to a model of a simple harmonic oscillator, for example:

$$A(\omega) = \frac{A_{max}\omega_0^2}{\sqrt{(\omega^2 - \omega_0^2)^2 + (\omega\omega_0/Q)^2}} \quad (3.1)$$

where  $A(\omega)$  is the amplitude of oscillation at some frequency  $\omega$ ,  $A_{max}$  is the maximum amplitude of oscillation,  $\omega_0$  is the resonant frequency, and  $Q$  is the quality factor, which describes energy dissipation [11].

This simple-harmonic-oscillator fit provides an amplitude and frequency

### **3.1 Scanning Probe Microscopy and Atomic Force Microscopy**

---

that is actually much more resilient against rapid changes than DART (so long as said frequency remains in the excitation band), while also capturing more overall data (and therefore can increase signal-to-noise) without the need for any additional lock-in amplifiers. There do remain considerable downsides, however; the use of wide bands of excitation slows down measurements, and operation and analysis is made significantly more complicated, both for the user and for the computer.

#### **3.1.3.1.6 G-Mode**

In single-frequency PFM, we determined an amplitude and phase for each pixel, and neglected any change in frequency in the system. In DART-PFM, we increased acquisition complexity by determining a second amplitude and phase for each pixel, and increased model complexity by adding the change in frequency. In BE-PFM, we further increased the complexity of the model by capturing the entire band response and in doing so can better fit our data to that of a simple harmonic oscillator.

General mode (G-Mode) can be considered the epitome of this progression [12]. In G-Mode, all raw deflection is captured and stored. No model is assumed at time of data acquisition. This maximises the complexity of data collected, and likewise maximises the possibility of any model fit.

This has key advantages and disadvantages. The biggest advantage is the much higher potential of the acquired data. More complex models and phenomena can be investigated beyond that of a simple harmonic oscillator. Since a time component is now acquired for each pixel, for example, the tip response to a full ferroelectric switch at each pixel could be determined.

The biggest disadvantage of G-Mode is a reflection of its same advantage; the immense complexity makes any analysis incredibly unwieldy. Suitable models for analysis must be chosen with a strong understanding of the physics of the system. SPM and computer setups must also be designed with large data volumes ( $\sim 40$  GB per file) and large corresponding reading and writing rates in mind.

#### **3.1.3.1.7 Switching Spectroscopy PFM**

We have thus far discussed variations of PFM based on changing the drive frequency, and subsequent possible changes in acquisition, in order to maximise signal-to-noise without exceeding drive voltages beyond the ferroelectric coercive voltage. But what if we intentionally want to investigate ferroelectric switching events at the nanoscale? We cannot simply increase the AC voltage beyond the coercive voltage: ferroelectric switching is a dynamic process, and the high frequencies used may not allow sufficient relaxation time for polarisation reversal to occur. A DC voltage is therefore needed; but when measuring high DC voltages, we are introducing electrostatic effects into the

### 3. Sample Characterisation

system that would undoubtedly change the cantilever dynamics, and thus, create additional artefacts.

Switching spectroscopy PFM (SS-PFM) is a variant of PFM that takes the AC drive voltage and superimposes it against a DC voltage that varies, and also switches on and off [13] (Fig. 3.6). The piezoelectric response to the AC voltage read when the DC voltage is switched off can be used to describe the local ferroelectric properties as a result of the most recent applied DC voltage.

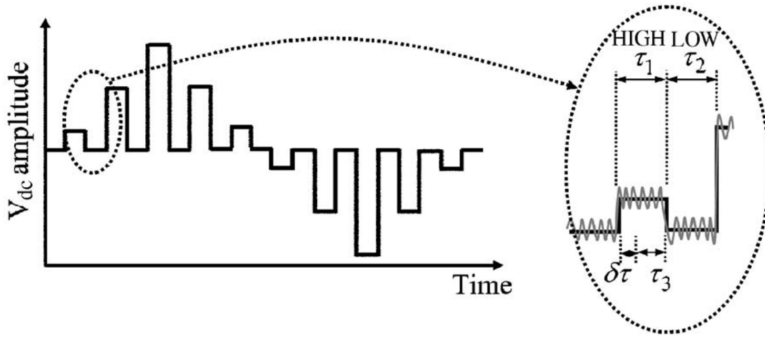


**Figure 3.6:** A pulse applied through SS-PFM, showing DC voltage changing and switching on and off, superimposed with a smaller AC voltage. Figure from Ref. [13]

Results from SS-PFM performed at a single point can be seen in Fig. 3.7(a–b). Here, we can see both the amplitude and phase response of the ferroelectric material as a function of the most recent applied DC voltage, when the DC voltage is itself switched off. Note the apparent similarity of the phase value to a classic ferroelectric polarisation-electric field hysteresis loop (Fig. 2.2, and the amplitude value to a classic strain vs. electric field butterfly loop (Fig. 2.3). In many ways, SS-PFM is a nanoscale variant of classic large-probe ferroelectric testing processes. When the DC voltage is well below the coercive voltage no significant change in phase or amplitude occurs with changes in the DC voltage. However, when the DC voltage approaches the coercive voltage, the phase itself begins to (and eventually fully) swap to that corresponding to the opposite ferroelectric domain. Likewise, the amplitude, now measuring a complex, partially switched region, drops in its magnitude before increasing again once the region is fully switched. The phase once again becomes consistent, until and unless the DC voltage is reversed below the opposite coercive voltage (or continued to increase in magnitude until a breakdown voltage is achieved)<sup>3</sup>.

<sup>3</sup>A reading of the phase and amplitude when the DC voltage is switched on can be seen in Fig. 3.7(c–d). Note the higher slope in the amplitude plot as we approach a

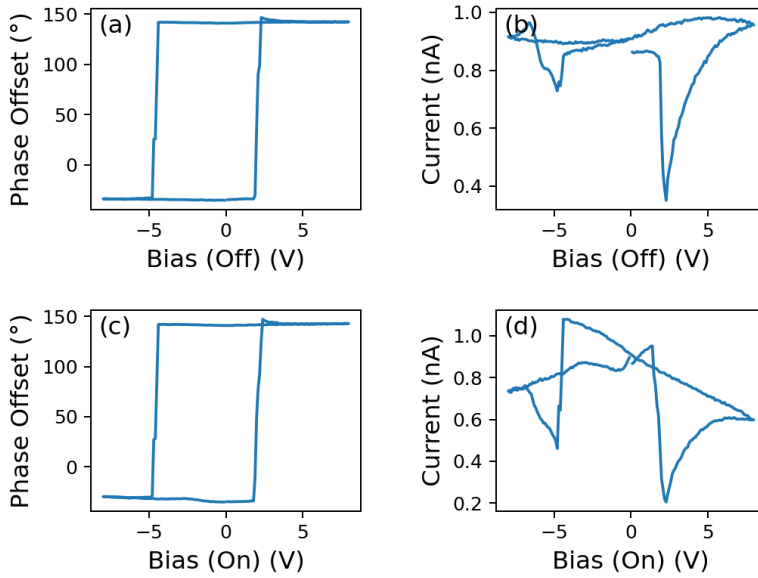


**Figure 3.7:** Result of SS-PFM on a point on a PTO ferroelectric thin film. a) Phase response, and b) amplitude response to the applied DC bias when the DC bias is off. c) and d) are the phase and amplitude responses respectively when the DC bias is set on.

There are two significant disadvantages of SS-PFM. One is that the high DC voltages may induce electrochemical reactions that significantly alter the sample, in addition to any effects of ferroelectric switching [14]. Additionally, the need for multiple on-off cycles mandates much greater experiment times. These two results in sum mean that SS-PFM is not usually done with a raster path. Rather, SS-PFM is performed on a point-by-point basis chosen intentionally, randomly, or in a regular grid. This means that results from SS-PFM cannot be presented with nearly as high resolution as conventional PFM images.

Despite these disadvantages, SS-PFM allows clear and local determination of coercive voltages, and therefore, information on imprint, remanent polarisation, and the like, akin to macroscale ferroelectric testers.

ferroelectric switch, due to the large DC voltage applied concurrently to the AC drive voltage. Fig. 3.7(a–b) shows a clean response without the concurrent DC voltage.



### 3. Sample Characterisation

---

#### 3.1.3.2 Conductive Atomic Force Microscopy

While PFM is the primary method of excitation used in this thesis, ferroelectric thin films can indeed be investigated through different and distinct methods of excitation. This introduction would therefore be incomplete without a brief discussion of other SPM methods to investigate ferroelectrics. One such variant is conductive atomic force microscopy (C-AFM), which was first developed to investigate the local conductivity of SiO<sub>2</sub> films in 1992 [15]. Here, contact mode AFM is performed as standard, and, like PFM measurements, a conductive probe and a potential difference applied. C-AFM differentiates from standard topography experiments by also measuring the current passed through the tip and sample. This current provides some information about the local conductivity, as:

$$I = J \cdot A_{eff} \quad (3.2)$$

where  $I$  is the current,  $J$  is the current density, and  $A_{eff}$  is the effective area that the current passes through. This, in combination with the topography, provides information about local conductivity.

In many ferroelectric materials, ferroelectric domain walls have a locally increased conductivity [16], or otherwise defects may ‘leak’ an applied current. C-AFM can therefore allow some capability of imaging ferroelectric domain walls or other relevant features.

#### 3.1.3.3 Kelvin Probe Force Microscopy

Kelvin probe force microscopy (KPFM) is an SPM variant sensitive to the local work function (in metals) or electrostatic potential (in non-metals) of the surface, and thus, contains information about the electrostatic conditions beneath the tip [17]. KPFM is typically done with two passes, where the trace is used to determine the topography, and the retrace being performed at a constant height above the sample. In this retrace, both a DC and AC voltage is applied through the tip. The DC voltage is used to nullify any potential difference formed between tip and sample, while the AC voltage generates an oscillating response on the cantilever. This response provides information related to the work function and electrostatics between the tip and sample.

As ferroelectric polarisation itself alters local electrostatics, KPFM is effective in imaging ferroelectric domains. A key distinction between KPFM and PFM is how KPFM can be entirely non-contact, while PFM is primarily performed in contact. This means that KPFM often intrinsically measures the (polarisation-dependent) adsorbates on the system. This can lead to more noisy data that does not directly probe the ferroelectric material, but rather (for better or worse) measures the response of the sample–adsorbate

---

## 3.1 Scanning Probe Microscopy and Atomic Force Microscopy

complex.

### 3.1.3.4 Magnetic Force Microscopy

Magnetic force microscopy (MFM) measures the local magnetic field of a sample surface [18], using a magnetic probe (usually made by coating a non-magnetic probe with a magnetic material, like cobalt). As with KPFM, a dual-pass method is used to ensure that the probe is kept at a constant height above the sample on the second pass. On this second pass, the probe is made to oscillate above the surface around this constant height, akin to a standard tapping mode measurement. The magnetic forces between the tip and sample cause potential variations in the phase, amplitude, and frequency of the cantilever oscillations, which can provide information about the local magnetic field beneath the tip.

While MFM is not directly relevant to ferro*electrics*, multiferroic materials that have both ferroelectric and ferromagnetic properties can be imaged with MFM to provide sample-dependent ferroelectric information.

### 3.1.4 Other Options for Atomic Force Microscopy

#### 3.1.4.1 Optical Beam Deflection vs. Interferometry

We have thus far discussed AFM where the tip position and cantilever dynamics are determined by the deflection of an optical beam onto a photodetector. This is not a necessity, and any method that can allow the tip position to be determined to sub-nanometre accuracy is suitable. Indeed, the earliest AFMs used a scanning tunnelling microscope on the back of the cantilever to determine tip position [3], but the complexity and cost of this setup meant it was soon superseded by other methods, including optical beam deflection.

One of the earlier methods to determine tip position is the use of an interferometer [19]. Interferometry relies on the interference of coherent light sources; if two coherent light sources have an offset in phase, they can destructively interfere with one another. This offset in phase can form between two beams if they are made to pass through different paths. So, for example, a coherent beam can be split so as to have one beam (the ‘measurement beam’) shine on the back of the cantilever, and the other (the ‘reference beam’) shine on the back of the chip [20]. Any difference in tip height would create a corresponding change in the path length of the measurement beam (relative to the reference beam), which would create a measurable interferometric response.

The key advantage of interferometry is that it provides a direct measurement of tip position, and thus, a more quantitative look into the true physics to be observed. Optical beam deflection, on the contrary, measures the angle of the cantilever’s deflection. While optical beam deflection does provide

### 3. Sample Characterisation

---

some insight onto the cantilever dynamics, any false flexion or buckling of the cantilever can cause spurious results [21].

Over the last decades, optical beam deflection has been preferred for two main reasons. First, the setup and centering of an optical beam for deflection is significantly more straightforward than setting up an interferometer. Second, an interferometer setup is significantly more expensive than photodetectors for an optical beam; this cost difference has classically made interferometric AFMs suboptimal for both researchers and manufacturers. The recent development of commercial interferometric SPMs, such as the *Oxford Instruments Asylum Research Vero*, show future potential for a shift back towards interferometry that has yet to be realised [20]. Some potential measurements and results are discussed in Chapter 7.

#### 3.1.4.2 Tip Scanning Paths, and the AFM as a Mobile Probe

We have thus far described two ways of moving the scanning probe to characterise the sample. The most standard is the simple raster scan, in which the tip zig-zags along the sample and potentially acquires data both during the ‘trace’ and ‘retrace’ of the scan. We also discussed SS-PFM, where the tip can be moved to particular points along the sample, and measurements can be taken at each point.

SS-PFM is not the only technique where the scanning probe measurements are taken at specific points on the surface. Rather than the complex excitation pulse applied to the sample, the  $z$ -piezo can simply be excited, for example, to measure the forces applied by the sample towards the tip. These force-distance curves provide information about sample mechanical properties, and have been used to suggest the presence of crackling noise and avalanche statistics in the compression of ferroelectric thin films [22].

While raster scans and SS-PFM or force curves are the most standard methods of using AFM, the high precision of the  $x$ - and  $y$ -piezoelectric actuators allow for more varied tip paths than just these. Spiral tip paths would have a lower maximum acceleration than a raster tip path, for example, which could allow for more rapid measurements than traditional raster patterns [23].

#### 3.1.4.3 The Potential for Automated Experiments in Atomic Force Microscopy

At the start of this section, we placed AFM in a simplified microscopy genealogy. However, when looking at AFM holistically, it is clear it is not so convenient to further split AFM in the same way. Rather, it may be more useful to consider AFM measurements and their subvariants as decisions made regarding a series of questions. Some questions we have highlighted in this section include:

### 3.1 Scanning Probe Microscopy and Atomic Force Microscopy

---

- **Where is the tip?** Are we always in contact? In intermittent contact? Non-contact? Are we raised at a constant distance?
- **What is being excited?** A tapping piezoelectric actuator? The sample itself? Or nothing at all?
- **What is the excitation pulse?** An AC voltage, or DC voltage, or something more complicated? What is the voltage? If it is an AC voltage, what is the frequency and is it changing?
- **What are we measuring?** Deflection? The amplitude of oscillation? The current?
- **How do we determine tip position?** Optical beam deflection, interferometry, or something else?
- **How are we moving the tip?** Rasters, point-by-point, or something more exotic?

An example on how different ‘variations’ of AFM answer each of these questions is shown in Table 3.1.

It is clear that by selecting different answers to the above questions, new variants of AFM could be developed that measure new, exciting, or just cleaner physics (or, if one is not careful, nothing at all...).

This vast array of options, and equivalently, the high control we have over the AFM–sample system, along with the diversity and breadth of data channels is what makes AFM such a powerful tool, and also leaves much room for optimisation via automation. The three measurements highlighted in Table 3.1, for example, are very different in terms of physics observed, but fundamentally can all be performed with the exact same physical setup (supposing that the utilised tip is both ferromagnetic and electrically conductive). All one would need to do is move the tip, reroute and change excitation pulses, and change channels captured; all problems simpler than the initial AFM setup itself. As such one could, for example, create an automated script that sequentially swaps between tapping-mode AFM, band excitation PFM, and MFM to holistically investigate a multiferroic film. A more complicated script could even use tapping-mode AFM and MFM to *direct* where to use PFM, thus avoiding direct contact and resulting tip wear for as long as possible, potentially leading to cleaner and more reliable results. Some could even allow for sequential measurement of AFM with STM, in cases where both techniques are needed for holistic material characterisation [24].

We will more clearly highlight the advantages and possibilities of automated scanning probe measurements in Chapter 8. The principle the reader is led to, however, is that while AFM was initially introduced as a microscopy technique through which a sample surface is imaged, it should

### 3. Sample Characterisation

---

**Table 3.1:** Variations of AFM, showing how one can define some AFM techniques as choices between options of tip excitation and data acquisition.

	<b>Topography, by tapping-mode AFM</b>	<b>Band-excitation PFM</b>	<b>Second pass of dual-pass MFM</b>
<b>Where is the tip?</b>	In intermittent contact with the sample.	In physical and electrical contact with the sample.	Oscillating around a constant height above the sample
<b>What is being excited?</b>	A piezoelectric actuator to oscillate the tip.	The sample (and equivalently, the tip).	A piezoelectric actuator to oscillate the tip.
<b>What is the excitation pulse?</b>	An AC voltage, near the resonant frequency of the free-standing cantilever.	A band of frequencies around the contact-resonant frequency of the tip-sample complex.	An AC voltage, near the resonant frequency of the free-standing cantilever.
<b>What are we measuring?</b>	The $z$ piezoelectric actuator response used to keep the cantilever oscillating at a constant amplitude.	The complex deflection of the cantilever to fit to a harmonic oscillator model.	Variations in the amplitude and phase of oscillations in a magnetic tip.
<b>How do we measure tip position?</b>	By optical beam deflection.	By optical beam deflection.	By optical beam deflection.
<b>How are we moving the tip?</b>	In a raster pattern.	In a raster pattern.	In a raster pattern.

## 3.1 Scanning Probe Microscopy and Atomic Force Microscopy

---

be clear that its potential is much higher. Rather, AFM is here used to represent a family of techniques in which a scanning probe can be used to electrically and mechanically excite a sample with nanoscale precision, and the surface material properties are determined from the associated physics of the scanning probe.

### 3.1.5 Practical Piezoresponse Force Microscopy

This section has thus far described AFM in more abstract, philosophical terms. It would be useful here to take some time to describe how conventional PFM measurements, such as those utilised through Chapter 6, are performed practically, and the important considerations one should have before performing a measurement or interpreting a result. To that end, we will conclude our this section of AFM with two final discussions. First, an assortment of practical advice for high quality, efficient PFM measurements; and second, a discussion of error and uncertainty that will still inevitably arise from such.

#### 3.1.5.1 Practical ‘Tips’ for PFM

Section 3.1.3.1 describes in general terms how the operation of PFM can be understood, but it will not necessarily help a new student understand what exactly to do to generate a good image. While there is no real substitute to direct instruction or tutelage from an experienced microscopist, some brief advice is included here.

- **Use Good Samples!**—The principle of ‘Garbage In, Garbage Out’ is important for more than just computation. Without a sample that is good for AFM and PFM, good data is difficult or impossible to acquire. A sample must, at the very least, be ‘reasonably’ smooth; thin films will typically be smooth enough (and is where my expertise generally lies), but ceramic samples may have difficulty without specific sample preparation—which may in turn change sample properties. For PFM in particular, consider too if the sample has a sufficiently conductive bottom electrode, or if the sample is leaky (conductive) enough to cause additional measurement noise.
- **Attach Your Sample Well!**—By the end of my PhD, I had started exclusively using silver paste, or some other dry setting adhesive, to attach my samples to the sample holder. I find that other methods, like tape, create key issues. Tape, which is ‘soft’, can create a mechanical hysteresis or capacitance in measurements, where different responses are gained in trace vs. retrace, or frame up vs. frame down, because the ‘soft’ tape allows the sample to move at least partially with the

### 3. Sample Characterisation

---

tip. Particular tapes can also ‘unstick’ itself, which is particularly problematic given the low vertical tolerance of the experimental setup—I have come back from overnight measurements to see a sample risen off its holder, and the tip subsequently destroyed!

- **Start with Tapping Mode!**—In general, I find it important to always start with at least a partial tapping mode AFM scan before performing any PFM scans. The reasons for this are at least fourfold. First, approaching in tapping mode prevents the tip from making any undesired, prolonged contact with the sample, which can serve to damage the tip. Second, a tapping mode scan can ensure that a subsequent PFM tune can be performed on a sample over a relevant region—this avoids the minute chance that a tune is performed over a singular particle, for example. Third, if the AFM scan is performed over a large region, a smaller subset can be examined and chosen for a particular PFM scan—completely avoiding making contact with, or dragging the tip across, any particles on the surface. Finally, as contact mode PFM can drag across adsorbates, this initial AFM scan could be the only measurement made of the ‘original’ sample state, and thus could be a useful image for subsequent analysis or context.
- **Change the Tip!**—Cost and experiment permitting, one should not be too hesitant to change the tip. Even in ideal use, tips inevitably get damaged, worn, or pick up adsorbates or other particles over prolonged use, particularly if voltages are applied in PFM. I have found the lifetime of tips to be highly variable, with some lasting days immediately followed by an identical model hardly surviving a couple of scans. The corollary is that, if a tip is good, one should very much value it and use it well—do not change it unnecessarily.
- **Use the Right Tool for the Job!**—Different tips have different mechanical and electrical properties, and so have different ideal use cases. The clearest use case is for the nanoindentation studies in Chapter 7, where the hardest tips and stiffest cantilevers were needed—justifying the use of the *Adama Innovations* AD-40-AS tip, which has a diamond probe and a cantilever with a stiffness of 40 N/m. For the PFM studies on PTO discussed in Chapter 6, a conductive coating was desired and so the *OPUS* OSCM-PT platinum-coated probes were used. For the subsequent PFM studies discussed in Section 8.1, we instead used *NANOSENSORS* PPP-EFM tips—these tips had a platinum-iridium coating that was more wear resistant than the platinum coating on the OSCM-PT tips, allowing for more repeatable measurements. The particular requirements, materials, and resources for each experiment should be considered to make a conscious choice

### 3.1 Scanning Probe Microscopy and Atomic Force Microscopy

---

about the type of tip.

- **Make Every Scan Count!**—Aside from the general advice to just not waste time in general, do keep in mind that tips tend to have a finite lifespan, their quality changes (generally decaying) over subsequent scans, and that a change of tip is a rather large ‘variable’ to change for an experiment (the region of interest could also be lost if the tip is changed). Thus, it is important to be prudent with your scans, particularly if a tip is good or expensive. If you can gather the same data with fewer scans, then that would generally be preferred—the lower wear means that the data that results should be higher quality.
- **Tip = Broom?**—If a tip will be thrown out, and your sample is prone to adsorbates, it can be useful to use your tip as a ‘broom’. Put your tip in contact with the sample, and simply allow it to scan across a region of the sample you are interested in (set the scan size to be at least a couple of  $\mu\text{m}$  more than the region of interest). Adsorbates and surface particles may be scraped off the sample to the perimeters of the image; these should be visible if you move to tapping mode and increase the scan size. The benefits of this are twofold. First, it should make it easier to find the same spot in a subsequent scan; after changing the tip, if you are in the same area, you should quite easily see the lines of adsorbates that were dragged to the edges of the scan frame. Most importantly, if you do find this same sample, the region of interest should now be ‘clean’—most of the surface particles and adsorbates should have been mechanically moved away, and so with any luck, the new tip should last longer and provide cleaner results.
- **Shake if Off!**—If you do not want to throw away a tip, but its quality has diminished, I have found some minor success in ‘cleaning’ a tip with the following method (though keep in mind this is more of a last resort before a tip is thrown out and cannot be used evermore): First raise the tip a great distance above the sample, and then set the scan size and scan rate arbitrarily high (I tend to go with about 20  $\mu\text{m}$  and 10 Hz respectively). Then, proceed to scan (you should see a blank space on screen). Through the scan, change the scan angle to different, arbitrary values. This should all work to effectively ‘shake’ the tip in various directions, which can have some success in removing particles adhered to the sample. At this point, the tip can be made to approach again (it should be in the same position as it was initially), and the tip quality could be at least somewhat improved. This entire process can be performed in less than a minute, and, since it should find the same initial position, this can be worth doing as a last hope if you want to conserve a tip or position for just a little bit longer.



### 3. Sample Characterisation

---

- **Some Useful Parameters (Tapping Mode)**—For my initial AFM measurements, I tend to image a relatively large area to find an area of interest, and image slowly as not to damage the tip—but not too slowly so as not to be time-prohibitive. As such I usually set a set point of about 800 mV in approach, a drive amplitude about 10% higher than a default tune, and scan a 20  $\mu\text{m}$  region with a 256 px  $\times$  256 px resolution. If a sample is unknown, or known to have large particles, I would use a low scan rate of around 0.5 Hz; the cleaner a sample is, the more I would increase the scan rate. If I need a more accurate AFM image, I would increase the resolution to 512 px  $\times$  512 px resolution, and image a smaller area.
- **Some Useful Parameters (PFM)**—PFM parameters tend to be very sample and experiment specific; a drive amplitude good for one sample could lead to switching or ferroelectric breakdown for another. A particular scan size may be appropriate to see one domain in one sample, but may be far too large or too small in another. For my measurements on PTO, particularly those in Chapter 6, I tend to scan a 2  $\mu\text{m}$  region with a 512 px  $\times$  512 px resolution. I use a set point of 1 V, a drive voltage of 500 mV, and a scan rate of 0.6 Hz. A general advice I have myself heard is that, especially for thin film or ceramic samples, if ones images are unsatisfactory, one should also not hesitate to increase the forces exerted by the tip (increase the set point).
- **Thermal Drift is Not Your Friend (Overnight Scans)**—The room you are working in will inevitably change temperature over time—not just because of the external environment outside the building, but also due to the presence of you (or other people) walking in and out of the labs. This inevitable change in temperature will change the alignment and positioning of the AFM. Attempts should be made to control this if you are operating overnight—make sure you at least check for sample drift, and correct for this drift if you see it; intermittently retune your cantilever and reset your photodetector, and the like.
- **Thermal Drift is Not Your Friend (Intialisation)**—The general running of the AFM will likely lead it to warm up marginally, while, when unused, it would be at room temperature. Time permitting, if no one is using the AFM before you, it may be worth setting the AFM early to start ‘scanning’ empty space in the approximate conditions of the desired scan. This should warm up the electronics sufficiently to avoid most of the ‘thermal shock’ of being switched on, and save you some recalibration time later on. (of course, if someone *is* using the AFM before you, then the machine should ideally be in the steady state and so no equilibration should be necessary).

## 3.1 Scanning Probe Microscopy and Atomic Force Microscopy

- **PowerPoint is Very Effective at Finding the Same Spot**—To fully characterise the 3-dimensional polarisation vectors in a sample, the sample must be physically rotated and the precise  $2\ \mu\text{m} \times 2\ \mu\text{m}$  region must be found again on a sample with an area approximately 10 million times more than that. This can be a difficult and time-intensive process without going in with a plan and proper preparation. My rough protocol is thus. First, when you are ready to move your sample, before you do so, make sure you move your tip to the centre of the image. Then, capture the optical microscopy image and place it into Microsoft PowerPoint (or any other equivalent that allows simple image manipulation. Mark four points on this capture: One should be the position of the tip, and three should be three recognisable points on the sample surface. Only then should you rotate your sample physically. When you do so, try and find those three recognisable points on the optical microscope, and move around until you find it. Once you do, take a screenshot and layer it on PowerPoint above the previous screenshot, but below the markers signifying point positions. Rotate the image and try to align your three recognisable sample points on the new image, to their associated markers (the rotation of the new image with respect to the old image should tell you how much you rotated the sample; if your rotation is too great or too little, please adjust). At this point, the vector from the marker of the old tip position to the new tip position is the additional translation needed to find the original tip location. At this point, you must simply adjust your sample position until it is possible to allow all four points to intersect between the new image and the old markers.

With any luck, this section should help a less-experienced microscopist perform more accurate, reliable measurements<sup>4</sup>. For further support, I would also encourage the reader of this thesis to also take time to read the manual and other documentation for their system of choice, as well as to judiciously ask for help from those more experienced—there will always be more to learn.

### 3.1.5.2 Limitations and Errors in Piezoresponse Force Microscopy

Regardless of microscopist skill and experience, however, there also remain physical limits to the potential of PFM. Considering these limitations are perhaps equally important if not more so, to understanding how best to use PFM. These limitations manifest as noises, errors, or artefacts in an image or subsequent analysis. Some particularly prominent limitations are worth considering, such as:

---

<sup>4</sup>It is also worth noting that some of these processes can indeed be automated, either with Python, or standard commercial packages on proprietary software; see Section 3.1.4.3.

### 3. Sample Characterisation

---

- **Finite Probe Size**—AFM relies on a scanning probe to image the sample surface, and thus, the resolution of all AFM techniques are ultimately limited by the area of the probe that makes contact with the sample. This precise area is not necessarily always well defined. Probe manufacturers report tip radii on the order of 10 nm or so [25], but any applied forces (such as those from being in contact with the sample) would elastically deform the tip and further increase the tip radius. This, combined with plastic deformation and wear [26], means that the practical tip width is going to be much greater than the theoretical values—and the fundamental limit of resolution much lesser.
- **Finite Interaction Area**—Electroactive variants of AFM have an additional factor to consider: the applied fields also have a finite area over which the material interacts. This interaction area is made more prominent if a sample is ‘leaky’, with non-negligible conductivities, that lead to a larger dispersion of electric fields and conduction. This makes accurate determination of, for example, the width of domain walls, almost impossible by AFM. The area of the sample ‘exposed’ to a field will be much greater than the width of the domain wall, and so the domain wall may ‘smear’ across a region much larger than its own thickness.
- **Surface Sensitivity**—For imaging purposes, the AFM probe will generally be on, or above, the sample surface. This makes determining what is happening *below* the surface particularly challenging. For our purposes, we assume that our thin-film samples are quasi-2-dimensional, but this is not always entirely correct. Domains could have a 3-dimensional character to them, while domain-walls may be buried, at an angle, or non-penetrant through the entire film. Determining the 3-dimensional character of features is difficult via AFM.
- **Slow Scan Axis**—Conventional AFM is performed with a single tip, and this tip can only be at a single point at a single time. To cover the entire area, a raster pattern is performed, and along the fast-scan axis that the tip moves across, the resolution is effectively guided by the probe size. Data along the perpendicular, slow scan axis is invariably of lower quality, however; the AFM and processing software must only infer data from line to line, and thus, errors may emerge when moving down the slow-scan axis. In particular, if topographical features are perfectly parallel to the fast scan axis (such as atomic terraces), they may less visible, or even completely invisible, in an AFM measurement, as the AFM may not ‘see’ the steps that go up or down with the slow scan axis. This phenomenon is particularly worth considering when performing lateral PFM; these measurements apply constraints on

### 3.1 Scanning Probe Microscopy and Atomic Force Microscopy

---

sample rotation to determine in-plane polarisation, and these same constraints could reduce image quality, as discussed in Section 8.1.

- **Non-Linearity in the Piezoelectric Actuators**—The engineering design of the piezoelectric actuators in conventional AFMs mean that the movement of the sample (relative to the tip) is not necessarily linear, and will have some cross-correlations with the perceived height of the sample. This phenomenon, where the central vertical stripe of the sample is measured as significantly higher or lower than features on their edges, is known as ‘buckling’, and is most significant in larger, otherwise smooth sample scans. These can be artificially removed by fitting a curve, but otherwise this is an inevitable problem that arises from AFM design. To diminish these effects, scanning a smaller region will be suitable.
- **Non-Linearity in Measured Heights**—In much the same way, the gathered signal may not always be perfectly linear. This is most notable with high deflections that are measured with an OBD setup. These OBD measurements rely on measuring the deflection of the optical beam across the back of the cantilever, which will not always be linear with the height and motion of the tip. This can give large errors when the values themselves are themselves large.
- **Crosstalk between in-plane and out-of-plane responses**—Determination of 3-dimensional polarisation vectors is also made somewhat more difficult by a 2-dimensional photodetector. While in-plane motion perpendicular to the axis of the tip can result in torsion of the cantilever, which yields a clear lateral response, the remaining two axes of motion are more ambiguous. Both an out-of-plane motion of the sample, and an in-plane motion of the sample parallel to the tip, will cause sections of the cantilever to alternately rise and fall—yielding a vertical response on the photodetector. These can only be minimised by mechanically rotating the sample and cross-correlating distinct results.
- **Sample Drift and Scan Time**—AFM takes a finite time to measure, and so conditions at the ‘start’ of a scan can be distinct from those at the ‘end’ of the scan. This is perhaps most obvious if the sample drifts; perhaps because of thermal changes, or perhaps because the sample is not adequately adhered to the holder. To check for this, one should examine the differences between trace and retrace; between frame up and frame down; and from repeated frame up (or frame down) measurements to ensure that the results from each of these are at least reasonably similar to one another. Algorithms like distortion

### 3. Sample Characterisation

---

correction can be used to correct some movement from scan to scan, but better original data is always ideal.

- **Generation of Defects**—PFM is, in many ways, a very aggressive type of measurement. While I would in no way call PFM a ‘destructive’ measurement, it does at least change the sample conditions in the process, and this is worth considering for all measurements, particular for repeated scans along the same region. Perhaps the most obvious and least perturbative is the removal of surface adsorbates or particles. There are also inevitable tribological effects, such as wear, that could happen and destroy a repeatedly scanned surface, particularly if high forces are applied. Perhaps more relevant to this thesis, however, is defect generation or migration as a result of the highly localised applied electric fields. These potential features could alter and affect any observed phenomena regarding domain wall migration.

These physical limitations of the capability of PFM could in theory result in some inevitable limitations to the veracity of the physical claims reported throughout the thesis. The impact of these limitations can be reduced with proper experimental control, however. Such examples are:

- The finite probe size and finite interaction sizes apply a functional limitation to the minimum event size of area switching avalanches as discussed in Chapter 6; this applies an effective lower bound to  $x_{min}$ , the minimum event cutoff as relevant to power-law distributions; all values of  $x_{min}$  must be limited to this  $> 100 \text{ nm}^2$  resolution.
- Sample drift is here addressed via distortion correction protocols, in which the movement of the sample from frame to frame is determined by analysis of the topography images, and used to adjust the position of all functional images (see Chapter 5). This method as performed for this thesis is performed at a pixel-by-pixel resolution, however, which reduces the maximum resolution to a pixel-by-pixel level; further raising the lower bound of  $x_{min}$ , and applying a small random error to the initial and final positions of all interfaces.
- Non-linearity in the AFM systems is problematic when investigating large  $z$ -ranges, as performed in Chapter 7. The impact of this non-linearity is reduced by the use of a QPDI detector for these measurements.
- The difficulty of measuring the buried character of  $a$ -domains is relevant for the analysis of  $a$ -domain interactions in Chapter 6. The discussed  $a$ -domains penetrate the sample at a  $45^\circ$  angle, and for a  $140 \text{ nm}$  thick film this creates an effective ‘maximum width’ of the domain wall at

also 140 nm. This can make it difficult to precisely determine local interactions between different domain walls.

- Crosstalk between in-plane and out-of-plane responses contributed to the choice of material as used in Section 8.1, and limits the effectiveness of this method to similar materials that also do not have a polarisation component in the direction of the tip. This configuration also constrained the slow-scan axis direction, which indirectly limited the quality of the acquired topography.

In general, while these physical limitations could reduce the resolution and sensitivity in determining the precise size and area of particular features, the nature of these experiments (in particular, the scale-free nature of power-law distributions) mean that the general trends remain clear and evident. As such, despite these potential limitations, AFM as a whole remains a remarkably powerful, highly adaptable tool that is useful to study not only ferroelectrics, but all types of materials for their topographical and functional properties.

## 3.2 X-Ray Diffraction

While SPM is a powerful tool to determine local, nanoscale physics of a material, we need other experimental techniques to determine more global material structure. For this, we primarily use *x-ray diffraction* (XRD).

Diffraction is a phenomenon in which waves, including electromagnetic radiation, diffuse when passing through an aperture. If multiple apertures are spaced sufficiently close together, the diffuse wavelets that exit from each aperture can interfere with each other and create a *diffraction pattern* that is a function of both the wave itself, and the apertures the wave passes through.

For condensed matter physics, the diffraction of x-rays yields a particularly important characterisation technique; XRD can thus provide simple and powerful visualisation of sample crystallography.

This section will first introduce and derive Bragg's law, an equation that describes the position of interference patterns that arise after waves passing through a crystal. We will then describe how Bragg's law can be used to describe the concept of *reciprocal space* and *reciprocal space mapping*, and its use in sample characterisation. Finally, we will analyse and discuss direct results from XRD experiments.

#### 3.2.1 Bragg's law and Reciprocal Space Mapping

Bragg's law can most formally be derived by an interpretation of the waves as associated wavevectors [27].

Consider two incident beams with wavevectors  $\mathbf{k}$  that scatter from points spaced  $\mathbf{r}$  apart. On diffraction, both outgoing beams have wavevectors  $\mathbf{k}'$ . In this case, the difference in path length between the two beams before they hit the diffracting element is  $r \sin \phi$ . This means that the phase angle between the two beams would be  $(\frac{2\pi}{\lambda}) r \sin \phi$ . This is geometrically equivalent to  $\mathbf{k} \cdot \mathbf{r}$ , as  $|\mathbf{k}| = \frac{2\pi}{\lambda}$ . The change in phase angle after diffraction can be calculated similarly, to produce a total phase angle change of  $(\mathbf{k} - \mathbf{k}') \cdot \mathbf{r}$  for a point at  $\mathbf{r}$  compared to a point at the origin  $O$ . The phase factor from the beam diffracted at  $\mathbf{r}$  can therefore be considered:

$$\exp\{-i\Delta\mathbf{k} \cdot \mathbf{r}\} \quad (3.3)$$

where  $\mathbf{k} + \Delta\mathbf{k} = \mathbf{k}'$ . The actual amplitude of the diffracted beam would further depend on some quantity,  $n(\mathbf{r})$ , that describes the proportion of scattering around the position  $\mathbf{r}$ . This means we can specifically look for the *scattering amplitude*  $F$ , which is the amplitude resulting from the scattering at the point  $\mathbf{r}$  in the direction of the chosen scattering vector  $\Delta\mathbf{k}$ , integrated over the entire region, which can be described as:

$$F = \int dV n(\mathbf{r}) \exp\{-i\Delta\mathbf{k} \cdot \mathbf{r}\} \quad (3.4)$$

But what is  $n(\mathbf{r})$ ? In reality, we can reasonably model this as the electron density around  $\mathbf{r}$ . The more electrons there are, the more likely a beam is to scatter, and thus there would be more scattering on average. This electron density would be defined entirely by the crystal structure that is being diffracted from.

To describe the crystal structure algebraically, it is most simple to describe the lattice as a Fourier series; that is, an infinite sum of individual waves. The electron density can therefore be described as:

$$n(\mathbf{r}) = \sum_{\mathbf{G}} n_{\mathbf{G}} \exp\{i\mathbf{G} \cdot \mathbf{r}\} \quad (3.5)$$

$n_{\mathbf{G}}$  is a coefficient, but the complex exponent is a periodic function, whose real component maximises when  $\mathbf{G} \cdot \mathbf{r}$  is a multiple of  $2\pi/\lambda$ .  $\mathbf{G}$  is a set of vectors that can be used to describe points on the lattice; for a three-dimensional crystal,  $\mathbf{G}$  would include three vectors that each describe one crystallographic axis.

Critically, while  $\mathbf{G}$  must describe the three principal crystallographic directions, they must not *be* those crystallographic directions. If we call the primitive lattice vectors  $\mathbf{a}_1$ ,  $\mathbf{a}_2$  and  $\mathbf{a}_3$ , for example, and therefore set

$\mathbf{G} = u_1\mathbf{a}_1 + u_2\mathbf{a}_2 + u_3\mathbf{a}_3$ , then the crystal, translated along the crystal lattice (say, by some vector  $\mathbf{T} = u'_1\mathbf{a}_1 + u'_2\mathbf{a}_2 + u'_3\mathbf{a}_3$ ) will have a completely distinct electron density. This is non-physical. Rather, we need to define a distinct basis where translation of a crystal along any or all of its crystallographic axis by the primitive lattice vectors will not change  $\mathbf{G}$ .

What we instead do is create alternative axes from which to consider our crystal, which we call reciprocal axes and set by definition:

$$\mathbf{b}_i \cdot \mathbf{a}_j = 2\pi\delta_{ij} \quad (3.6)$$

where  $\delta_{ij} = 1$  when  $i = j$  and  $\delta_{ij} = 0$  otherwise. This creates the reciprocal lattice vectors:

$$\begin{aligned} \mathbf{b}_1 &= 2\pi \frac{\mathbf{a}_2 \times \mathbf{a}_3}{\mathbf{a}_1 \cdot \mathbf{a}_2 \times \mathbf{a}_3} \\ \mathbf{b}_2 &= 2\pi \frac{\mathbf{a}_3 \times \mathbf{a}_1}{\mathbf{a}_2 \cdot \mathbf{a}_3 \times \mathbf{a}_1} \\ \mathbf{b}_3 &= 2\pi \frac{\mathbf{a}_1 \times \mathbf{a}_2}{\mathbf{a}_3 \cdot \mathbf{a}_1 \times \mathbf{a}_2} \end{aligned} \quad (3.7)$$

In this case, if we set  $\mathbf{G} = v_1\mathbf{b}_1 + v_2\mathbf{b}_2 + v_3\mathbf{b}_3$ , and separately, undergo the arbitrary translation in the crystal lattice  $\mathbf{T} = u_1\mathbf{a}_1 + u_2\mathbf{a}_2 + u_3\mathbf{a}_3$ , then:

$$\begin{aligned} n(\mathbf{r} + \mathbf{T}) &= \Sigma_G n_G \exp\{i\mathbf{G} \cdot (\mathbf{r} + \mathbf{T})\} \\ &= \Sigma_G n_G \exp\{i\mathbf{G} \cdot \mathbf{r}\} \exp\{i\mathbf{G} \cdot \mathbf{T}\} \\ &= \Sigma_G n_G \exp\{i\mathbf{G} \cdot \mathbf{r}\} \\ &= n(\mathbf{r}) \end{aligned} \quad (3.8)$$

This only occurs in cases where  $\exp(i\mathbf{G} \cdot \mathbf{T}) = 1$ , which arises from the definition in Eq. 3.6.

Now that we finally have an equation that describes the crystal lattice (and the associated translational invariance), we can return to Eq. 3.4 and substitute Eq. 3.5:

$$\begin{aligned} F &= \int dV n(\mathbf{r}) \exp\{-i\Delta\mathbf{k} \cdot \mathbf{r}\} \\ &= \int dV \Sigma_G n_G \exp\{i\mathbf{G} \cdot \mathbf{r}\} \exp\{-i\Delta\mathbf{k} \cdot \mathbf{r}\} \\ &= \int dV \Sigma_G n_G \exp\{i(\mathbf{G} - \Delta\mathbf{k}) \cdot \mathbf{r}\} \end{aligned} \quad (3.9)$$

This means that maxima occur when:



### 3. Sample Characterisation

---

$$\mathbf{G} = \Delta \mathbf{k} \quad (3.10)$$

This is a key result; a change in the wavevector to one of the positions on the reciprocal lattice creates a maximum in diffraction.

To relate this to the original wavevector  $\mathbf{k}$ , we can rewrite the equation as  $\mathbf{k} + \mathbf{G} = \mathbf{k}'$ . Note that in an elastic scattering condition,  $|\mathbf{k}| = |\mathbf{k}'|$ , and we can thus square both sides and show that:

$$\begin{aligned} |\mathbf{k} + \mathbf{G}|^2 &= |\mathbf{k}'|^2 \\ |\mathbf{k}|^2 + 2\mathbf{k} \cdot \mathbf{G} + |\mathbf{G}|^2 &= |\mathbf{k}|^2 \\ 2\mathbf{k} \cdot \mathbf{G} + |\mathbf{G}|^2 &= 0 \end{aligned} \quad (3.11)$$

Noting that if  $\mathbf{G}$  describes a point in a reciprocal lattice,  $-\mathbf{G}$  must also, allows the simplification:

$$2\mathbf{k} \cdot \mathbf{G} = |\mathbf{G}|^2 \quad (3.12)$$

This is the diffraction consideration as only a function of the wavevector  $\mathbf{k}$  and the crystal lattice, whose reciprocal is described by  $\mathbf{G}$ .

This general diffraction condition can be restated as what is known as *Bragg's law*. Geometrically, the real-space distance between the planes normal to the reciprocal space vector  $\mathbf{G} = h\mathbf{b}_1 + k\mathbf{b}_2 + l\mathbf{b}_3$  is  $d = 2\pi/|\mathbf{G}|$ . Thus, if the angle  $\theta$  is the angle between  $\mathbf{k}$  and  $\mathbf{G}$ :

$$\begin{aligned} 2|\mathbf{k}||\mathbf{G}| \sin \theta &= |\mathbf{G}|^2 \\ 2|\mathbf{k}| \sin \theta &= |\mathbf{G}| \\ 2\frac{2\pi}{\lambda} \sin \theta &= \frac{2\pi}{d} \end{aligned} \quad (3.13)$$

Considering that higher-order indices would also allow Bragg condition leads to the final statement of Bragg's law:

$$n\lambda = 2d \sin \theta \quad (3.14)$$

where  $\lambda$  is the wavelength,  $\theta$  is the angle between the wave and the planes, which are spaced  $d$  apart and described by the indices  $h/n$ ,  $k/n$  and  $l/n$ .

#### 3.2.2 Ewald's sphere and other practical considerations

We note that, from Eq. 3.12, a change in the original wavevector (both angle and wavelength) will change the corresponding diffraction pattern. So

how should we align the wavevector such that we satisfy some diffraction condition? What is the most appropriate wavelength to choose?

Say we want to achieve diffraction at a point in reciprocal space  $\mathbf{G}$  (corresponding to a planar spacing in real space). Geometrically, from Eq. 3.12 it can be shown that diffraction from  $\mathbf{G}$  occurs if the reciprocal lattice point at  $\mathbf{G}$  and another point in the reciprocal lattice chosen as the origin, with a radius  $2\pi/\lambda$  centred in the direction of  $\mathbf{k}$ . This construction is known as Ewald's sphere.

Practically, this has two conclusions. One, particular incident angle of  $\mathbf{k}$  must be chosen or searched for for diffraction to occur; this is often done practically by sweeping across various incident angles. Second, the range of valid reciprocal lattice points is limited for any chosen  $\lambda$ ; a  $\lambda$  too large may generate an Ewald's sphere much smaller than the reciprocal lattice, while a  $\lambda$  too small may generate an Ewald's sphere so large it may be difficult to identify a particular reciprocal lattice point.

### 3.2.3 X-Ray Diffraction for Materials Characterisation

The previous subsections yield key experimental implications:

1. Since maxima occur when  $\mathbf{G} = \Delta\mathbf{K}$ , a beam passing through a crystal creates points of maximum diffraction that describe the reciprocal lattice of a crystal.
2. Per Ewald's sphere, and since  $n\lambda = 2d \sin \theta$ , it is most experimentally viable to measure  $d$  as a function of  $\theta$  if  $\lambda$  is in a similar order of magnitude to  $d$ . For real crystals, with unit cells on the order of size of angstroms, this means we would prefer electromagnetic radiation with a micron-order wavelength; that is, x-rays.
3. In a real experiment, it is not possible to simultaneously capture all possible diffraction peaks with infinite sensitivity. Rather, an x-ray source and x-ray detector are moved relative to the sample position to capture the position and shape of diffraction peaks in reciprocal space. The x-ray detector may either be a point (0D detector), linear array (1D detector) or 2-dimensional array (2D detector) of sensors. More sensors in simultaneous use increase acquisition rate.
4. The practical requirement for the detector to be 'in position' to receive diffraction through the crystal from the source is symmetrical to the initial requirement for the source to itself be 'in position'; that is, diffraction would be the same if the source and detector were swapped. This means the detector also has an equivalent Ewald's sphere, and a signal can only be collected if the reciprocal lattice point falls on the Ewald's sphere of both the source and detector.

### 3. Sample Characterisation

---

5. A 0D or 1D detector moving continuously can capture a 1D slice of reciprocal space and in it can capture multiple aligned diffraction peaks of different orders. This, via Bragg's law, allows one associated lattice spacing  $d$  to be determined with reasonable accuracy, limited functionally by the collimation of the x-ray beam, but nonetheless reliable do the picometre range.
6. A 1D or 2D detector moving continuously (or a 0D or 1D detector moving non-continuously) can capture a 2D slice of reciprocal space. This provides a crystallographer a more general view of the shape of diffraction peaks in reciprocal space, which may give more information on the crystal structure in real space, beyond what would be gathered from a 1-dimensional slice.

Altogether, through XRD, we move the sample, x-ray source, and x-ray detector relative to another such that the associated Ewald's spheres of the source and detector align with the reciprocal lattice point. This images the reciprocal lattice point, and provides information about the real-space crystal lattice. We will now go through experimental examples and results of this.

#### 3.2.4 Crystalline X-Ray Diffraction in Practice

XRD is performed inside an x-ray diffractometer, which consists of three main components [28]:

- **An x-ray source.** X-rays are usually generated by firing at a metal target anode with an electron beam. The generated x-rays are made to pass through a collimator (a series of slits that make the x-rays parallel) and a monochromator (a single crystal that causes diffraction, such that only a particular wavelength can pass on through). This ensures that x-rays with a known wavelength are transmitted towards a known direction, towards the
- **sample stage**, which is used to hold the sample. When measuring monocrystalline samples, like our ferroelectric thin films, this sample stage must be precisely mobile to ensure that the exact desired crystallographic axes can be aligned with the x-ray source and the
- **x-ray detector.** This allows the diffractometer to count the intensity. An additional collimator can be used before the x-ray detector to once again limit the incident output to only parallel beams. The x-ray detector can also be segmented to create a 1D or 2D detector.

Further, all three of these components should be able to move relative to one another (in reality, if the sample stage is already mobile, only one of the

x-ray source and x-ray detector must be mobile too). A list of conventions for all possible motion paths of these three elements are shown in Fig. 3.8. We here call a ‘scan’ a measurement of intensity as a function of one of these paths; so an ‘ $x$  scan’ is a measure of intensity as a function of movement along  $x$ .

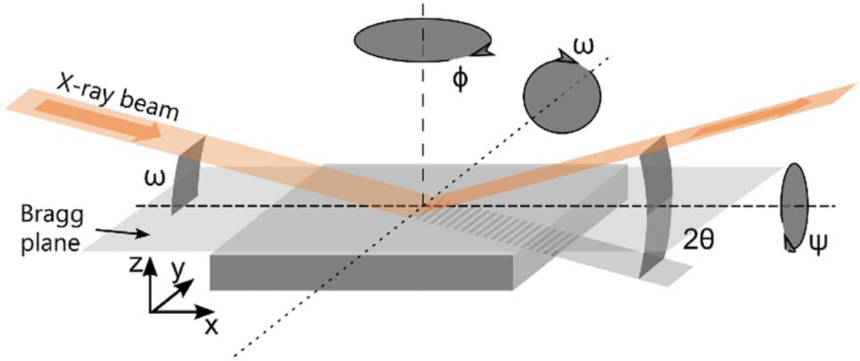


**Figure 3.8:** Conventions for arcs and axes of motion for source, sample stage, and detector in XRD measurements. In some conventions, the angle listed as  $\psi$  may instead be known as  $\chi$ . Image from Ref. [29].

When analysing single crystals, XRD involves the following steps.

1. The sample is placed on the sample stage. At this point, the sample stage should be set far enough away (ie. with low enough  $z$  so that it is not measured).
2. The alignment between the source and detector is verified by performing a sensitive  $2\theta$  scan across 0 and setting the  $2\theta$  where intensity is at maximum to be the new 0. This is known as direct beam alignment.
3. The sample is raised (along  $z$ ) and a  $z$  scan is performed until the sample cuts roughly half the beam intensity. We therefore know an approximate position of the sample in  $z$ .
4. If needed,  $x$  scans and  $y$  scans are performed to locate the sample in 3D space.
5. Bragg’s Law (Eq. 3.14) is used to estimate the position of the sample (substrate) peak, in terms of  $2\theta$  and  $\omega$ . An  $\omega$  scan is used to verify the presence of this sample (substrate) peak.
6. The intensity of this substrate peak is optimised. This is performed by successively scanning across each possible movement axis of the

### 3. Sample Characterisation

---

sample stage, and then setting the value of this axis so as to maximise the intensity.

Once the sample position is fully optimised, the scan of interest can be performed. For our measurements, there are three types of scans that we tend to perform.

#### 3.2.5 Rocking Curves ( $\omega$ Scans)

Rocking curves are  $\omega$  scans performed across a diffraction peak, and are so named because a scan in  $\omega$  simple involves the rotation (or ‘rocking’) of the sample stage in line with the beam axis.

This rotation in  $\omega$  corresponds to an identical rotation of the reciprocal lattice (or equivalently, the simultaneous rotation of both the x-ray source and detector about a stationary reciprocal lattice). This means that a rocking curve provides information the crystalline quality of the sample measured. If the peak observed from a rocking curve is narrow, this means that the crystallographic axes of all unit cells also tends to be distributed along a narrow breadth. Meanwhile, a wider peak in a rocking curve means a larger distribution of crystallographic orientations.

Rocking curves therefore provide important information about the quality of ferroelectric thin film growth. Preliminary characterisation of thin films often involves two rocking curves: one performed around the substrate peak [Fig. 3.9(a)] and one performed around the film peak [Fig. 3.9(b)]. Here, we can see the full-width at half maximum (FWHM) of the substrate peak is approximately  $0.015^\circ$ , while the FWHM of the film peak is approximately  $0.059^\circ$ . This tells us that the film peak had some substantial loss in crystallinity and a greater variation in lattice parameter than that of the substrate peak. We later use this information in Chapter 6, particularly Fig. 6.2.

Rocking curves can also provide unique sample-dependent information. Lanthanum aluminate, for example, has a lattice distorted such that twins (adjacent regions with similar but reflected crystallographic axes) form. A well-aligned rocking curve around this substrate peaks allows the observation of both twins [Fig. 3.9(c)] and some insight into their relative proportions, which can have further implications on subsequent layers grown.

#### 3.2.6 $2\theta$ - $\omega$ Scans

A  $2\theta$ - $\omega$  scan is a scan in which both  $2\theta$  and  $\omega$  move. From Fig. 3.8, it is clear  $2\theta$  is the angle between the incident beam and the diffracted beam, while  $\omega$  is the rotation of the sample plate in line with both beams. We can define an  $\omega$  offset,  $\Delta\omega$  from these two variables as:

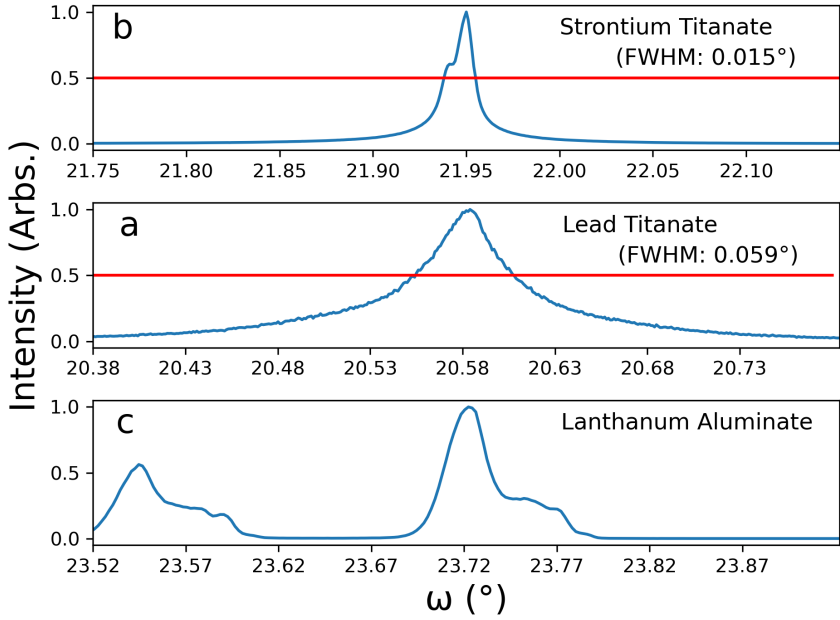


**Figure 3.9:** Normalised rocking curves around the (002) peak for various materials. Red line marks half of the maximum peak height. (a) A rocking curve on STO, on which (b) PTO is grown, shows the change in crystallinity. (c) A rocking curve on LAO, showing peak twinning.

$$\Delta\omega = \omega - \frac{1}{2}(2\theta) \quad (3.15)$$

which is in effect the rotation of the sample stage with respect to a particular beam configuration (it can be seen that a change in  $\omega$  with a constant  $2\theta$  leads to an identical change in  $\Delta\omega$ ; so an  $\omega$  scan is identical to a  $\Delta\omega$  scan).

In a  $2\theta$ - $\omega$  scan, both  $2\theta$  and  $\omega$  change while  $\Delta\omega$  is kept constant. In effect, this is a symmetrical movement of both the source and detector towards (or away) from each other. This is equivalent to a symmetrical rotation of the Ewald's spheres of both incident and diffracted beams in reciprocal space, and so their intersection—the regions of reciprocal space we are sensitive to—is a line radiating out of the origin, at an angle of  $\Delta\omega$ .

A broad  $2\theta$ - $\omega$  scan therefore allows one to capture multiple peaks of a single crystal; if a sample is aligned for the (002) peak to be observed, then the (004) peak should also be observable, for example (assuming Ewald's sphere is of a size sufficient for both to be imaged). Bragg's Law also allows the calculation of the  $c$ -axis, and a secondary measurement over another

### 3. Sample Characterisation

---

peak [eg. the (103) peak or (013) peak] could allow for calculation of the  $a$ - and  $b$ -axes respectively.

For epitaxial thin films,  $2\theta$ - $\omega$  scans are particularly useful. A *symmetric*  $2\theta$ - $\omega$  scan<sup>5</sup> should be able to capture both film and substrate simultaneously. This can allow the determination of the lattice parameters of both film and substrate in a single scan, and therefore a quick check on if a film is truly epitaxial.

#### 3.2.7 Reciprocal Space Mapping

We have discussed how an  $\omega$  scan is a measurement of an arc through reciprocal space, and how a  $2\theta$ - $\omega$  scan is a vertical line radiating from the origin. Both of these measurements are 1-dimensional, in which we only take a 1-dimensional cut of reciprocal space. By independently varying both  $2\theta$  and  $\omega$ , we can instead take a 2-dimensional slice of reciprocal space; a reciprocal space map (RSM).

We described in Section 3.2.3 that the physical diffraction condition occurs when the Ewald's sphere of the source intersects with the Ewald's sphere of the detector. This creates a geometric relationship between the diffractometer angles  $2\theta$  and  $\omega$  and the physical parameters of reciprocal space  $Q_x$  and  $Q_z$  (to access some  $Q_y$ , we would have to rotate the sample; and thus also change  $\phi$  or  $\psi$ ). This relationship is as follows:

$$\begin{aligned} Q_x &= \frac{2\pi}{\lambda} [\cos(\omega) - \cos(2\theta - \omega)] \\ Q_z &= \frac{2\pi}{\lambda} [\sin(\omega) + \sin(2\theta - \omega)] \end{aligned} \tag{3.16}$$

By taking samples at various values of  $2\theta$  and  $\omega$ , we can therefore create such a reciprocal space map. Experimentally, this can be done by setting some  $2\theta$  and performing an  $\omega$  scan, then shifting  $2\theta$  and repeating continuously<sup>6</sup>. This is more experimentally simple with a 1D or 2D detector; these segmented detectors can simultaneously measure at different  $2\theta$  values and therefore create more rapid measurements.

Reciprocal space maps are particularly important for the primary characterisation of ferroelectric thin films. Some sample data of a PTO thin film on an SRO electrode and STO substrate can be seen in Fig. 3.10. Here, the sharpest peak is that of the substrate, STO, which appears at

---

<sup>5</sup>A *symmetric*  $2\theta$ - $\omega$  scan is one in which  $\Delta\omega$  is about 0 and thus we primarily investigate the  $c$ -axis. An *asymmetric* scan has a higher-magnitude  $\Delta\omega$ , and thus can let us look at other axes.

<sup>6</sup>Those who have read the AFM section of this thesis could draw comparison to the raster paths and slow- and fast-scan axes inherent to that technique. Surprisingly and unfortunately, this is not standard vocabulary for RSM measurements.

the position we would expect from Bragg's law. PTO and SRO peaks can also be observed, with their positions also calculated by Bragg's law. We do see that the SRO peak is rather broad along the  $Q_z$  axis, though; this tells us that there is some distribution of  $c$  lattice parameters in the SRO electrode. Most interesting, however, are the two satellite peaks on either side of the STO substrate. These two peaks would not be observable in a  $2\theta$ - $\omega$  scan that captures the other peaks, but are significant enough to suggest the presence of an additional crystalline phase. We can convert the reciprocal space lattice parameters into real space lattice parameters and see that this peak corresponds to tetragonal PTO, with its shorter  $a$ -axis pointing out-of-plane. The position of these peaks off-centre suggest that this  $a$ -axis is also not pointing wholly out-of-plane, but rather at an angle (which we can directly calculate from  $Q_x$  and  $Q_z$ ).

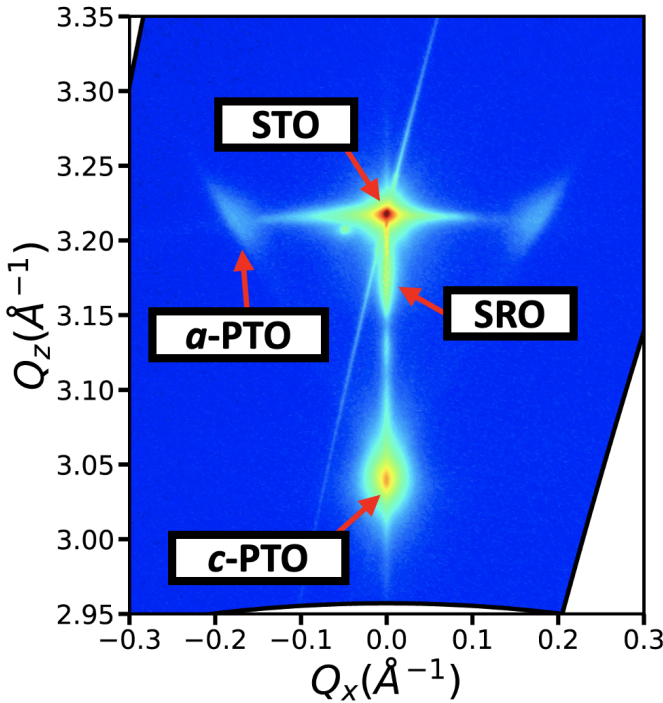


**Figure 3.10:** Sample XRD data of a PTO film grown on an STO substrate, with an SRO interelectrode.

This RSM data corresponds to the same sample from which the PFM data in Fig. 3.4 were collected. This provides the supplementary information we were looking for in that section: we know that there is this  $a$ -PTO in the



### 3. Sample Characterisation

---

film, and as we saw in Fig. 3.4(b) there are these regions of lower out-of-plane polarisation. We can expect that these two phenomena are one and the same: that is, the *a*-PTO coalesces into these *a*-domains, and this rotation of the unit cell would naturally reduce the out-of-plane polarisation, causing the reduced amplitude in Fig. 3.4(b).

#### 3.2.8 X-Ray Reflectivity, Fringes, and Film Thickness

XRD measurements taken at low incident and reflected angles ( $< 1^\circ$ ) are known as *x-ray reflectivity* (XRR). At such low angles, the x-ray intensity is particularly sensitive to surface features on the sample. XRR measurements are thus useful to measure the quality of a sample surface.

For thin film samples, XRR measurements are particularly useful for their ability to provide an estimate of sample thickness. If a thin film and substrate have distinct refractive indexes, then at low angles the incident beam can transmit through the thin film, and then reflect off the thin film–substrate interface. Some of this reflected beam can reach the detectors, while another part may reflect off the thin film–air interface, back towards the substrate, where it can reflect off the film–substrate interface once more. This process can repeat, creating a decaying series of oscillations of identical symmetry.

If the divergence of the incident beam is ignored, the film thickness  $t$  can be determined by a variation of Bragg’s law (Eq. 3.14). If we consider that the distance we are looking at is the film thickness (ie.  $d = t$ ) and we take the small angle approximation (ie.  $\sin \theta \approx \theta$ ), then the condition for constructive interference from Bragg’s law is:

$$\begin{aligned} n\lambda &= 2d \sin \theta \\ &\approx 2t\theta \end{aligned} \tag{3.17}$$

Thus, between any two adjacent oscillations, we can approximate the thickness as:

$$t = \lambda / \Delta 2\theta \tag{3.18}$$

where  $\Delta 2\theta$  is the distance (in radians) between the crests or troughs of adjacent oscillations in a plot of intensity against  $2\theta$ . An equivalent variation is:

$$t = \lambda f_{2\theta,^\circ} \times \frac{180}{\pi} \tag{3.19}$$

where  $f_{2\theta,^\circ}$  is simply the frequency of the oscillations in  $2\theta$ , when the distance between the oscillations are measured in degrees.

Experimentally, the close proximity between these oscillations mean that measuring their precise location (and therefore, the precise thickness of the

film) can be difficult. To improve the accuracy of the analysis, the following procedure is performed:

1. An XRR measurement is taken, which shows clear Kiessig fringes [Fig. 3.11(a)].
2. The ‘envelope’ hiding the XRR measurements is removed. In Fig. 3.11(b), this is done by taking a rolling average of the spectrum.
3. A Fourier transformation is applied to fit the measured oscillations [frequency domain plotted in Fig. 3.11(c)].

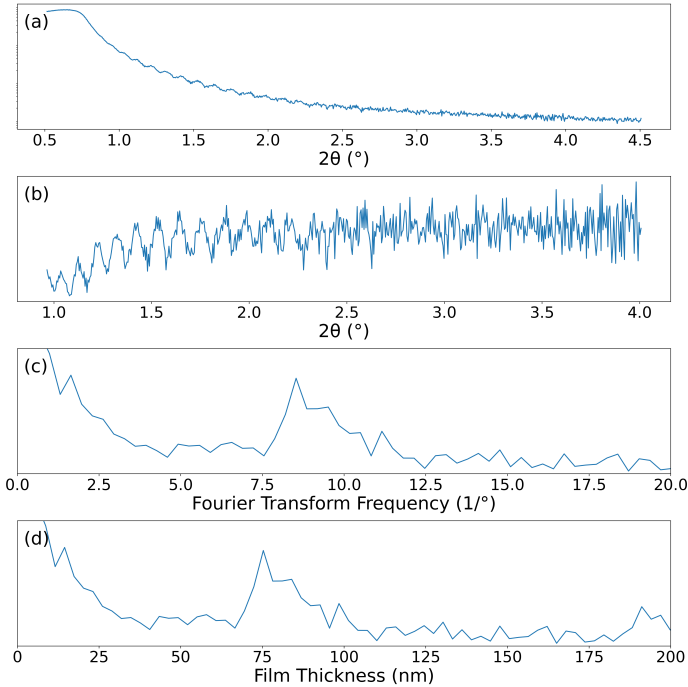


**Figure 3.11:** Sample XRR data of a film of  $\text{BiFeO}_3$  grown on  $\text{SrTiO}_3$ . a) Raw XRR data. b) XRR data with the envelope removed, to emphasis oscillations. a) Fourier transform of the XRR oscillations a) Oscillation frequencies rescaled to represent film thickness.

Fig. 3.11(c) shows a peak at  $8.53$  /°, which is the best estimation for the frequency of the oscillations in Fig. 3.11(a). We can then substitute this into Eq. 3.19 to convert this value to a film thickness of  $t \approx 75$  nm.

### 3. Sample Characterisation

---

We can also alternatively use Eq. 3.19 to rescale the frequencies in Fig. 3.11(c) to film thicknesses, as in Fig. 3.11(d), and read the film thicknesses directly.

If multiple layers of thin films (with different refractive indices) exist, multiple peaks should also be visible in the frequency domain.

In standard  $2\theta$ - $\omega$  measurements, we may also view similar oscillations around intense peaks. These oscillations are called *Laue fringes*, and like Kiessig fringes, appear from total internal reflection and mark a high quality thin film growth. Laue fringes can thus be used similarly to determine film thicknesses, as for example to verify the thickness of a BFO film in Chapter 7.

We have discussed in this chapter two main experimental techniques: AFM, in which we locally probe a material to observe sample physics; and XRD, in which we gather structural information about an entire sample. These two techniques have marked differences, but also marked similarities, and any analysis of one could indeed be comparable or equivalent to analysis of the other. Through the next chapter, we will discuss *Hystorian*, a programming package developed to increase the ease of analysis of these distinct data types.

## References

- [1] G. Binnig and H. Rohrer, “Scanning tunneling microscopy”, *Surface science* **126**, 236–244 (1983).
- [2] U. Durig, D. W. Pohl, and F. Rohner, “Near-field optical-scanning microscopy”, *Journal of Applied Physics* **59**, 3318 (1986).
- [3] G. Binnig, C. F. Quate, and C. Gerber, “Atomic force microscope”, *Physical Review Letters* **56**, 930 (1986).
- [4] B. Voigtländer, *Atomic force microscopy* (Springer, 2019).
- [5] J. Cleveland, B. Anczykowski, A. Schmid, and V. Elings, “Energy dissipation in tapping-mode atomic force microscopy”, *Applied Physics Letters* **72**, 2613–2615 (1998).
- [6] M. Salapaka, D. J. Chen, and J. Cleveland, “Linearity of amplitude and phase in tapping-mode atomic force microscopy”, *Physical Review B* **61**, 1106 (2000).
- [7] Park Systems, *True non-contact<sup>TM</sup> mode*, <https://www.parksystems.com/index.php/park-spm-modes/217-true-non-contact-mode>, Accessed: 2024-03-11.
- [8] P. Güthner and K. Dransfeld, “Local poling of ferroelectric polymers by scanning force microscopy”, *Applied Physics Letters* **61**, 1137–1139 (1992).

- 
- [9] C. A. Van Eysden and J. E. Sader, “Resonant frequencies of a rectangular cantilever beam immersed in a fluid”, *Journal of Applied Physics* **100** (2006).
  - [10] B. J. Rodriguez, C. Callahan, S. V. Kalinin, and R. Proksch, “Dual-frequency resonance-tracking atomic force microscopy”, *Nanotechnology* **18**, 475504 (2007).
  - [11] S. Jesse, S. V. Kalinin, R. Proksch, A. Baddorf, and B. Rodriguez, “The band excitation method in scanning probe microscopy for rapid mapping of energy dissipation on the nanoscale”, *Nanotechnology* **18**, 435503 (2007).
  - [12] S. Jesse, S. Somnath, L. Collins, and S. V. Kalinin, “Full information acquisition in scanning probe microscopy”, *Microscopy Today* **25**, 34–45 (2017).
  - [13] S. Jesse, A. P. Baddorf, and S. V. Kalinin, “Switching spectroscopy piezoresponse force microscopy of ferroelectric materials”, *Applied Physics Letters* **88**, 062908 (2006).
  - [14] S. V. Kalinin, S. Jesse, A. Tselev, A. P. Baddorf, and N. Balke, “The role of electrochemical phenomena in scanning probe microscopy of ferroelectric thin films”, *ACS Nano* **5**, 5683–5691 (2011).
  - [15] M. Murrell, M. Welland, S. O’Shea, T. Wong, J. Barnes, A. McKinnon, M. Heyns, and S. Verhaverbeke, “Spatially resolved electrical measurements of SiO<sub>2</sub> gate oxides using atomic force microscopy”, *Applied Physics Letters* **62**, 786–788 (1993).
  - [16] J. Seidel, L. W. Martin, Q. He, Q. Zhan, Y.-H. Chu, A. Rother, M. Hawkrige, P. Maksymovych, P. Yu, M. e. Gajek, et al., “Conduction at domain walls in oxide multiferroics”, *Nature Materials* **8**, 229–234 (2009).
  - [17] M. Nonnenmacher, M. o’Boyle, and H. K. Wickramasinghe, “Kelvin probe force microscopy”, *Applied Physics Letters* **58**, 2921–2923 (1991).
  - [18] Y. Martin and H. K. Wickramasinghe, “Magnetic imaging by “force microscopy” with 1000 Å resolution”, *Applied Physics Letters* **50**, 1455–1457 (1987).
  - [19] R. Erlandsson, G. McClelland, C. Mate, and S. Chiang, “Atomic force microscopy using optical interferometry”, *Journal of Vacuum Science & Technology A: Vacuum, Surfaces, and Films* **6**, 266–270 (1988).
  - [20] Oxford Instruments, *Quadrature Phase Differential Interferometry (QPDI) technology in the Asylum Research Vero AFM*, <https://afm.oxinst.com/assets/uploads/products/asylum/documents/Technical%20Note:%20QPDI%20technology%20in%20the%20AR%20Vero%20AFM%20WEB.pdf>, Accessed: 2024-03-11.

### 3. Sample Characterisation

---

- [21] J. P. Killgore, L. Robins, and L. Collins, “Electrostatically-blind quantitative piezoresponse force microscopy free of distributed-force artifacts”, *Nanoscale Advances* **4**, 2036–2045 (2022).
- [22] C.-P. T. Nguyen, P. Schoenherr, E. K. Salje, and J. Seidel, “Crackling noise microscopy”, *Nature Communications* **14**, 4963 (2023).
- [23] M. Checa, A. S. Fuhr, C. Sun, R. Vasudevan, M. Ziatdinov, I. Ivanov, S. J. Yun, K. Xiao, A. Sehirlioglu, Y. Kim, et al., “High-speed mapping of surface charge dynamics using sparse scanning kelvin probe force microscopy”, *Nature Communications* **14**, 7196 (2023).
- [24] C. Masens, J. Schulte, M. Phillips, and S. Dligatch, “Ultra flat gold surfaces for use in chemical force microscopy: scanning probe microscopy studies of the effect of preparation regime on surface morphology”, *Microscopy and Microanalysis* **6**, 113–120 (2000).
- [25] Adama Innovations, *Apex Sharp Diamond AFM Probes*, <https://www.adama.tips/products-apex-sharp>, Accessed: 2024-07-03.
- [26] C. Blaser and P. Paruch, “Subcritical switching dynamics and humidity effects in nanoscale studies of domain growth in ferroelectric thin films”, *New Journal of Physics* **17**, 013002 (2015).
- [27] C. Kittel and P. McEuen, *Introduction to solid state physics* (John Wiley & Sons, 2018).
- [28] C. Suryanarayana, M. G. Norton, C. Suryanarayana, and M. G. Norton, *X-rays and diffraction* (Springer, 1998).
- [29] G. F. Harrington and J. Santiso, “Back-to-basics tutorial: x-ray diffraction of thin films”, *Journal of Electroceramics* **47**, 141–163 (2021).

## CHAPTER 4

---

### *Hystorian*: A Processing Tool for Scanning Probe Microscopy and Other $n$ -Dimensional Datasets

---

Research in materials science increasingly depends on the correlation of information from multiple characterisation techniques, acquired in ever larger datasets. Efficient methods of processing and storing these complex datasets are therefore crucial. Reliably keeping track of data processing is also essential to conform with the goals of open science. Here, we introduce *Hystorian*, a generic materials science data analysis Python package built at its core to improve the traceability, reproducibility, and archival ability of data processing.

Produced in partnership with Loïc Musy at the University of Geneva, *Hystorian* converts proprietary data formats into open hierarchical data format (HDF5) files, with both datasets and subsequent workflows automatically stored into a single location, thus allowing easy management of multiple data types. At present, *Hystorian* provides a basic scanning probe microscopy and x-ray diffraction analysis toolkit, and is readily extensible to suit user needs. It is also able to wrap over any existing processing functions, making it easy to append in an extant workflow. This package has been used as a backbone for analysis in many subsequent chapters of this thesis.

This Chapter is based on a publication by L. Musy, R. Bulanadi, I. Gaponenko and P. Paruch in *Ultramicroscopy* (Elsevier) in 2021, under the title *Hystorian: A Processing Tool for Scanning Probe Microscopy and Other  $n$ -Dimensional Datasets* [1]. R. Bulanadi and L. Musy contributed equally to this work, with R. Bulanadi taking particular focus on the implementation

of `m_apply`, the distortion correction algorithms, and the implementation of many additional processing functions for XRD and PFM. R. Bulanadi also performed and plotted all analyses displayed in this chapter.

This work was supported by the Swiss National Science Foundation under Division II (Grant No. 200021-178782). The source code for *Hystorian* openly available at GitLab <https://gitlab.unige.ch/paruch-group/hystorian>, and Yareta at <https://doi.org/10.26037/yareta:pkujtpch4vhqbhyxyw63vhsc6m>. The latter also contains the PFM and SHG data, in compliance with SNSF Data Management Plan guidelines.

### 4.1 Introduction

Current materials science increasingly relies on ever more data-intensive techniques for fundamental and applied characterisation [2]. Additionally, since the nanoscale structure and properties of materials are related to their macroscopic response, correlating measurements on different materials [3], or with various techniques that probe different time or length scales [4], has become increasingly necessary, and can lead to a deeper understanding of the underlying mechanisms [5]. Big Data approaches can also give new insight into the design of functional materials [6, 7]. For example, deep learning has allowed the properties of solid state solutions to be predicted hundreds of times faster than with conventional first-principles density functional theory [8], and facilitated the rapid extraction of structural information from neutron scattering spectroscopy [9]. In complex, multifunctional ferroelectric materials, such approaches have also successfully identified phase transitions [10] or relaxation behaviour [11].

As data processing becomes an increasingly important and unavoidable aspect of scientific work, this information paradigm shift presents challenges for modern researchers [12]. First, the acquired data has to be extracted from (usually) proprietary data formats and transformed into a shape more suitable for further analysis [13]. In the process, useful physical metadata, such as the physical scale of an image, or values of externally applied experimental parameters such as temperature, pressure, or magnetic field, may be lost. Furthermore, during the subsequent processing, pre-existing methods in statistics and data analysis are often redeveloped or reinvented, sometimes inadvertently leading to implementation mistakes. Data analysis is further complicated by the use of datasets from multiple disparate sources, especially when quantitative comparison and correlation are required, as is increasingly becoming the norm in large scale collaborations between groups with complementary areas of expertise [14, 15].

In this paper, we present *Hystorian*, a cross-platform Python package developed to address these challenges by keeping track of all operations

and parameters during multistep data processing workflows. This package is capable of loading, merging, and operating on data from arbitrary sources by transforming proprietary file types into  $n$ -dimensional datasets in a hierarchical data format (HDF5) file. *Hystorian* easily inserts itself into existing workflows due to a series of wrapper functions that can take any extant function and apply it on data stored in the HDF5 files, while keeping track of the function parameters.

We begin by discussing the structure of the *Hystorian* package and the HDF5 files it creates, focusing on the benefits and ease of use brought by the file conversion process and use of wrapper functions. We then illustrate a few of the in-built functions such as phase binarisation for piezoresponse force microscopy and peak detection for x-ray diffraction analysis. Finally, we present a typical use case where we integrate second harmonic generation data with piezoresponse force microscopy images of domains in ferroelectric thin films to show how these techniques may be correlated to highlight the non-Ising, chiral behaviour of ferroelectric domain walls.

## 4.2 Working Principle

The advantages of using *Hystorian* during data processing are achieved in two ways.

First, *Hystorian* provides support to convert a variety of proprietary data formats into a single, standardised format. By keeping to one consistent format, subsequent data processing is streamlined and dissimilar data sources can be treated equivalently. We use HDF5 files for their traditional use in data preservation [16] and because their hierarchical structure allows for close storage of process outputs. The current version of *Hystorian* allows conversion of the following formats: .ardf and .ibw files from *Asylum Research* instruments; .sxm files from *Nanonis* instruments; .gsf files from the free and open-source *Gwyddion* software [17]; and .xrdml from *Philips* x-ray diffractometers. It can also convert standard .jpg, .png, .bmp and .csv file formats. This list can easily be expanded by users in custom code and in further library updates.

Secondly, *Hystorian* provides a group of wrapper functions that can be applied over external functions to seamlessly manage the storage of the process outputs and function arguments utilised during analysis. This allows for easy integration of both custom code and most standard data science packages such as NumPy[18] or SciPy[19] into the ecosystem provided by *Hystorian*. These are also supplemented by a library of in-built functions that accomplish standard data processing or presentation needs.

It is the combination of these two mechanisms which constitutes *Hystorian*'s key advantage: the wrapper function allows standard functions to



interact with the HDF5 file outputs, and, in doing so, automatically perform and archive the operation on behalf of the user. To establish how this is done, however, the properties of the generated HDF5 structures must be understood.

### 4.2.1 Unification of File Structures

To facilitate data processing, a uniform file structure is required. The HDF5 file format used here consists of two objects: datasets, which are multidimensional arrays; and groups, which are containers capable of storing either data or further nested groups. This allows the outputs of *Hystorian* to have a hierarchical tree structure, similar to the standard directory structure used in computer operating systems.

Each object may also possess one or more attributes. Each individual attribute is described by a *Name* and consists of a *Value* that itself can be an  $n$ -dimensional array of various types. In *Hystorian*, these attributes are used to store metadata parameters and, where applicable, the arguments of processing functions.

HDF5 files created and read by *Hystorian*, by our convention, contain the following groups in the root directory (Fig. 4.1).

- *datasets* group [Fig. 4.1(a)]: Contains the raw data extracted from proprietary files as a  $n$ -dimensional array. Within this *datasets* group are additional subgroups for each converted file or experiment. Each of these (sub)groups contains raw datasets for each data channel collected within the experiment. Each dataset is labelled with key attributes that describe the fundamental data, such as the physical units (if available) or the initial data type.
- *metadata* group [Fig. 4.1(b)]: Contains the raw metadata extracted from the proprietary files. This should contain the full extent of all experimental information that cannot be included in the  $n$ -dimensional array of a dataset.
- *processes* group [Fig. 4.1(c)]: Contains subgroups labelled by process number and process name. Within each process is a similar directory to that of the *datasets* group, where a group corresponding to an experiment contains datasets corresponding to a particular data channel. As in the *datasets* group, each dataset in the *processes* group is labelled with attributes, but here the attributes are extended to collect all raw arguments passed into the function call, as well as other key outputs of the argument process that may find later use.

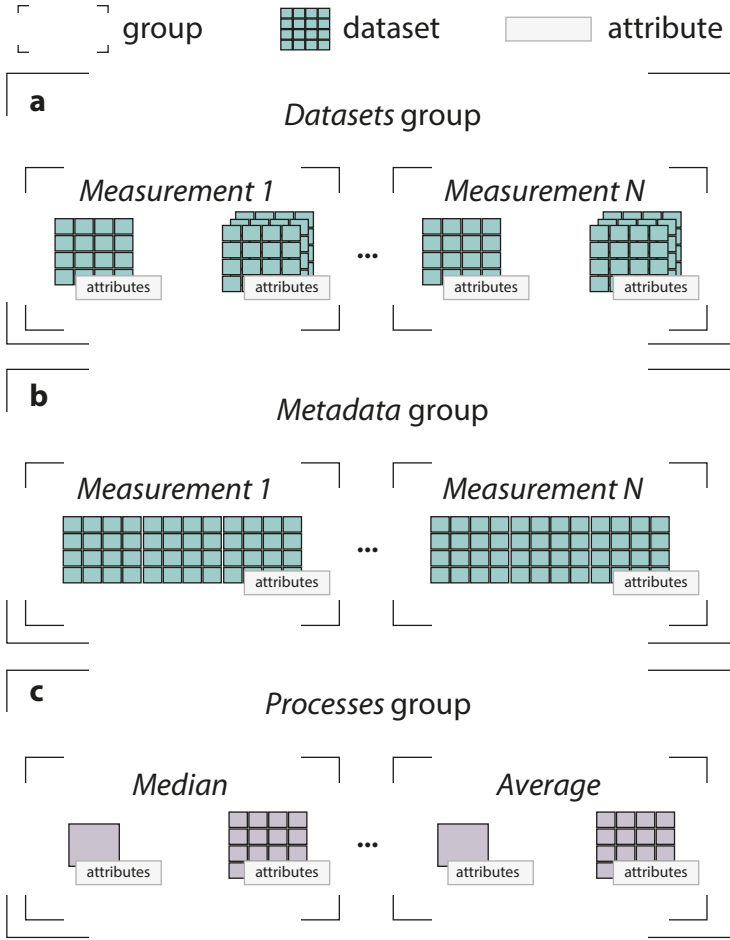


**Figure 4.1:** The file structure of HDF5 outputs from Hystorian consisting of three groups. (a), *datasets*, containing the raw data converted from the experiment file; (b), *metadata*, containing the raw metadata from the experiment; and (c), *processes*, containing all process outputs. Every group has attached attributes which contain meaningful metadata and a history of the processing when required. Each processing step is binned in its own folder, with the processing input and arguments saved as attributes.

### 4.2.2 File Conversion

To streamline and standardise future data processing, proprietary data formats are initially converted into the array-like  $n$ -dimensional datasets of the HDF5 file. On the user side, this is performed by simply calling the function: `hystorian.io.read_file.tohdf5(filename)` where `filename`

## 4. *Hystorian*: A Processing Tool for Scanning Probe Microscopy and Other $n$ -Dimensional Datasets

---

is a string designating the name of the proprietary file to be converted. *Hystorian* then reads the filetype passed into `tohdf5()` and calls upon a function written for that specific filetype. Each particular filetype is read using customised code that extracts the main bulk of the datatype as a  $n$ -dimensional array, which is stored in the *dataset* group. All raw metadata is extracted as raw text into the *metadata* group, while particularly physically important experimental parameters specific to the dataset, such as temperature and applied bias, is stored as an attribute inside the *dataset* group.

In cases where data is stored as several mathematically related 1-dimensional arrays in the proprietary format, as in the case of .xrdml outputs from *Philips* x-ray diffractometers, the conversion automatically expands the data into a  $n$ -dimensional array to increase compatibility with future processes.

### 4.2.3 `m_apply` and Data Processing

To interact with the converted HDF5 files, *Hystorian* primarily uses `m_apply`, a wrapper function which can be applied over any function that manipulates  $n$ -dimensional arrays. The `m_apply` wrapper takes as main arguments: the filename of the HDF5 file operated on; the function to be applied; the path (or paths) to the datasets being processed; and any additional arguments required or used by the particular applied functions (Fig. 4.2).

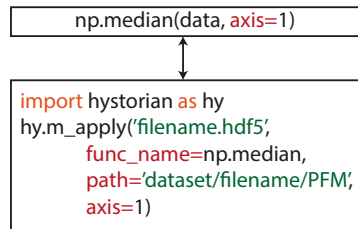


**Figure 4.2:** An example call of an external data processing function, `np.median`, and how it may be used within the *Hystorian* wrapper function `m_apply`. Note how the argument of `np.median` known as `axis` may easily be called within the `m_apply` wrapper in an identical way.

`m_apply` seamlessly reads and navigates the HDF5 file, loads only the relevant datasets, applies the function to these datasets, and writes the function output (or outputs) into the appropriate group. All function parameters are also automatically written into the file as a dataset attribute, allowing users to easily recover and track the utilised parameters.

Data outputs from `m_apply` are treated equivalently to the raw datasets

within *Hystorian*. This allows data outputs to be subsequently used as an input to another function. Additionally, paths to multiple datasets can be passed into `m_apply` as a list, allowing for multiple inputs into utilised processes. This permits complex processing networks to be used and maintained while saving each intermediate step.

#### 4.2.4 Archiving, Compression, and Regeneration

While tracking the full processing history may be convenient for accessibility, if multiple functions are successively employed, the total size of the HDF5 file will rapidly increase beyond desirable levels. To diminish the impact of this data inflation, *Hystorian* includes functionality to compress datasets calculated during intermediate process steps and regenerate them when necessary.

Archiving and compression utilise the predictability of scientific data processing; when passing identical arguments into a function, identical results may logically be expected. *Hystorian* utilises this fact to compress HDF5 outputs by removing calculable datasets and leaving their metadata.

By calling the compression function `compress_hdf5`, *Hystorian* will read each processed dataset and first attempt to regenerate it by utilising metadata stored in the dataset attributes. If the reproduced dataset is identical to the processed dataset, or with differences below a given threshold, the processed dataset will be ‘compressed’ by clearing the stored dataset and leaving only its attached attributes, diminishing the overall size of the file.

At a later point, these ‘compressed’ datasets can be automatically regenerated from the remaining attributes using the function `decompress_hdf5`.

### 4.3 Pre-Implemented Functions

In addition to conversion and wrapper functionality, *Hystorian* also includes a library of analytical functions to further increase the efficiency of data processing. These functions are more specialised than the generic wrapper function, but due to the uniform nature of the datasets in the HDF5 outputs, the functions can be applied generally to different data sources, and can therefore be used to apply well-understood functions to a researcher’s own ends.

#### 4.3.1 Distortion Correction

New trends and novel physics may often be elucidated by analysing sequentially acquired images from a variety of microscopy techniques. For example, tracking individual ferroelectric polarisation switching events in distortion corrected piezoresponse force microscopy image series recently

#### 4. *Hystorian*: A Processing Tool for Scanning Probe Microscopy and Other $n$ -Dimensional Datasets

allowed avalanche statistics to be compared between different dynamics regimes, showing distinct power-law scaling exponents [20]. However, small changes in the equipment or environment can cause distortions or drift between these images, producing detrimental artifacts.

Based on a previously developed computer-vision-based distortion correction algorithm designed for scanning probe microscopy (SPM) [21], *Hystorian* contains a dedicated variant which can be extended to other 2-dimensional images. The in-built function `distortion_params_` can take in a series of 2-dimensional images [Fig. 4.3(a–b)] and calculate the distortion matrices used to align subsequent images to the first image. The image sequence can then be corrected using the function `distortion_correction_` [Fig. 4.3(c–d)]. Moreover, the calculated distortion matrices can then be used to correct other, concurrently collected data channels [Fig. 4.3(e–g)] in order to elucidate new physics, such as the progressive displacement of ferroelectric domain walls under an externally applied electric field [Fig. 4.3(h)].

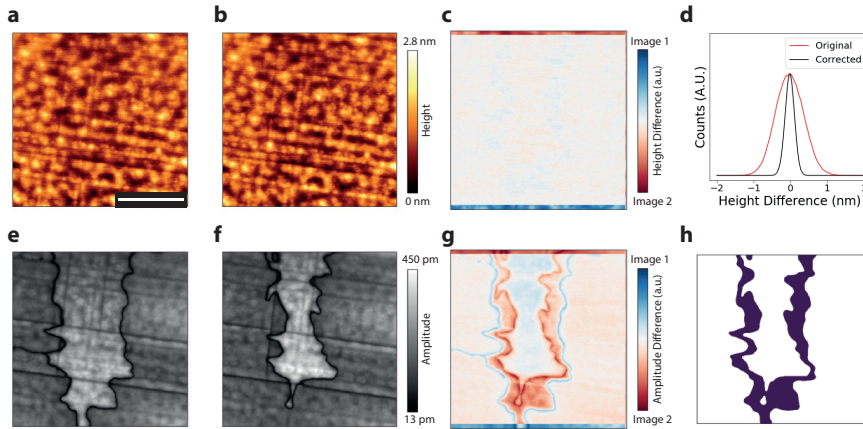


**Figure 4.3:** `distortion_params_` as applied on a multichannel SPM dataset. Raw topography images (a,b) are taken sequentially during a switching dynamics study, concurrently with PFM amplitude images (e,f) respectively, in which the positions of domain walls are visible as the dark wavy lines. The differential image (c) shows excellent matching after distortion correction is performed on these two topography images. Note the decrease in intensity between these two images, particularly compared to the non-overlapping regions towards the top and bottom. The height differences (d) between the corrected (black) and original (red) coordinate pairs in the topography images show a narrower distribution around 0 nm after distortion correction. Using *Hystorian*, the same distortion correction transformation matrix can be applied on the PFM amplitude data to produce the corresponding differential image (g), allowing area subtended by the motion of the domain walls to be identified in (h). Scalebar measures 5  $\mu\text{m}$  and all images are shown on the same scale

### 4.3.2 Piezoresponse Force Microscopy Analysis

Piezoresponse force microscopy (PFM) is an SPM variant that tracks the amplitude and phase offset of the mechanical response excited in a piezoelectric sample by an oscillating voltage input, while simultaneously collecting data corresponding to a sample surface topography. This technique is immensely useful in the characterisation of ferroelectric or piezoelectric domains [22]. As data analysis generally relies on simultaneously utilising and tracking the PFM amplitude, PFM phase, and topography datasets, PFM is a key instance in which the advantages of *Hystorian* are clearly apparent.

To show how *Hystorian* can streamline typical use cases, we include a variety of functions that process raw piezoresponse force microscopy (PFM) data to extract key features:

- **line\_flatten\_image**: Basic SPM image treatment, correcting for deviations in the slow scan axis.
- **phase\_linearisation**: Converts raw phase outputs into a value between 0 and 1, which approximately describes the likelihood of polarisation oriented in a particular direction
- **phase\_binarisation**: Threshold function that converts phase data to booleans that represent one of two polarisations.
- **find\_a\_domains**: Finds linear features in the amplitude data, while excluding those features also present in the phase data.

These functions are all written to directly process data arrays, and are thus intended to be called via the wrapper function `m_apply`.

### 4.3.3 X-Ray Diffraction Analysis (2-Axes)

The analysis of 2-axes x-ray diffraction spectra is another key case where data processing may be complex. X-Ray diffraction is a technique in which a sample is moved in 3D space relative to both an x-ray source and a detector to determine diffraction patterns, from which crystal lattice parameters and other long range ordering in a sample can be identified. This identification relies on the joint application of multiple data channels, once again bringing a case where *Hystorian*'s ability to track processing is of great use. Routinely used transformations and mathematical processes are therefore implemented directly into *Hystorian*.

- **centre\_peak**: Adjusts for slight translations and artefacts resulting from the physical positioning and displacement of the machine by aligning to theoretical peaks.

## 4. *Hystorian*: A Processing Tool for Scanning Probe Microscopy and Other $n$ -Dimensional Datasets

---

- **qvector**: Converts raw  $2\theta$ - $\omega$  data into reciprocal space.
- **find\_peak\_position**: Identifies the position of 2-dimensional Gaussian peaks; in the context of x-ray diffraction scans, these correspond to characteristic sample reflections.
- **add\_lattice\_param\_attributes**: Utilising the identified peak positions, adds attributes to the HDF5 file that show the real-space lattice parameters corresponding to the reflection positions in reciprocal space.

### 4.3.4 Data Visualisation

In addition to processing data, *Hystorian* is also capable of utilising the physical metadata in the attributes to help with data visualisation.

- **save\_image**: Powered by `matplotlib.pyplot.imshow` and `matplotlib.scalebar`, this function is further capable of using scale attributes to automatically generate scalebars on 2-dimensional images.
- **plot\_hysteresis\_parameters\_**: This function uses the output from the PFM analysis' built-in function to return plots of meaningful physical properties in the context of ferroelectric switching loops, including coercive voltages, imprint, and phase shift.
- **plot\_RSM**: Utilises the outputs of **qvector** to plot a x-ray diffraction reciprocal space map.
- **multi\_power\_law**: Generates and visualises the maximum likelihood estimation of a power-law fit [23].

## 4.4 Synthesising Disparate Data Sources

While *Hystorian* is capable of treating data sources separately, an important use of this package lies in its ability to equivalently treat data from different sources by converting them into the uniform HDF5 format. To showcase this advantage, we present how raw data from an *Asylum Research Cypher* atomic force microscope can be directly compared with second harmonic generation (SHG) data to overlay the positions of ferroelectric domain walls and therefore allow the precise study of the domain wall's chirality. This analysis is based on data showing non-Ising polarisation at domain walls, where the feature matching between images acquired via the two techniques was carried out by visual inspection [24]. Here, the *Hystorian* environment is used to perform the correlation after automatic image registration.

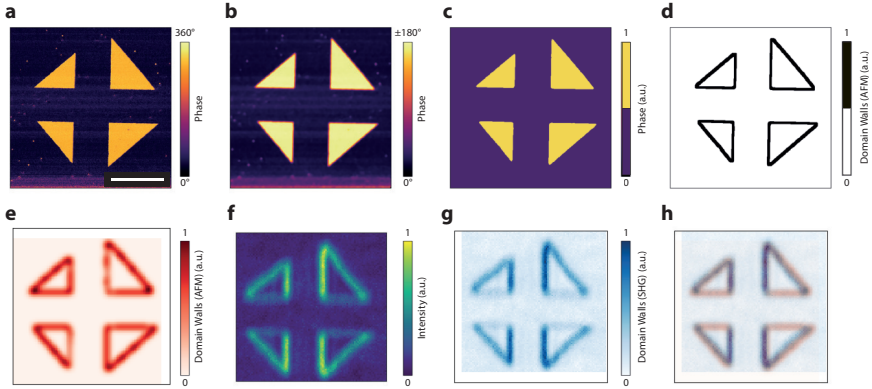


**Figure 4.4:** *Hystorian* is used to reveal structure-property correlations at ferroelectric domain walls from complementary local piezoresponse force microscopy and nonlinear optical microscopy measurements. Raw PFM phase data, (a), is corrected with `phase_linearisation` to improve contrast in (b), and binarised to highlight the two distinct polarisation orientations in (c), allowing *Hystorian* to determine the domain wall positions in (d). The domain wall positions are blurred (e) to allow direct comparison to the SHG data. The SHG data for a single scan (f), with their normalised, median values of the set (g), demonstrate the non-Ising nature of the domain walls. In (h), the domain walls calculated from both PFM and SHG are overlaid using `distortion_correction_`, showing perfect correlation in the structures visible by both techniques. Scalebars in all images measure 5  $\mu\text{m}$ .

#### 4.4.1 Conversion of Raw Data

Conversion of SHG and PFM data is supported in *Hystorian*, with both files converted to the HDF5 file output with the default `tohdf5` function. These files can then be merged into a single HDF5 file to further increase simplicity using `merge_hdf5`.

#### 4.4.2 Domain Wall Extraction from Piezoresponse Force Microscopy

A single PFM scan is used to generate our data. Of most relevance are the *Phase* data channels that correspond to the phase of the piezoelectric response, [Fig. 4.4(a)]. A combination of in-built *Hystorian* functions with other publicly available external functions allows the position of domain walls to be easily extracted from these channels. The following data processes are performed in sequence:

1. Phase Offset Correction: Utilising *Hystorian*'s `phase_linearisation` function, an offset is applied to the *Phase* channel such that the up oriented polarisation corresponds to an  $180^\circ$  phase shift and the down oriented polarisation corresponds to a  $0^\circ$  phase shift [Fig. 4.4(b)]



2. Summation: Use of a summation function allows collation of multiple phase channels together to create a better estimate of the polarisation as the average of multiple phase channels if present.
3. Phase Binarisation: The `phase_binarisation` function within *Hystorian* can be utilised to automatically set the determined ferroelectric polarisation to one of two binary states (ie. 1 or 0, representing ‘Up’ or ‘Down’) [Fig. 4.4(c)].
4. Domain Wall Identification: The domain walls can be found at the border between the two domain states. This can be simply found by morphological erosion and dilation functions given the binarised states found by `phase_binarisation` [Fig. 4.4(d)].
5. Blurring: The erosion-dilation process calculates the domain wall position to the pixel. To allow comparison with the much lower spatial resolution of SHG imaging, these need to be broadened via the application of a Gaussian blur, such as those provided by openCV’s `GaussianBlur` function [25].
6. Normalisation: The data can be normalised to values between 0 and 1 for easy comparison with SHG data. This can be done with *Hystorian*’s `normalise` function [Fig. 4.4(e)].

### 4.4.3 Domain Wall Extraction from Second Harmonic Generation

In the SHG data, a series of images is sequentially captured with different analyser angles. Individual images can directly observe domain walls in particular directions [Fig. 4.4(f)], and so the sequence of images must be handled together to view all relevant domain walls. This can also be done with both in-built and external functions.

1. Median: NumPy’s default `median` function can be used to find the median values of each of the sequential SHG scans. This allows the calculation to take into account the variety of utilised analyser angles.
2. Normalisation: As with the PFM data, the SHG data should be normalised to a value between 0 and 1 to allow direct comparison between these experiments [Fig. 4.4(g)].

### 4.4.4 Correlating and Visualising Domain Walls

With normalisation of both datasets, `distortion_params_` and `distortion_correction_` functions can be used to overlay the two datasets.

Following this, the `save_image` function can be used to create the final output. The final correlation between both the PFM and SHG datasets can be seen in Fig. 4.4(h). This confirms how the domain walls visualised by both SHG and PFM are in similar locations, and in combination with physical knowledge that the SHG signal corresponds to in-plane polarisation [24], shows that the domain walls visible in this sample are non-Ising, with Néel polarisation components.

## 4.5 Conclusions

We have developed *Hystorian*, a Python package designed to help the user keep track of data processing by providing a thorough history of the operations applied during multistep workflows. To reach this goal, we provide a set of wrapper functions which can be seamlessly integrated into an existing workflow while keeping track of all required processing parameters and meta-data. To further facilitate implementation, we also provide a toolkit allowing the conversion of proprietary formats into a unified HDF5 file output and some general in-built functions useful for analysing SPM and XRD data, with a library that can easily be expanded by users to accommodate other characterisation techniques as required. In the future, user-driven expansion could lead to a wider toolkit for applications in other domains of science.

In automatically handling most of the data archiving, saving, and storage associated with data processing, *Hystorian* will assist researchers who extensively utilise data processing in their work by providing an easy to use and user-adaptable tool.

## References

- [1] L. Musy, R. Bulanadi, I. Gaponenko, and P. Paruch, “Hystorian: a processing tool for scanning probe microscopy and other n-dimensional datasets”, *Ultramicroscopy*, 113345 (2021).
- [2] J. Schmidt, M. R. G. Marques, S. Botti, and M. A. L. Marques, “Recent advances and applications of machine learning in solid-state materials science”, *npj Computational Materials* **5**, 83 (2019).
- [3] D. Scott, P. Coveney, J. Kilner, J. Rossiny, and N. N. Alford, “Prediction of the functional properties of ceramic materials from composition using artificial neural networks”, *Journal of the European Ceramic Society* **27**, 4425–4435 (2007).

- [4] S. Pannala, J. A. Turner, S. Allu, W. R. Elwasif, S. Kalnaus, S. Simunovic, A. Kumar, J. J. Billings, H. Wang, and J. Nanda, “Multiscale modeling and characterization for performance and safety of lithium-ion batteries”, *Journal of Applied Physics* **118**, 072017 (2015).
- [5] L. A. Griffin, I. Gaponenko, S. Zhang, and N. Bassiri-Gharb, “Smart machine learning or discovering meaningful physical and chemical contributions through dimensional stacking”, *npj Computational Materials* **5**, 85 (2019).
- [6] S. V. Kalinin, I. Foster, S. Kalidindi, S. V. Kalinin, T. Lookman, K. K. van Dam, K. G. Yager, S. I. Campbell, R. Farnsworth, and M. van Dam, *Handbook on big data and machine learning in the physical sciences* (World Scientific, 2020).
- [7] S. V. Kalinin, B. G. Sumpter, and R. K. Archibald, “Big-deep-smart data in imaging for guiding materials design”, *Nature Materials* **14**, 973–980 (2015).
- [8] M. L. Pasini, Y. W. Li, J. Yin, J. Zhang, K. Barros, and M. Eisenbach, “Fast and stable deep-learning predictions of material properties for solid solution alloys”, *Journal of Physics: Condensed Matter* **33**, 084005 (2020).
- [9] M. Doucet, A. M. Samarakoon, C. Do, W. T. Heller, R. Archibald, D. A. Tennant, T. Proffen, and G. E. Granroth, “Machine learning for neutron scattering at ORNL”, *Machine Learning: Science and Technology* **2**, 023001 (2021).
- [10] L. Li, Y. Yang, D. Zhang, Z.-G. Ye, S. Jesse, S. V. Kalinin, and R. K. Vasudevan, “Machine learning-enabled identification of material phase transitions based on experimental data: exploring collective dynamics in ferroelectric relaxors”, *Science Advances* **4**, eaap8672 (2018).
- [11] R. K. Vasudevan, S. Zhang, M. Baris Okatan, S. Jesse, S. V. Kalinin, and N. Bassiri-Gharb, “Multidimensional dynamic piezoresponse measurements: unraveling local relaxation behavior in relaxor-ferroelectrics via big data”, *Journal of Applied Physics* **118**, 072003 (2015).
- [12] A. Agrawal and A. Choudhary, “Perspective: materials informatics and big data: realization of the “fourth paradigm” of science in materials science”, *APL Materials* **4**, 053208 (2016).
- [13] S. Somnath, C. R. Smith, N. Laanait, R. K. Vasudevan, A. Ievlev, A. Belianinov, A. R. Lupini, M. Shankar, S. V. Kalinin, and S. Jesse, *Usid and pycroscopy – open frameworks for storing and analyzing spectroscopic and imaging data*, 2019.

- 
- [14] M. Otoničar, A. Bradeško, L. Fulanović, T. Kos, H. Uršič, A. Benčan, M. J. Cabral, A. Henriques, J. L. Jones, L. Riemer, D. Damjanovic, G. Dražić, B. Malič, and T. Rojac, “Connecting the multiscale structure with macroscopic response of relaxor ferroelectrics”, *Advanced Functional Materials* **30**, 2006823 (2020).
- [15] A. K. Yadav, C. T. Nelson, S. L. Hsu, Z. Hong, J. D. Clarkson, C. M. Schlepütz, A. R. Damodaran, P. Shafer, E. Arenholz, L. R. Dedon, D. Chen, A. Vishwanath, A. M. Minor, L. Q. Chen, J. F. Scott, L. W. Martin, and R. Ramesh, “Observation of polar vortices in oxide superlattices”, *Nature* **530**, 198–201 (2016).
- [16] M. Folk and E. Pourmal, “Balancing performance and preservation lessons learned with HDF5”, in *Proceedings of the 2010 roadmap for digital preservation interoperability framework workshop*, US-DPIF ’10 (2010).
- [17] D. Nečas and P. Klapetek, “Gwyddion: an open-source software for SPM data analysis”, *Central European Journal of Physics* **10**, 181–188 (2012).
- [18] C. R. Harris, K. J. Millman, S. J. van der Walt, R. Gommers, P. Virtanen, D. Cournapeau, E. Wieser, J. Taylor, S. Berg, N. J. Smith, R. Kern, M. Picus, S. Hoyer, M. H. van Kerkwijk, M. Brett, A. Haldane, J. F. del Río, M. Wiebe, P. Peterson, P. Gérard-Marchant, K. Sheppard, T. Reddy, W. Weckesser, H. Abbasi, C. Gohlke, and T. E. Oliphant, “Array programming with NumPy”, *Nature* **585**, 357–362 (2020).
- [19] P. Virtanen, R. Gommers, T. E. Oliphant, M. Haberland, T. Reddy, D. Cournapeau, E. Burovski, P. Peterson, W. Weckesser, J. Bright, S. J. van der Walt, M. Brett, J. Wilson, K. J. Millman, N. Mayorov, A. R. J. Nelson, E. Jones, R. Kern, E. Larson, C. J. Carey, İ. Polat, Y. Feng, E. W. Moore, J. VanderPlas, D. Laxalde, J. Perktold, R. Cimrman, I. Henriksen, E. A. Quintero, C. R. Harris, A. M. Archibald, A. H. Ribeiro, F. Pedregosa, P. van Mulbregt, and SciPy 1.0 Contributors, “SciPy 1.0: Fundamental Algorithms for Scientific Computing in Python”, *Nature Methods* **17**, 261–272 (2020).
- [20] P. Tückmantel, I. Gaponenko, N. Caballero, J. C. Agar, L. W. Martin, T. Giamarchi, and P. Paruch, “Local probe comparison of ferroelectric switching event statistics in the creep and depinning regimes in  $\text{Pb}(\text{Zr}_{0.2}\text{Ti}_{0.8})\text{O}_3$  thin films”, *Physical Review Letters* **126**, 117601 (2021).
- [21] I. Gaponenko, P. Tückmantel, B. Ziegler, G. Rapin, M. Chhikara, and P. P., “Computer vision distortion correction of scanning probe microscopy images”, *Scientific Reports* **7**, 669 (2017).

- [22] A. Gruverman, M. Alexe, and D. Meier, “Piezoresponse force microscopy and nanoferroic phenomena”, *Nature Communications* **10** (2019) 10.1038/s41467-019-09650-8.
- [23] A. Clauset, C. R. Shalizi, and M. E. Newman, “Power-law distributions in empirical data”, *SIAM review* **51**, 661–703 (2009).
- [24] S. Cherifi-Hertel, H. Bulou, R. Hertel, G. Taupier, K. D. Dorkenoo, C. Andreas, J. Guyonnet, I. Gaponenko, K. Gallo, and P. Paruch, “Non-ising and chiral ferroelectric domain walls revealed by nonlinear optical microscopy”, *Nature Communications* **8** (2017) 10.1038/ncomms15768.
- [25] G. Bradski, “The OpenCV Library”, *Dr. Dobb’s Journal of Software Tools*, <https://github.com/opencv/opencv> (2000).

---

## Identifying and Analysing Power-Law Scaling in 2-Dimensional Image Datasets

---

Power-law distributions provide a general description of diverse natural phenomena in which events with a logarithmically increasing size occur with logarithmically decreasing probability. However, experimentally derived correlated 2-dimensional information is often difficult to cleanly interpret as discrete events of defined size. Moreover, physical limitation of techniques such as those based on scanning probe microscopy, which can ideally be used to observe power-law behavior, reduce event number and thus render straightforward power-law fits even more challenging.

Here, we develop and compare different techniques to analyse event distribution from 2-dimensional images. We show that tracking interface position allows the associated scaling parameters to be accurately extracted from both experimental and synthetic image-based datasets. We also show how these techniques can differentiate between power-law and non-power-law behavior by comparison of Hill, Moments, and Kernel estimators of these scaling parameter. We thus present computational tools to analyse power-law fits in 2-dimensional datasets, and identify the scaling parameters that best describe these distributions.

This Chapter is based on a publication by R. Bulanadi and P. Paruch accepted for publication in *Physical Review E* (American Physical Society) in 2024, under the title *Identifying and analyzing Power-Law Scaling in 2-Dimensional Image Datasets* [1]. R. Bulanadi conceived and implemented the described analysis and extraction techniques. I would also like to thank

## 5. Identifying and Analysing Power-Law Scaling in 2-Dimensional Image Datasets

---

Ms. Michelle Wang (Technical University of Denmark) and Dr. Elisabeth Agoritsas (University of Geneva) for reading the manuscript and assisting with mathematical detail—particularly for stopping me from going down the rabbit hole of analytically integrating the limits of a divergent expression.

This work was supported by the Swiss National Science Foundation under Division II (Grant No. 200021-178782). The data and source code which support the findings of this study are available on Yareta at <https://doi.org/10.26037/yareta:aedka5yvzhojc7pxbtkapvg6i>, in compliance with SNSF Data Management Plan guidelines.

### 5.1 Introduction

Power-law distributions as a statistical construct can be broadly characterised by linearity on a log-log scale plot. They furnish the most general description of the scale invariance of self-affine geometries [2–5] and avalanche statistics—considering the size of discrete, jerky events against their frequency of occurring under the influence of some external stimulus [6–12]—across a wide range of natural phenomena. The energy released from depinning events in disordered materials [13], such as ferroelectric [14–16], ferromagnetic [17–19], or ferroelastic [20] domain wall motion matches power-law distributions for example, as do plasticity, deformation, and fracture mechanics in materials as varied as single crystals [21] and bulk metallic glasses [22]. Beyond the realms of solid-state physics, similar statistical trends under their own scales of event-magnitude and time-span are also expressed in earthquake intensity [23] and wildfire spread [24].

In fact, the universality of these power-law distributions across multiple physically distinct systems confers unique advantages in analysis. The same computational algorithms can be used to investigate similar behaviors across disparate fields, and advances in one field can be extended to solve problems in another. The continued development and optimisation of more extensive statistical tools that can accurately and easily extract scaling parameters from raw datasets is thus of immense and broad practical use.

One avenue where power-law correlations are perhaps unexplored is for the analysis of sequential 2-dimensional image datasets. Measurements of power-law distributions typically involve the acquisition of single events over some period of time, with no spatial correlation; in solid-state physics, for example, standard “Barkhausen noise” experiments typically involve the measurement of sudden jumps of a material’s magnetisation that result from controlled, gradual changes in external magnetic fields. In contrast, a 2-dimensional image is inherently a spatial map—but with no temporal information. Indeed, power-law distributions of spatial correlations in a single image dataset are widely used to analyse diverse phenomena such as the

morphology [25] or proliferation [26, 27] of mammalian cell fronts in biological systems, or the self-affine roughness of domain walls in ferroic materials [28]. Observing a sequence of several 2-dimensional image datasets should thus provide physics-relevant information about both the time evolution and spatial correlations of some phenomenon, even if the number of images is fewer than the orders of magnitude of datapoints required for a power-law fit of event sizes.

In practical terms, one materials characterisation technique for which extracting power laws from such sequential, spatially-correlated data is particularly important is scanning probe microscopy (SPM). At its most basic, SPM can be used to sequentially image the topography of a sample surface at atomic scales. Moreover, appropriate choice of probe functionalisation and input signals render SPM measurements sensitive to diverse physical phenomena including electrostatic, magnetic, and chemical interactions, as well as local variations in conductivity, friction, mechanical stiffness, piezoelectric response, and many more [29]. This allows investigation of particular physical events localised around features of interest, and the evolution of such phenomena via sequential imaging across a dizzying range of material properties, with extremely precise spatial resolution.

The presence and investigation of power laws from sequential 2-dimensional image datasets are of course not unique to materials characterisation and SPM. Optical phase microscopy can be used to intermittently ascertain biological cell position [27], for example, while satellite images can periodically acquire information about wildfire spread [24]. Like SPM, these imaging techniques can possess extensive spatial information, but minimal temporal information.

Analysis of power-law dynamics from these sequential 2-dimensional image datasets requires a different approach than the analysis of an event spectrum or a single image dataset. There thus remains a significant lacuna in the literature for tools that can convert an image-based dataset into event sizes for subsequent analysis of power-law behavior. We here attempt to resolve this gap. In this Chapter, we first describe the artificial generation of well-characterised sequential, 2-dimensional datasets to serve as test models. We then present and discuss three distinct techniques for the analysis of such sequential data, based on: (i) the rectangular boxing of datasets; (ii) random boxing of datasets; and (iii) the tracking of interfaces. We then establish the suitability of interface tracking to differentiate whether a 2-dimensional sequential dataset indeed follows a power-law distribution, and use this to establish this interface-tracking approach as optimal.



## 5. Identifying and Analysing Power-Law Scaling in 2-Dimensional Image Datasets

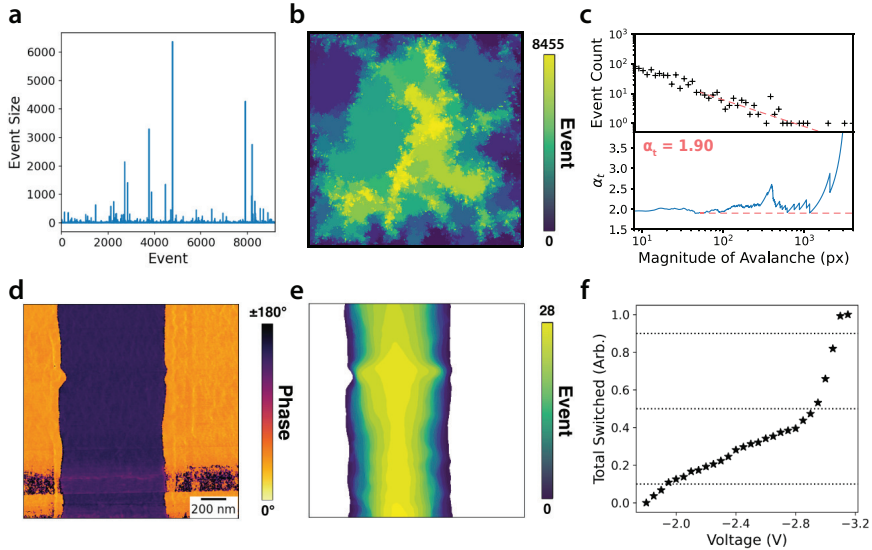


**Figure 5.1:** *Switching dynamics in simulated and experimental data.* (a) A raw power-law spectrum generated from a scaling parameter of  $\alpha = 2.0$ . (b) A map of the sequential 2-dimensional power-law data, generated from (a), showing when each pixel was switched, i.e. traversed by the interface between states 0 and 1. (c) A MLE plot (upper) and log-log plot (lower) to define the scaling parameters. (d) A representative PFM scan of a PTO ferroelectric film showing domains and domain walls. (e) The switching event map of when the polarisation in each pixel of the central domain was reversed. (f) The corresponding evolution of the polarisation, calculated as the ratio of the total area switched as a function of the applied tip bias.

## 5.2 Sequential 2-Dimensional Datasets

### 5.2.1 Generation of Sequential 2-Dimensional Datasets

Power-law distributions of the form  $p(x) \propto x^{-\alpha}$ , where  $\alpha$  is the *scaling parameter*, can be most simply generated from the equation:

$$x = x_{min}(1 - X)^{\frac{1}{1-\alpha}} \quad (5.1)$$

where  $0 \leq X < 1$  is randomly sampled from a uniform distribution, and  $x_{min}$  is some minimum value, as detailed in Section 2.5. A typical crackling noise or power-law spectrum generated by events from Eq. 2.8, where  $x_{min} = 1$  and  $\alpha = 2$ , is shown in Fig. 5.1(a) ( $\alpha$  here is arbitrary, but chosen to be comparable to later experimental data). Such power-law spectra can be used to construct 2-dimensional sequential image datasets like those in Fig. 5.1(b).

Specifically, we first generate an empty array corresponding to the image size. Every point inside this array is considered to be in an initial state 0, and

we consider this array to be bounded by a different state 1. To generate the subsequent image, we begin by randomly selecting a point of state 0 which borders a point of state 1 (this necessarily selects for points on the array boundary in the first iteration, but all subsequent arrays will have points in both states 0 and 1 [Fig. 5.2(a)]), and switch the selected point to state 1 [Fig. 5.2(b–c)]. Then, depending on the number generated from the power-law spectrum, we select and switch adjacent points from state 0 to state 1 on a one-by-one basis as follows: if the power-law spectrum generates a value of 1, then no more points are switched; if a larger value  $X$  is generated, then up to  $X - 1$  additional points are switched. [Fig. 5.2(d–e, g–h)]. We allow the following exceptions: 1) if any single point of state 0 is fully enclosed by neighbors of state 1 during this process, it is automatically chosen to be switched as well [Fig. 5.2(f)] to better resemble experimental data and minimise calculation time, and; 2) if no other adjacent points of state 0 are present for switching during this iteration, the process is considered complete, even if  $X - 1$  additional points could not be switched. Otherwise, once all  $X$  points are switched (including the initial switching point), thus randomly creating an event whose size follows the target distribution determined by the power-law spectrum, the new array is finalised, stored, and added to the image sequence. This most recent array also becomes the starting point for the generation of the subsequent image, with a new seed point randomly selected from all points of state 0 now bordering a point of state 1.

We repeat this process until all points in the image are in state 1. The amount of steps is random, but depends on the size of the array and the power-law attributes. For an array of size  $256 \text{ px} \times 256 \text{ px}$ , 1000–10000 events would be expected for  $x_{min} = 1$ ,  $\alpha = 2$ . To show all 1000–10000 sequential images concurrently, we mark the event number (ie., image number) during which a given point switched, and show these ‘event numbers’ in Fig. 5.1(b).

Note that the distribution of event sizes in Fig. 5.1(b) is not precisely drawn as a power law for three reasons. First, all values for event sizes must be integers; partial pixel switches were not considered. This ensures both a minimum value for  $x_{min}$  at 1, and also increases the variation from a true power law for lower event sizes. This leads to an effective increase of the lower cutoff. Secondly, as a switching step terminates if there are no points of state 0 adjacent to the recently switched points of state 1, the sizes of events are given an upper bound, with an absolute upper bound equal to the size of the final array (compared to the otherwise unbound ‘true’ power law).

This preference for smaller events may lead to an effective increase in scaling parameters. Indeed, this absolute upper bound inherently reduces the validity of power-law distributions from datasets when the true scaling parameter  $\alpha \gtrsim 1$  (even without directly plotting onto a 2-dimensional dataset). For example, in cases where the scaling parameter is less than

## 5. Identifying and Analysing Power-Law Scaling in 2-Dimensional Image Datasets

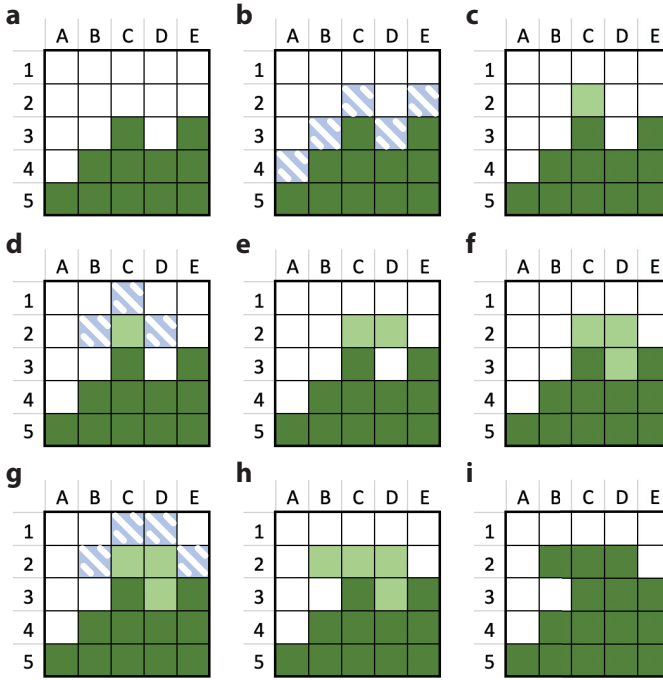


**Figure 5.2:** *Generation of sequential 2-dimensional dataset. (a) One array in sequence, with regions of state 0 (solid white) and regions of state 1 (solid dark green). (b) Points at state 0 which can be randomly chosen to shift to state 1 (dashed light blue). (c) The array after the point C2 is switched to state 1 (points switched in this iteration step are solid light green). (d) Points of state 0 which can be randomly selected to switch to state 1 in the same iteration step, depending on the corresponding value in the power-law spectrum. (e) The array after point D2 shifts to state 1. (f) The array after point D3 is forced to shift to state 1, since D3 is a single point completely enclosed by regions of state 1. (g) Points of state 0 which can be randomly selected to switch to state 1 in the same iteration step, after D2 and D3 have already switched state. (h) The array after point B2 switches to state 1. (i) The array corresponding to the final image that could appear in sequence after that shown in (a), if a value of 4 was determined from the power-law spectrum, and the process proceeded as described through (b-h).*

about 1.47, a double-digit number of events are expected for the sum of all events to be equal to  $256 \times 256$ , and any trend across multiple orders of magnitude would not be observed (Fig. 5.3). This suggests that datasets with a summed size of  $256 \times 256$  cannot reliably be used to show or identify a power-law distribution with a scaling parameter less than 1.47.

Despite these changes, the distribution of event sizes in Fig. 5.1(b) still follows a power law, with a scaling parameter comparable to that of the spectrum from which it was drawn. In Fig. 5.1(c), a log-log plot of the

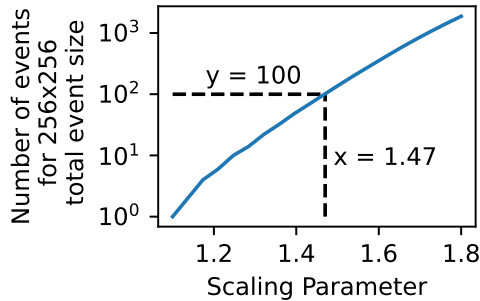


**Figure 5.3:** Number of events needed to combine into a total event size of  $256 \times 256 = 65536$ . Power-law distributions were generated with  $x_{min} = 1$  and  $\alpha$  ranging from 1.1 to 1.8. The number of events needed for the sum of all event sizes to be at least 65536 were determined. This process was repeated 10000 times. The median number of events were then determined and are here shown.

magnitude of the switching events in Fig. 5.1(b) alongside their frequency can be seen, showing a linear relationship expected of power-law distributions. This is supported by a plot of the maximum-likelihood estimation (MLE; see Section 2.5 and Ref. [9]) of the power-law fit. A scaling parameter of  $\alpha = 1.90$  is found by minimisation of the Kolmogorov-Smirnov statistic, which both matches a visible plateau in the plot of the MLE, and is also comparable to the scaling parameter used to generate the power-law distribution.

In this synthetic case, with sufficient spatial resolution ( $256 \text{ px} \times 256 \text{ px}$ ) and temporal resolution (over 1000 events) the power-law characteristics can be trivially extracted. Purely temporally, this synthetic dataset also matches what one would expect from Barkhausen noise or other power-law distributions: note the high frequency of small switching events alongside the much rarer large switching events.

### 5.2.2 Comparison with Experimental Sequential 2-Dimensional Image Datasets

In experimental measurements such a direct approach to event size determination is severely disadvantaged by limits on data resolution and acquisition time. As an example, we consider measurements within the broad suite of SPM techniques allowing multifunctional characterisation of diverse physical phenomena. Among these, piezoresponse force microscopy (PFM) tracks the phase and amplitude of a localised piezoelectric response to an applied ac voltage, thus allowing ferroelectric domains and the domain walls between them to be imaged [30]. While PFM can generate images with nanometer-scale resolution, if these images are to be of a reasonable size (ie. microns), a

## 5. Identifying and Analysing Power-Law Scaling in 2-Dimensional Image Datasets

---

single image acquisition typically takes approximately 10–20 mins. For power-law analysis requiring large datasets with event sizes ranging across several orders of magnitude, taking 10–20 mins to measure a single event would be prohibitively slow, and the assignment of power-law distributions becomes less viable. These difficulties can be exacerbated by pixel-to-pixel crosstalk, where limitations due to size effects like tip size can cause observations in one pixel to be attributed to adjacent pixels.

These problems are emphasised in Fig. 5.1(d–f). In Fig. 5.1(d) a PFM image of a thin film of lead titanate ( $\text{PbTiO}_3$ —henceforth PTO) is presented, showing patterned ferroelectric stripe domains with opposite polarisation orientation, separated by domain walls. A gradual polarisation reversal in the central stripe (from its initial orientation [*dark*] to that of its surrounding [*bright*]) was implemented and tracked by interleaving switching scans with a defined and incrementally increasing tip bias and imaging PFM scans. The resulting switching events, corresponding to the inward motion of the ferroelectric domain walls at each of the 28 imaging steps are shown in Fig. 5.1(e), and the corresponding evolution of the total switched area as a function of voltage is shown in Fig. 5.1(f). In analogy with the synthetic example, a log-log plot of the distribution of the switching events would ideally be used to extract power-law behavior. However, the paucity of such events (28 datapoints) precludes any reasonable log-log plot or power-law distribution considering switching from one image to another as single event from being designated as a valid description of the data.

From a physical perspective, understanding the underlying physical processes can introduce additional constraints on event size. For example, two distinct domain walls are observed in Fig. 5.1(e). More generally, if they are independent, the motion of one ferroelectric domain should not be expected to have a direct causal link with the motion of a separate and distinct domain wall some microns away, even if they were to occur in the same imaging step. The associated domain wall motion should thus, equally clearly, be identified as (at least) two distinct events in some supposed power-law distribution, not only for the ensuing increase in statistics it provides, but to reflect the underlying physical reality—the separation of such events as distinct is necessary to extract the correct values of the power-law parameters, which could otherwise be under-estimated.

On the other hand, inflating event statistics by artificial constraints on event size can lead to both an over-estimate of the key power-law parameters as a result of over-representation of low-size events, and potentially introduce spurious spatial (de)correlations between them, if they were initially part of one larger event.

In practice, most transitional cases are more ambiguous. If two moving segments of the same ferroelectric domain wall are separated by some large distance, could we still consider the events as distinct? If so, how large would

this separation need to be in 2-dimensional space, and how large would each event need to be for it to be considered statistically valid? Indeed, more fundamentally, how can these localised 2-dimensional images even be accurately converted into 1-dimensional event sizes?

We thus present three techniques to extract event sizes from experimental and synthetic data: in order, we box our datasets, either with rectangular or with random shapes, and then we alternatively track and follow the interfaces between states. Once these event sizes are gathered, we can determine the scaling parameter via MLE (Section 2.5). These approaches are benchmarked on synthetic datasets that have a pre-established, known scaling parameter as a ‘ground truth’, and a comparison made to scaling parameters as ‘measured’ by these distinct techniques. To better reproduce the limitations of spatial and temporal resolution in real experiments, we apply a 1 px Gaussian blur (to replicate crosstalk between adjacent pixels), and then threshold the result so that only 50 discrete motion events were measured (to simulate how a finite-time image acquisition may artificially connect temporally independent events).

## 5.3 Power-Law Extraction Through Different Boxing and Tracking Techniques

### 5.3.1 Rectangular Boxing

An attempt to utilise the distance between regions of the 2-dimensional image to separate out events has previously been discussed by Tückmantel *et al.* in Ref. [31]. Since the experimental datasets utilized in this study were generated by a local application of voltage using a biased SPM tip, then imaged via PFM, the authors convincingly argue that the dwell time of the scanning probe over any individual point on the image during switching justifies a separation into distinct, non-interacting regions. The event sizes of the overall experiment is then considered to be the size of the events contained within each of the regions.

Statistically, the primary advantage of this ‘boxing’ approach is the increase of the number of events, which, however, necessarily results in a decrease of the size of the measured events themselves. An array of size 256 px  $\times$  256 px already cannot have a single event of size greater than 655356 px (ie.  $256 \times 256$ ), and smaller regions are similarly bound; if boxes as small as 2 px  $\times$  10 px are used, a maximum pixel size of 20 px is possible. Such a small difference between maximum and minimum event size would prevent a valid attribution to a power-law distribution. Even less severe reductions still preclude the measurement of data points at upper ranges, which in a generic dataset could correspondingly decrease the validity and

## 5. Identifying and Analysing Power-Law Scaling in 2-Dimensional Image Datasets

---

range of the resulting power-law fit.

To mitigate this risk in the particular case of Ref. [31], the authors box their datasets into rectangular regions with a high aspect ratio, with the elongated edge of the rectangle roughly parallel with the motion of the ferroelectric domain walls. This anisotropy allows the magnitude of particularly large switching events and corresponding domain wall motion to be captured in its entirety. A less extended boxing length in this direction could more significantly limit the identification of large switching events, further restricting both the upper bound of the collected data and the accuracy of the power-law fit. On the other hand, there is a greater freedom to choose the extent of the boxing width along the direction of the domain walls themselves—as long as these allow a physically meaningful decorrelation between events occurring far enough from each other. If the orientation and direction of motion of the domain walls in the image is known, such anisotropic boxing therefore maximises the number of independent events while minimizing artificial restrictions on the maximum event size.

This rectangular boxing technique applied to a synthetic dataset is shown in Fig. 5.4(a). Overlaid onto this image are rectangular boxes 15 px in height, corresponding to a representative choice of rectangular area selection. Events within different boxes were considered distinct. Measuring their total area allowed us to extract their statistics, as shown in the log-log and MLE plots in Fig. 5.4(b). We observe a clear power-law relationship, although with a measured scaling parameter value of 2.41, substantially higher than the target value of 2.0.

To test the validity and reliability of this rectangular boxing process in general, we generated a set of sequential 2-dimensional datasets with varying scaling parameters. 130 datasets were generated as described for Fig. 5.1(b), but with the scaling parameter used to generate the dataset varying from 1.4 to 2.6. The ‘true’ scaling parameter of each of these datasets were then determined by MLE on the events of the dataset prior to blurring and thresholding. Only datasets with a scaling parameter  $1.5 < \alpha_t < 3.1$  were used for further analysis, yielding 123 datasets of the original 130.

The ‘true’ scaling parameters were plotted against the scaling parameter ‘measured’ by boxing after blurring and thresholding, as shown in Fig. 5.4(c). Here, a strong linear correlation between the true and measured scaling parameters is visible, but the precise numerical value of the true and measured scaling parameters are not necessarily the same. Rather, the measured scaling parameter via 15 px rectangular boxes,  $\alpha_{m,rect,15} = 2.6\alpha_t - 2.6$ .

The residual mean standard error (RMSE) of this linear fit is 0.71. This RMSE, encompassing 123 applications of the rectangular boxing technique, should carry over all errors implicit in the estimation of the scaling parameters, such as those inherent to MLE. As such, we can conclude that the error of the scaling parameter estimated via this boxing, including the errors

### 5.3 Power-Law Extraction Through Different Boxing and Tracking Techniques

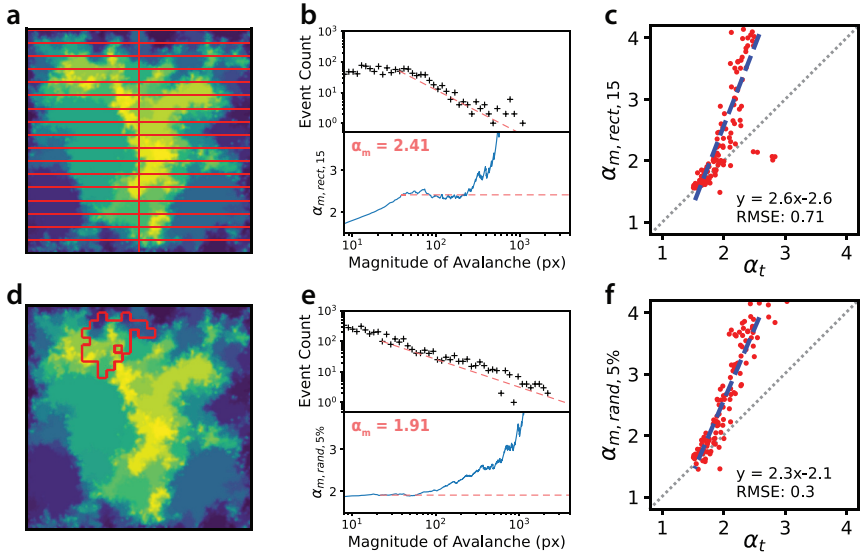


**Figure 5.4:** Extracting power-law trends via boxing on blurred synthesised datasets. (a) Blurred synthesised dataset, with all rectangular boxes of 15 px width outlined. (b) MLE and log-log plots corresponding to the boxes shown in (a). (c) Comparison of scaling parameters measured via rectangular boxing with a 15 px width on blurred synthesised datasets, to true scaling parameters used to generate the dataset. (d) One representative random box encompassing 5% of the image area. (e) MLE and log-log plots corresponding to 200 such boxes. (f) Comparison of scaling parameters measured from 200 random boxes each of 5% total area on blurred synthesised datasets to true scaling parameters.

from MLE, is the RMSE of 0.71. If the measured scaling parameter were considered to be equal to the true scaling parameter (that is,  $\alpha_{m, rect, 15} = \alpha_t$ ), then the RMSE is greater, at 1.12.

The impact of changing box widths is shown in Fig. 5.5(a-c), where the relationship between true and measured scaling parameters appears similar among different box widths, although with varying RMSEs.

The RMSEs themselves are particularly high, and, on the face of it, this technique does not appear to be suitable for interface motion without known anisotropy. Critically, however, the work by Tückmantel *et al.* does assume the interface moves in a preferred direction, and such a preferred direction is not necessarily present in this randomly switched dataset. We can instead create this directional motion in the synthetic dataset by altering the initial conditions of the array, however. Rather than interpret the entire array to be surrounded by points of state 1, we can set only two opposite edges of the array to state 1; this encourages a bidirectional inward motion of the interface.



## 5. Identifying and Analysing Power-Law Scaling in 2-Dimensional Image Datasets

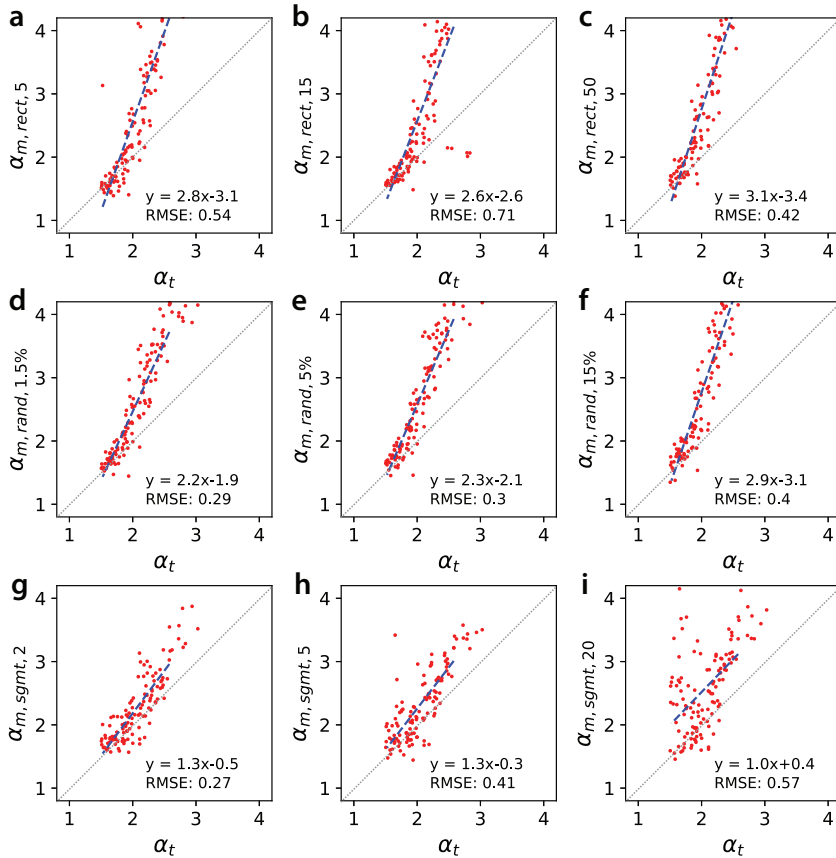


**Figure 5.5:** Benchmarking scaling parameter measurements with different techniques via MLE. (a-c) Rectangular boxing. (d-f) Random boxing. (g-i) Interface interpolation and tracking. Dotted gray line denotes where  $\alpha_m = \alpha_t$ .

A marked difference is visible in the case of these directional datasets. Here, 62 sequential datasets were utilised, with the same constraints as the non-directional data. When the elongated edge of the rectangle was parallel with interface motion, the gradient of the trend decreased ( $\alpha_{m, rect, 15, \parallel} = 2.2\alpha_t - 2.1$ ) and had its error approximately halved (RMSE: 0.34) [Fig. 5.6(a-c)]. On the other hand, when the elongated edge of the rectangle was perpendicular to interface motion, the gradient of the trend increased ( $\alpha_{m, rect, 15, \perp} = 3.5\alpha_t - 4.3$ ) and the error was comparable to the non-directional case (RMSE: 0.68) [Fig. 5.6(d-f)]. If these measured scaling parameters are considered 1-to-1 with the true scaling parameters, the RMSEs are greater but follow a similar trend, with parallel interface motion once

### 5.3 Power-Law Extraction Through Different Boxing and Tracking Techniques

again having almost half the RMSE of the non-directional case (at 0.66), while perpendicular interface motion once again had a similar RMSE to it (at 1.31). These differences were less prominent when boxes were decreased in width (where this decreased size prevents the preferred direction from being captured) and increased in width (where this increased size makes the preferred direction itself less prominent).

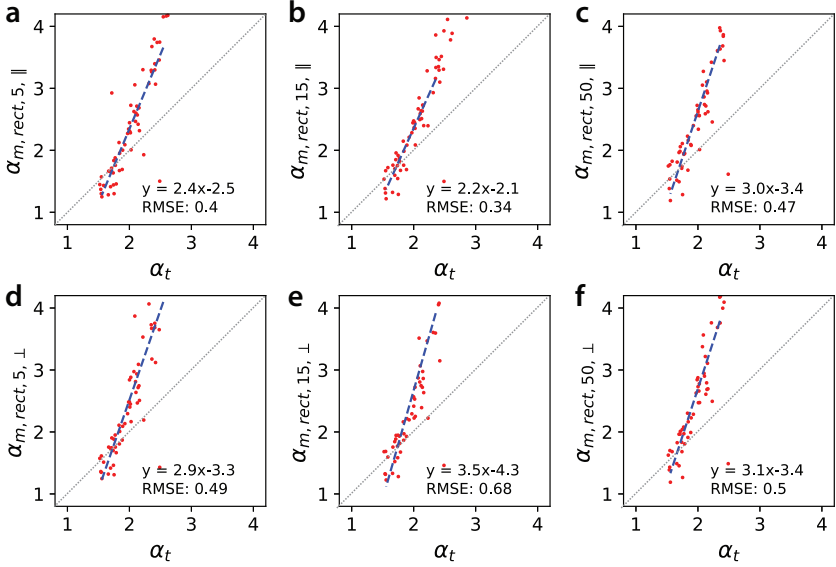


**Figure 5.6:** Benchmarking scaling parameter measurements from rectangular boxing. The long edge of the box is aligned (a-c) parallel, or (d-f) perpendicular to the primary axis of interface motion. Dotted gray line denotes where  $\alpha_m = \alpha_t$ .

Thus, while the ratio between the true and measured scaling parameters is not directly one-to-one, this approach does seem able to directly probe the power-law scaling itself in cases where a preferential direction is both present and known. While the rectangular boxing technique therefore shows moderate success in capturing power-law behavior, its key disadvantage is this necessity for directional correlations. This can introduce error based on choice of box orientation, as illustrated when the approach is applied to the experimental dataset in Fig. 5.7. If boxes are aligned with the ferroelectric domain wall motion [Fig. 5.7(a)], the acquired statistics, log-log plots, and ensuing scaling parameters remain consistent among all box widths  $\geq 10$  px [Fig. 5.7(b)], with a large proportion of the area used in calculating the MLE. This is not true if the boxes are transposed [Fig. 5.7(c)]. In this case, the domain walls stretch parallel to the length of the box. Thus, even if a domain wall segment moves only a short distance, a large switched area is

## 5. Identifying and Analysing Power-Law Scaling in 2-Dimensional Image Datasets

still measured within the observed box as a single event. The ensuing scaling parameters can be seen in Fig. 5.7(d), which significantly change in value as box widths decrease. The choice of boxing anisotropy therefore adds a potentially unwelcome bias to this approach and complicates the selection of the area of interest in a generic dataset where events can occur along different orientations.

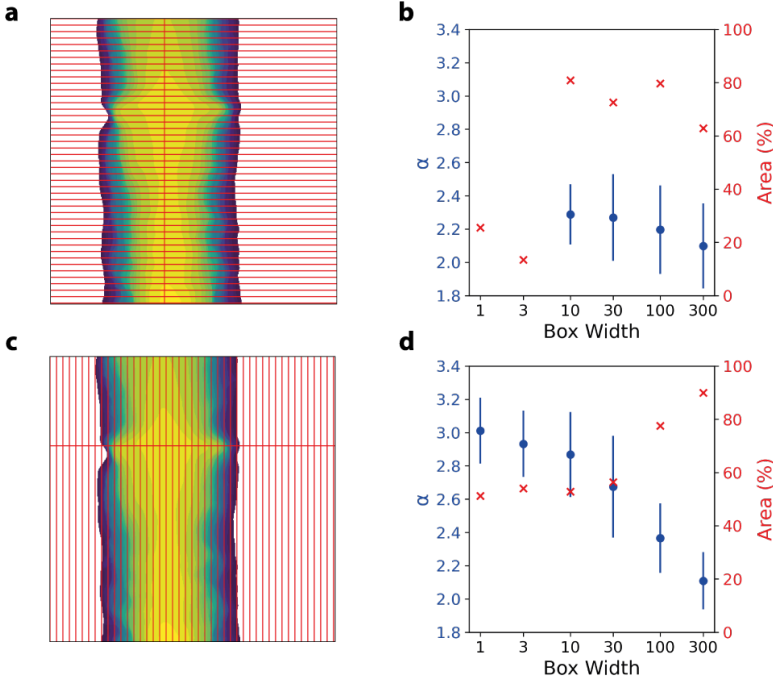


**Figure 5.7:** Comparison of rectangular boxing directions. (a) 15 px wide boxes oriented horizontally. (b) Scaling parameter [blue circles, left axis], and the percentage of the area used by the MLE to calculate that scaling parameter [red crosses, right axis], compared to box width. (c–d) As (a–b), but with transposed boxes.

### 5.3.2 Random Boxing

For cases without a preferential direction, we thus propose the replacement of rectangular boxes with wholly random, contiguous shapes of a known and constant area. In this approach, a random pixel is selected on the area of interest as the seed of a ‘shape’. One of its nearest neighbors is then randomly selected to be added to increase the size of the ‘shape’. This growth is then repeated, recursively adding one external pixel at a time until the generated shape has a total area that overlaps to a desired extent with the

### 5.3 Power-Law Extraction Through Different Boxing and Tracking Techniques

area of interest on the initial dataset [Fig. 5.4(d)]. This process is continually repeated to generate new shapes. Within each of these shapes, the total sizes of events are considered, and the concatenation of these events within the random shapes is considered to be the sequence of events in the overall experiment. To increase the speed of this process, the generation of the random box is performed on a grid with lower resolution than the original dataset; once generated, these boxes are expanded over the original dataset.

We note here that these randomly generated shapes allow for the possibility of overlap with one another, and thus particular pixels on the original dataset may be repeatedly considered. This is preferable to the alternative; if pixels are excluded from repeated selection, then any subsequent shapes may have their sizes constrained. The inclusion of these constrained shapes would arbitrarily reduce the maximum event size possible, while the exclusion of these constrained shapes would decrease and omit otherwise relevant data.

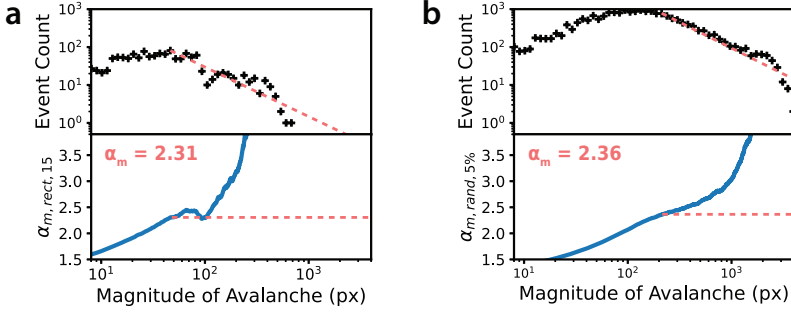


**Figure 5.8:** *MLE and log-log plots of scaling parameters on experimental data (a) Scaling parameters measured via rectangular boxing. (b) Scaling parameters measured via random boxing.*

A representative log-log plot and MLE of this dataset is shown in Fig. 5.4(e). Here, 100 boxes are generated, with each box composing 5% of the total area in size. The measured scaling parameter of 1.91 is closer to the target scaling parameter of 2.0, suggesting the improved validity of this technique. The larger amount of events analysed in this sequence also allows a smoother plot than in previous methods.

This random boxing approach is again benchmarked against the same 123 datasets used to validate the rectangular boxing. Different box sizes are again used and a comparison of the true and measured scaling parameters is shown in Fig. 5.5(d–f), with the best parameters replicated in Fig. 5.4(f). With this 5% box size, the measured scaling parameter  $\alpha_{m,rand,5\%} = 2.3\alpha_t - 2.1$  with an RMSE of 0.30. It is notable that this RMSE is significantly lower than the RMSE of the rectangular boxes used in the non-directional case; in fact, both the trend itself and the RMSE is very similar to the 15 px rectangular boxes

## 5. Identifying and Analysing Power-Law Scaling in 2-Dimensional Image Datasets

---

used on appropriately rectangular data [Fig. 5.6(b)]. The trend between measured and scaling parameter, and the RMSE, is also consistent with differing event sizes [Fig. 5.5(d–f)]. This benchmarking suggests that random boxing is generally superior than rectangular boxing; with random boxing appearing similar to rectangular boxing with appropriately-sized rectangular boxes aligned with interface motion, but with behavior more consistent for non-directional motion and with different box sizes. This trend follows if the measured scaling parameter is considered to be the true scaling parameter, in which case the RMSE of the measurement is 0.86.

The equivalence of random boxing to rectangular boxing also carries over to experimental data (Fig. 5.8). Both rectangular boxing parallel to domain wall motion [Fig. 5.8(a)], and random boxing [Fig. 5.8(b)] show a linear trend in the log-log event size distribution plot. Both techniques also extract similar scaling parameters by MLE (2.31 and 2.36 respectively), but random boxing appears to generate a more consistent plateau and linear trend than rectangular boxing.

While random boxing avoids the assumption of a preferred direction, one potential error with this methodology lies in the necessarily repeated consideration of some pixels. This repetition tends not to be consistent (Fig. 5.9) as pixels near—but not on—the extrema are preferentially selected. This results in a bias related to the positioning of features, as events that occur earlier or later in the experiment may therefore be considered with higher or lower frequency. This could be particularly problematic if, for example, temperature or another external condition is changed over the course of the experiment; the earlier experimental conditions may be preferentially sampled and therefore alter the final result.

### 5.3.3 Interface Tracking

To avoid both these positional and directional biases completely, a final proposed technique involves the repeated calculation of the interface direction at each point. Between any two successive images, an interface would either have to nucleate, move, or collapse, traversing over some region that could then be appropriately considered an ‘event’. Tracking the motion of segments of an interface between each successive image could therefore be used to generate data to which a power-law could be fit.

To track the interface motion, interpolation is first performed between each image via iterative and morphological calculation of the medial contour, as described in [32]. In brief, starting from the initial dataset [Fig. 5.10(a)], the interfaces between two successive images are considered [Fig. 5.10(b)]. The lower interface is repeatedly morphologically dilated, and the upper interface repeatedly morphologically eroded, until they meet at some medial contour line [Fig. 5.10(c)]. This medial line is used, along with one of the

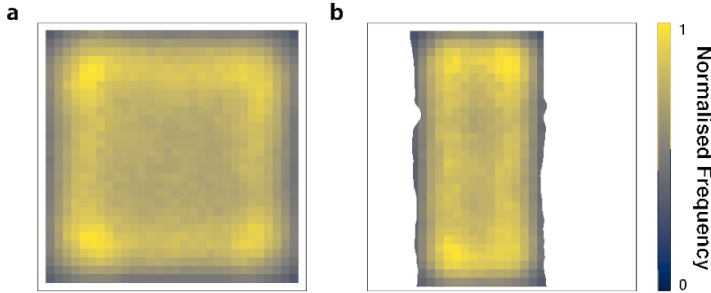


**Figure 5.9:** *Frequency of pixel selection via random boxing.* (a) Applied to the synthetic dataset. (b) Applied to the experimental dataset. Note the lower frequency at the borders of the data, a middling frequency at the centre, and the highest frequency near the corners of the shapes.

initial interfaces, to generate a new medial line; this new line can be used to generate another line, and so on, until every pixel between the initial and final interfaces is assigned its own intermediary value [Fig. 5.10(d)]. From this interpolation, the localised gradient can be calculated. The ‘path’ taken by each point along the interface from one image to another can then be determined by following the direction of the maximal gradient. Such paths can be determined for every point on every interface.

The initial interface can therefore be split into smaller segments [Fig. 5.10(e)]. Each point of these segments can be made to follow the gradient of the interpolation; the area subtended by the interface segment as it moves from the initial position to the final position can therefore be considered to be an event [Fig. 5.10(f)]. This process can be repeated for each successive pair of images.

This process, as applied to an entire synthetic dataset, is shown in Fig 5.11. From the initial dataset [Fig. 5.11(a)], events are generated from segments of width 2 px [Fig. 5.11(b)]. A clear spread in event size and frequency can be observed in this dataset. The sizes of each of these areas can be fit to a power-law distribution, as summarized in Fig. 5.11(c). A particularly clear plateau can be observed here, with its height, again found by minimisation of the Kolmogorov-Smirnov statistic, corresponding to the red line and a scaling parameter of 2.16—this is particularly close to the target scaling parameter of 2.0.

This technique was again benchmarked against the series of synthetic datasets, as shown via the red dots and corresponding blue trendline in Fig. 5.11(d), and the effect of selecting different interface segment lengths is shown in Fig. 5.5(g-i). Compared to the values extracted using the two

## 5. Identifying and Analysing Power-Law Scaling in 2-Dimensional Image Datasets

---

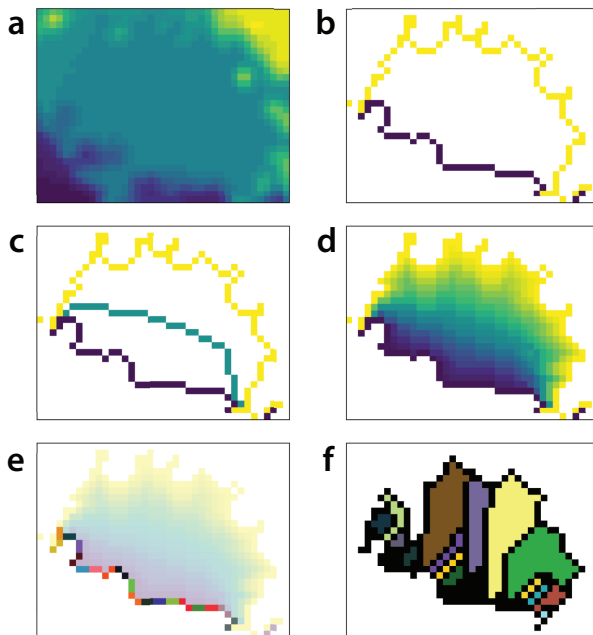


**Figure 5.10:** *An illustration of the methods used to track interfaces* (a) A section of a blurred synthetic dataset. (b) Two particular interfaces isolated from the synthetic dataset. (c) The medial contour line, extracted by recursive erosion-dilation. (d) The interpolation between the two initial interfaces, gathered by repetitive calculation of medial contour lines. (e) Segmentation of the first interface into 2 px units. (f) Events gathered between the two initial interfaces, made from the segments shown in (e) following the gradient of the interpolation shown in (d).

boxing methods, this approach gives the smallest difference between true and measured scaling parameters, with the measured scaling parameter from a 2 px segment ( $\alpha_{m,sgmt,2} = 1.3\alpha_t - 0.5$ ) yielding the lowest RMSE of 0.27. In fact, if the measured scaling parameter is assumed to be the true scaling parameter, the RMSE of this trend is 0.36; comparable to the fitted RMSEs of both boxing techniques under appropriate conditions. With the synthetic data, this interface-tracking method therefore appears to yield the most accurate measurement of the scaling parameter.

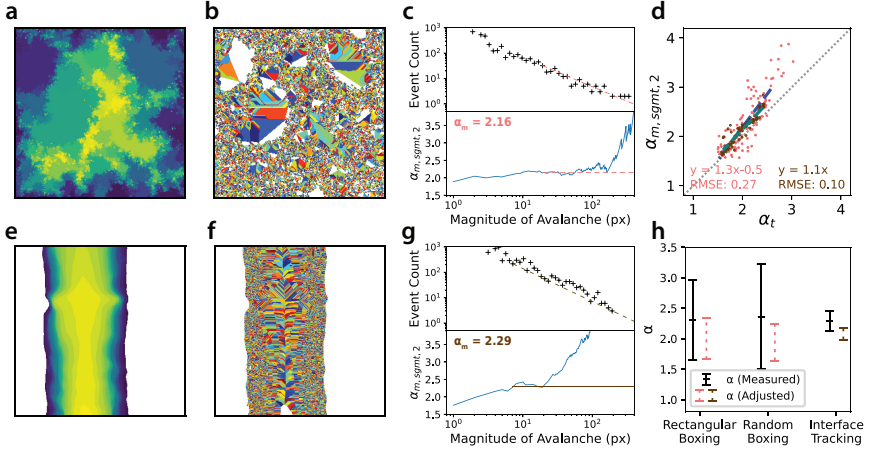


**Figure 5.11:** *Interface tracking on experimental and synthetic data.* (a) The blurred synthetic dataset, with interface motion interpolated. (b) Areas traversed by interface segments 2 px in width. Each of these are considered distinct events. (c) MLE and log-log plots of these distinct events. (d) Benchmarking the 2 px interface-segment tracking technique by comparing true and measured scaling parameters. (e–g) As (a–c), but with a PFM dataset. (h) Measured scaling parameters of the PFM dataset, as well as scaling parameters adjusted from these measured datasets by using the linear correlations extracting from benchmarking. For (c,d,h,i), red colour refers to parameters found by minimisation of the Kolmogorov-Smirnov statistic; gold colour refers to parameters found through double-bootstrapping consistent estimators.

## 5.4 Improving Power-Law Extraction via Multiple Consistent Estimators

### 5.4.1 Differentiation of Power-Law Distributions from Non-Power-Law Distributions via Multiple Consistent Estimators

This chapter has thus far used MLE to find the scaling parameter  $\alpha$  along a range of values of  $x_{min}$ , and found the point with a minimum Kolmogorov-Smirnov statistic to identify the optimum value of  $x_{min}$ , and therefore  $\alpha$ . Other methods exist to find the precise value of  $\alpha$ , however, and bring their own unique advantages and disadvantages. The methods discussed by Voitalov *et al.* [6] in which multiple estimators are found by double-bootstrapping and compared, allow identification of whether a trend does or does not follow a power law. This would, in itself, be incredibly useful for any further analysis, and we therefore elect to compare the scaling parameters found via Kolmogorov-Smirnov statistic minimisation against those found via double-bootstrapping multiple consistent estimators.



## 5. Identifying and Analysing Power-Law Scaling in 2-Dimensional Image Datasets

---

In brief, Voitalov *et al.* calculates the first moment estimate (also known as the Hill estimate, and roughly equivalent to the MLE) by double-bootstrapping with the second moment, separately calculates the second moment estimate by double-bootstrapping with the third moment, and double-bootsraps two kernel estimators to create a third estimate of the scaling parameter [6]. If the scaling parameter of the dataset is calculable and similar among these multiple estimators, a true power-law distribution is likely; if any of these estimators are fully unbounded, a power-law distribution is not present. If individual estimators are substantially different, a power-law distribution is less likely, but not necessarily impossible.

These estimators, as applied to a synthetic power-law dataset via the interface-tracking technique, are shown in Fig. 5.12(a–c), all ultimately yielding similar values, both to each other and to the ‘true’ scaling parameter, further validating this technique. However, a very different result emerges when they are tested on a synthetic non-power-law dataset. The latter, shown in Fig. 5.12(d–f), was generated from the normal distribution defined by  $p(x) = \frac{1}{\sqrt{2\pi\sigma^2}} e^{-\frac{(x-\mu)^2}{2\sigma^2}}$ . Here,  $\mu$  was set to 0 and only positive values considered to create a pseudo-‘tail probability’. A  $\sigma$  of 25 was chosen such that the expectation value for the event size is similar to those generated by the power-law distribution with a scaling parameter of 2.0 (determined numerically; the analytical expectation diverges). This event spectra was used to generate a 2-dimensional dataset through identical means to the 2-dimensional power-law datasets described previously. When the interface-tracking technique is applied to this non-power-law dataset, the scaling parameter values extracted via the different estimators diverge significantly. Voitalov *et al.* describes how, if any estimated scaling parameter  $\alpha > 5$ , then the distribution is not a clear power law [6]. Interface tracking, combined with the use of these multiple consistent estimators, therefore successfully identifies this dataset as a non-power-law distribution.

### 5.4.2 Power-Law Analysis of 2-Dimensional Sequential Datasets via Multiple Consistent Estimators

The capacity for this method of multiple consistent estimators to differentiate between power-law and non-power-law datasets can also be employed on the distributions intended to follow a power law. As previously discussed, a combination of a smaller maximum possible event size, and a lower scaling parameter, can prohibitively impact the quality of a power-law distribution; these lower-quality distributions would invariably decrease the value of any subsequent power-law fit.

We can therefore attempt to better characterise all previously discussed methods on the same datasets by supplanting the more common method

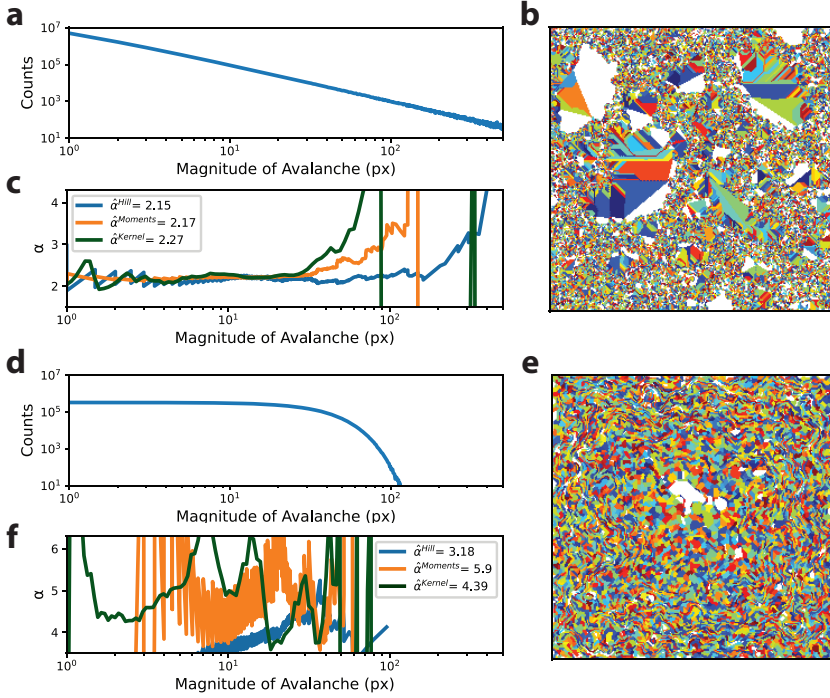


**Figure 5.12:** Comparison of the interface interpolation and tracking technique in synthetic datasets composed from (a–c) power-law and (d–f) normal distributions (a, d) Log-log plot of events used to generate a 2-d dataset. (b, e) Areas traversed by interfaces with 5-px length. (c, f) Hill, moments and kernel estimators of scaling parameters as a function of lower event-size cutoff.

of estimation on MLE via minimum Kolmogorov-Smirnov statistic, with an evaluation of the consistency of Hill (equivalent to MLE), second-order moment, and kernel estimators described by Voitalov *et al.*

These multiple consistent estimators can be applied at two points in the process. First, the establishment of the ‘true’ scaling parameter as generated onto the 2-dimensional array; and second, the measurement of the scaling parameter by either random boxing, rectangular boxing, or interface tracking. Here, if any of the three estimators do not converge, or if any of the three estimators greatly differ in value from one another, we consider the method of boxing (or tracking) non-viable.

In this case, we first exclude 10 of the original 130 sequential datasets from all further analysis, due to non-convergence of the kernel estimator (all datasets removed had an intended scaling parameter of  $1.4 < \alpha < 1.6$ , which is in agreement with Fig. 5.3 and earlier pruning of this dataset performed for the Kolmogorov-Smirnov based analyses). We then ran every estimator

## 5. Identifying and Analysing Power-Law Scaling in 2-Dimensional Image Datasets

on all three power-law analysis techniques, and, if consistent estimators were established, plotted and fit the measured Hill estimate against the scaling parameter of the plotted dataset (also extracted via Hill) in Fig. 5.13. The number of 2-dimensional arrays,  $n$ , with all consistent estimators similar and used for the fit are shown on the plot.

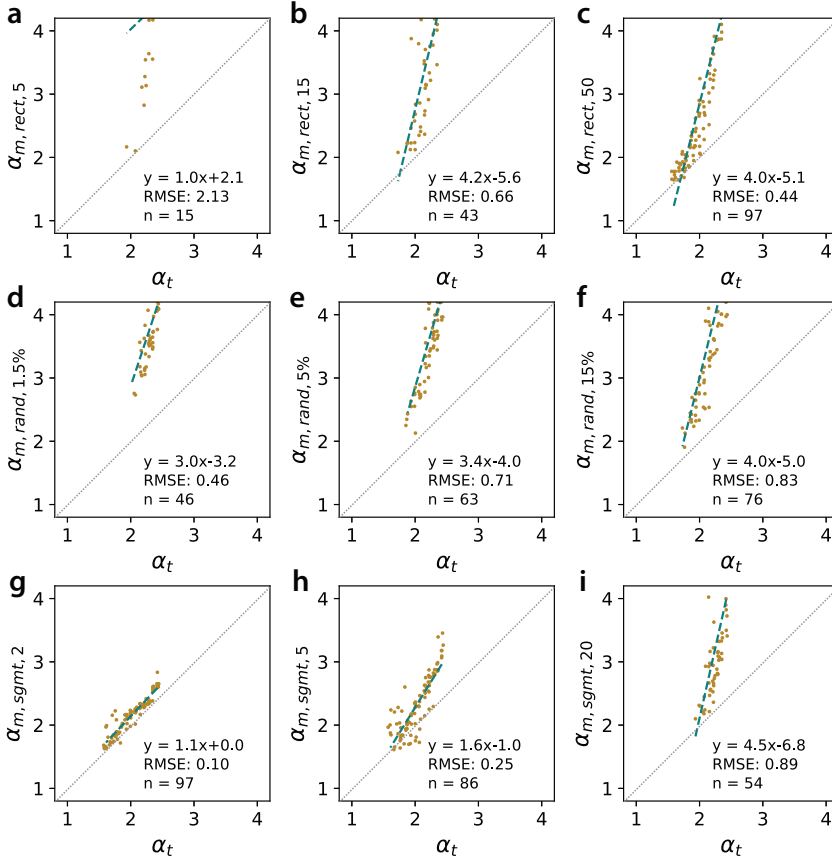


**Figure 5.13:** Benchmarking scaling parameter measurements with different techniques via multiple consistent estimators. (a-c) Rectangular boxing. (d-f) Random boxing. (g-i) Interface interpolation and tracking. The number of datapoints used in this fit are labeled as  $n$ . Dotted gray line denotes where  $\alpha_m = \alpha_t$ .

Here, rectangular boxing is once again shown to be unreliable [Fig. 5.13(a–c)], at least in cases of isotropic interface motion with small rectangular boxes, where estimators greatly diverged from one another. Random boxing showed reasonable reliability and consistency among all estimators, although greater RMSEs were observed in comparison to the scaling parameters gathered

via Kolmogorov-Smirnov statistics [Fig. 5.13(d–f)]. However, for both cases, particularly when the boxes themselves were smaller, the three estimators tended to diverge from each other in value [note the low values of  $n$  in Fig. 5.13(a–f)]. The use of Kolmogorov-Smirnov minimisation may therefore still be preferred for these boxing techniques.

The application of these multiple estimators is particularly promising when applied to interface tracking, however [Fig. 5.13(g–i)]. Here, the multiple consistent estimators generally agree with one another, particularly when tracking small, 2 px segments (successfully calculating a scaling parameter in 97 of the 120 remaining datasets). The RMSE also drops considerably; the scaling parameter via the tracking of 2 px segments yields the lowest RMSE of 0.10 [ $\alpha_{m,sgmt,2} = 1.1\alpha_t$  in the gold markers and corresponding trendline in Fig. 5.11(d)]. If the measured scaling parameter were considered to be equal to the true scaling parameter (that is,  $\alpha_{m,sgmt,2} = \alpha_t$ , then the RMSE is still a rather low 0.17, ensuring the measured scaling parameter is roughly equivalent to the true scaling parameter of the dataset.

This reduced RMSE, in combination with this method’s ability to differentiate between power-law and non-power-law distributions ensures it is preferable to use these multiple consistent estimators to find the scaling parameter from the interface tracking method.

### 5.4.3 Effect of Number of Image Datasets on Rectangular Boxing, Random boxing, and Interface Tracking Techniques

This Chapter has thus far consistently thresholded the original synthetic dataset to 50 bins to replicate an experimental method in which 50 finite-time image acquisitions are performed. We here investigate if 50 image acquisitions are sufficient or necessary, and if fewer or greater images are needed to reliably obtain a scaling parameter by all three discussed methods. To do this, we took the previously generated datasets that were intended to have a scaling parameter of 2, and thresholded the dataset (after blurring) to a number of bins ranging from 2 to 150. The scaling parameters were acquired by rectangular boxing, random boxing, and interface tracking as discussed previously.

The relative error in the scaling parameters measured,  $\alpha_m$ , against the true scaling parameter,  $\alpha_t$ , are plotted in Fig. 5.14(a). Both rectangular and random boxing have large errors that stabilise after approximately 20–30 images are gathered. Meanwhile, the interface tracking technique appears to consistently acquire accurate scaling parameters, independent of the number of images. While these extracted scaling parameters are similar to the target scaling parameter, however, the quality of the power-law fit decreases with fewer images [Fig. 5.14(b)]. When the scaling parameters

## 5. Identifying and Analysing Power-Law Scaling in 2-Dimensional Image Datasets

from the interface tracking technique are checked for power-law behavior between the three consistent estimators, it was found that 10-15 images are needed for power-law behavior to be reliable. This suggests one further advantage of the interface tracking technique; while rectangular and random boxing need 20-30 distinct images for reliable power-law extraction, interface tracking needs only 10-15. Nonetheless, after 30 distinct images are acquired, all techniques appear to stabilise and become reliable.

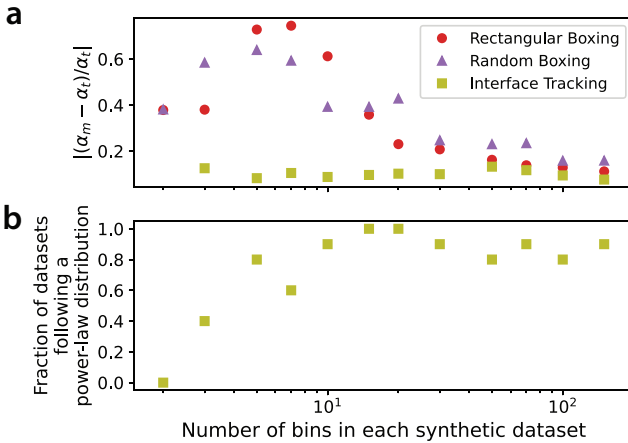


**Figure 5.14:** *Effect of the number of bins of the synthetic dataset on the accuracy of extracted scaling parameters (a) Relative error of the measured scaling parameter from each extraction technique. (b) Fraction of datasets that accurately follow a power-law distribution when the interface-tracking method is assessed with the Hill, second-order moment, and kernel estimators.*

### 5.4.4 Interface Tracking and Real Datasets

We can now finally return to our experimental dataset and compare the scaling parameters found by interface tracking (followed by double-bootstrapping multiple consistent estimators) to both rectangular and random boxing (followed by minimisation of the Kolmogorov-Smirnov statistic).

The interpolation and tracking technique applied to the experimental dataset [Fig. 5.11(e)] is shown in Fig. 5.11(f), where a distribution of small and large events is apparent. The log-log plot of event sizes and MLE is shown in Fig. 5.11(g), where the double-bootstrapped Hill estimate is marked as  $\alpha_m = 2.29$ .

The MLE via interface tracking in Fig. 5.11(g) can be compared with the MLEs obtained via boxing; this is shown in Fig. 5.11(h). While interface

tracking does bear the clearest plateau, the scaling parameters measured with all three techniques are ultimately very similar, ranging from 2.29 to 2.36. When adjusted for deviations due to the analysis technique, all measurements overlap in error at approximately  $\alpha_m = 2.1 \pm 0.1$ , and entirely encompass the error expected of the interface tracking technique.

All three approaches clearly allow power-law behavior to be identified and analysed, and approach identical values, but each have distinct advantages and disadvantages. Rectangular boxing is the most rapid and easily implemented, but relies on a known preferential direction from the underlying dataset. Random boxing avoids this need for preferential direction, but can disproportionally over- or under-sample particular regions of the dataset. Interface tracking is the most algorithmically complex, but brings several advantages: it has the lowest error in measurements of the scaling parameter; these measured scaling parameters are most similar to true value; it is compatible with multiple estimators and thus can enable differentiation between power laws and non-power laws; and needs the fewer image datasets for a consistent result.

## 5.5 Conclusions

We have here presented three techniques to extract and identify power-law scaling in experimental 2-dimensional image datasets, and validate them against synthetic 2-dimensional datasets. All three techniques rely upon the inherent 2-dimensional nature of the datasets to separate distinct events. Utilising rectangular boxing can be useful in datasets that show motion in preferential directions. Random shapes can be used to box datasets in which a preferential direction is absent, although this approach can preferentially bias the analysis towards certain locations of the 2-dimensional image. Finally, tracking interface motion using medial contours can very accurately determine a power law. All three techniques extract a scaling parameter very close to the known target value, and can similarly be used to unambiguously identify non-power-law datasets. Together, these techniques can be a powerful and easily applicable tool for the calculation of power-law statistics in a wide variety of experimental image datasets.

## References

- [1] R. Bulanadi and P. Paruch, “Identifying and analyzing power-law scaling in two-dimensional image datasets”, *Physical Review E* **109**, 064135 (2024).
- [2] T. Vicsek, *Fractal growth phenomena* (World Scientific, 1992).

## 5. Identifying and Analysing Power-Law Scaling in 2-Dimensional Image Datasets

---

- [3] T. Giamarchi, “Disordered elastic media.”, *Encyclopedia of complexity and systems science* **112**, 2019–2038 (2009).
- [4] E. Agoritsas, V. Lecomte, and T. Giamarchi, “Disordered elastic systems and one-dimensional interfaces”, *Physica B: Condensed Matter* **407**, 1725–1733 (2012).
- [5] E. E. Ferrero, L. Foini, T. Giamarchi, A. B. Kolton, and A. Rosso, “Creep motion of elastic interfaces driven in a disordered landscape”, *Annual Review of Condensed Matter Physics* **12**, 111–134 (2021).
- [6] I. Voitalov, P. van der Hoorn, R. van der Hofstad, and D. Krioukov, “Scale-free networks well done”, *Physical Review Research* **1**, 033034 (2019).
- [7] M. E. Newman, “Power laws, Pareto distributions and Zipf’s law”, *Contemporary Physics* **46**, 323–351 (2005).
- [8] J. P. Sethna, K. A. Dahmen, and C. R. Myers, “Crackling noise”, *Nature* **410**, 242–250 (2001).
- [9] A. Clauset, C. R. Shalizi, and M. E. Newman, “Power-law distributions in empirical data”, *SIAM Review* **51**, 661–703 (2009).
- [10] A. D. Broido and A. Clauset, “Scale-free networks are rare”, *Nature Communications* **10**, 1–10 (2019).
- [11] H. Bauke, “Parameter estimation for power-law distributions by maximum likelihood methods”, *The European Physical Journal B* **58**, 167–173 (2007).
- [12] Y. S. Virkar, “Power-law distributions and binned empirical data”, PhD thesis (University of Colorado at Boulder, 2012).
- [13] T. Nattermann, S. Stepanow, L.-H. Tang, and H. Leschhorn, “Dynamics of interface depinning in a disordered medium”, *Journal de Physique II* **2**, 1483–1488 (1992).
- [14] B. Casals, G. F. Nataf, D. Pesquera, and E. K. Salje, “Avalanches from charged domain wall motion in BaTiO<sub>3</sub> during ferroelectric switching”, *APL Materials* **8**, 011105 (2020).
- [15] C. Tan, C. Flannigan, J. Gardner, F. Morrison, E. Salje, and J. Scott, “Electrical studies of Barkhausen switching noise in ferroelectric PZT: critical exponents and temperature dependence”, *Physical Review Materials* **3**, 034402 (2019).
- [16] E. Salje, D. Xue, X. Ding, K. A. Dahmen, and J. Scott, “Ferroelectric switching and scale invariant avalanches in BaTiO<sub>3</sub>”, *Physical Review Materials* **3**, 014415 (2019).

- 
- [17] G. Bertotti, G. Durin, and A. Magni, “Scaling aspects of domain wall dynamics and Barkhausen effect in ferromagnetic materials”, *Journal of Applied Physics* **75**, 5490–5492 (1994).
  - [18] B. Alessandro, C. Beatrice, G. Bertotti, and A. Montorsi, “Domain-wall dynamics and Barkhausen effect in metallic ferromagnetic materials. I. theory”, *Journal of Applied Physics* **68**, 2901–2907 (1990).
  - [19] B. Alessandro, C. Beatrice, G. Bertotti, and A. Montorsi, “Domain-wall dynamics and Barkhausen effect in metallic ferromagnetic materials. II. experiments”, *Journal of Applied Physics* **68**, 2908–2915 (1990).
  - [20] E. Salje, “On the dynamics of ferroelastic domain boundaries under thermal and elastic forcing”, *Phase Transitions* **83**, 657–669 (2010).
  - [21] N. Friedman, A. T. Jennings, G. Tsekenis, J.-Y. Kim, M. Tao, J. T. Uhl, J. R. Greer, and K. A. Dahmen, “Statistics of dislocation slip avalanches in nanosized single crystals show tuned critical behavior predicted by a simple mean field model”, *Physical Review Letters* **109**, 095507 (2012).
  - [22] Z. Wang, J. Qiao, G. Wang, K. Dahmen, P. Liaw, Z. Wang, B. Wang, and B. Xu, “The mechanism of power-law scaling behavior by controlling shear bands in bulk metallic glass”, *Materials Science and Engineering: A* **639**, 663–670 (2015).
  - [23] J. Baró, Á. Corral, X. Illa, A. Planes, E. K. Salje, W. Schranz, D. E. Soto-Parra, and E. Vives, “Statistical similarity between the compression of a porous material and earthquakes”, *Physical Review Letters* **110**, 088702 (2013).
  - [24] S. Hantson, S. Pueyo, and E. Chuvieco, “Global fire size distribution: from power law to log-normal”, *International Journal of Wildland Fire* **25**, 403–412 (2016).
  - [25] M. Huergo, M. Pasquale, P. González, A. Bolzán, and A. Arvia, “Dynamics and morphology characteristics of cell colonies with radially spreading growth fronts”, *Physical Review E* **84**, 021917 (2011).
  - [26] M. A. C. Huergo, M. Pasquale, P. H. González, A. E. Bolzán, and A. J. Arvia, “Growth dynamics of cancer cell colonies and their comparison with noncancerous cells”, *Physical Review E* **85**, 011918 (2012).
  - [27] G. Rapin, N. Caballero, I. Gaponenko, B. Ziegler, A. Rawleigh, E. Moriggi, T. Giamarchi, S. A. Brown, and P. Paruch, “Roughness and dynamics of proliferating cell fronts as a probe of cell–cell interactions”, *Scientific Reports* **11**, 1–9 (2021).
  - [28] P. Paruch and J. Guyonnet, “Nanoscale studies of ferroelectric domain walls as pinned elastic interfaces”, *Comptes Rendus Physique* **14**, 667–684 (2013).



## 5. Identifying and Analysing Power-Law Scaling in 2-Dimensional Image Datasets

---

- [29] S. V. Kalinin and A. Gruverman, *Scanning probe microscopy: electrical and electromechanical phenomena at the nanoscale*, Vol. 1 (Springer Science & Business Media, 2007).
- [30] A. Gruverman, O. Auciello, and H. Tokumoto, “Imaging and control of domain structures in ferroelectric thin films via scanning force microscopy”, *Annual Review of Materials Science* **28**, 101–123 (1998).
- [31] P. Tückmantel, I. Gaponenko, N. Caballero, J. C. Agar, L. W. Martin, T. Giamarchi, and P. Paruch, “Local probe comparison of ferroelectric switching event statistics in the creep and depinning regimes in  $\text{Pb}(\text{Zr}_{0.2}\text{Ti}_{0.8})\text{O}_3$  thin films”, *Physical Review Letters* **126**, 117601 (2021).
- [32] E. N. Mortensen and W. A. Barrett, “Morphological interpolation between contour lines”, in *Medical imaging 1993: image processing*, Vol. 1898 (International Society for Optics and Photonics, 1993), pp. 501–510.

## CHAPTER 6

---

### The Interplay Between Point and Extended Defects and their Effects on Jerky Domain-Wall Motion in Ferroelectric Thin Films

---

Defects have a significant influence on the polarisation and electromechanical properties of ferroelectric materials. Statistically, they can be seen as random pinning centres acting on an elastic manifold, slowing domain-wall propagation and raising the energy required to switch polarisation.

In this Chapter, building off the methods of extracting power-laws from 2-dimensional datasets described in Chapter 6, we show that the ‘dressing’ of defects can lead to unprecedented control of domain-wall dynamics. We engineer defects of two different dimensionalities in ferroelectric oxide thin films—point defects externally induced via  $\text{He}^{2+}$  bombardment, and extended quasi-1-dimensional  $a$ -domains formed in response to internal strains. The  $a$ -domains act as extended strong pinning sites (as expected) imposing highly localised directional constraints. Surprisingly, the induced point defects in the  $\text{He}^{2+}$ -bombarded samples orient and align to impose further directional pinning, screening the effect of  $a$ -domains. This defect interplay produces more uniform and predictable domain-wall dynamics. Such engineered interactions between defects are crucial for advancements in ferroelectric devices.

This Chapter is based on a publication by R. Bulanadi, K. Cordero-Edwards, P. Tückmantel, S. Saremi, G. Morpurgo, Q. Zhang, L. W. Martin, V. Nagarajan, and P. Paruch under review in *Physical Review Letters* (American Physical Society) under the title *The interplay between point and extended*

## 6. The Interplay Between Point and Extended Defects and their Effects on Jerky Domain-Wall Motion in Ferroelectric Thin Films

---

*defects and their effects on jerky domain-wall motion in ferroelectric thin films* [1]. R. Bulanadi performed all measurements and analysis reported in this Chapter.

This work was supported by the Swiss National Science Foundation under Division II (Grant No. 200021-178782). G.M. acknowledges additional support under Grant No. 2000020-188687. S.S. acknowledges support from the National Science Foundation under Grant DMR-2102895. L.W.M. acknowledges support from the Army Research Office under Grant W911NF-21-1-0118. The research at the UNSW is supported by the Australian Research Council Centre of Excellence in Future Low-Energy Electronics Technologies (Project Number CE170100039). The data and source code which support the findings of this study will be available on Yareta at <https://doi.org/10.26037/yareta:sqti2pvttnak3f6qoyqlpu6mc4>, in compliance with SNSF Data Management Plan guidelines.

### 6.1 Introduction

Ferroelectric oxides have long excited broad interest for both industrial applications in memory, sensing, and actuation [2–4], as well as fundamental physics, most recently with non-trivial, highly local polarisation textures [5–9], and emergent functional properties at domain walls [10–12]. However, the observations and uses of ferroelectrics are invariably mediated by the defects ubiquitous to these materials, which can both inhibit and enhance desired properties [13–15]. Indeed, the intentional generation of defects has been used to stabilise the target multiferroic tetragonal-like phase of  $\text{BiFeO}_3$  [16], control wake-up in  $\text{HfO}_2$ -based ferroelectrics [17, 18] or enable novel properties like effective negative capacitance [19]. Defects induced through ion bombardment have been of particular interest in recent years, with ion-bombarded ferroelectric films showing increased resistivity [20], increased energy density [21], or induced ferroelectricity in  $\text{HfO}_2$ -based films [22].

The plethora of potential properties and applications resulting from defect engineering should be of no surprise given the immense diversity of defects themselves [23–25]. Oxygen vacancies—point defects inevitable in oxide thin films—can be modulated via composition or growth conditions, and act both as pinning sites [26] and charge carriers [27, 28]; features inexorably relevant to any ferroelectric application. In addition, phase boundaries and twins can introduce long-range strain effects, altering the continuity of polarisation in their vicinity [29], and acting as extended defects (2-dimensional in bulk, quasi-1-dimensional in thin films) [30, 31].

Despite this high diversity of defects in ferroelectric oxide thin films, properties emergent from their *interplay* remain as yet largely unexplored.

In this Chapter, we investigate the effects of an engineered, complex disorder landscape, including both point and extended defects, on the pinning and motion of ferroelectric domain walls during polarisation switching under an applied electric field.

## 6.2 Growth and Characterisation of Ion-Bombarded PbTiO<sub>3</sub> Thin Films

To minimise innate defect variations across samples, five PbTiO<sub>3</sub> films were simultaneously grown via pulsed laser deposition (PLD) on SrTiO<sub>3</sub> (001) substrates (CrysTec GmbH), with a 20 nm SrRuO<sub>3</sub> bottom electrode. As detailed in [20], the films were sufficiently thick (140 nm) for *a*-domains to form during growth. To probe the effects of increasing point defect concentration, four samples were bombarded by He<sup>2+</sup> ions with an energy of 5 MeV, at flux densities of 10<sup>13</sup>, 10<sup>14</sup>, 10<sup>15</sup>, and 10<sup>16</sup> ions/cm<sup>2</sup> (this bombardment energy was chosen to be sufficiently high for the ions to penetrate entirely through the film and stop within the substrate). One sample was maintained in its pristine as-grown state, so that the only defects present were those formed during growth. High crystalline quality and out-of-plane *c*-axis orientation in all samples were verified by x-ray diffraction, with reciprocal space maps around the (002)-diffraction peak revealing the presence of *a*-axis-oriented twin domains (Fig. 6.1). Diffraction peak positions were comparable amongst all samples, but the full width at half maximum of the film diffraction peak gradually increased with increasing ion bombardment (Fig. 6.2). This suggests that the He<sup>2+</sup> ions are not themselves injected into the sample [32], but rather cause radiation damage and the formation of complex defect clusters [20].

Piezoresponse force microscopy (PFM) measurements were performed by Dual AC Resonance Tracking in an *Asylum Research Cypher* atomic force microscope with OSCM-Pt (Olympus) tips. Sample raw PFM data are shown in Fig. 6.3. This image is taken of the film bombarded with 10<sup>15</sup> ions/cm<sup>2</sup>, after domain walls are constructed and allowed to fully relax. It is from this polarisation state that ferroelectric domain-wall tracking can be performed.

A majority *c*-phase of PbTiO<sub>3</sub> was identified. A full 180° phase shift is observed in the phase channel [Fig. 6.3(c)], and accompanied by minima in the amplitude channel [Fig. 6.3(b)], verifying a boundary in out-of-plane polarisation. These out-of-plane domain walls do not have any correlation with sample topography [Fig. 6.3(a)]. However, the *a*-domains, which are clearly visible in the amplitude channel as slightly weaker minima—and which correspond to an in-plane rotation of the unit cells—do appear in topography.

PFM phase micrographs from non-bombarded and all bombarded sam-

## 6. The Interplay Between Point and Extended Defects and their Effects on Jerky Domain-Wall Motion in Ferroelectric Thin Films

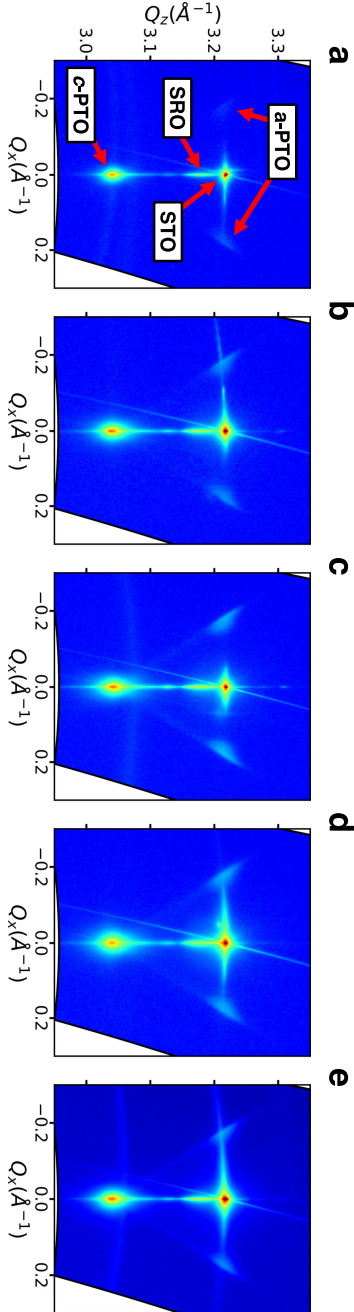


**Figure 6.1:** X-ray diffraction reciprocal space maps of the (002) reflection of the  $\text{PbTiO}_3$  film series. 140 nm  $\text{PbTiO}_3$  is grown on 20 nm  $\text{SrRuO}_3$  electrodes on  $\text{SrTiO}_3$  (001) substrates, with (a) no  $\text{He}^+$  bombardment; and  $\text{He}^+$  bombardment of (b)  $10^{13}$ , (c)  $10^{14}$ , (d)  $10^{15}$ , and (e)  $10^{16}$  ions/ $\text{cm}^2$ .

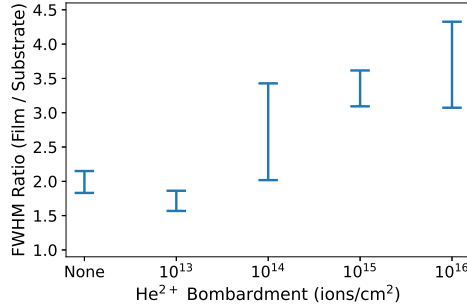


**Figure 6.2:** Comparison of the full width at half maximum of diffraction peaks of films and substrates at the (002) reflection of the  $\text{PbTiO}_3$  film series. A gradual broadening of the film diffraction peaks in comparison to the substrate diffraction peaks can be seen.

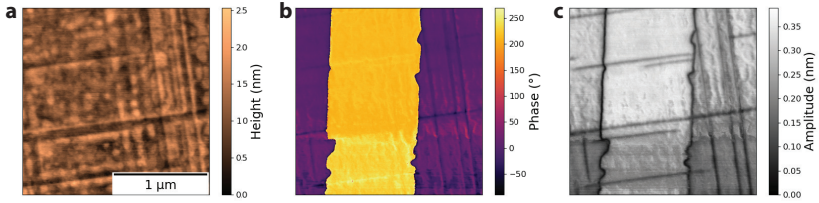


**Figure 6.3:** Sample raw PFM data of the  $10^{15}$  ions/cm<sup>2</sup>, after domain-wall construction and relaxation. The channels shown represent (a) height, (b) amplitude, and (c) phase.

ples are shown in Fig. 6.4(a–e). Both up- and down-oriented  $c$ -domains were observed, with their relative proportion varying significantly with  $\text{He}^{2+}$  bombardment density. The pristine sample showed a predominantly up-orientated polarisation, with small down-oriented domains preferentially segregating at the  $a$ -domain network. The volume of these down domains increased with  $\text{He}^{2+}$  bombardment density to become the dominant orientation. However, at the highest bombardment density, we observed a return to the majority up-polarisation orientation. The  $a$ -domains were observed in all samples as sparse, irregular grids, aligned with the in-plane axes and marked by a drop in the out-of-plane amplitude without a corresponding phase shift.

To track domain-wall motion in a controlled configuration [Fig. 6.4(f–j)], a vertical stripe domain was first patterned using a biased scanning probe microscopy tip. Once the domain wall position stabilised and relaxed (Fig. 6.3), a gradual polarisation reversal was then carried out by stroboscopic measurements: switching scans with a defined DC bias were interleaved with

## 6. The Interplay Between Point and Extended Defects and their Effects on Jerky Domain-Wall Motion in Ferroelectric Thin Films

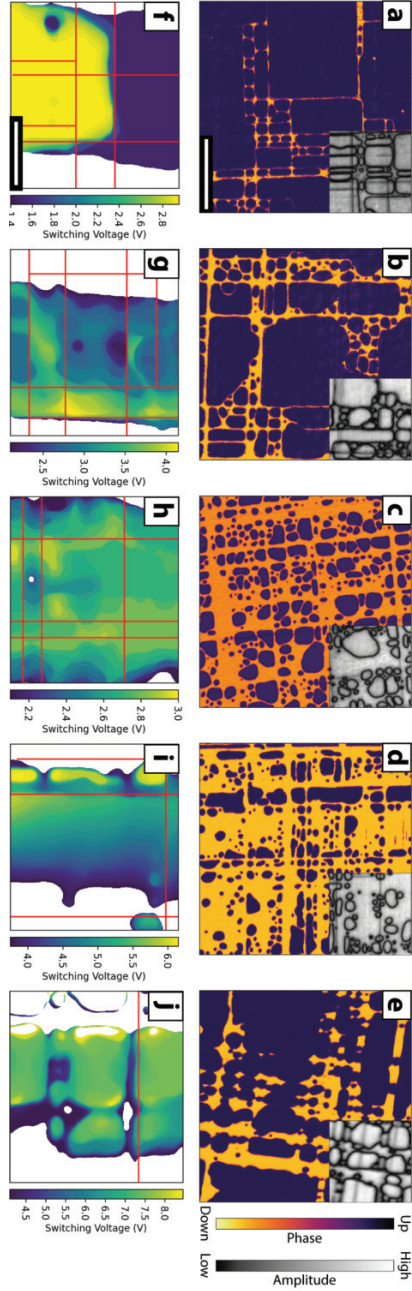


**Figure 6.4:** *Polarisation switching studies in  $PbTiO_3$  thin films.* PFM phase imaging of the polarisation state of (a) the as grown sample, as well as samples with  $He^+$  bombardment densities of (b)  $10^{13}$ , (c)  $10^{14}$ , (d)  $10^{15}$ , and (e)  $10^{16}$  ions/cm<sup>2</sup>. PFM amplitudes appear inset, corresponding to the regions overlaid. (f–j) Representative ferroelectric switching maps of corresponding samples. colour bars show the voltage needed to switch this region. Positions of  $a$ -domains are highlighted as red lines. Scalebars on the PFM images and switching maps mark 1  $\mu$ m and 500 nm respectively.

PFM scans to image the evolution of the domain-wall position, with the bias gradually incremented between cycles by a fixed interval of 50 mV. This stroboscopic switch-image cycling proceeded until either complete polarisation reversal or until no further evolution of the domain configuration was observed over at least five cycles. The evolution of both up- and down-oriented stripe domains were examined, with each measurement repeated 2–3 times on different regions of each sample.

Ferroelectric switching in each sample appears qualitatively distinct [Fig. 6.4(f–j)]. In the pristine sample, we observe the abrupt reversal of relatively large areas, whose boundaries correlate strongly with the presence of the *a*-domains. With increasing He<sup>2+</sup> bombardment flux density, polarisation reversal is generally slower—significantly so for the highest bombardment densities—and proceeds more gradually via smaller switching steps, suggesting increased pinning effects less correlated with the *a*-domain positions.

The global effects of He<sup>2+</sup> bombardment can be more quantitatively gauged by measuring the evolution of polarisation reversal [Fig. 6.5(a)], calculated as the ratio of the area switched through the stroboscopic switching scans, compared to the area of the initially patterned stripe. The pristine films present a slight negative imprint: the onset of switching ( $\sim 1.50$  V) and the coercive voltage  $V_P$  ( $\sim 2.75$  V, where 50% polarisation reversal occurred) were lower magnitude under positive tip biases than the onset and coercive voltage ( $V_N$ , defined analogously) under negative tip biases ( $\sim -3.25$  V and  $\sim -3.5$  V, respectively). Low bombardment densities, up to about  $10^{15}$  ions/cm<sup>2</sup>, slightly decrease the magnitude of  $V_N$  and increases  $V_P$ , potentially making the imprint more positive and the overall switching response more symmetric [Fig. 6.5(b)]. The coercive voltages did not appear to significantly change with bombardment level.

With yet increasing bombardment densities, however, the effects on switching become more dramatic, with both positive and negative coercive voltages significantly increased. As expected given the charged nature of the bombarding ions, these effects are themselves highly asymmetric [33], potentially further increasing the imprint by extending the range of voltages over which switching occurs under positive tip bias, while switching under negative tip bias is rendered even more abrupt. These direct, nanoscale measurements also support prior work by Saremi *et al.* that similarly show dramatic changes of the ferroelectric switching loops only above  $10^{15}$  ions/cm<sup>2</sup> [34].

These observations of the global switching dynamics are further corroborated by switching spectroscopy PFM measurements (Fig. 6.6). Switching spectroscopy piezoresponse force microscopy [35] measurements of piezoresponse vs. tip bias hysteresis loops (Fig. 6.6) were carried out using a *Asylum Research Cypher* atomic force microscope with an OSCM-Pt (Olympus) tip. During these measurements, the tip was placed in contact with a



## 6. The Interplay Between Point and Extended Defects and their Effects on Jerky Domain-Wall Motion in Ferroelectric Thin Films

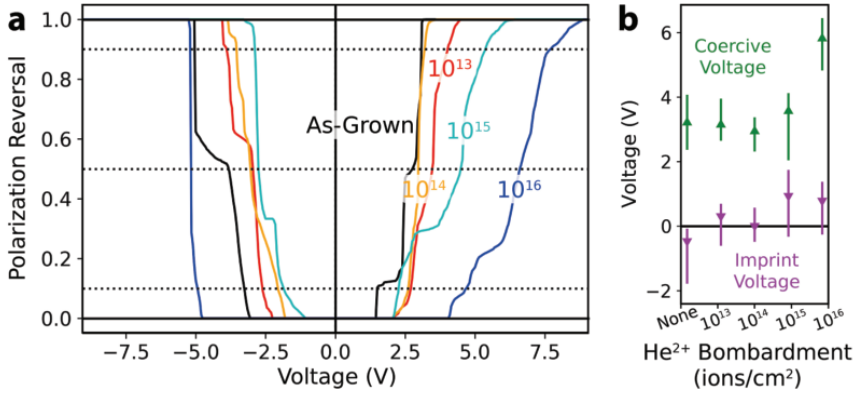


**Figure 6.5:** Switching dynamics in  $\text{PbTiO}_3$  thin films under incrementally increasing voltage. (a) Polarisation reversal as a function of applied voltage, averaged over 2–3 experiments. Dashed lines represent 10%, 50% and 90% reversal. Inscribed values mark  $\text{He}^{2+}$  bombardment levels in  $\text{ions}/\text{cm}^2$ . (b) Corresponding switching characteristics, with average coercive voltage  $V_C = \frac{|V_P| + |V_N|}{2}$  and imprint  $V_I = \frac{|V_P| - |V_N|}{2}$ . Markers denote the  $V_P$  and  $V_N$  for which 50% polarisation reversal was observed, while error bars span the voltage range between 10% and 90% polarisation reversal.

region of initially up-oriented polarisation, and a cyclic triangular-rectangular waveform was applied. During each cycle, starting at 0 V, rectangular wave pulses with 0.05 s on–0.05 s off were incremented by 0.1 V at each step, until a final voltage of 8 V, upon which the wave pulses were decremented to -8 V, then incremented back up to 0 V, giving a full piezoresponse vs. tip bias hysteresis loop, and the the cycle would begin again. Five successive hysteresis loops were acquired at each point, resulting in a total scan time of 160 s per point. The initial hysteresis loops were collected and plotted separately from all successive loops, and show minor but noticeable differences, as previously reported in such samples by Tückmantel et al. [36]. To ensure the maximum consistency in this analysis, only the successive loops were considered.

### 6.3 Power-Law Distributions and Global Switching Dynamics

To ascertain the *dynamics* of the ferroelectric switching, we look to the distribution of sizes of switching events, with a particular interest in ultra-slow creep dynamics occurring for highly subcritical electric fields [36, 37]. Ferroelectric switching dynamics are known to follow a highly stable, scale-invariant power law, where the logarithm of the probability of a switching ‘event’ occurring decreases linearly with the logarithm of the magnitude of the area reoriented, or the energy released by this reorientation [36, 38–

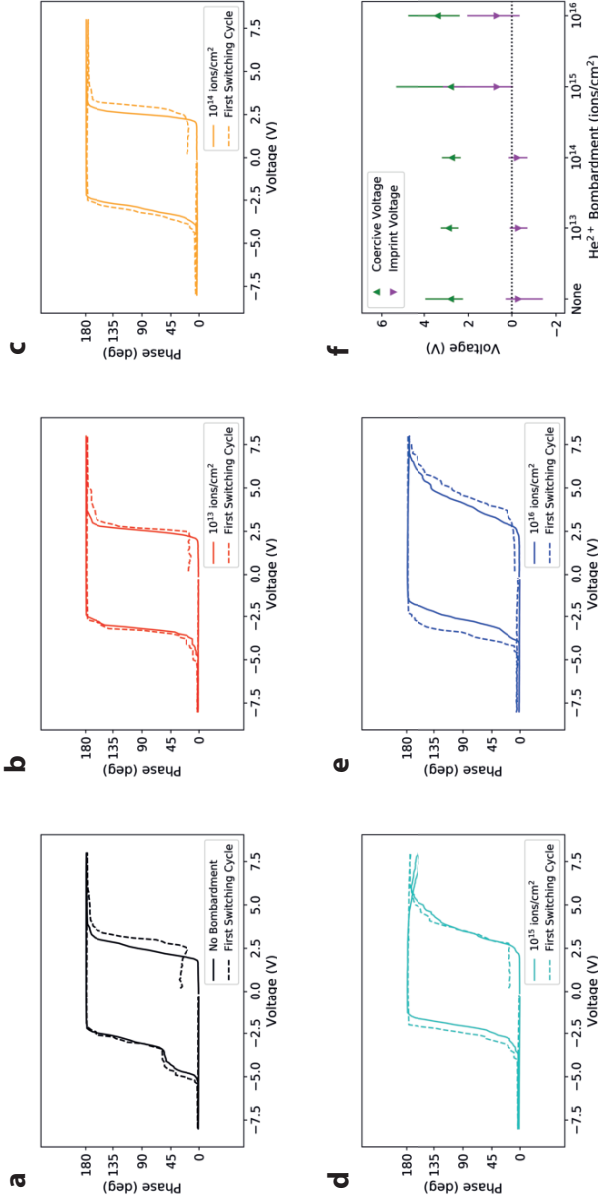


**Figure 6.6:** Results of switching spectroscopy piezoresponse force microscopy studies. Piezoresponse hysteresis loops were measured by applying cyclic tip voltages to regions with initially up-oriented polarisation, averaged over at least 30 different locations. At each location, 5 successive hysteresis loops were acquired: the average of the first hysteresis measurement is shown with a dashed line, and of all subsequent hysteresis measurements in a solid line, for samples with (a) no- $\text{He}^+$  bombardment; and samples with  $\text{He}^+$  bombardment levels of (b)  $10^{13}$ , (c)  $10^{14}$ , (d)  $10^{15}$ , and (e)  $10^{16}$  ions/cm<sup>2</sup>. In (f), the coercive and imprint voltages are calculated, with error bars denoting coercive and imprint voltages when the measured phase signal reaches 10% or 90% of the target switching volume.

## 6. The Interplay Between Point and Extended Defects and their Effects on Jerky Domain-Wall Motion in Ferroelectric Thin Films

---

44]. Changes in this global power-law distribution would therefore indicate changes to the underlying switching mechanism resulting from modifications to the disorder landscape. Individual switching events are therefore extracted from the switching maps of each measurement series, such as those shown in Fig. 6.4(f-j), through the following process.

The sizes of the switching events were extracted from sequential imaging scans of the vertical written stripe domain. The domain-wall positions in each image (at each time  $t$ ) were determined, and the position of the domain walls between each frame were then interpolated via an algorithm discussed in Ref. [45]. In brief, morphological erosion-dilation cycles were performed until a medial line was obtained between the two interfaces, and, following this, new erosion-dilation cycles were recursively performed using each of the new interfaces until all intermediary pixels were assigned their own intermediate time  $t$ .

Each sequential pair of images was then considered, starting from the initial domain-wall positions defined by the first scan in each pair. The path of each pixel on the initial domain wall was traced by following the direction of the maximum gradient of  $t$  at that pixel, until no further displacement occurred, or until the final domain-wall position was reached, as defined by the second of each pair of scans.

The shapes that were bounded by a segment on the initial interface, the paths traced by the first and last pixels on that segment, and the final positions of those pixels were then used as boundaries to define the shape whose area was considered as the event size.

An example of this algorithm being performed on one set of images can be seen in Fig. 6.7. In Fig. 6.7(a-e), segments of increasing size are shown. In Fig. 6.7(e) in particular, these events are visually distinguishable by eye; initial events nearer the outer perimeter are wide, but small steps of domain-wall motion ensure that each segment moves only a small distance, and thus, only small switching events are encountered. Towards the centre of these shapes, however, larger switching events that sweep longer distances are observed.

The increasing tip voltage experiment was performed 4-6 times for each sample. Events from these experiments were collated, and their distribution as a function of event size is plotted on log-log axes on the top panel of [Fig. 6.8(a)]. A clear linear regime can be seen here across multiple orders of magnitude, providing a strong indication of power-law scaling.

We observe power-law scaling of event sizes in all five samples [Fig. 6.8(a)]. The estimated scaling parameter  $\hat{\alpha}$  was identified through maximum-likelihood methods, following Clauset *et al.* [46], and described in Section. resection:MLE. In brief, the  $y$ -axis marks the exponent calculated to be maximally likely, as a function of a cutoff at which all lower values are ignored and excluded. With low magnitude cutoffs, we are vulnerable to ran-

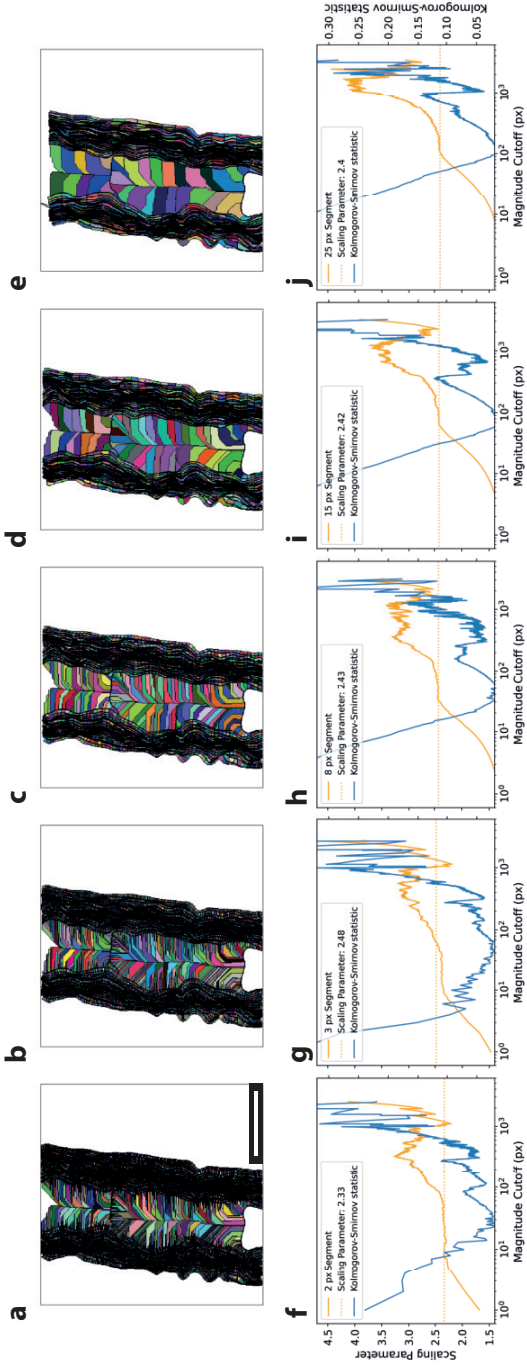


**Figure 6.7:** MLE power-law trends identified from switching events starting from different line segment events. Switching events extracted from the  $\text{PbTiO}_3$  film bombarded with  $10^{14}$  ions/ $\text{cm}^2$  are shown, with the areas originating from line segments of length (a) 2 pixels, (b) 3 pixels, (c) 8 pixels, (d) 15 pixels, (e) 25 pixels. The corresponding MLE fits of all switching events on this sample, as well as their Kolmogorov-Smirnov statistics, are shown in (f-j), where a shortening of the plateau and a narrowing of the dip in the Kolmogorov-Smirnov statistic can be observed with increasing segment size.

## 6. The Interplay Between Point and Extended Defects and their Effects on Jerky Domain-Wall Motion in Ferroelectric Thin Films

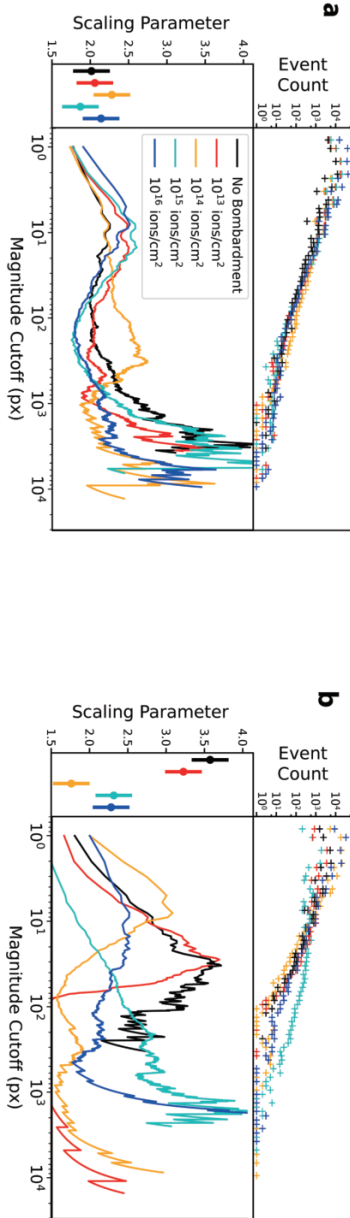


**Figure 6.8:** Power-law fits of ferroelectric switching dynamics, under (a) incrementally increasing voltage and (b) constant voltage. Top panels: Log-Log plots of the distribution of switching event size. Centre panels: Optimal power-law scaling parameters for different event-size cutoffs calculated via maximum-likelihood estimation. Left panels: The scaling parameter corresponding to minimum Kolmogorov-Smirnov statistic. Error bars use a root-mean-squared error of 0.2 as expected for this method of domain-wall extraction (See Chapter 5)

dom noise in measurement, while with high magnitude cutoffs we eliminate relevant data. In all five samples, however,  $\hat{\alpha} \sim 2.0$  over approximately two orders of magnitude of the magnitude cutoff.

A plot of the Kolmogorov-Smirnov statistic can be seen in Fig. 6.9, while the calculated plateau heights are shown in the left panel of Fig. 3(a). The Kolmogorov-Smirnov statistics tend to be repressed at the same  $x_{min}$  as the corresponding plateaus, as expected. These emphasise the continued similarity of the measured scaling parameter across all samples.

In Fig. 6.7(f-j), MLE plots and the Kolmogorov-Smirnov statistic are calculated and shown for all experiments on this sample, using each of the corresponding line lengths in Fig. 6.7(a-e). Note how the heights of the plateaus on each of these graphs are roughly identical to one another, albeit with a narrower MLE plateau and a shorter range of low Kolmogorov-Smirnov statistics. This suggests that the choice of segment length is largely irrelevant to the established trend, which further supports the validity of the MLE-Power-Law model, as well as the domain-wall-tracking algorithm. Similar trends were indeed observed by Tückmantel *et al.* [36], in which the authors also suggest larger boxes (or segments) may be preferable to ensure that the switching events are uncorrelated. With this in mind, 3-pixel segments were therefore used, as shown in Fig. 6.7(b,g), which show a sufficiently broad range, while allowing events to decorrelate. This also allowed a single experiment to yield datasets consisting of  $10^4$ – $10^5$  events.

This consistency in the estimated critical exponent is remarkable given the qualitative differences in switching maps between the different samples [Fig. 6.4(f-j)]. Moreover, one could expect that the increased defects in the most bombarded samples may increase conduction or leakage [23], and thus alter the distribution of switching events. Despite this, the similarity of the final critical exponent indicates that all samples show similar crackling behavior. These experimental observations are also exceptionally consistent: the stability of the critical exponent over two orders of magnitude on the plot of maximum-likelihood exponents is particularly extensive given the inevitable noise and size constraints of real data [46].

We note that this analysis is based on the full dataset of all switching events, including the largest ones occurring at the highest tip bias. As previously reported by Tückmantel *et al.* [36], these large events may indicate a combination of creep and depinning regimes which could depress the value of the power-law scaling exponent. We therefore performed a further investigation of switching dynamics at constant tip bias well below the coercive voltage determined for each sample from Fig. 6.5. Specifically, we used 1 V for the samples bombarded with  $10^{13}$  and  $10^{14}$  ions/cm<sup>2</sup>, as well as the non-ion-bombarded sample, and 1.5 V for the sample bombarded with  $10^{15}$  ions/cm<sup>2</sup> and  $10^{16}$  ions/cm<sup>2</sup>, carrying out three independent stroboscopic switching-imaging experiments in each sample.

## 6. The Interplay Between Point and Extended Defects and their Effects on Jerky Domain-Wall Motion in Ferroelectric Thin Films

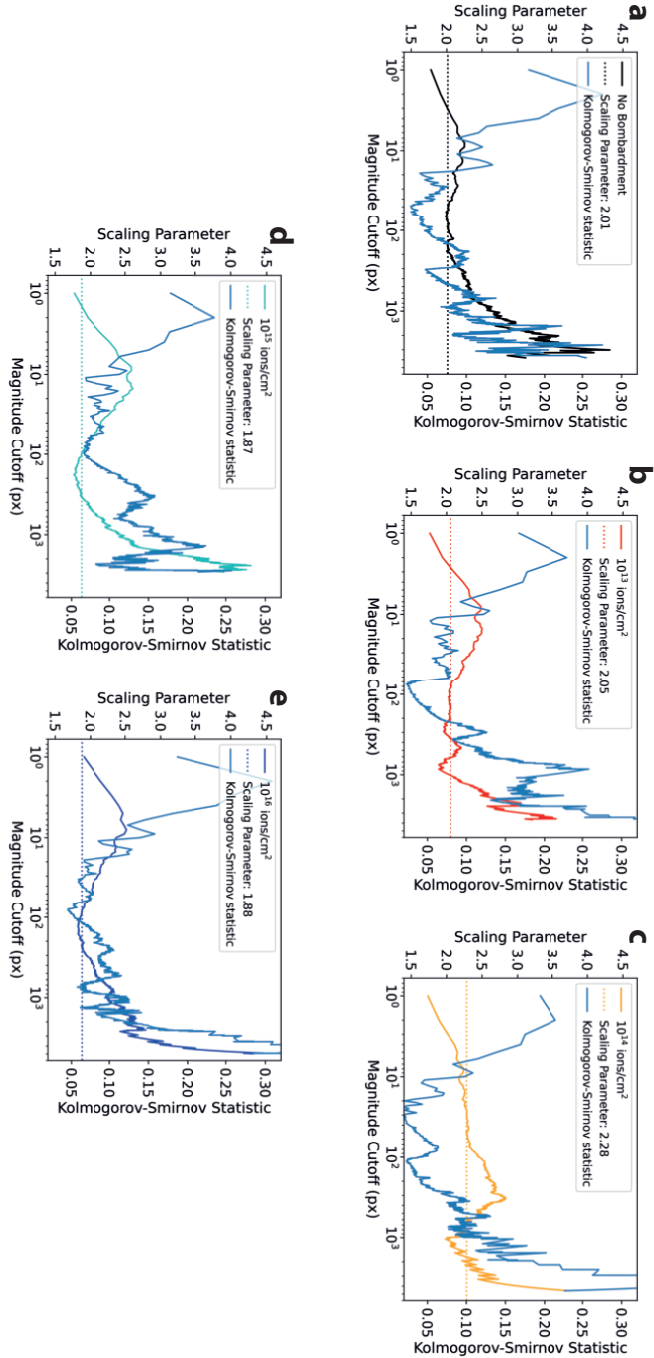


**Figure 6.9:** MLE of scaling parameters obtained from polarisation switching experiments carried out under increasing tip voltage, alongside their Kolmogorov-Smirnov statistic for each event size cutoff. (a) As-grown sample; and samples that had undergone  $\text{He}^+$  to densities of (b)  $10^{13}$ , (c)  $10^{14}$ , (d)  $10^{15}$ , and (e)  $10^{16}$  ions/cm<sup>2</sup>.

The same analysis was then performed on the dataset obtained in analogous experiments, but with a constant sub-coercive tip bias applied during the switching scans. The scaling parameters are far less stable for these constant-voltage studies [Fig. 6.8(b)]. This is particularly true for the as-grown (non-ion-bombarded) and lowest-bombardment density samples, where the high values obtained for the scaling parameter (above 3) could be a marker for non-power-law behavior (See Chapter 5). This may be related to the switching voltage magnitude: for these samples in particular, switching proceeded at rapid enough rate that statistics were insufficient for an adequate power-law fit. However, at lower biases, no significant domain-wall motion could be observed within a reasonable timeframe. This trend is akin to those seen in Fig. 6.5(a), where polarisation switching in these samples proceeds over a smaller threshold. In the higher-bombardment-density samples, the scaling parameter appears physically meaningful, but smaller events play a more significant role, and increase the measured value to closer to 2.5, consistent with previous observations in the creep regime [36].

The plot of the MLE scaling parameter plateau appears to be more unstable than in the switching observed with increasing tip voltage. This is to be expected given the higher proportion of small events, and the inherently decreased probability of large switching events taking place. As more of the region is already switched by small events, the largest possible events are increasingly restricted in size, and thus the maximum extent of the MLE plateaus is inhibited. This is also borne out by the values of the Kolmogorov-Smirnov statistic  $D$  shown along the ranges of the MLE in Fig. 6.10, which still present a dip corresponding to the MLE plateau position (and therefore, suitability for a power-law description in that range), but over a similarly narrow extent. This further suggests non-power-law behaviour in these constant-voltage studies, particularly for the less-bombarded samples.

In both analyses, we find that the bombardment density has only weak effects on the value of the scaling parameter  $\hat{\alpha}$ , which varies between 1.8 and 2.3 for the incrementally increased tip bias measurements, and between 1.9 and 2.4 for the constant tip bias measurements. The consistency of the scaling exponent across samples further suggests that (a) the creep regime dominates the switching dynamics in these samples, and (b) the pinning effects stay in the same universality class, regardless of defect density.

## 6.4 *a*-Domain Contributions and Local Switching Dynamics

At a local, rather than global level, however, the effects of the *a*-domains can be quite significant; this can be seen qualitatively in Fig. 6.4(f-j), where much of the pinning appears in the vicinity of—and parallel to—nearby *a*-domains.



## 6. The Interplay Between Point and Extended Defects and their Effects on Jerky Domain-Wall Motion in Ferroelectric Thin Films

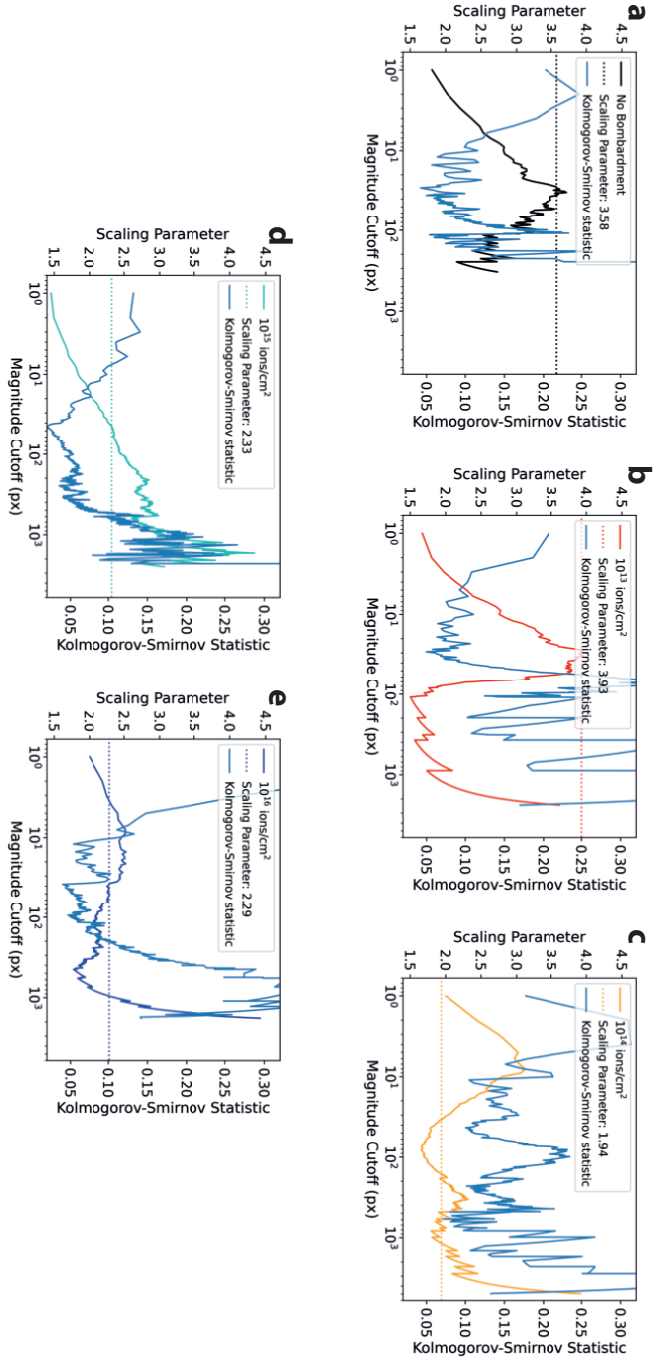


**Figure 6.10:** MLE of scaling parameters in constant voltage experiments, alongside their Kolmogorov-Smirnov statistic for each event size cutoff. (a) As grown sample; and samples that had undergone  $\text{He}^+$  bombardment to densities of (b)  $10^{13}$ , (c)  $10^{14}$ , (d)  $10^{15}$ , and (e)  $10^{16}$  ions/cm<sup>2</sup>.

To better understand their role in conjunction with the bombardment-induced point defects, we therefore focus on local variations in domain-wall dynamics. This analysis is again based on the domain switching maps, of which a subset is shown in Fig. 6.4(f–j). As before, the positions of the *a*-domains are individually tracked, and each switching map is interpolated to obtain a smooth and continuously varying representation of the switching voltage across the ferroelectric surface.

One such interpolated switching map, obtained on the pristine sample and projected into 3 dimensions, is shown in Fig. 6.11(a), with *a*-domains indicated in red. Parallel to the  $a_1$ -domain and  $\sim 100$  nm away from it, a rapid increase in the magnitude of the switching voltage can be seen. This increase corresponds physically to an abrupt and marked increase in switching difficulty, and thus higher pinning than in the surrounding regions. This observation is even clearer after taking a spatial derivative in the  $a_1$  direction [Fig. 6.11(b)], where high values of the derivative appear parallel to the  $a_1$ -domain, clearly indicating the strong domain-walls pinning in this region.

A line profile of the average height of the derivative along the  $a_1$  direction is shown in Fig. 6.11(c). We observe a distinct peak, which we believe corresponds to the pinning effect of the *a*-domain. The pinning strength, indicated by the dashed line, is far above the baseline level of the sample. This analysis therefore allows us to distinguish two regions with qualitatively different contributions; a low-level *baseline* pinning which corresponds to behavior consistent throughout the entire sample, and an *a*-domain contribution identifiable in the line profile by a sharp peak in the vicinity of an *a*-domain. Plots of these respective contributions across the samples (Fig. 6.12), show both increasing after  $\text{He}^{2+}$  bombardment. The ratio between the two, however, shows a vastly different trend [Fig. 6.11(d)], where the pristine (non-bombarded) sample presents a uniquely higher pinning contribution from the *a*-domains as compared to the baseline.

Under as-grown conditions, therefore, the *a*-domains have significant local contributions to the pinning, which in turn carries heavy implications for the global pinning and power-law scaling. As a significant portion of small domain-wall motion events occurs in the direct vicinity of *a*-domains (particularly in the as-grown sample), we conclude that these extended quasi-1-dimensional defects contribute to an increase in the value of the scaling parameter measured across the whole sample. Indeed, in similar thin films of the related material  $\text{Pb}(\text{Zr}_{0.2}\text{Ti}_{0.8})\text{O}_3$  without *a*-domains, lower values of the global scaling parameter were observed in the creep regime [36].

However, quite different domain-wall interactions emerge in the bombarded samples, where the relative difference between the baseline pinning and *a*-domain contribution is nowhere near so significant. Specifically, at any level of  $\text{He}^{2+}$  bombardment we see a marked increase in baseline pinning

## 6. The Interplay Between Point and Extended Defects and their Effects on Jerky Domain-Wall Motion in Ferroelectric Thin Films

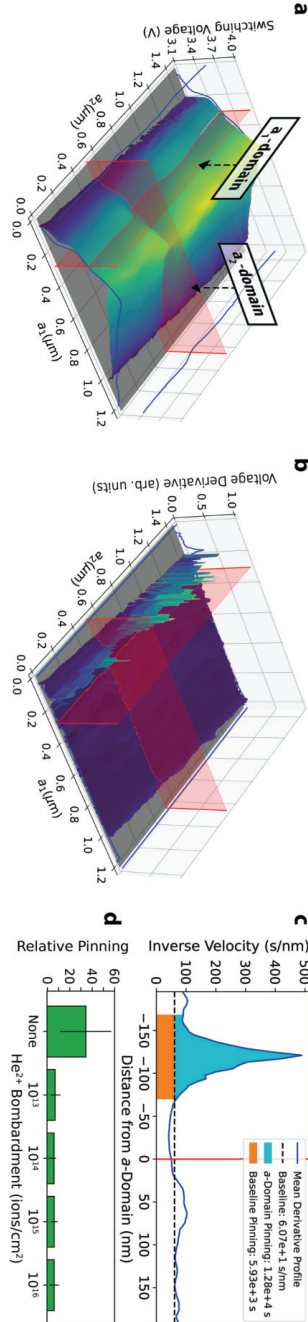


**Figure 6.11:** *Extraction of the pinning contribution of quasi-1-dimensional  $a$ -domains.* (a) Interpolated switching map of the non-ion-bombarded  $\text{PbTiO}_3$  thin film, projected into three dimensions. Red lines mark the positions of  $a$ -domains at the ferroelectric surface. Blue lines show the switching voltage profile averaged along the  $a_1$  and  $a_2$  crystalline axes. (b) Normalised  $a_1$  derivative of the switching map. (c) Line profile of the  $a_1$  spatial derivative in the vicinity of the  $a_1$  domain (marked in a red solid line). The dashed black line corresponds to the average derivative value in the switching map after neglecting events in the vicinity of  $a$ -domains. A peak in the derivative and pinning is highlighted in cyan, with the area beneath it corresponding to the average pinning, marked in orange. (d) A column plot comparing the ratio of the pinning attributed to the  $a$ -domains to the pinning attributed to the baseline for all samples.

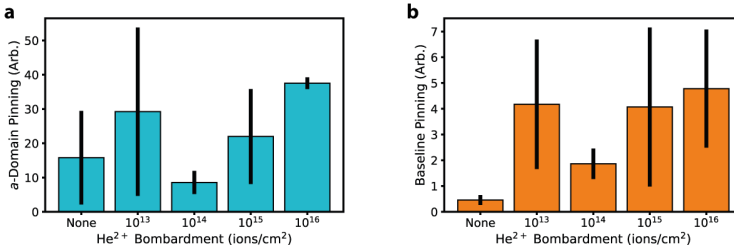


**Figure 6.12:** Quantifying pinning effects on domain-wall motion (a) Pinning contribution of  $a$ -domains (extended defects). (b) Average baseline pinning throughout the sample (point defects).

[Fig. 6.12(b)]. Rather than being strongly pinned only at the  $a$ -domains, the domain walls in these samples are subject to comparable variations throughout the entire potential energy landscape. Effectively, the bombardment defects can be seen as ‘dressing’ the strong confinement effects of the  $a$ -domains, which are reflected in the corresponding decrease in the value of the scaling parameter.

This ‘dressing’ of  $a$ -domains after any ion bombardment may appear to contrast with Fig. 6.5 and Ref. [34], where significant variations in switching voltage are observed only with bombardment above 10<sup>15</sup> ions/cm<sup>2</sup>; and with as Fig. 6.8(a), where similar scaling parameters are observed across all samples. How can similar distributions of event sizes be observed in both the as-grown sample with strong, highly directional pinning by  $a$ -domains, and in the ion-bombarded samples with an increased but not presumably directional collective pinning due to the He<sup>2+</sup> ions?

This answer is revealed by the switching maps themselves [Fig 6.4(f–j)]. In the most bombarded sample [Fig. 6.4(j)], significant pinning appears parallel to the crystallographic axes, but far removed from any observed  $a$ -domains. These regions act akin to the  $a$ -domains and contribute to a similar distribution of small and large events among all samples. Likewise, while the switching voltages may change, these changes need not impact switching event size.

As to the nature of these regions, we note that the identical and simultaneous growth of these thin films minimises potential variations between them. Rather, the only notable difference between these samples is the increasing level of He<sup>2+</sup> bombardment and the resulting point-defect density, which must therefore selectively segregate or orient along the crystallographic axes.

Indeed, previous simulations actually suggest that aligned point defects may have strikingly similar pinning effects to those of  $a$ -domains. Kimmel *et al.* used *ab initio* calculations to show that oxygen vacancies prefer  $c$ -axis sites over  $a$ -axis sites, and this preference can drive the rotation of the entire unit cell around the vacancy [47]. In our case, defects induced

## 6. The Interplay Between Point and Extended Defects and their Effects on Jerky Domain-Wall Motion in Ferroelectric Thin Films

---

by  $\text{He}^{2+}$  ion bombardment could be a preferential site for oxygen vacancy co-localisation, and thus drive such axial rotations, resulting in the formation of features acting akin to  $a$ -domains, with associated directional pinning in the bombarded samples.

The implications of this screening of  $a$ -domain pinning by point defects are twofold. First, our work suggests that the key to more controllable ferroelectric switching may not be more perfect, less-defective films, but indeed the opposite, with induced defects ensuring more consistent switching dynamics. Meanwhile, at the nanoscale, the inferred organisation of point-defects along crystallographic axes could potentially lead to the formation and stabilisation of new polarisation textures.

### 6.5 Conclusions

In summary, we investigated the interplay between extended quasi-1-dimensional ( $a$ -domain) and point ( $\text{He}^{2+}$  bombardment and implantation) defects, and their effects on ferroelectric switching and domain-wall motion. We found more intense  $\text{He}^{2+}$  bombardment associated with an increase in coercive voltage. Despite the subsequent increase in driving voltages required, all samples maintained a power-law distribution of switching event size dominated by creep dynamics, with critical exponent values highly stable both within an individual experiment and across samples that had undergone different levels of  $\text{He}^{2+}$  bombardment. We simultaneously observed a remarkable local-scale interaction between the bombardment defects and the  $a$ -domains, where the point defects appear to ‘dress’ the extended defects, effectively screening their pinning strength. Such additional point defects can thus induce more uniform and predictable domain-wall dynamics. Moreover, at increasing  $\text{He}^{2+}$  bombardment densities, the point defects themselves appear to segregate and align with the crystalline axes of the ferroelectric, giving rise to directional pinning more evenly distributed through the sample. This understanding of the effects of  $a$ -domains and point defects on ferroelectric switching dynamics and scaling parameters can therefore help to further enhance ferroelectric device performance via defect engineering.

## References

- [1] R. Bulanadi, K. Cordero-Edwards, P. Tückmantel, G. Morpurgo, Q. Zhang, L. W. Martin, V. Nagarajan, and P. Paruch, “The interplay between point and extended defects and their effects on jerky domain-wall motion in ferroelectric thin films”, Physical Review Letters [Accepted].

- 
- [2] P. Muralt, “Ferroelectric thin films for micro-sensors and actuators: a review”, *Journal of Micromechanics and Microengineering* **10**, 136 (2000).
  - [3] P. Lopez-Varo, L. Bertoluzzi, J. Bisquert, M. Alexe, M. Coll, J. Huang, J. A. Jimenez-Tejada, T. Kirchartz, R. Nechache, F. Rosei, et al., “Physical aspects of ferroelectric semiconductors for photovoltaic solar energy conversion”, *Physics Reports* **653**, 1–40 (2016).
  - [4] J. F. Scott and C. A. P. De Araujo, “Ferroelectric memories”, *Science* **246**, 1400–1405 (1989).
  - [5] A. Yadav, C. Nelson, S. Hsu, Z. Hong, J. Clarkson, C. Schlepütz, A. Damodaran, P. Shafer, E. Arenholz, L. Dedon, et al., “Observation of polar vortices in oxide superlattices”, *Nature* **530**, 198–201 (2016).
  - [6] I. I. Naumov, L. Bellaiche, and H. Fu, “Unusual phase transitions in ferroelectric nanodisks and nanorods”, *Nature* **432**, 737–740 (2004).
  - [7] C.-L. Jia, K. W. Urban, M. Alexe, D. Hesse, and I. Vrejoiu, “Direct observation of continuous electric dipole rotation in flux-closure domains in ferroelectric  $\text{Pb}(\text{Zr,Ti})\text{O}_3$ ”, *Science* **331**, 1420–1423 (2011).
  - [8] S. Das, Y. Tang, Z. Hong, M. Gonçalves, M. McCarter, C. Klewe, K. Nguyen, F. Gómez-Ortiz, P. Shafer, E. Arenholz, et al., “Observation of room-temperature polar skyrmions”, *Nature* **568**, 368–372 (2019).
  - [9] B.-K. Lai, I. Ponomareva, I. Naumov, I. Kornev, H. Fu, L. Bellaiche, and G. Salamo, “Electric-field-induced domain evolution in ferroelectric ultrathin films”, *Physical Review Letters* **96**, 137602 (2006).
  - [10] G. Catalan, J. Seidel, R. Ramesh, and J. F. Scott, “Domain wall nanoelectronics”, *Reviews of Modern Physics* **84**, 119 (2012).
  - [11] D. Meier, “Functional domain walls in multiferroics”, *Journal of Physics: Condensed Matter* **27**, 463003 (2015).
  - [12] E. K. Salje, “Multiferroic domain boundaries as active memory devices: trajectories towards domain boundary engineering”, *ChemPhysChem* **11**, 940–950 (2010).
  - [13] D. Damjanovic, “Hysteresis in piezoelectric and ferroelectric materials”, *Science of Hysteresis*, 337–465 (2006).
  - [14] Y. Feng, J. Wu, Q. Chi, W. Li, Y. Yu, and W. Fei, “Defects and aliovalent doping engineering in electroceramics”, *Chemical Reviews* **120**, 1710–1787 (2020).
  - [15] W. Dong, H. Xiao, Y. Jia, L. Chen, H. Geng, S. U. H. Bakhtiar, Q. Fu, and Y. Guo, “Engineering the defects and microstructures in ferroelectrics for enhanced/novel properties: an emerging way to cope with energy crisis and environmental pollution”, *Advanced Science* **9**, 2105368 (2022).

## **6. The Interplay Between Point and Extended Defects and their Effects on Jerky Domain-Wall Motion in Ferroelectric Thin Films**

---

- [16] D. Sando, T. Young, R. Bulanadi, X. Cheng, Y. Zhou, M. Weyland, P. Munroe, and V. Nagarajan, “Designer defect stabilization of the super tetragonal phase in >70-nm-thick BiFeO<sub>3</sub> films on LaAlO<sub>3</sub> substrates”, *Japanese Journal of Applied Physics* **57**, 0902B2 (2018).
- [17] A. Kashir, S. Oh, and H. Hwang, “Defect engineering to achieve wake-up free HfO<sub>2</sub>-based ferroelectrics”, *Advanced Engineering Materials* **23**, 2000791 (2021).
- [18] B. Noheda, P. Nukala, and M. Acuautila, “Lessons from hafnium dioxide-based ferroelectrics”, *Nature Materials* **22**, 562–569 (2023).
- [19] P. Zubko, J. C. Wojdeł, M. Hadjimichael, S. Fernandez-Pena, A. Sené, I. Luk’yanchuk, J.-M. Triscone, and J. Íñiguez, “Negative capacitance in multidomain ferroelectric superlattices”, *Nature* **534**, 524–528 (2016).
- [20] S. Saremi, R. Xu, L. R. Dedon, J. A. Mundy, S.-L. Hsu, Z. Chen, A. R. Damodaran, S. P. Chapman, J. T. Evans, and L. W. Martin, “Enhanced electrical resistivity and properties via ion bombardment of ferroelectric thin films”, *Advanced Materials* **28**, 10750–10756 (2016).
- [21] J. Kim, S. Saremi, M. Acharya, G. Velarde, E. Parsonnet, P. Donahue, A. Qualls, D. Garcia, and L. W. Martin, “Ultrahigh capacitive energy density in ion-bombarded relaxor ferroelectric films”, *Science* **369**, 81–84 (2020).
- [22] S. Kang, W.-S. Jang, A. N. Morozovska, O. Kwon, Y. Jin, Y.-H. Kim, H. Bae, C. Wang, S.-H. Yang, A. Belianinov, et al., “Highly enhanced ferroelectricity in HfO<sub>2</sub>-based ferroelectric thin film by light ion bombardment”, *Science* **376**, 731–738 (2022).
- [23] S. Aggarwal and R. Ramesh, “Point defect chemistry of metal oxide heterostructures”, *Annual Review of Materials Science* **28**, 463–499 (1998).
- [24] S. V. Kalinin, S. Jesse, A. Tselev, A. P. Baddorf, and N. Balke, “The role of electrochemical phenomena in scanning probe microscopy of ferroelectric thin films”, *ACS Nano* **5**, 5683–5691 (2011).
- [25] D. M. Evans, T. S. Holstad, A. B. Mosberg, D. R. Småbråten, P. E. Vullum, A. L. Dadlani, K. Shapovalov, Z. Yan, E. Bourret, D. Gao, et al., “Conductivity control via minimally invasive anti-Frenkel defects in a functional oxide”, *Nature Materials* **19**, 1195–1200 (2020).
- [26] S. Jesse, B. J. Rodriguez, S. Choudhury, A. P. Baddorf, I. Vrejoiu, D. Hesse, M. Alexe, E. A. Eliseev, A. N. Morozovska, J. Zhang, et al., “Direct imaging of the spatial and energy distribution of nucleation centres in ferroelectric materials”, *Nature Materials* **7**, 209–215 (2008).

- 
- [27] M. Raymond and D. Smyth, “Defects and charge transport in perovskite ferroelectrics”, *Journal of Physics and Chemistry of Solids* **57**, 1507–1511 (1996).
  - [28] A. Pramanick, A. D. Prewitt, J. S. Forrester, and J. L. Jones, “Domains, domain walls and defects in perovskite ferroelectric oxides: a review of present understanding and recent contributions”, *Critical Reviews in Solid State and Materials Sciences* **37**, 243–275 (2012).
  - [29] C. Stefani, L. Ponet, K. Shapovalov, P. Chen, E. Langenberg, D. G. Schlom, S. Artyukhin, M. Stengel, N. Domingo, and G. Catalan, “Mechanical softness of ferroelectric 180° domain walls”, *Physical Review X* **10**, 041001 (2020).
  - [30] L. Puntigam, M. Althaler, S. Ghara, L. Prodan, V. Tsurkan, S. Krohns, I. Kézsmárki, and D. M. Evans, “Strain driven conducting domain walls in a Mott insulator”, *Advanced Electronic Materials* **8**, 2200366 (2022).
  - [31] E. K. Salje and X. Ding, “Ferroelastic domain boundary-based multiferroicity”, *Crystals* **6**, 163 (2016).
  - [32] H. Guo, S. Dong, P. D. Rack, J. D. Budai, C. Beekman, Z. Gai, W. Siemons, C. Gonzalez, R. Timilsina, A. T. Wong, et al., “Strain doping: reversible single-axis control of a complex oxide lattice via helium implantation”, *Physical Review Letters* **114**, 256801 (2015).
  - [33] E. D. Roede, A. B. Mosberg, D. M. Evans, E. Bourret, Z. Yan, A. T. van Helvoort, and D. Meier, “Contact-free reversible switching of improper ferroelectric domains by electron and ion irradiation”, *APL Materials* **9** (2021).
  - [34] S. Saremi, J. Kim, A. Ghosh, D. Meyers, and L. W. Martin, “Defect-induced (dis) order in relaxor ferroelectric thin films”, *Physical Review Letters* **123**, 207602 (2019).
  - [35] S. Jesse, A. P. Baddorf, and S. V. Kalinin, “Switching spectroscopy piezoresponse force microscopy of ferroelectric materials”, *Applied Physics Letters* **88**, 062908 (2006).
  - [36] P. Tückmantel, I. Gaponenko, N. Caballero, J. C. Agar, L. W. Martin, T. Giamarchi, and P. Paruch, “Local probe comparison of ferroelectric switching event statistics in the creep and depinning regimes in  $\text{Pb}(\text{Zr}_{0.2}\text{Ti}_{0.8})\text{O}_3$  thin films”, *Physical Review Letters* **126**, 117601 (2021).
  - [37] P. Paruch and J. Guyonnet, “Nanoscale studies of ferroelectric domain walls as pinned elastic interfaces”, *Comptes Rendus Physique* **14**, 667–684 (2013).



## **6. The Interplay Between Point and Extended Defects and their Effects on Jerky Domain-Wall Motion in Ferroelectric Thin Films**

---

- [38] J. P. Sethna, K. A. Dahmen, and C. R. Myers, “Crackling noise”, *Nature* **410**, 242–250 (2001).
- [39] N. Friedman, A. T. Jennings, G. Tsekenis, J.-Y. Kim, M. Tao, J. T. Uhl, J. R. Greer, and K. A. Dahmen, “Statistics of dislocation slip avalanches in nanosized single crystals show tuned critical behavior predicted by a simple mean field model”, *Physical Review Letters* **109**, 095507 (2012).
- [40] E. K. Salje and K. A. Dahmen, “Crackling noise in disordered materials”, *Annu. Rev. Condens. Matter Phys.* **5**, 233–254 (2014).
- [41] E. Salje, D. Xue, X. Ding, K. A. Dahmen, and J. Scott, “Ferroelectric switching and scale invariant avalanches in BaTiO<sub>3</sub>”, *Physical Review Materials* **3**, 014415 (2019).
- [42] C. Tan, C. Flannigan, J. Gardner, F. Morrison, E. Salje, and J. Scott, “Electrical studies of Barkhausen switching noise in ferroelectric PZT: critical exponents and temperature dependence”, *Physical Review Materials* **3**, 034402 (2019).
- [43] B. Casals, G. F. Nataf, D. Pesquera, and E. K. Salje, “Avalanches from charged domain wall motion in BaTiO<sub>3</sub> during ferroelectric switching”, *APL Materials* **8**, 011105 (2020).
- [44] T. Tybell, P. Paruch, T. Giamarchi, and J.-M. Triscone, “Domain wall creep in epitaxial ferroelectric Pb(Zr<sub>0.2</sub>Ti<sub>0.8</sub>)O<sub>3</sub> thin films”, *Physical Review Letters* **89**, 097601 (2002).
- [45] E. N. Mortensen and W. A. Barrett, “Morphological interpolation between contour lines”, in *Medical imaging 1993: image processing*, Vol. 1898 (International Society for Optics and Photonics, 1993), pp. 501–510.
- [46] A. Clauset, C. R. Shalizi, and M. E. Newman, “Power-law distributions in empirical data”, *SIAM Review* **51**, 661–703 (2009).
- [47] A. V. Kimmel, P. M. Weaver, M. G. Cain, and P. V. Sushko, “Defect-mediated lattice relaxation and domain stability in ferroelectric oxides”, *Physical Review Letters* **109**, 117601 (2012).

---

## Tracking the Nanoscale Dynamics of Martensitic-like Phase Transitions via Interferometric Nanoindentation

---

Bismuth ferrite ( $\text{BiFeO}_3$ , BFO) is a multiferroic material that, though of rhombohedral structure in bulk, can be grown as a thin film to stabilise rhombohedral-like (R') or, at higher compressive strains, tetragonal-like (T') monoclinic phases [1–4]. Films grown in the T' phase tend to undergo a stress-induced martensitic-like phase transition to form a localised mixture of both T' and R' phases [5, 6]. This local, stress-induced symmetry breaking provides a fascinating playground to investigate the effects and dynamics of these martensitic-like phase transitions at the nanoscale. While in previous chapters we have used scanning probe microscopy to image sub- $\mu\text{m}$  domain switching events, we here attempt the first direct-probe characterisation of these structural phase transition dynamics.

To achieve this goal, we utilise a new quadrature-phase differential interferometry detector in an atomic force microscope, and demonstrate its capability to measure the avalanche statistics and consistent critical scaling phenomena that arise from the nanoindentation and plastic deformation of a standard lead titanate ( $\text{PbTiO}_3$ , PTO) thin film. In addition, we have grown a BFO thin film in a pulsed-laser deposition chamber with a unique geometry that encourages the formation of point defects that stabilise the T' phase to a 70-nm thickness. We perform these same nanoindentation–avalanche measurements on this ultrathick T'-BFO film, and compare the distinct scaling phenomena.

We observe that the scaling characteristics of the T'-BFO film under

## 7. Tracking the Nanoscale Dynamics of Martensitic-like Phase Transitions via Interferometric Nanoindentation

---

nanoindentation are distinct from those of the tetragonal PTO. We attribute this distinct scaling behavior to the martensitic-like phase transition between T' and R' phases of BFO. Our observations are compatible with theoretical predictions of martensitic-like phase transitions in a simplified 2-dimensional system. In doing so, we take key steps forward in the characterisation of nanoscale phase-transition dynamics, and also demonstrate the capability for quadrature-phase differential interferometry in atomic force microscopy to investigate these structural phase transitions.

This Chapter is based on a publication in preparation. The present version of this manuscript has been written by R. Bulanadi and P. Paruch, with substantial scientific and experimental contributions by R. Bulanadi, J. Lefever, I. Gaponenko, K.-F. Luo, S. Saremi, L. W. Martin, V. Nagarajan, R. Proksch, and P. Paruch. The final version of this manuscript is expected to be submitted with approval and co-authorship with these collaborators. R. Bulanadi conceived and executed these nanoindentation measurements, with support and supervision by I. Gaponenko and P. Paruch. J. Lefever and R. Proksch provided access and training on the use of the *Asylum Research Vero* AFM. K.-F. Luo, S. Saremi, L. W. Martin, and V. Nagarajan provided the samples.

I would also like to thank Prof. Jirka Hlinka (Czech Academy of Sciences) for fruitful conversations about phase transitions, Aleks Labuda and Dara Walters (Asylum Research) for their assistance with the *Vero*, and Dr. Daniel Sando (University of Canterbury) for suggestions on BFO growth and characterisation. This work was supported by the Swiss National Science Foundation under Division II (Grant No. 200021-178782).

### 7.1 Introduction

As temperature or another non-conjugate parameter is varied across the critical point, ferroelectric materials undergo a symmetry-lowering structural phase transition characterised by the appearance of a spontaneous polarisation [7–11]. When these transitions are second-order, with a continuous change of the order parameter across symmetry-compatible structures, the rate at which the order parameter changes near the critical point is expected to follow power-law dynamics [7–11], with  $P \propto (T - T_C)^{-\alpha}$ , where  $P$  is the polarisation,  $T$  the temperature,  $T_C$  its critical point value, and  $\alpha$  the critical exponent. This critical exponent can be universal across physically distinct systems, with values reflecting a more general character, such as dimension or symmetry, and independent of the microscopic material parameters [12, 13]. This generality is made more extensive by self-organised criticality—a principle where local physics can act to drive a system to a critical point in which some critical phenomena is observed [14–16].

One case where self-organised criticality occurs is in martensitic phase transitions [12, 13, 17, 18]—phase transitions in which atoms move cooperatively along an interface to produce a shape change [13, 19]—whose external application leads to the formation of martensitic phases, which in turn locally reduce the internal strain of the system and therefore inhibit further phase transformations. This negative feedback loop drives self-organisation around the critical strain, and thus, martensitic phase transformations are expected to reasonably follow power-law dynamics, even when the applied stresses are comparatively far from some critical threshold. This behaviour has been observed experimentally by monitoring the acoustic emissions as a function of applied strain [13], and this work and subsequent theoretical investigations have suggested that the critical exponents varies depending on the symmetry of the resulting martensitic phase [12, 13].

While prior work investigated martensitic transitions from macroscale forces on large polycrystalline metal alloys, and they play an important role from metallurgical considerations, research on the critical behaviour of thin films and other nanoscale disordered materials has been less intensive. These materials are of particular interest as many ferroic materials of industrial and research applications, like bismuth ferrite ( $\text{BiFeO}_3$ —BFO) thin films, express martensitic-like phase transitions [1–4]. In BFO, this martensitic-like transition occurs between a tetragonal-like monoclinic phase (T'-phase) and a rhombohedral-like monoclinic phase (R'-phase), where the T'-phase can give way to a mixed T'-phase and R'-phase region, both of which have distinct ferroelectric and magnetic properties [5, 6].

Control and understanding of this phase transition and associated multi-ferroic properties could be of immense research and industrial interest, but any investigation of these properties are limited by the small size of the R'-phase domains. While the nanoscale power-law dynamics of ferroelastic and ferroelectric domains can be imaged via optical [20, 21] or scanning probe microscopy (See Ref. [22], or Chapters 5–6), even these methods examine regions far greater in size than relevant R'-phase transitions. More generally, nanoscale investigations of this particular material system could be compared to other material systems to observe the effects of, for example, local symmetry changes. Recently, Nguyen *et al.* have proposed 'crackling noise microscopy' measurements [23] in which optical beam deflection is used to infer avalanche behaviour under increasing force applied by a stationary diamond probe, but low signal-to-noise limits the validity of the measured power-law fit to half-decade ranges.

Despite this prior difficulty, recent improvements in interferometric detectors in atomic force microscope systems has enabled key advancements in local investigation of these critical phenomena. *Asylum Research* has developed quadrature-phase differential interferometric (QPDI) detectors [24] for new-generation atomic force microscopes, for example, which allow for more

## 7. Tracking the Nanoscale Dynamics of Martensitic-like Phase Transitions via Interferometric Nanoindentation

---

quantitative measurements of strain [25], with an approximate 10x drop in the noise floor. These advantages complement the more linear response regimes of quadrature-phase interferometry measurements at high displacements, which reduce false hysteretic responses and allow for the measurement of the high displacements intrinsic to martensitic and martensitic-like phase transitions [24].

Here, we therefore use a QPDI detector in an atomic force microscope, along with high forces applied by a diamond probe, to drive and investigate the critical scaling behaviour of the T' to R' martensitic-like phase transition in BFO. We compare these observations to the scaling behaviour of plastic deformation on lead titanate ( $\text{PbTiO}_3$ —PTO) thin films, in which no structural phase change occurs as a result of the applied mechanical force. As hoped, we find that the difference in symmetry constraints in the deformation mechanisms in these two samples results in distinct values of the critical exponent. Our investigations both verify the capability of QPDI to measure the scaling parameter of ferroelectric thin films, and also advance our understanding of nanoscale martensitic-like phase transitions in general, and of the multiferroic phase transitions in BFO in particular.

### 7.2 Nanoindentation and Critical Scaling from Plastic Deformation

To verify the capability of nanoindentation and QPDI to measure critical phenomena, we first investigate PTO, a tetragonal perovskite oxide ferroelectric, readily grown in epitaxial thin film form on single-crystal substrates [26]. As discussed in Chapter 6, avalanche statistics related to phase transitions have been well reported. In the ferroelectric tetragonal phase, PTO is conformationally restricted to combinations of out-of-plane  $c$ -domains, and in-plane  $a_1$ - or  $a_2$ -domains [27, 28], which are guided by internal stresses, and can be engineered during growth by choice of substrate, temperature, and partial oxygen pressure to adopt an out-of-plane polarisation axis orientation with little to no in-plane oriented  $a$ -domains [29–31].

Under high stress and nanoindentation studies with no applied electric field, we do not expect changes between the different domain conformations in such films to be relevant. The  $180^\circ$  domain walls between oppositely oriented out-of-plane domains are not ferroelastic [32], and so out-of-plane switching, even when possible (induced by flexoelectric effects, for example [33]), should not affect sample strains. The  $90^\circ$  domain walls between  $a$ - and  $c$ -domains are ferroelastic [32], but previous reports on flexoelectric switching in such films suggest that  $c$ -domains are preferentially formed under nanoindentation [33–35]. We therefore expect PTO thin films with predominantly out-of-plane polarisation to be stable against particular structural phase transitions, and

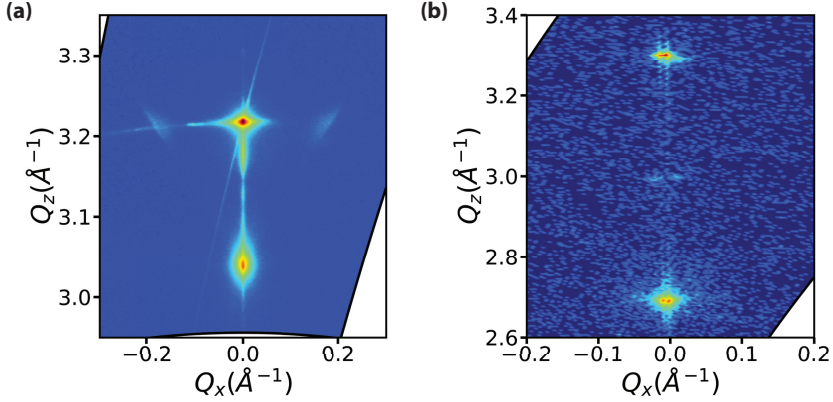


**Figure 7.1:** *X-ray diffraction reciprocal space maps of the (002) reflection of our ferroelectric thin films. (a) A film of 140 nm PTO on STO (001), with a 20 nm SRO interelectrode. (b) A film of 70 nm T'-phase BFO grown on LAO (001)*

therefore provide a useful control system in which we consider only the effects of plastic deformation from nanoindentation. In this case, mean-field theory suggests that slip-avalanches—which we expect to be a major contributor to plastic deformation in single crystals—should express a stress-independent distribution of events with a critical exponent of precisely 2 [36, 37]. We therefore would expect an event distribution with a critical exponent similar to this value.

The 140 nm PTO thin film used in this studies was grown by PLD on a (001)-oriented  $\text{SrTiO}_3$  substrate, with a 20 nm  $\text{SrRuO}_3$  bottom electrode. This particular PFM thin film corresponds to the film bombarded by  $10^{13} \text{ He}^{2+}$  ions/ $\text{cm}^2$  (lowest bombardment) discussed through Chapter 6.

In brief, PTO films were grown via pulsed laser deposition (PLD) on  $\text{SrTiO}_3$  (001) substrates (Crys-Tec GmbH), with a 20 nm  $\text{SrRuO}_3$  bottom electrode. The film was grown to 140-nm thick, such that  $a$ -domains to form during growth. These  $a$ -domains, and the greater crystallographic structure, can be observed via x-ray diffraction reciprocal space mapping [Fig. 7.1(a)]. PFM measurements also show a polydomain structure, as well as shorter  $a$ -domains (Fig. 7.2). Given the extremely small size of the  $a$ -domains, compared to the slide and penetration depth of the indentation, we did not concern ourselves with  $a$ -domain position. As discussed in Chapter 6, a scaling parameter of  $\alpha = 2.0$  was measured for out-of-plane ferroelectric switching, which, curiously, we will find is almost identical to the scaling parameter acquired here.

Nanoindentation was performed with single crystal diamond tips (Adama Innovations, Ireland), with a spring constant determined via a thermal

## 7. Tracking the Nanoscale Dynamics of Martensitic-like Phase Transitions via Interferometric Nanoindentation

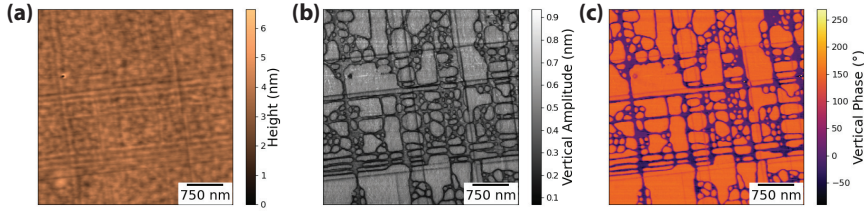


**Figure 7.2:** Sample raw PFM data of the as-grown 140 nm PTO/20 nm SRO/STO (001) thin films. The channels shown represent (a) height, (b) amplitude, and (c) phase.

method as 68.275 N/m. The tip was approached to the sample surface until contact, with the indentation force increased to 100  $\mu\text{N}$  over a period of approximately 3 minutes, before the tip was retracted at approximately the same rate. Data were collected at a rate of 50 kHz, yielding well over  $10^7$  datapoints per repetition.

This indentation process created a high-resolution, low-noise force-indentation curve, which can be seen in Fig. 7.3. Initially, as the tip is brought into contact with the sample, snap-in occurs resulting in a sudden drop of force applied (lower inset, red). The indentation depth then gradually increases (marked by a decrease in separation, here defined as the difference between tip height and interferometric displacement) with an increase in applied force. After the 100  $\mu\text{N}$  force trigger is achieved, the tip begins to slowly retract from the sample. The release of the tip from the sample is marked by pull-off effects (lower inset, blue), which occur at a separation approximately 25 nm lower than the snap-in effects.

This high resolution force curve highlights two interesting phenomena. First, the high forces create significant deformation; the tip is observed to indent 130 nm into the sample, of which 25 nm are attributed to plastic deformation. This plastic deformation can be observed as troughs in the film surface in subsequent AFM micrographs (Fig. 7.4). Given that the film is grown to 140 nm in thickness, it is reasonable to expect that all plastic deformation occurs in the film itself, rather than the underlying substrate.

Second, close inspection of this high-resolution force curve reveals small, erratic, and non-linear jumps in indentation (upper inset). These jumps correspond to ‘avalanches’, where large regions of the material yield concurrently. These avalanches are intrinsic to disordered crystalline materials like these thin films, where local changes in response to a stimulus can drive changes in adjacent regions of the material, leading to large-scale collective behaviour.

Given the gradual indentation of the tip into the sample surface, and to increase comparability with prior mean-field theory work [36, 37], we here consider our avalanche events as sudden changes in the velocity  $v$  of the

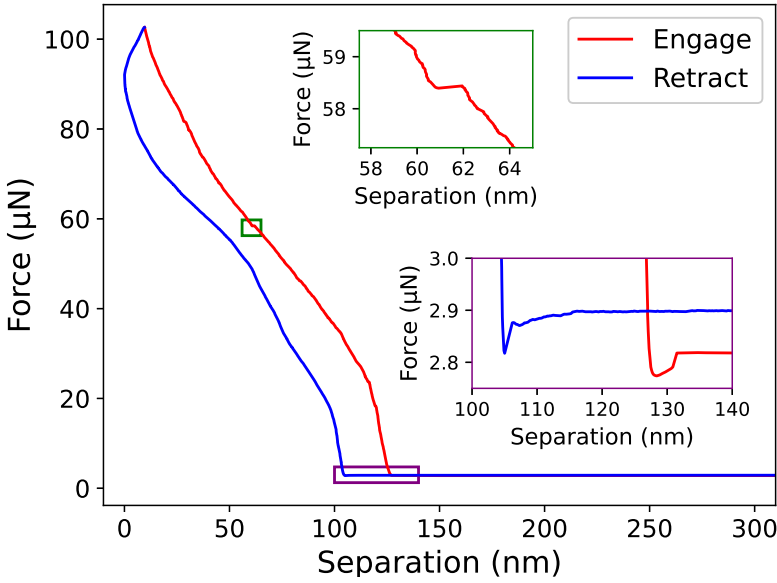


**Figure 7.3:** High resolution force curve on PTO thin films generated through quadrature-phase differential interferometry. Main figure: Force curve showing indentation force as a function of indentation. Upper inset (green): A section of the force curve that shows jumps in the indentation during tip engage. Lower inset (purple): A section of the force curve that shows snap-in and pull-off phenomena, as well as  $\sim 25$  nm of plastic deformation.

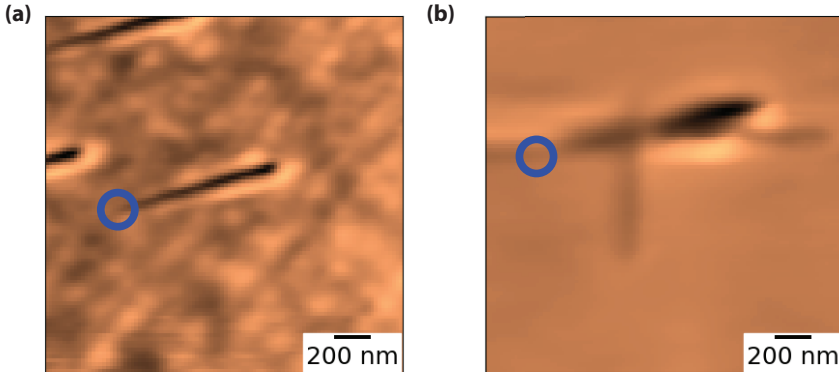


**Figure 7.4:** Sample contact-mode atomic force microscopy images of the samples after indentation. Blue circles mark the initial point of indentation. (a) Indentation on the PTO thin film. (b) Indentation on the BFO thin film, showing the formation of some R'-phase.



## 7. Tracking the Nanoscale Dynamics of Martensitic-like Phase Transitions via Interferometric Nanoindentation

---

tip motion during the engagement and approach of the tip. The events are therefore defined as  $E$ , where:

$$E \propto \left( \Delta \frac{dh}{dt} \right)^2 \quad (7.1)$$

To maximise physicality in the observed power-law spectra, we analysed only data collected when the tip was pressing into the sample. To avoid the impact of attractive van der Waals interactions (at low forces) and potential non-linearity (at high forces), we further limited our dataset to only events generated when the applied forces were between 15  $\mu\text{N}$  and 90  $\mu\text{N}$ . To increase statistics and generality, three indentations were performed at three different locations on the sample. For the following analysis, the data from all three indentations were collapsed into a single dataset containing 19222 independent events, but an analysis of measurement-by-measurement data is reported in the Supplementary Material.

This full, collated power-law spectra is shown in Fig. 7.5(a–c), and a log-log plot of event frequency against event size with logarithmic binning can be seen in Fig. 7.5(d). A clear linear trend is visible. As outlined in Section 2.5, we verify the gradient of this linear trend by assessing the likelihood ( $L$ ) of all possible scaling parameters for the power-law fit; that is:

$$L(\theta) = \prod_{i=1}^n f(x_i; \theta) \quad (7.2)$$

where  $\theta$  is the scaling parameter assessed for the function  $f$  that is used to describe events  $x_1, x_2, \dots, x_n$ . Here, the scaling parameter  $\alpha$  is assessed in the probability-density function for a power-law fit:

$$p_X(x) = \frac{\alpha - 1}{x_{min}} \left( \frac{x}{x_{min}} \right)^{-\alpha} \quad (7.3)$$

where  $x_{min}$  is the minimum event size cutoff for which the probability-density function holds. The maximum-likelihood exponent can therefore be assessed as:

$$\hat{\alpha} = 1 + n \left( \sum_{i=1}^n \log \frac{x_i}{x_{min}} \right)^{-1} \quad (7.4)$$

which is itself still a function of  $x_{min}$ , the minimum event cutoff. A plot against  $\hat{\alpha}$  against  $x_{min}$  can therefore be used gauge the stability of the power-law fit: if  $\hat{\alpha}$  varies greatly with a change in  $x_{min}$ , then  $\hat{\alpha}$  also varies greatly with the precise datapoints included or excluded, which implies the power-law fit is not valid. On the contrary, if  $\hat{\alpha}$  is stable over a large

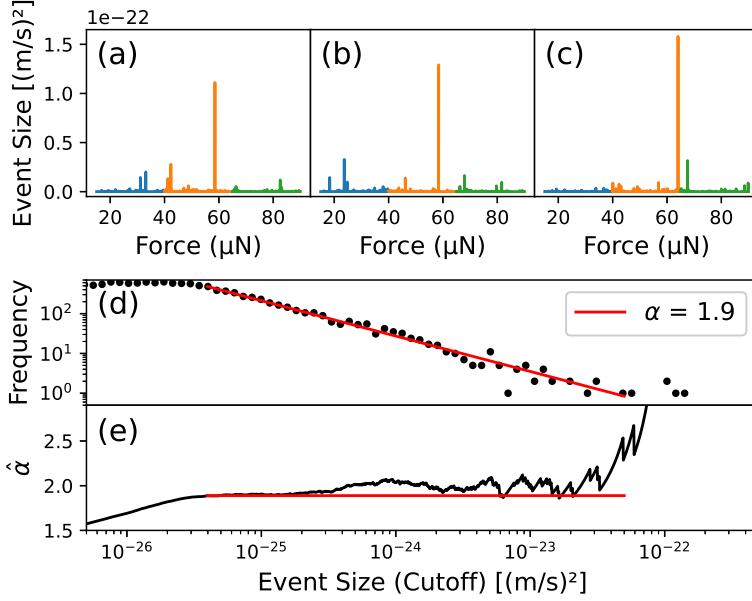


**Figure 7.5:** *Avalanche statistics from nanoindentation on PTO thin films* (a–c) Event spectra from three repetitions on three different positions on the sample. Blue lines represent ‘low’ forces ( $15 \mu\text{N} < F < 40 \mu\text{N}$ ), orange lines represent ‘medium’ forces ( $40 \mu\text{N} < F < 65 \mu\text{N}$ ), and green lines represent ‘high’ forces ( $65 \mu\text{N} < F < 90 \mu\text{N}$ ), (d) log-log plot of event size and frequency, showing a linear trend. (e) Maximum likelihood estimate of the scaling parameter, as a function of event size cutoff.

## 7. Tracking the Nanoscale Dynamics of Martensitic-like Phase Transitions via Interferometric Nanoindentation

---

range, then the power-law fit is likely appropriate over that range, with  $\hat{\alpha}$  a reasonable estimate of the scaling parameter.

For this dataset, we have a consistent scaling parameter estimate of  $\hat{\alpha} = 1.9$  across more than three orders of magnitude of event size in the plot of the maximum-likelihood estimate [Fig. 7.5(b)], and this correlates well with the log-log plot of event size and frequency in Fig. 7.5(a). This same trend is observed in all three measurements performed at different locations of the sample (Figs. 7.7–7.9). The value of the critical exponent we obtain is almost identical to theoretical predictions of  $\alpha = 2$  from mean-field theory [36, 37].

We note, however, that while this scaling parameter appears to be location-independent, we observe what appears to be a force-dependant indentation rate. This can be seen in the slight S-shape of the force curve shown in Fig. 7.3; the amount of indentation depth as a function of force appears to be greater at intermediate forces than at forces that are either much lower or much higher. This can also be inferred from Fig. 7.5(a–c), where the largest spikes in velocity all occur at intermediate forces of approximately  $60 \mu\text{N}$  in all three repetitions.

This apparent force-dependent indentation rate be physically meaningful. First, it could imply the presence of characteristically distinct phenomena at different forces (such as, for example, a transition from creep to depinning regimes in the dynamic response) in which case we may expect different values of the scaling parameter [22]. Alternatively, it could be an artefact related to the specific nanoindentation configuration used in our experiments – as a result of the horizontal sliding of the tip, and the clearly visible ploughing of the sample surface, at the highest applied forces more energy is lost in horizontal displacement of material than at intermediate or small forces. In such a case, scaling parameter should nonetheless show consistent values in agreement with the plastic deformation predictions at all forces.

To discriminate between these two scenarios, we separated each of our three repetitions into regions of different force—‘low’ forces ( $15 \mu\text{N}$  to  $40 \mu\text{N}$ ), ‘medium’ forces ( $40 \mu\text{N}$  to  $65 \mu\text{N}$ ), and ‘high’ forces ( $65 \mu\text{N}$  to  $90 \mu\text{N}$ )—and then collate data correspondingly. We then performed our maximum-likelihood analysis of the scaling parameters in these three force categories, as shown in Fig. 7.6. We find that in all three force categories, we obtain the same or similar scaling parameters as when we consider the entire collated dataset (albeit at a shorter range than shown in Fig 7.5, which is expected given the truncated dataset in each category). These results suggest that we are indeed here measuring the expected plastic deformation in a single phase material with no martensitic-like structural transitions.

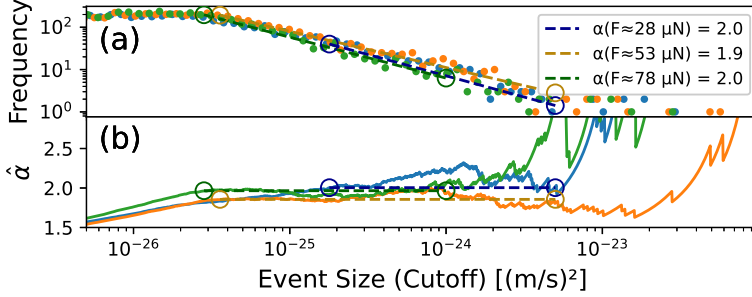


**Figure 7.6:** *Avalanche statistics from nanoindentation on PTO thin films, split into distinct force regimes. (a) log-log plot of event size and frequency, showing a linear trend overlapping between all forces. (b) Maximum likelihood estimate of the scaling parameter, as a function of event size cutoff, showing a linear trend overlapping between all forces.*

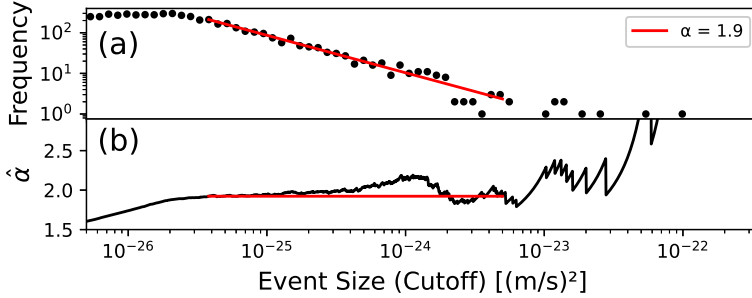


**Figure 7.7:** *Avalanche statistics from a first measurement of nanoindentation on PTO thin films. (a) log-log plot of event size and frequency. (b) Maximum likelihood estimate of the scaling parameter, as a function of event size cutoff.*

### 7.2.1 Verification of Measured Scaling Parameters

To ensure the reliability of this technique, we performed multiple supplementary measurements.

*Reproducibility between measurements:* The log-log plots and maximum-likelihood exponents reported in the main manuscript are produced by first collapsing multiple nanoindentations experiments performed at different locations into a single dataset. These datasets are shown individually for PTO in Figs. 7.7–7.9, and for BFO in Figs. 7.10–7.12. The scaling parameters for each individual measurement are roughly equal to one another, and to the collated dataset, but as expected to a lower extent. This verifies that each measurement is highly reproducible.

*Stability between measurements:* After the conclusion of nanoindentation

## 7. Tracking the Nanoscale Dynamics of Martensitic-like Phase Transitions via Interferometric Nanoindentation

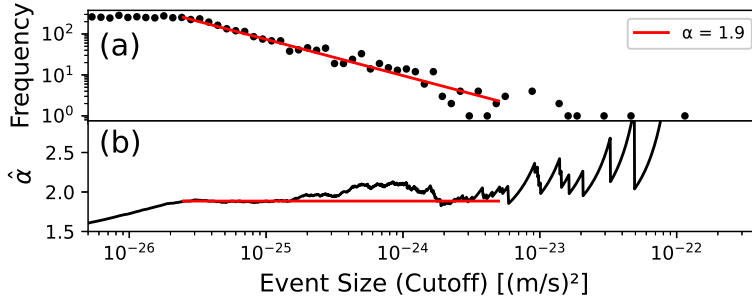


**Figure 7.8:** *Avalanche statistics from a second measurement of nanoindentation on PTO thin films. (a) log-log plot of event size and frequency. (b) Maximum likelihood estimate of the scaling parameter, as a function of event size cutoff.*

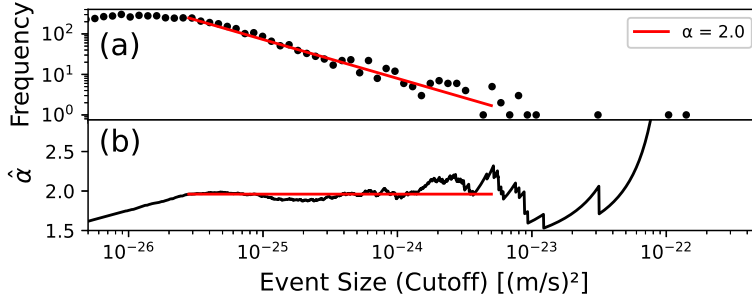


**Figure 7.9:** *Avalanche statistics from a third measurement of nanoindentation on PTO thin films. (a) log-log plot of event size and frequency. (b) Maximum likelihood estimate of the scaling parameter, as a function of event size cutoff.*

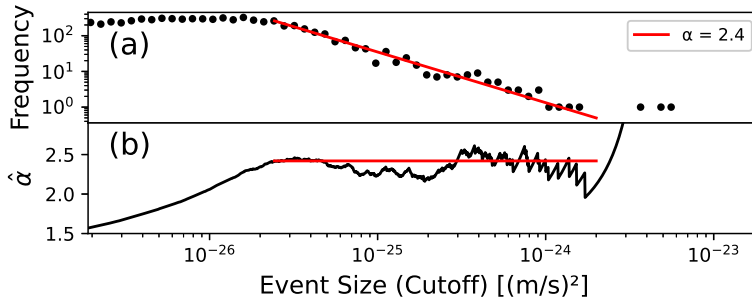


**Figure 7.10:** *Avalanche statistics from a first measurement of nanoindentation on BFO thin films. (a) log-log plot of event size and frequency. (b) Maximum likelihood estimate of the scaling parameter, as a function of event size cutoff.*

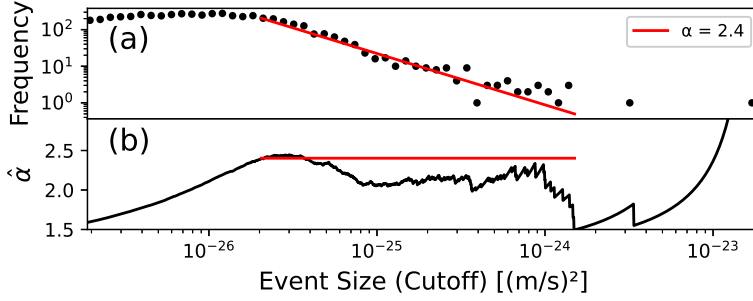


**Figure 7.11:** *Avalanche statistics from a second measurement of nanoindentation on BFO thin films. (a) log-log plot of event size and frequency. (b) Maximum likelihood estimate of the scaling parameter, as a function of event size cutoff.*

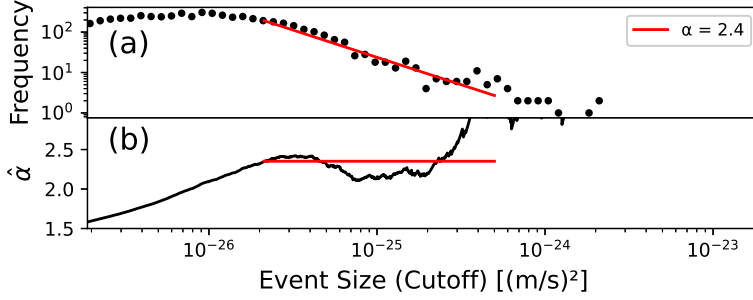


**Figure 7.12:** *Avalanche statistics from a third measurement of nanoindentation on BFO thin films. (a) log-log plot of event size and frequency. (b) Maximum likelihood estimate of the scaling parameter, as a function of event size cutoff.*

## 7. Tracking the Nanoscale Dynamics of Martensitic-like Phase Transitions via Interferometric Nanoindentation

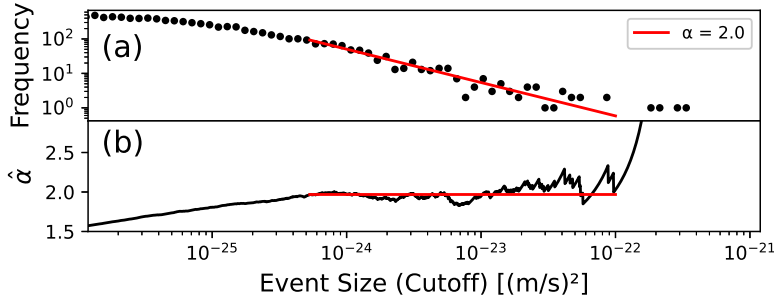


**Figure 7.13:** *Avalanche statistics from a repeat on measurements on the PTO thin films, after measurements on BFO had concluded. (a) log-log plot of event size and frequency. (b) Maximum likelihood estimate of the scaling parameter, as a function of event size cutoff.*

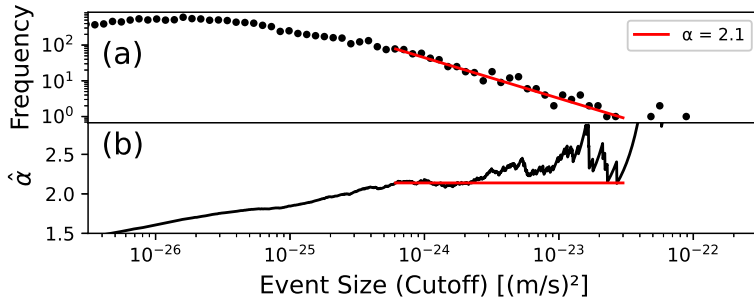


**Figure 7.14:** *Avalanche statistics from a repeat on measurements on the PTO thin films, with a second tip. (a) log-log plot of event size and frequency. (b) Maximum likelihood estimate of the scaling parameter, as a function of event size cutoff.*

measurements on BFO, experiments were repeated with the same tip at different regions on the PTO sample. The results from three nanoindentations are collated and shown in Fig. 7.13. The observed scaling parameter is 2.0; consistent with those extracted prior to BFO measurements and presented in the main paper.

*Reproducibility between tips:* To ensure control of all variables in this manuscript, all measurements reported in the main text were performed with a single AD-40-AS diamond tip. To check for reproducibility, we repeated the experiments on PTO with a second tip (spring constant: 83.089), and report them in Fig. Test. The measured scaling parameter is here 2.1 (Fig. 7.14; once more consistent with results presented in the main manuscript, showing that this is not tip-dependent behaviour.

*Measurements during dwell time:* To ensure that these measurements

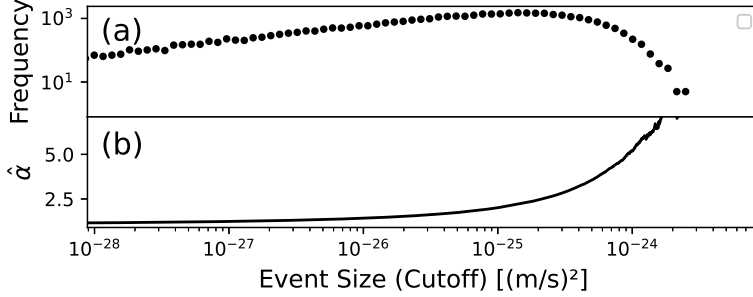


**Figure 7.15:** *Avalanche statistics from when holding the tip at  $\sim 100 \mu\text{N}$*  (a) log-log plot of event size and frequency. (b) Maximum likelihood estimate of the scaling parameter, as a function of event size cutoff.

are not intrinsic to the technique or external system, we collected statistics of tip height while the tip was indented and held at  $\sim 100 \mu\text{N}$ . This is shown in Fig. 7.15. Here, no clear avalanche data is observed. This suggests that the observed power-law distributions arise from the indentation and increasing force, and not as a function of the measurement system or external environment.

*Optical Beam Deflection:* While all data otherwise shown in this manuscript are from the QPDI detector, we performed a set of measurements in which both the QPDI response and a standard optical beam deflection (OBD) response were gathered simultaneously. This data is shown in Fig. 7.16, with the event sizes multiplied by a factor of  $3 \times 10^{-16}$ . While a scaling parameter of  $\alpha \approx 2$  is once again observed in QPDI, the significant noise values in OBD yield no power-law distribution. This suggests that OBD may not be suitable to determine critical exponents from nanoindentation.

In sum, we establish that these QPDI measurements of the sample surface measure a critical exponent of 1.9 for the distribution of force-independent events of plastic deformation under nanoindentation. This value is almost identical to the mean-field theory exponent of 2, is observed over more than three orders of magnitude, and is highly repeatable. This suggests that this technique is particularly capable for this study, and presents a marked improvement over previous attempts to measure critical exponents under indentation.



## 7. Tracking the Nanoscale Dynamics of Martensitic-like Phase Transitions via Interferometric Nanoindentation

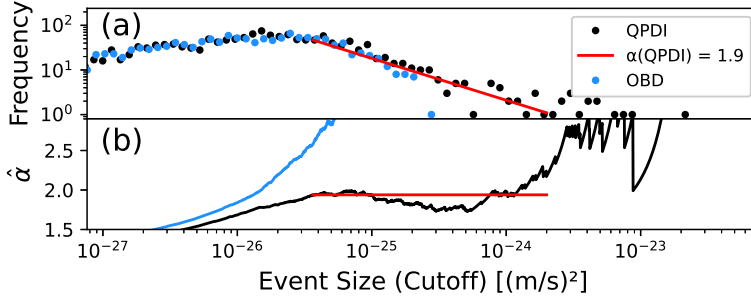


**Figure 7.16:** *Avalanche statistics from simultaneous QPDI and OBD measurements, showing power-law behaviour captured via QPDI but not OBD. OBD response has been multiplied by a factor of  $3 \times 10^{-16}$  (a) log-log plot of event size and frequency. (b) Maximum likelihood estimate of the scaling parameter, as a function of event size cutoff.*

### 7.3 Nanoindentation and Critical Scaling of a Martensitic-like Phase Transition

Having established the capability of interferometric nanoindentation for measurements of nanoscale shape change dynamics during elastic and plastic deformation in ferroelectrics, we can now repeat these experiments on a more complex material that undergoes a local martensitic-like phase transition—BFO. BFO, when grown on  $\text{LaAlO}_3$  (001)<sub>pc</sub> substrates that apply in-plane compressive strain, stabilises into its T'-phase. If the film is grown sufficiently thick, such that this strain relaxes [38], or alternatively, if sufficient out-of-plane compressive stresses are applied [5, 6], stripe domains of alternating T'- and R'-phases form.

These mixed T'- and R'-phases manifest at thicknesses greater than  $\sim 20$  nm [38], and once mixed phase formation stabilises, further R'-phase growth appears to be energetically unfavourable [6]. This thickness is less than the 25 nm penetration depth measured in the PTO studies.

To account for these differences, we grow our BFO films in previously reported PLD conditions [38] that encourage the formation of bismuth oxide pockets and further stabilise the T'-phase to  $\sim 70$ -nm thicknesses. In this method, films of BFO were grown by PLD on a  $\text{LaAlO}_3$  single crystal substrates with a 10% bismuth excess target at 600 °C in a 23 mTorr oxygen atmosphere. The distance between the substrate and target was kept at 10.5 cm, which resulted in a low growth rate of  $\sim 0.026$  Å/pulse.

X-ray diffraction reciprocal space maps revealed two distinct reflections for the LAO substrate, corresponding to two crystallographic twins [Fig. 7.1(a)], which are reasonably expected for these LAO substrates. The BFO films,

### 7.3 Nanoindentation and Critical Scaling of a Martensitic-like Phase Transition

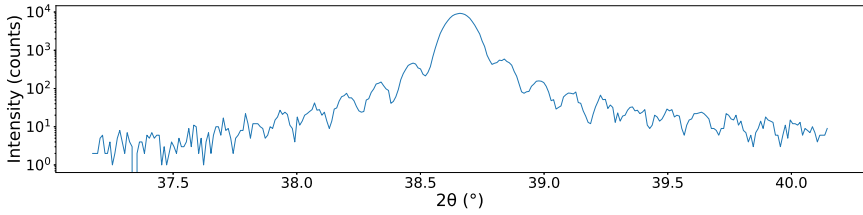


**Figure 7.17:** *Laue fringes around the (002) reflection of the strained BFO peak, with a periodicity that corresponds to  $\sim 70$ -nm thickness.*

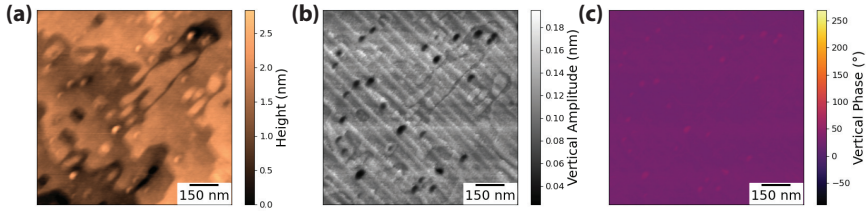


**Figure 7.18:** *Sample raw PFM data of the as-grown 140 nm PTO/20 nm SRO/STO (001) thin films. The channels shown represent (a) height, (b) amplitude, and (c) phase.*

grown on top of the LAO, also expresses two twin peaks, each fully epitaxial with a corresponding substrate peak.  $2\theta$ - $\omega$  scans unveil show Laue fringes around the BFO peak, which verify high-quality growth, and can be used to establish the film thickness to about 70 nm (Fig. 7.17).

Topography atomic force microscopy and piezoresponse force microscopy measurements were used to verify the terrace structures [Fig. 7.18], and reveal underlying stripe domains, which suggest some in-plane character to the polarisation. Small circular dips in amplitude are also observed, which we attribute to underlying pockets of (non-piezoelectric) bismuth oxide that stabilise the film structure. The sample presents a constant out-of-plane polarisation.

In these 70-nm-thick BFO films, indentation of the T'-phase locally yields the expected R'-phase, which forms as stripes oriented towards the  $\langle 110 \rangle_{\text{pc}}$  crystallographic axes [Fig. 7.4]. Setting the sample position with respect to the cantilever can thus allow T-phase growth parallel or perpendicular to the direction of indentation. For avalanche statistic studies, we selected for parallel-grown R'-phase formation (these directions were also preferably formed).

We then repeated the nanoindentation studies on these BFO thin films under identical conditions to those on PTO thin films. We once again acquired three force curves, of which one is shown in Fig. 7.19. As with Fig. 7.3, we can observe both jumps in strain and plastic deformation. The

## 7. Tracking the Nanoscale Dynamics of Martensitic-like Phase Transitions via Interferometric Nanoindentation

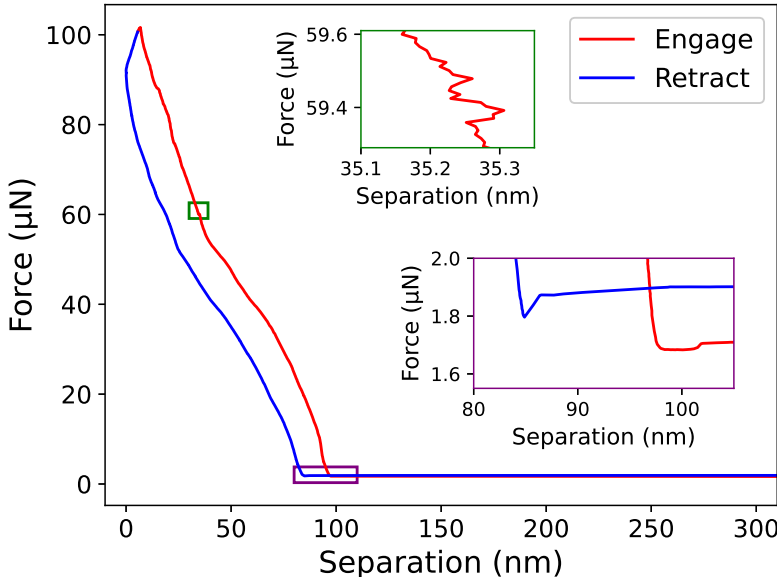


**Figure 7.19:** High resolution force curve on BFO thin films generated through quadrature-phase differential interferometry. Main figure: Force curve showing indentation force as a function of indentation. Upper inset (green): A section of the force curve that shows jumps in the indentation during tip engage. Lower inset (purple): A section of the force curve that shows snap-in and pull-off phenomena, as well as  $\sim 15$  nm of plastic deformation.

deformation observed in BFO appears to be significantly less than that in PTO under similar forces, with a maximum deformation of only about 100 nm, of which only 15 nm is plastic. These jumps in energy also appear to have a reduced maximum size, which is shown in Fig. 7.20(a–c), where we have comparatively fewer events of size greater than  $10^{-22}$  (m/s)<sup>2</sup>.

The scaling parameter values obtained from these thin films are collated and shown in Fig. 7.20(d), and each individual measurement can be seen in Figs. 7.10–7.12. Once more, we observe marked stability of the scaling parameter, but at a consistently higher value of approximately 2.4.

Unlike the results from nanoindentation on PTO, we also see the maximum-likelihood exponent to alter slightly with  $x_{min}$ , which could correspond to a mixing of power laws [36]. This may also be visible in the event spectra shown in Fig. 7.19(a–c): here, after about 50  $\mu$ N force is applied, the event size tends to increase. We thus once more split events into ‘low’ forces (15  $\mu$ N to 53  $\mu$ N) and ‘high’ forces (53  $\mu$ N to 90  $\mu$ N) and compare our scaling parameter values.

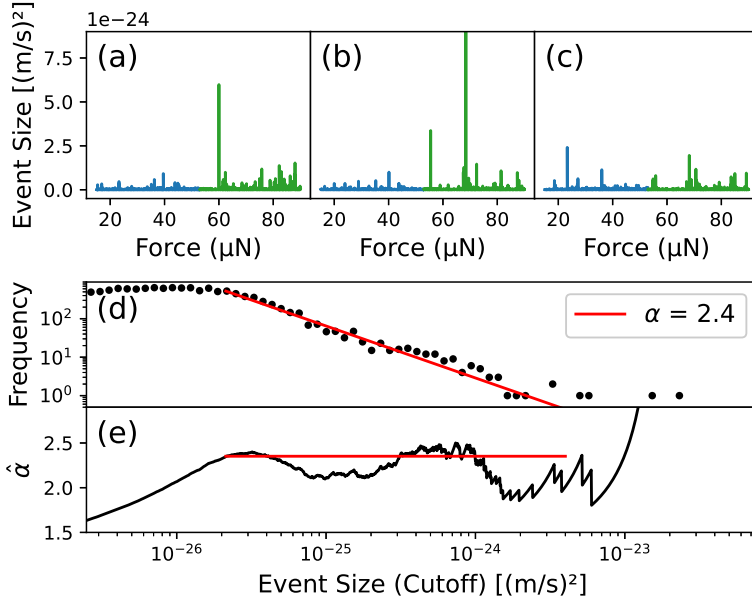


**Figure 7.20:** *Avalanche statistics from nanoindentation on BFO thin films (a–c)* Event spectra from three repetitions on three different positions on the sample. Blue lines represent ‘low’ forces ( $15 \mu\text{N} < F < 53 \mu\text{N}$ ), and green lines represent ‘high’ forces ( $53 \mu\text{N} < F < 90 \mu\text{N}$ ), (d) log-log plot of event size and frequency, showing a linear trend. (e) Maximum likelihood estimate of the scaling parameter, as a function of event size cutoff.

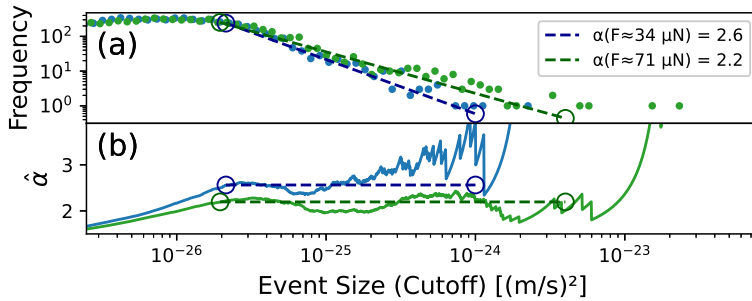


**Figure 7.21:** *Avalanche statistics from nanoindentation on BFO thin films, split into distinct force regimes.* (a) log-log plot of event size and frequency, showing distinct linear trends at different forces. (b) Maximum likelihood estimate of the scaling parameter, as a function of event size cutoff, showing different scaling parameters for different forces.

## 7. Tracking the Nanoscale Dynamics of Martensitic-like Phase Transitions via Interferometric Nanoindentation

---

In this case, we do observe a marked difference in the scaling parameter values between lower and higher force. At lower forces, the critical exponent appears to be higher, at about 2.6; while at higher forces, the critical exponent is depressed, to approximately 2.2.

### 7.4 Martensitic-like Phase Transitions and Plastic Deformation

These results from nanoindentation on both PTO and BFO yield two interesting, and potentially related, questions. First, why is the critical exponent under nanoindentation higher in BFO than in PTO? And second, why is it that the measured critical exponent appears to reduce at higher forces for BFO?

The first question has previously been addressed in metallurgical contexts, as discussed in Ref. [12, 13]. Here, transitions to lower-symmetry phases are generally characterised by higher scaling parameter values than transitions to higher-symmetry phases or plastic deformation. This occurs in part because these lower-symmetry phases allow for more ‘choices’ through which energy can be more gradually decreased: in PTO, localised stresses need to exceed some value such that plastic deformation occurs, but in BFO, either plastic deformation *or* a martensitic-like phase transition can occur. Further, if the martensitic-like phase transition can occur, there are in addition multiple ‘choices’ as to which direction the crystal shears and deforms. This means that there are more potential choices for a transition to a lower-energy state in BFO, and thus a buildup to a large jump is less likely; this increases the critical exponent value.

Indeed, this increase in the scaling parameter is precisely what we observe. In PTO, per mean-field theory, we expect and show a scaling parameter of approximately 2 from plastic deformation, while in BFO—which expresses plastic deformation, but also the martensitic-like phase transition from the T'-phase to the lower symmetry R'-phase—we observe an increased scaling parameter of 2.2–2.6, depending on force.

This explanation also provides hints as to the source of this force-dependent scaling parameter. Previous work has shown that T'- to R'-phase transitions in BFO occur when applied forces are in the range of  $\sim 300$  nN to 3000 nN [5, 6]. While the precise stresses are difficult to ascertain, due to differences in tip size (particularly under such high forces), these forces for BFO transition are much smaller than the maximum forces applied here. We may thus expect most of the martensitic-like phase transition to complete along the lower range of our applied stress. Meanwhile, plastic deformation on mixed-phase BFO films is reported to occur with stresses of  $\sim 14$  GPa [39]. If we do assume a tip-contact radius of 25 nm, then this

threshold occurs with applied forces of  $\sim 27 \mu\text{N}$ , supporting our observations in BFO films. Below a  $53 \mu\text{N}$  threshold, we observe mixed, but primarily martensitic-like-phase-transition-driven critical behaviour, resulting in a critical scaling parameter much higher than that observed in PTO and predicted by mean-field theory. Above that  $53 \mu\text{N}$  threshold, we observe mixed, but plastic-deformation-driven critical behaviour, resulting in a critical scaling parameter only slightly higher than that observed in PTO and predicted by mean-field theory.

Despite these key advancements, there still remain key questions open for further investigation. In this study, we restricted our indentation time to only approximately 3 minutes, as we wished to avoid any additional noise relating to tip drift over the extent of the measurement; longer and more extensive measurements that better adjust for this drift could yield even clearer trends. Longer measurements could also allow investigation over a larger range of forces, which, particularly in the BFO samples, could cover more distinct regimes and critical behaviours. Additionally, in these studies, while we accurately report the *forces* directly applied by the tip, the *stresses* on the sample surface are less clear without direct observation of the contact area, and are clearly quite complex, given the observed ploughing effects. Use of custom tips with a known contact radius and a shorter cantilever could allow for even more quantitative measurement of stresses applied.

## 7.5 Conclusions

In this report, we have not only established the capability of QPDI nanoindentation to observe critical behaviour in plastic deformation in PTO, which matches theoretical predictions with over three orders of magnitude of data, but we have also shown that in BFO we can observe and measure the scaling parameters of two mixed, stress-dependent regimes; one dominated by a martensitic-like phase transition, and one dominated by plastic deformation. The practicality of this technique and analysis suggests broad capability for the investigation of nanoscale phase transitions through multiple disciplines of solid-state physics.

## References

- [1] J. Zhang, X. Ke, G. Gou, J. Seidel, B. Xiang, P. Yu, W.-I. Liang, A. M. Minor, Y.-h. Chu, G. Van Tendeloo, et al., “A nanoscale shape memory oxide”, *Nature Communications* **4**, 2768 (2013).

## 7. Tracking the Nanoscale Dynamics of Martensitic-like Phase Transitions via Interferometric Nanoindentation

---

- [2] D. Sando, A. Barthélémy, and M. Bibes, “BiFeO<sub>3</sub> epitaxial thin films and devices: past, present and future”, *Journal of Physics: Condensed Matter* **26**, 473201 (2014).
- [3] D. Sando, B. Xu, L. Bellaiche, and V. Nagarajan, “A multiferroic on the brink: uncovering the nuances of strain-induced transitions in BiFeO<sub>3</sub>”, *Applied Physics Reviews* **3** (2016).
- [4] H. M. Christen, J. H. Nam, H. S. Kim, A. J. Hatt, and N. A. Spaldin, “Stress-induced R-MA-MC-T symmetry changes in BiFeO<sub>3</sub> films”, *Physical Review B* **83**, 144107 (2011).
- [5] Y. Heo, B.-K. Jang, S. J. Kim, C.-H. Yang, and J. Seidel, “Nanoscale mechanical softening of morphotropic BiFeO<sub>3</sub>”, *Advanced Materials (Deerfield Beach, Fla.)* **26**, 7568–7572 (2014).
- [6] A. B. Naden, D. Edwards, S. M. Neumayer, J. G. Guy, B. J. Rodriguez, N. Bassiri-Gharb, and A. Kumar, “Revealing the interplay of structural phase transitions and ferroelectric switching in mixed phase BiFeO<sub>3</sub>”, *Advanced Materials Interfaces* **5**, 1801019 (2018).
- [7] M. E. Lines and A. M. Glass, *Principles and applications of ferroelectrics and related materials* (Oxford university press, 2001).
- [8] N. Sicron, B. Ravel, Y. Yacoby, E. A. Stern, F. Dogan, and J. J. Rehr, “Nature of the ferroelectric phase transition in PbTiO<sub>3</sub>”, *Physical Review B* **50**, 13168 (1994).
- [9] K. M. Rabe, C. H. Ahn, and J.-M. Triscone, *Physics of ferroelectrics: a modern perspective*, Vol. 105 (Springer Science & Business Media, 2007).
- [10] K. Uchino and S. Nomura, “Critical exponents of the dielectric constants in diffused-phase-transition crystals”, *Ferroelectrics* **44**, 55–61 (1982).
- [11] K. Müller and W. Berlinger, “Static critical exponents at structural phase transitions”, *Physical Review Letters* **26**, 13 (1971).
- [12] M. Porta, T. Castán, A. Saxena, and A. Planes, “Influence of the number of orientational domains on avalanche criticality in ferroelastic transitions”, *Physical Review E* **100**, 062115 (2019).
- [13] A. Planes, L. Mañosa, and E. Vives, “Acoustic emission in martensitic transformations”, *Journal of Alloys and Compounds* **577**, S699–S704 (2013).
- [14] P. Bak, C. Tang, and K. Wiesenfeld, “Self-organized criticality: an explanation of the 1/f noise”, *Physical Review Letters* **59**, 381 (1987).
- [15] A. Clauset, C. R. Shalizi, and M. E. Newman, “Power-law distributions in empirical data”, *SIAM Review* **51**, 661–703 (2009).

- [16] J. P. Sethna, K. A. Dahmen, and C. R. Myers, “Crackling noise”, *Nature* **410**, 242–250 (2001).
- [17] F.-J. Pérez-Reche, L. Truskinovsky, and G. Zanzotto, “Training-induced criticality in martensites”, *Physical Review Letters* **99**, 075501 (2007).
- [18] P. Shanthraj and M. Zikry, “Microstructurally induced fracture nucleation and propagation in martensitic steels”, *Journal of the Mechanics and Physics of Solids* **61**, 1091–1105 (2013).
- [19] P. Clapp, “How would we recognize a martensitic transformation if it bumped into us on a dark & austy night?”, *Le Journal de Physique IV* **5**, C8–11 (1995).
- [20] B. Casals, G. F. Nataf, D. Pesquera, and E. K. Salje, “Avalanches from charged domain wall motion in BaTiO<sub>3</sub> during ferroelectric switching”, *APL Materials* **8**, 011105 (2020).
- [21] B. Casals, G. F. Nataf, and E. K. Salje, “Avalanche criticality during ferroelectric/ferroelastic switching”, *Nature Communications* **12**, 345 (2021).
- [22] P. Tückmantel, I. Gaponenko, N. Caballero, J. C. Agar, L. W. Martin, T. Giamarchi, and P. Paruch, “Local probe comparison of ferroelectric switching event statistics in the creep and depinning regimes in Pb(Zr<sub>0.2</sub>Ti<sub>0.8</sub>)O<sub>3</sub> thin films”, *Physical Review Letters* **126**, 117601 (2021).
- [23] C.-P. T. Nguyen, P. Schoenherr, E. K. Salje, and J. Seidel, “Crackling noise microscopy”, *Nature Communications* **14**, 4963 (2023).
- [24] Oxford Instruments, *Quadrature Phase Differential Interferometry (QPDI) technology in the Asylum Research Vero AFM*, <https://afm.oxinst.com/assets/uploads/products/asylum/documents/Technical%20Note:%20QPDI%20technology%20in%20the%20AR%20Vero%20AFM%20WEB.pdf>, Accessed: 2024-03-11.
- [25] R. Proksch, R. Wagner, and J. Lefever, “Accurate vertical nanoelectromechanical measurements”, *Journal of Applied Physics* **135** (2024).
- [26] C. Lichtensteiger, J.-M. Triscone, J. Junquera, and P. Ghosez, “Ferroelectricity and tetragonality in ultrathin PbTiO<sub>3</sub> films”, *Physical Review Letters* **94**, 047603 (2005).
- [27] S. Alpay, A. Prakash, S. Aggarwal, P. Shuk, M. Greenblatt, R. Ramesh, and A. Roytburd, “Polydomain formation in epitaxial PbTiO<sub>3</sub> films”, *Scripta materialia* **39**, 1435–1441 (1998).
- [28] N. Pertsev, A. Zembilgotov, and A. Tagantsev, “Effect of mechanical boundary conditions on phase diagrams of epitaxial ferroelectric thin films”, *Physical Review Letters* **80**, 1988 (1998).



## 7. Tracking the Nanoscale Dynamics of Martensitic-like Phase Transitions via Interferometric Nanoindentation

---

- [29] C. Weymann, C. Lichtensteiger, S. Fernandez-Peña, K. Cordero-Edwards, and P. Paruch, “Improved thin film growth using slow kinetics intermittent sputtering”, *Applied Surface Science* **516**, 146077 (2020).
- [30] S. Saremi, R. Xu, L. R. Dedon, J. A. Mundy, S.-L. Hsu, Z. Chen, A. R. Damodaran, S. P. Chapman, J. T. Evans, and L. W. Martin, “Enhanced electrical resistivity and properties via ion bombardment of ferroelectric thin films”, *Advanced Materials* **28**, 10750–10756 (2016).
- [31] L. Feigl, L. McGilly, C. Sandu, and N. Setter, “Compliant ferroelastic domains in epitaxial Pb(ZrTi)O<sub>3</sub> thin films”, *Applied Physics Letters* **104** (2014).
- [32] V. Koval, M. Reece, and A. Bushby, “Ferroelectric/ferroelastic behavior and piezoelectric response of lead zirconate titanate thin films under nanoindentation”, *Journal of Applied Physics* **97** (2005).
- [33] Y. Ahn and J. Y. Son, “Flexoelectric effect via piezoresponse force microscopy of domain switching in epitaxial PbTiO<sub>3</sub> thin films”, *Journal of the Korean Ceramic Society* **61**, 55–62 (2024).
- [34] X. Lu, Z. Chen, Y. Cao, Y. Tang, R. Xu, S. Saremi, Z. Zhang, L. You, Y. Dong, S. Das, et al., “Mechanical-force-induced non-local collective ferroelastic switching in epitaxial lead-titanate thin films”, *Nature Communications* **10**, 3951 (2019).
- [35] H. Lu, S. Liu, Z. Ye, S. Yasui, H. Funakubo, A. M. Rappe, and A. Gruverman, “Asymmetry in mechanical polarization switching”, *Applied Physics Letters* **110** (2017).
- [36] E. K. Salje and K. A. Dahmen, “Crackling noise in disordered materials”, *Annu. Rev. Condens. Matter Phys.* **5**, 233–254 (2014).
- [37] N. Friedman, A. T. Jennings, G. Tsekenis, J.-Y. Kim, M. Tao, J. T. Uhl, J. R. Greer, and K. A. Dahmen, “Statistics of dislocation slip avalanches in nanosized single crystals show tuned critical behavior predicted by a simple mean field model”, *Physical Review Letters* **109**, 095507 (2012).
- [38] D. Sando, T. Young, R. Bulanadi, X. Cheng, Y. Zhou, M. Weyland, P. Munroe, and V. Nagarajan, “Designer defect stabilization of the super tetragonal phase in >70-nm-thick BiFeO<sub>3</sub> films on LaAlO<sub>3</sub> substrates”, *Japanese Journal of Applied Physics* **57**, 0902B2 (2018).
- [39] Y.-J. Li, J.-J. Wang, J.-C. Ye, X.-X. Ke, G.-Y. Gou, Y. Wei, F. Xue, J. Wang, C.-S. Wang, R.-C. Peng, et al., “Mechanical switching of nanoscale multiferroic phase boundaries”, *Advanced Functional Materials* **25**, 3405–3413 (2015).

## CHAPTER 8

---

### Current Investigations in Domain Wall Dynamics, Automated Experiments, and Visualisation Tools

---

Chapters 4–7 of this thesis have discussed and reported ‘completed’ segments of my work that are, at time of writing, published, accepted, under review, and in final preparation, respectively. Unlike ferroelectrics, however, a PhD is not time-symmetric, which means that there remain substantial volumes of work that are under continuing or preliminary investigation at the conclusion of this PhD. As many of these build up off concepts discussed at length in the previous chapters, and took substantial time during this PhD programme, I would consider it a shame if some of these were not discussed at least somewhat here.

I have limited myself to the two current projects I find most relevant to this thesis, and will discuss each in turn. In Section 8.1 I will report preliminary results of the work performed at Oak Ridge National Laboratory and co-supervised by Rama Vasudevan, in which we investigate the characteristics of domain-wall motion in BFO, as opposed to the studies in PTO as described in Chapter 6. Finally, in Section 8.2, we will discuss tools for x-ray diffraction analysis, planned for development with Lucas Mayor, to help better understand and comprehend reciprocal space mapping and Fourier transformations.

### 8.1 Domain-Wall Orientation and its Effect on Domain-Wall Dynamics, as Measured by Automated Experiments

We ended Chapter 6 with two general conclusions. The first is that we observe globally similar scaling parameters and critical exponents for domain wall motion, regardless of defect bombardment densities. The second is that we observe local deviations in domain-wall mobility, which we associate with proximity to *a*-domains—regions of in-plane polarisation across which electrostatic and elastic conditions change with respect to the bulk material [1] and which thus act as pinning sites.

In our PTO thin films, these *a*-domains were stationary under our experimental conditions, and the 180° domain walls moved across them. To better ascertain the relationship between out-of-plane domain walls and in-plane polarisation and associated strains, we sought to investigate a material system in which some in-plane polarisation domains are mobile, and thus moving domain walls could change their character between different possible crystallographic orientations allowed by the symmetry of the parent material [2]. For such studies, the rich domain structure of BFO with both in-plane and out-of-plane polarisation components when grown on many common substrates provides an ideal test case.

To carry out our research, we grew a 50-nm-thick-film of BFO on a substrate of (110)-oriented STO and a 20-nm-thick SRO interelectrode. The rhombohedral structure of BFO ensures that polarisation is oriented along the  $\langle 111 \rangle$  crystallographic axes; further, we expect that elastic and misfit characteristics of the system would lead to preferential formation of the four polarisation vectors in this material that are a combination of an out-of-plane polarisation vector and an in-plane polarisation vector (Fig. 8.1), as opposed to the four polarisation vectors with fully in-plane character..

As all four polarisation orientations have an out-of-plane polarisation component, and this out-of-plane polarisation component can be switched by applying an electric field between a scanning probe and the SRO electrode, accompanied in many cases by reorientation of the in-plane polarisation component, we thus have some limited control of the in-plane polarisation orientation. Further, this structure enables three possible ‘classes’ of domain-wall orientation and ferroelectric switching (Fig. 8.1): a 71° domain wall between two adjacent domains of identical out-of-plane polarisation but different in-plane polarisation; a 109° domain wall between two adjacent domains of identical in-plane polarisation but different out-of-plane polarisation; and a 180° domain wall in which both in-plane and out-of-plane polarisation change. What is particularly appealing is that a full polarisation determination can be performed with a single vector PFM measurement, if

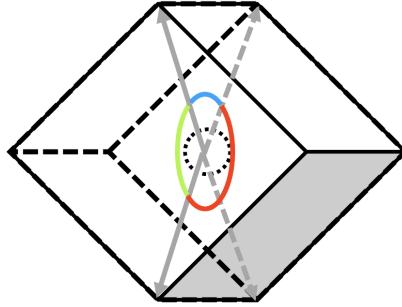


**Figure 8.1:** A unit cell of ferroelectric rhombohedral BFO thin film grown on a (110)-oriented substrate. Gray arrows show valid polarisation directions. Between any two directions, we have a  $71^\circ$  angle (blue),  $109^\circ$  angle (green), or  $180^\circ$  angle (red).

the cantilever is oriented to be sensitive to the expected polarisation axis.

This configuration allows us to ask and attempt to answer numerous questions. Is one particular type of domain wall preferred? Is one particular ferroelectric switching path preferred? Do we see any attraction and repulsion between different domain-wall or polarisation orientations? These are the questions we here attempt to answer.

### 8.1.1 Growth of (110)-oriented BFO Thin Films

The necessary (110)-oriented BFO thin films were grown by pulsed laser deposition. An SRO electrode layer was grown at  $660^\circ\text{C}$  and 100 mTorr to a 10-nm thickness. The sample was then cooled to  $590^\circ\text{C}$  and 100 mTorr and grown to a 50-nm thickness. Film thicknesses were verified by XRD (not shown), and film topography consisted of terraced stripes aligned along the [001] crystallographic axis (Fig. 8.2).

### 8.1.2 Verification of Domain-Wall Orientation

With films grown, we first verified whether these domain-wall orientations can indeed be identified and differentiated. In the configuration shown in Fig. 8.2, polarisation is only present along the  $[111]$ ,  $[1\bar{1}\bar{1}]$ ,  $[\bar{1}\bar{1}1]$  and  $[\bar{1}11]$  axes; the remaining axes are fully in-plane and would be energetically unfavourable in this configuration.

A cantilever aligned in the  $[\bar{1}10]$  direction would have a lateral deflection that is responsive to shear in the [001] direction, and vertical deflection responsive to extension in the  $[110]$  direction. This allows the determination of the polarisation from both lateral and vertical deflection responses, and so we perform a  $[\bar{1}10]$ -oriented cantilever scan with [001] as a fast-scan axis.

We constructed two vertical stripe domains of  $1.33\text{-}\mu\text{m}$  thickness with

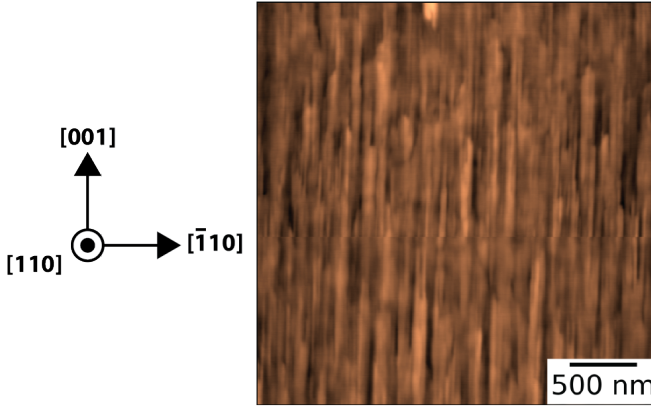


**Figure 8.2:** AFM topography image with associated crystallographic axes.

a -9 V bias applied via the tip, and then performed the vector PFM scan (Fig. 8.3). In Fig. 8.3(a), we observe a clear  $180^\circ$  shift in vertical phase, which suggests two distinct orientations of the out-of-plane polarisation component (two ‘Up’ domains with a  $[110]$ -oriented component, and one central ‘Down’ domain with a  $[\bar{1}\bar{1}0]$  component).

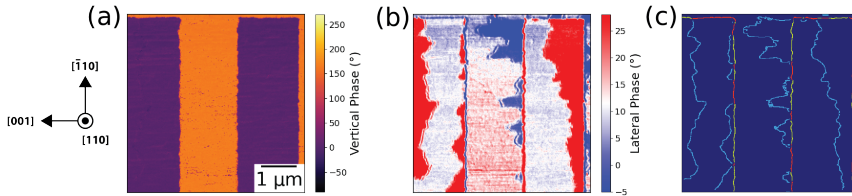


**Figure 8.3:** Vector PFM performed on BFO/SRO/STO (110) thin films. The cantilever was oriented along the  $[\bar{1}\bar{1}0]$  direction and scanned with a  $[001]$  fast scan axis. (a) Vertical phase channel. (b) Lateral phase channel. (c) Assignment of the three identified domain-wall configurations.

In Fig. 8.3(b), our lateral-phase measurements show some clear changes without any corresponding change observed in vertical phase; this is a clear marker expected of  $71^\circ$  domain walls. However, differentiating between  $109^\circ$  and  $180^\circ$  domain walls is substantially more difficult; the precise lateral phase value *always* seems to change with a change in vertical phase. It is thus not clear from this measurement alone for which domain walls is the in-plane polarisation conserved, and thus, which are the  $109^\circ$  domain walls.

To verify the orientation of these in-plane polarisations, we performed supplementary measurements with a QPDI-based system for its reduced

## 8.1 Domain-Wall Orientation and its Effect on Domain-Wall Dynamics, as Measured by Automated Experiments

noise and crosstalk with lateral signal [3]. We then took two measurements; one standard vertical PFM image [Fig. 8.4(a)] and one in which the interferometric laser is adjusted to be off the cantilever axis [Fig. 8.4(b)]. In the former case, we see the expected behaviour for the PFM amplitude, with a consistent response in our ferroelectric domains and a depressed response in the ferroelectric domain walls. In the latter case, however, we see some patchy domains with an *increased* amplitude response, and others with a *decreased* amplitude response. These features we attribute to the lateral response from the in-plane polarisation components, which is expected to cause change in vertical displacement.

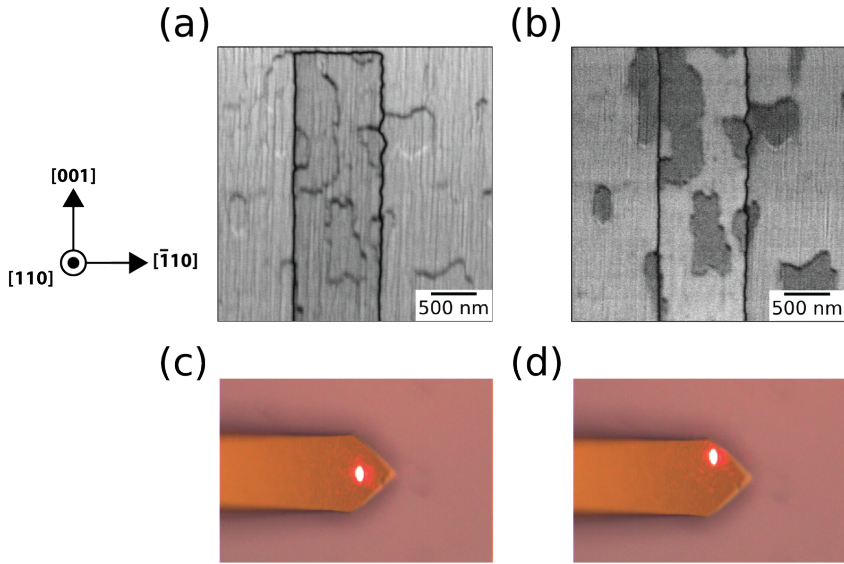


**Figure 8.4:** PFM amplitude measurements performed with a QPDI detector. The cantilever was oriented along the  $[\bar{1}10]$  direction and scanned with a  $[\bar{1}10]$  fast scan axis. Amplitude channel is shown with laser spot on (a) on the central axis, and (b) off the central axis of the cantilever. (c–d) show respective optical microscopy images where the laser spot is visible. The cantilever has a nominal width of  $35\ \mu\text{m}$ .

From these measurements, we observe that the in-plane polarisation vectors appear to be mostly continuous across the out-of-plane boundary. While we do observe both  $109^\circ$  and  $180^\circ$  domain walls, the ‘patchy’ domains (bounded by  $71^\circ$  walls) appear to contain  $109^\circ$  domain walls when they straddle the out-of-plane boundary, and consist of  $180^\circ$  domain walls when they coincide with it.

As such, we are able to assign the full vector components of the polarisation to the measurements of Fig.8.3. In Fig. 8.3(c), we mark the  $71^\circ$  domain

walls in light blue, the 109° domain wall in green, and the 180° domain wall in red.

### 8.1.3 Domain-Wall Tracking and Improvements through Automated Experiments

In principle, we could then have repeated the same measurements as reported in Chapter 6—in which we perform stroboscopic reading and writing scans with our scanning probe—but in which these more complex domain-wall dynamics are observed. We have, however, taken the time to make additional improvements to this measurement protocol. Rather than perform all analysis after experiments are complete, we instead integrate our analysis into our data acquisition, and use it to guide the present experiment. Some improvements this has allowed include:

- We use and analyse band excitation PFM, rather than DART PFM as previously performed. This allows us to use the advantages we have outlined in Section 3.1.3.1.5; in particular, we are more resilient to drift of the resonant frequency over our long-duration scans, and also, we collect additional data to improve our signal-to-noise and thus more precisely measure domain wall positions.
- After every reading scan, we use code initially designed for *Hystorian* (Chapter 4) to precisely determine the position of the out-of-plane domain walls. Using this information, when we perform our interleaved ‘writing’ scans, rather than apply a DC voltage over the entire scanned region, we instead only apply the voltage in the vicinity around the domain wall. This prevents nucleation of new domains and allows for the linear motion of the domain wall to be directly monitored, and also prevents any tip or sample damage that could occur from excessive application of voltage.
- We additionally limit our reading scans to the area around a domain wall (as determined by a previous reading scan). The smaller imaging area substantially reduces tip wear and increases the amount of scans that can be performed in any particular time span, without losing any relevant data.
- By following domain-wall positions with our scans (rather than scanning continuously over one particular region, as done prior), we also allow ourselves to track domain-wall motion over regions much larger than the 2  $\mu\text{m}$  scan size we have previously reported.

These advantages together mark a substantial improvement over what we have previously implemented. In addition, once this experiment is set

## 8.1 Domain-Wall Orientation and its Effect on Domain-Wall Dynamics, as Measured by Automated Experiments

up, the entire process can be performed automatically, allowing the ‘user’ to perform other work and only intermittently monitor the experiment.

An example switching map we have acquired for out-of-plane domain motion can be seen in Fig. 8.5; comparisons should be drawn between this figure and Fig. 6.4. Our present switching map follows the domain wall for a considerably longer distance (approx.  $7.5\ \mu\text{m}$ , compared to maximum  $1\ \mu\text{m}$ ), and is captured over more scans (102 scans here, compared 20–50 scans typically).



**Figure 8.5:** An out-of-plane switching map acquired on the BFO/SRO/STO (110) film by our automated experiment. Black lines mark positions of the out-of-plane domain wall. The cantilever was oriented along the  $[\bar{1}10]$  direction and scanned with a  $[001]$  fast scan axis.

Overall, these improvements allow for more reliable assessment of these domain-wall dynamics.

### 8.1.4 Preliminary Domain-Wall Dynamics Results

While, at time of writing, we have not yet completed comprehensive analysis of our domain-wall dynamics data, a small subset of our raw data is presented in Fig. 8.6.

Here, moving down the figure we examine sequential ‘reading’ scans, interspersed with ‘writing’ scans. In the two left columns, we measure vertical phase and vertical amplitude, respectively, where we see the out-of-plane domain wall proceed from left to right. In the next two columns, we measure lateral phase and lateral amplitude, respectively. Here, we see an in-plane polarisation configuration develop that is distinct from the pristine polarisation configuration. This polarisation reconstruction also appears *behind* the initial out-of-plane polarisation switch, which suggests some complex domain interactions between in-plane and out-of-plane polarisation vectors. In the rightmost column, we assign the different domain-wall orientations to the image; once more,  $71^\circ$  domain walls are marked in light blue,  $109^\circ$  domain walls in green, and  $180^\circ$  domain walls in red. The reconstruction of the  $71^\circ$  domain walls are prominent from this domain assignment.

In sum, these preliminary results suggest that there are indeed complex correlations between in-plane and out-of-plane domain configurations. Continued work is needed to determine more rigorously what precisely these effects are.



## 8. Current Investigations in Domain Wall Dynamics, Automated Experiments, and Visualisation Tools

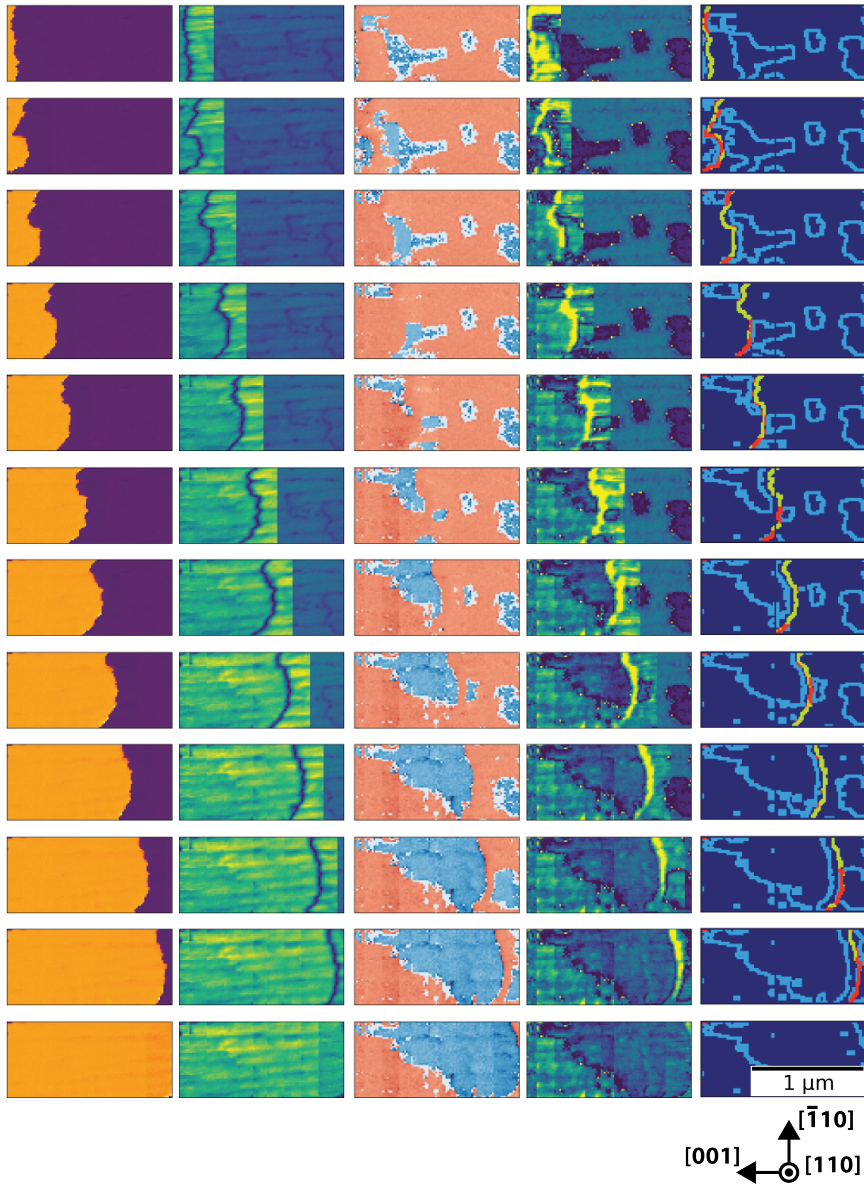


**Figure 8.6:** A series of switching experiments (proceeding from top to bottom) with interleaved writing scans. From left to right: Vertical phase; vertical amplitude; lateral phase; lateral amplitude; assignment of domain-wall orientation, with 71°, 109°, and 180° domain walls marked in light blue, green, and red respectively. The cantilever was oriented along the  $[110]$  direction and scanned with a  $[001]$  fast scan axis.

## 8.2 Tools for Reciprocal Space Visualisation and Analysis

Before we reach the final conclusions of this thesis, I wanted to briefly talk about a small pet project of mine—improved tools for visualisation of x-ray diffraction reciprocal space maps (RSMs). In Section 3.2 I have discussed the theory of RSMs in some<sup>1</sup> detail; however, what I have found over all my attempts to perform and interpret RSMs is that it is particularly difficult to develop an intuitive understanding of what these maps even mean. Over this particular PhD program, I have also been fortunate enough to have the responsibility to teach *Travaux Pratiques*, or practical works, to undergraduate students within the University of Geneva. I have found that, with regards to RSMs, the experiences of my students have very much echoed my own: determining what a particular RSM or x-ray diffraction spectra *means* for a real-space crystallographic lattice is inherently unintuitive; how do transformations in a real-space coordinate systems affect transformations in reciprocal-space coordinate systems, and vice versa?

Some particular transformations I present in Fig. 8.7. In Fig. 8.7(a), I show a square lattice of unit size one, whose reciprocal space transformation is itself. In Figs. 8.7(b-e), the effects of translation, scaling, rotation, and shear are respectively shown. While each of these transformations in real (reciprocal) space have a simple respective transformation in reciprocal (real) space, intuiting the effects of all four together, as shown in Fig. 8.7(f), is substantially more difficult. In much the same way, the concept of a point in reciprocal space corresponding to a set of parallel planes in real space (or at least, in 3-dimensional real space; it would correspond to a set of parallel lines in 2-dimensional real space) can also be difficult to intuitively discern.

To that end, I have developed a tool to help appreciate how transformations in real space affect reciprocal space and vice versa. A screenshot of this tool can be seen in Fig. 8.8; see its associated caption for particular details on interactive elements.

A key advantage of this tool is that the user is provided direct control of the reciprocal lattice point, and can control it in either Cartesian or polar coordinates via a slider to see how even slight changes affect the real-space lattice. The user is also able to directly enter real-space coordinates from which to start from, and this tool can also connect to the Materials Project website and API to acquire lattice parameters from the associated Materials Project ID [4]. This, in combination with visualisation of the incident and diffracted beams, and associated Ewald’s spheres, allows the user to fully perceive the effects of these lattice transformations on each other, and the x-ray sources they use to experimentally monitor them.

---

<sup>1</sup>Perhaps too much...

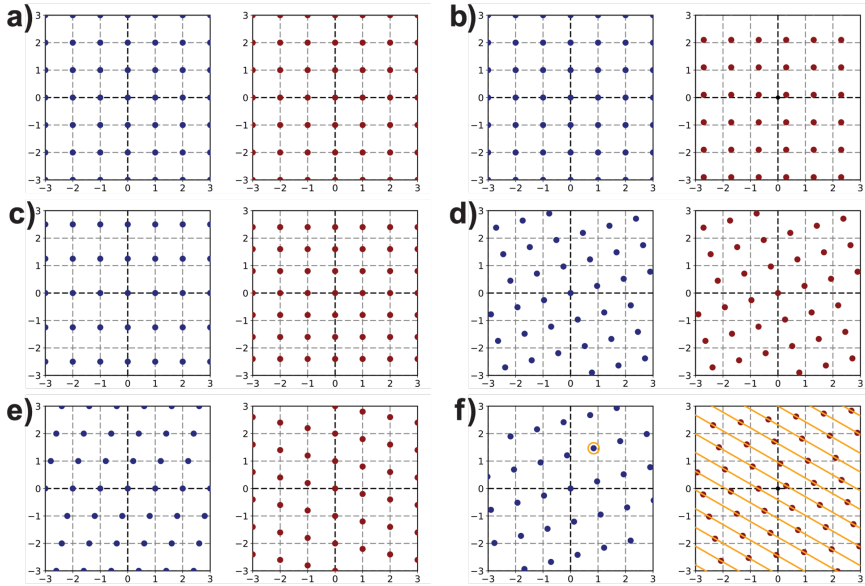


**Figure 8.7:** Effects of common transformations of real space (right, red) on reciprocal space (left, blue). (a) Square lattices are unchanged between real and reciprocal space. (b) Translations in a real lattice have no effect on a reciprocal lattice. (c) Size scaling is inverted along the same axis. (d) Rotations are directly conserved. (e) Shear strains affect orthogonal axes. (f) Compounding transformations in (b-e) on the square lattice shown in (a) creates complex behaviour. The orange lines in real space correspond to the orange-circled point in reciprocal space.

Beyond these practical and scientific goals, I have also taken inspiration from educational games, and the impact some such games have on student learning [5, 6]. I have added some prototype gaming elements, in which the user (or, in this context, the ‘player’) must transform their reciprocal lattice to find the point in reciprocal space that corresponds to a randomly generated real-space crystallographic system within a limited time span. While we have performed no comprehensive, double-blind studies, this tool has indeed seemed to help myself and some collaborators in perceiving the effects of reciprocal lattice transformation.

While this program is primitive<sup>2</sup> there do remain substantial and key areas of improvement. The shown prototype is coded entirely in the Python package Matplotlib, which I suspect was now the developer’s intended use. For more real, practical use, the ability to display 3-dimensional crystals, and complex unit cells (like perovskites) or material systems (like thin films or superlattices) would be highly beneficial. Education and gameplay elements could also be strongly refined and reiterated on. To that end, I

<sup>2</sup>The unit cells are also.

## 8.2 Tools for Reciprocal Space Visualisation and Analysis

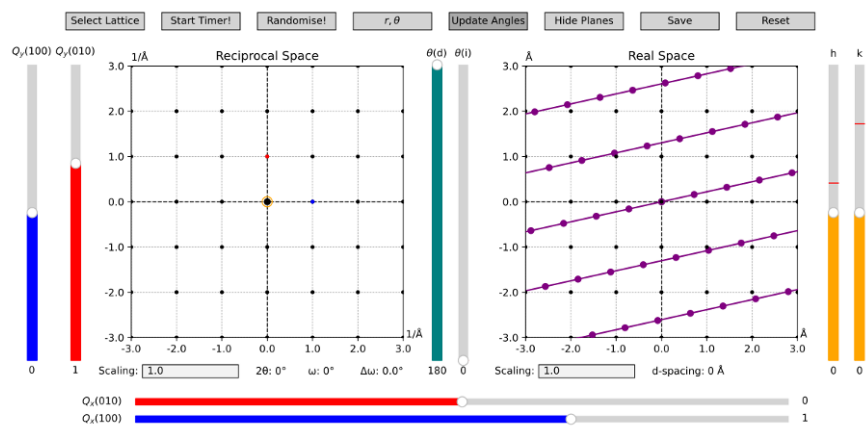


**Figure 8.8:** Screenshot of a prototype of the proposed tool. Red and blue sliders (left and bottom) alter the position of the red and blue lattice points in reciprocal space, leading to corresponding motion of the lattice in real space. Orange sliders (right) allow selection of a particular point in reciprocal space, and corresponding plane (line) in real space.  $\theta(i)$  and  $\theta(d)$  control an ‘incident’ and ‘diffracted’ x-ray beam analogous to experimental x-ray diffraction that provides an alternative method of plane selection. Left and right arrow keys can present example ‘instructions; to the player. Buttons from left to right are as follows: *Select Lattice* allows direct input of a particular real crystal lattice via crystal structure or Materials Project ID [4]; *Start Timer* starts 100-second countdown so users can record the speed with which they can reach alignment; *Randomise!* generates a random plane to be aligned to; *r,  $\theta$*  switches control of the position of principal vectors in reciprocal space from Cartesian coordinates to polar coordinates; *Update Angles* updates  $\theta(i)$  and  $\theta(d)$  sliders if possible to allow measurement of a particular point in reciprocal space and makes the relevant ‘x-rays’ visible; *Hide Planes* hides the planes (lines) in real space section, leaving only the lattice points; *Save* generates an image for display purposes; *Reset* restores the program to its initial configuration.

have partnered with game developer Lucas Mayor to help continue creation of this visualisation tool.

This Chapter has outlined two current projects I am working on; domain wall dynamics in a complex rhombohedral system, and a visualisation tool for x-ray diffraction RSMs. In their own ways, both of these projects build up off work and expertise reported in previous Chapters of this thesis. In the following, final Chapter, in the context of current and potential future results and applications, I will conclude my thesis and give my perspective on the future of this work.

### References

- [1] W. Cao and L. Cross, “Theory of tetragonal twin structures in ferroelectric perovskites with a first-order phase transition”, *Physical Review B* **44**, 5 (1991).
- [2] J. Přívratská and V. Janovec, “Spontaneous polarization and/or magnetization in non-ferroelastic domain walls: symmetry predictions”, *Ferroelectrics* **222**, 23–32 (1999).
- [3] Oxford Instruments, *Quadrature Phase Differential Interferometry (QPDI) technology in the Asylum Research Vero AFM*, <https://afm.oxinst.com/assets/uploads/products/asylum/documents/Technical%20Note:%20QPDI%20technology%20in%20the%20AR%20Vero%20AFM%20WEB.pdf>, Accessed: 2024-03-11.
- [4] <https://next-gen.materialsproject.org/>, Accessed: 2024-05-17.
- [5] U. Tokac, E. Novak, and C. G. Thompson, “Effects of game-based learning on students’ mathematics achievement: a meta-analysis”, *Journal of Computer Assisted Learning* **35**, 407–420 (2019).
- [6] L.-H. Wang, B. Chen, G.-J. Hwang, J.-Q. Guan, and Y.-Q. Wang, “Effects of digital game-based STEM education on students’ learning achievement: a meta-analysis”, *International Journal of STEM Education* **9**, 26 (2022).

---

## Conclusions and Perspectives

---

Through this thesis, we have used scanning probe microscopy as a tool to investigate the power-law distributions key to the domain-wall dynamics of ferroelectric materials. In doing so, we have made several key technical and scientific achievements that we have discussed through this report.

With our *Hystorian* package, we have developed a new tool to improve, track, and streamline data processing from different datasets. A recurring theme in this thesis is that of universality; power-law distributions are invariant in scale and reoccur in seemingly distinct systems, and ferroelectrics are model systems from which to investigate more general phenomena. In much this same way, *Hystorian* succeeds in generalising data processing as a whole, and has the potential to ease investigations of distinct phenomena in distinct physical systems.

For analysing power-law distributions in particular, our most notable technical achievement lay in our new tools to enable the study of power-law statistics in 2-dimensional datasets. We have managed to establish and validate the ability to map a power-law distribution onto a 2-dimensional array, and used this to compare techniques of analysing such datasets that have previously been discussed in the literature with two original approaches. We establish our novel ‘interface-tracking’ technique as generally most ideal, and describe where data size constraints preclude power-law distributions from being established. We expect this new capability to both create and analyse power-law distributions in such 2-dimensional image datasets will be particularly useful for scientists using and optimising various imaging tools.

This interface-tracking technique, when applied to pristine and ion-

## 9. Conclusions and Perspectives

---

bombarded PTO thin films, was used in this thesis to examine the impact of defects on the scaling exponent of the domain-wall motion. While it was initially expected that increased pinning would alter the critical scaling of such domain-wall motion, we verified that the global avalanche behaviour was indeed consistent—despite the different coercive voltages being needed for such domain-wall motion to occur.

On closer inspection, however, we observed a distinct and surprising phenomena in the domain-wall motion in these PTO thin films; while, in all cases, the  $180^\circ$  domain walls slowed down in the vicinity of the  $a$ -domains, which acted as strong pinning sites, the decrease in domain-wall velocity was far greater in the sole non-bombarded sample. We conclude that such complex defect ‘dressing’ effects, in which the induced defects screen the effects of  $a$ -domains, can be attributed to the segregation and orientation of point defects along the crystallographic axes, and thus suggest that this local defect organisation can and should be considered for future ferroelectric devices and research.

Finally, measuring the truly nanoscale power-law dynamics in ferroelectric materials through nanoindentation begets another advancement. We were able to measure a scaling parameter for mechanical slip-avalanches in PTO thin films that is compatible with theoretical results and consistent over multiple orders of magnitude—an achievement beyond that reported in prior work. Further, in BFO, we measure an increased, force-dependent scaling parameter which we attribute to the structural phase transition between T’- and R’-phases, verifying the suitability of this technique to measure the critical exponent for other such transformations.

The work here performed has, as is the case for many theses, nonetheless opened up more questions than it has answered. Some of these questions we have already started to address; others are much further off on the horizon.

My own current interest lies in part in the complex relationship between out-of-plane and in-plane orientations, and their affects on domain dynamics. We have already in this thesis discussed how (110)-oriented BFO, combined with automated experiments, can be used as a model system to discuss this phenomenon. How does our combined out-of-plane and in-plane polarisation, and our distinct domain-wall orientations, affect the resulting complex domain wall dynamics? We hope to step towards an answer in the coming months.

The monitoring of local structural power-law dynamics via nanoindentation also allows for various future experiments in structural transitions and how they relate to ferroelectrics. Strain gradients and flexoelectricity can drive ferroelectric polarisation switching [1], and combined flexoelectric–ferroelectric interactions can have potential applications in nanostructure lithography via asymmetric polarisation-dependent nanotribology responses [2]. Nanoindentation studies on particular ferroelectric or

ferroelastic domains, or performed with concurrent applied voltages, could allow for more precise measurements of ferroelectric switching than otherwise outlined in this thesis.

The programming tools developed also have various potential uses and applications. We have discussed already how our development of reciprocal-space visualisation tools could be expanded for educational use. Beyond this, our interface-tracking protocol can be used beyond ferroelectrics for more general cases where we track an interface via stroboscopic measurements; for example, to analyse simulated, theoretical, or experimental datasets for different disordered elastic systems.

While we have focused on SPM in this thesis, many of the tools developed also stretch beyond this one technique. Such comparisons between these techniques could also be a future direction of research. As already discussed in this thesis, avalanche statistics in domain switching can be observed by both optical and scanning probe microscopy; though difficult, simultaneous acquisition of domain avalanche critical scaling via different techniques, analysed by identical methods, could provide an incomparable display of scale invariance in this system.

While we have here used scanning probe microscopy to investigate ferroelectric materials in the context of power-law distributions, and in this thesis we have made key steps forward in all three together, the generality and universality of all these components are applicable work far outside it. As such, I can only hope that, with the conclusion of this thesis, I have left the reader with a better, more well-rounded understanding of the diverse, distinct, and yet surprisingly self-similar phenomena we find in our world—as I know I have.

## References

- [1] G. Catalan, A. Lubk, A. Vlooswijk, E. Snoeck, C. Magen, A. Janssens, G. Rispens, G. Rijnders, D. H. Blank, and B. Noheda, “Flexoelectric rotation of polarization in ferroelectric thin films”, *Nature Materials* **10**, 963–967 (2011).
- [2] S. Cho, I. Gaponenko, K. Cordero-Edwards, J. Barceló-Mercader, I. Arias, D. Kim, C. Lichtensteiger, J. Yeom, L. Musy, H. Kim, et al., “Switchable tribology of ferroelectrics”, *Nature Communications* **15**, 387 (2024).





# APPENDIX A

---

## False Power-Law Distributions through Inverting Optical Beam Deflection

---

This appendix briefly describes a fun ‘negative result’ for which I could not otherwise find a good location. This appendix builds up off the concept of power-law distributions by inversion around a zero value as discussed in Section 2.7.2, and was performed in the preparatory work for what would become Chapter 7 of this thesis. I also assume the reader has a comprehensive understanding of scanning probe microscopy, as discussed in Section 3.1.

Now, in the original conception of our nanoindentation results, we gathered deflection data from OBD-based methods. In Fig. A.1, we measured this deflection during the tip engage. The deflection value increases as the tip indents into the sample. To ensure that the full data range can be used by the machine, we set the photodetector such that the experiment the deflection is at a negative value when the tip is initially engaged. This was to allow optical beam to stay within the centre of the photodetector for as long as possible (which we expect to be more accurate and linear), and also to allow measurements over a longer range (to prevent us from hitting the limits of the photodetector). For this reason, the deflection starts at a negative value, then becomes positive during the experiment.

Next, we tried to assess our deflection jumps, which is reported in Fig. A.2. Here, an issue with the photodetector becomes prominent; we have a ‘noise envelope’, with high noise values when the magnitude of the deflection is also high. We attribute this to otherwise normal functioning of a split photodetector, where, since the AFM system measures the deflection as a

## A. False Power-Law Distributions through Inverting Optical Beam Deflection

---

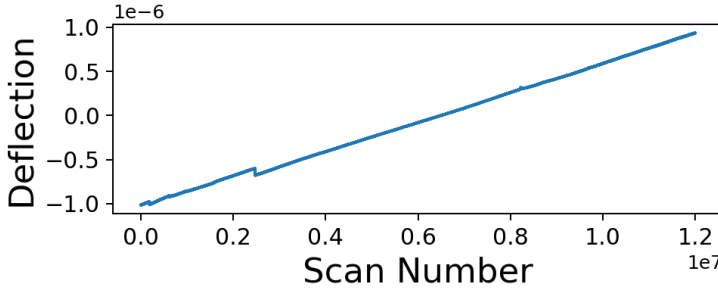


**Figure A.1:** Raw deflection data obtained by nanoindentation with an OBD-based setup, after tip engage and during the indentation process.

difference between two separate photodetecting units, moving so far away from one would increase the relative noise of that measurement. In standard use of an AFM, where we stay within the centre of the photodetector, and we are not subtracting deflection values, this is not relevant, but is observed here as a consequence of these two goals.

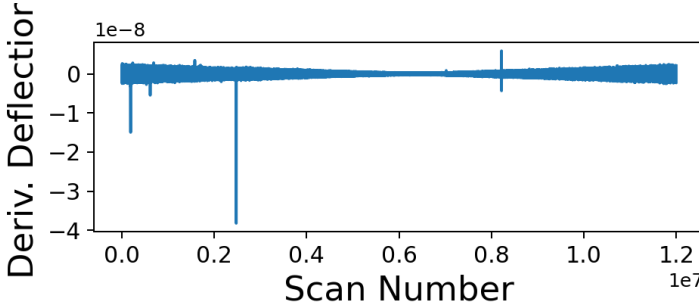


**Figure A.2:** Derivative of raw deflection data obtained by nanoindentation with an OBD-based setup.

In pondering how to adjust for this noise envelope, we quickly noticed that this noise envelope is roughly linear—and physically, probably derived from the OBD method itself. Thus, we considered the best way to adjust for this noise envelope would be to normalise our deflection derivative by the value of the deflection (Fig. A.3). In this case, we do actually see what appears to be crackling noise, and a nice distribution between large and small events... however, in reality, we induced a false power law by inverting around zero—the deflection passed zero during the experiment!

As such, when we generate a log-log plot or MLE plot (Fig. A.4, we apparently get an almost perfect power-law distribution, with a critical

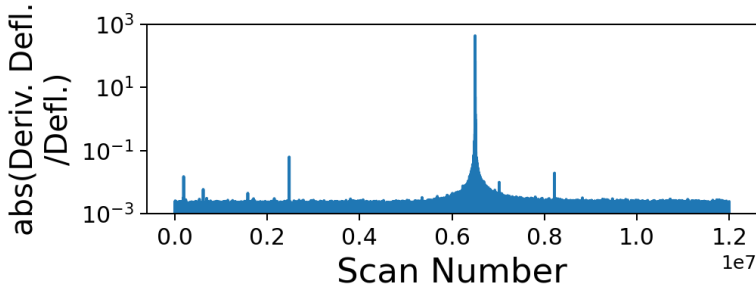


**Figure A.3:** Derivative of raw deflection data, divided by the raw deflection data obtained by nanoindentation with an OBD-based setup.

exponent of 1.994..., or otherwise very near to 2. This is not physical. Indeed, in this particular case, all that was observed was an inversion around a zero value of deflection. The moral of the story, if there is one, is that particular care should be taken not to divide by (or in this case, near) zero. Which when put that way I suppose is pretty obvious.

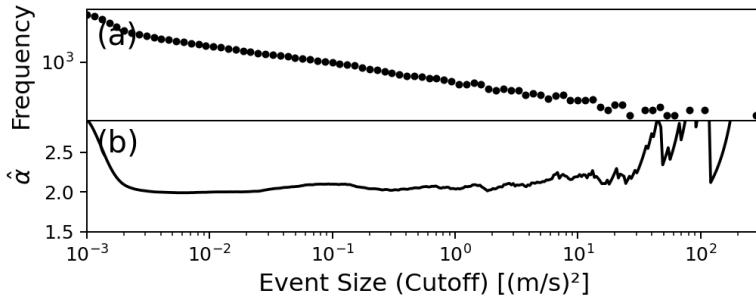


**Figure A.4:** Apparent, but false, power-law behaviour. (a) log-log plot and (b) MLE plot.



---

## Abbreviations

---

**AC:** alternating current

**AFM:** atomic force microscopy

**BFO:** bismuth ferrite ( $\text{BiFeO}_3$ )

**R-phase:** rhombohedral phase ( $R\bar{3}c$ ), stable at bulk

**R'-phase:** rhombohedral-like monoclinic phase ( $Cc$ )

**T-phase:** tetragonal phase ( $P4mm$ )

**T'-phase:** tetragonal-like monoclinic phase ( $Cm$ )

**CDF:** cumulative distributive function

**FWHM:** full width at half maximum

**HDF5:** Hierarchical Data Format 5

**KPFM:** Kelvin probe force microscopy

**LAO:** lanthanum aluminate ( $\text{LaAlO}_3$ )

**MFM:** magnetic force microscopy

**MLE:** maximum-likelihood estimation

**OBD:** optical beam deflection

**PDF:** probability distribution function

**PFM:** piezoresponse force microscopy

**BE:** band excitation

**DART:** dual AC resonance tracking

**DFRT:** dual frequency resonance tracking

## A. Abbreviations

---

**LPFM:** lateral piezoresponse force microscopy

**SS-PFM:** switching spectroscopy piezoresponse force microscopy

**VPFM:** vertical piezoresponse force microscopy

**PLD:** pulsed laser deposition

**PTO:** lead titanate ( $\text{PbTiO}_3$ )

***a*-domain:** domain with in-plane, *a*-axis-oriented polarisation

***c*-domain:** domain with out-of-plane, *c*-axis-oriented polarisation

**PZT:** lead zirconate titanate ( $\text{PbZr}_x\text{Ti}_{1-x}\text{O}_3$ ,  $[0 \leq x \leq 1]$ )

**QPDI:** quadrature-phase differential interferometry

**RMSE:** root-mean-square error

**SPM:** scanning probe microscopy

**SRO:** strontium ruthenate ( $\text{SrRuO}_3$ )

**STM:** scanning tunneling microscopy

**STO:** strontium titanate ( $\text{SrTiO}_3$ )

**TAFF:** thermally assisted flux flow

**XRD:** x-ray diffraction

**RSM:** reciprocal space map

**XRR:** x-ray reflectivity

---

## Acknowledgements

---

So for better or worse I've left this section as the very last thing to write. I know it's a cliché to say that this thesis wouldn't have been possible without the help of anyone or everyone, but the truth really is that I doubt my words could grasp the smallest portion of the thanks I have for those around me. Though there is no way I can ever thank you enough, I will do my best.

First and foremost, I want to thank the Paruch group and related members in the Department of Quantum Matter Physics. Kumara, Philippe, Christian and Guillaume; you made me feel so very welcome from the moment I came, taught me so much, and helped set the stage for my PhD. Iaro, your advice and perspective on everything, science and non-science, has always been immensely valuable to me, and our periodic AFM masterclasses have taught me so much, and left me realising I still have so much more to learn. Marios, your deep insight into everything about ferroelectrics in particular, and the world of science in general, is something I am immeasurably appreciative of. Nirvana, every time I speak to you I'm stunned by how much you know. Seongwoo, Lukas, Greta, Céline, Vivienne; our various meetings and coffees and beers and journal clubs have been so very fruitful and have helped make my time here so vibrant. All the past group members too—though we may never have spoken, your own works have been an invaluable resource to me.

I'm also incredibly thankful for the time I've had at other labs and institutions, and with all the people who I've spoken with there, or who've helped me while there, who have helped contribute to my own knowledge and understanding of this strange world of microscopy, ferroelectrics, and programming. From the the Center for Nanophase Materials Sciences at Oak Ridge National Labs, I particularly want to thank Rama, Neus, Shiva, Marti, Liam, Yongtao and Soyun, without whom my understanding of AFM would be far less complete, and without whom wouldn't have known where even to start with automating experiments. The *Vero* team at Asylum Research, including Joel, Aleks, Dara and Roger, also allowed me use of their QPDI



## A. Acknowledgements

---

setups, leading to the creation of Chapter 7 of this thesis; for this and all the knowledge of the underlying design and engineering of their AFM models, I, again, am grateful.

This thesis also would not have made it nearly that far without support from Nagy Valanoor, and the current and past members of the Thin Film Ferroelectrics group at the University of New South Wales. The thick T'-phase BFO films in particular were grown by Gordon Luo, from conditions initially developed by Thomas Young; all other BFO films here I had grown, but only with training and supervision throughout the years by Dan Sando. Dan and Nagy, along with Stu, Tom, Vivasha, Peggy, Amanda, Jackson, along with all my other immediate TFF predecessors I'd also like to extend particular thanks to—you trusted me and gave me my start, and I hope the training I've received from all of you in film growth, XRD, and AFM, flows through this thesis. Beyond this training and teaching, I'm also immensely grateful to the group for allowing me to use their AFM while the rest of the world was stuck in a COVID lockdown.

I'd be loath not to thank all my other previous supervisors and seniors in my previous research groups as well, be they ferro or non-ferro, for the general knowledge and understanding that the years have brought. Scarlet, John, Jason, Jacob, Lawrence, Kristina, Damia, Robert, Ky, Adam, Ulises, Penny, Laura, and all my fellow students in the research groups therein; I've been incredibly lucky for having your past, present, and future guidance, and I can only hope to pay it forward.

To those students I've had, officially or otherwise, I wish you all the best of luck in wherever you are at with life, and I hope you learned at least something with me. My TP3 students at the University of Geneva—Kenji, Florian, Laure, Brayan, Laura, Tanguy, Franck, Michael, Adonis and Nicolas—, and my fellow students in the Support for Laser Ablation and Virtually every other Experiment team at the University of New South Wales—Liam, Christie, Xi, Vicki—thank you for our chats, for listening, for our conversations, for helping me grow as well. To the rest of this new generation of PhDs—Tancredi, Gordon, Kayla, Xueqing, Ian (you're all still new, right?)—wherever you are, I wish you the best of luck as well.

Some miscellaneous, practical thanks are also in order as well. I would like to thank Rama Vasudevan (Center for Nanophase Materials Sciences), Miryam Arredondo (Queens University Belfast) and Thierry Giamarchi (University of Geneva) for serving on my jury committee. This PhD as a whole also wouldn't have been possible without funding from the Swiss National Science Foundation under Division II (Grant No. 200021-178782). The PTO thin films used in Chapters 6 and 7 were grown by Sahar Saremi in the group of Lane Martin while they were working at the University of California, Berkeley. Chapter 7 was greatly improved by conversations with Jirka Hlinka (Czech Academy of Sciences). Chapter 5 was closely

---

read by Elisabeth Agoritsas (University of Geneva), and Michelle Wang (Technical University of Denmark). Michelle also constructed Table 2.1 and the schematics therein, fully in L<sup>A</sup>T<sub>E</sub>X, from a much worse initial scrawl I presented to her. Michelle, your L<sup>A</sup>T<sub>E</sub>X and Python wizardry, and your willingness to read and help with so much of such an experimental (!) thesis discussing actual materials (!!!) is a testament to your grace as a friend and capability as a scientist. Additional diagrams for my thesis defence were also produced with the Manim Python package, created, maintained and promoted by James Schloss, Grant Sanderson, and the rest of the Manim and Summer of Math Exposition communities, while Andreas helped 3D print a wonderful model of mixed-phase BFO to help bring some ‘structure’ to my talk.

I believe the Ultrasonics, Ferroelectrics and Frequency Control (UFFC) Society of the Institute of Electrical and Electronics Engineers (IEEE) is also particularly worth thanking. Stu, Andreja, Federica, Brooke, Ipek, Mark, Dragan, Colleen, Julia, and everyone else in the various committees have provided not only me, but so many other students the ability to learn and meet and network with our peers, our seniors, and our juniors, through all the various conferences, schools, meetings and events. I’d like to extend this thanks to all the conference and event organisers (UFFC or otherwise), and all my friends who I’ve made at such—there are far too many to list, but you know who you are. As they say, maybe the real PhD experience was the friends we made along the way!

Closer to home, closer to Geneva, though, it really is my friends who keep things going, keep me driving and pushing myself forward. To all the other PhDs and postdocs around, you made my time in Geneva and my time in this PhD so memorable and so valuable. I don’t have the space here to thank all of you by name (I think this section is already stretching far longer than most!), but in particular: Loïc, thank you so much for all our small chats, for helping me settle in, for helping me work through all the various issues, big and small, technical and non-technical, Python, python, and non-Python that pop up over the years; and Ludo too, practically for the help with electrodes and with the MFP, but also for your great company and for being such a great friend. And I suppose, now that I’ve finished thanking all my friends, I ought to thank Lucia as well... though sincerely, thank you, for the physics and the XRD and the oxides but more importantly for everything else and the countless little things. Thank you all. I wish all of you luck when it’s your turn to defend, and for everything that comes afterwards.

Though perhaps I have very much buried the lede here. Five years ago I wouldn’t have imagined I’d learn even a fraction of what I’ve learned from you, Patrycja. Not just about the science, about ferroelectrics and scanning probe and disordered elastic systems and power laws, but about how to learn, how to grow. How to keep on going forward and moving on when

things goes wrong, and how to find joy and success when things go right. All these lessons I will carry on through life.

And Kathryn, with all your love and kindness and support we've gotten through this! Now it's our turn to take a step, day by day moving forward along the paths we can still choose.

There is no way I can thank you—all of you—for your help and guidance. Through the successes and the failures, the good times and the bad, your support over the years has been invaluable.

And to you dear reader, I thank you for taking the time to read this. I hope you find some value in this, learn something new, or at least see a new perspective; and in return I just ask you forgive my uncaught typos and the 3-am-written bad jokes. If you are, like I was, a final-months PhD student looking through past theses, trying to gleam some hidden knowledge or secrets on how to move on proceed, all I have left, all I can do, is to encourage you to take it on, step by step, do what you can, and wish you luck.

---

*“And if we don't manage, then what?  
My lifetime... it's barely a blip.”*

*“If you don't,  
pass it on.”*

*“Huh?”*

*“Let someone else carry on your dream.  
That's how we've always rolled. Us lot.”*

*Rex and Glimmer, Future Redeemed*